Universitat Autònoma de Barcelona

A BIRD'S-EYE VIEW OF CHARGE AND SPIN DENSITY WAVES FROM FIRST PRINCIPLES CALCULATIONS

Ionel Bogdan Guster

Universitat Autònoma de Barcelona

Doctoral Thesis

A BIRD'S-EYE VIEW OF CHARGE AND SPIN DENSITY WAVES FROM FIRST PRINCIPLES CALCULATIONS

Student:
Ionel Bogdan Guster

Supervisors:
Prof. Dr. Pablo Ordejón
Prof. Dr. Enric Canadell
Dr. Miguel Pruneda

Tutor:
Dr. Miguel Pruneda

A thesis submitted in fulfillment of the requirements for the degree of Doctor of Philosophy in Physics

Theory and Simulation Group

Catalan Institute of Nanoscience and Nanotechnology
Autonomous University of Barcelona

June 2019

Declaration of Authorship

I, Ionel Bogdan GUSTER, declare that this thesis titled, ' **A BIRD'S-EYE VIEW OF CHARGE AND SPIN DENSITY WAVES FROM FIRST PRINCIPLES CALCULATIONS**' and the work presented in it are my own. I confirm that:

- This work was done wholly or mainly while in candidature for a research degree at this University.
- Where any part of this thesis has previously been submitted for a degree or any other qualification at this University or any other institution, this has been clearly stated.
- Where I have consulted the published work of others, this is always clearly attributed.
- Where I have quoted from the work of others, the source is always given. With the exception of such quotations, this thesis is entirely my own work.
- I have acknowledged all main sources of help.
- Where the thesis is based on work done by myself jointly with others, I have made clear exactly what was done by others and what I have contributed myself.

Signed: _____

Date: _____

To Olga

Man has gone out to explore other worlds and other civilizations withouth having explored his own labyrinth of dark passages and secret chambers, and without finding what lies behind doorways that he himself has sealed.(Solaris)

Acknowledgements

The PhD metamorphosis was enriched by the many people that I am grateful to have met during these past four years of my life.

Firstly, I would like to thank to my thesis advisors, Pablo, Enric and Miguel, for trusting me with the interesting and intellectually provocative projects, for all the knowledge that they have shared with me about physics principles and how to do rigorous scientific work, inspiring me with all the values that comes with it, for their constant feedback, for their motivating enthusiasm for science, for their patience in general.

I would like to thank to the collaborators on the papers that we published, especially to Jean-Paul Pouget, who shared from his immense knowledge about density waves, and to Roberto, who always brought a different perspective.

To my friends and colleagues from ICN2 with whom I had a good laugh or an interesting discussion, in particular to the friends from the Theory and Simulation group (Lorenzo, Ruben, Sergio, Ramón, Laura, Vladimir, Desanka, Jose, Nick, Arsalan, Zeila, Matthieu, Nils and many more); to the friends of ICN2 that taught me to play padel or with whom I had a good run in a football game.

To my friends and flatmates, Andreea and Lili, with whom I always had a great time in our activities in or outside the flat.

To my friends from Bucharest, that always received me with the warmest welcomes and shared their time with me whenever I stopped by.

I would like to thank my family for their unconditional love, support and understanding, for the little time we spent together that made it so much more special.

Last but not least, to my partner, Olga, for always being there no matter what, for her infinite patience, for her carrying love and for her believing in me, for the time we spent together to discover the most amazing places around us in our most beautiful years so far.

For all this I believe I couldn't have been in a better place to pursue my PhD work and my passion for physics.

CONTENTS

LIST OF FIGURES

LIST OF TABLES

ABBREVIATIONS

AO	**A**nion **O**rdering
ARPES	**A**ngle **R**esolved **P**hoto**E**mission **S**pectroscopy
BEDT-TTF	**B**i**E**thylene**D**i**T**hio-**T**etra**T**hia**F**ulvalene
BOW	**B**ond **O**rder **W**ave
BZ	**B**rillouin **Z**one
CDW	**C**harge **D**ensity **W**ave
DOS	**D**ensity **O**f **S**tates
DFT	**D**ensity **F**unctional **T**heory
EPC	**E**lectron **P**honon **C**oupling
FS	**F**ermi **S**urface
GGA	**G**eneralized **G**radient **A**pproximation
HREM	**H**igh **R**esolution **E**lectron **M**icroscopy
LDA	**L**ocal **D**ensity **A**pproximation
LRF	**L**indhard **R**esponse **F**unction
NMR	**N**uclear **M**agnetic **R**esonance
SCF	**S**elf **C**onsistent **F**ield
SDW	**S**pin **D**ensity **W**ave
SIESTA	**S**panish **I**nitiative (for) **E**lectronic **S**tructure (with) **T**housands (of) **A**toms
STM	**S**canning **T**unneling **M**icroscopy
STS	**S**canning **T**unneling **S**pectroscopy
TMDC	**T**ransition **M**etal **D**i**C**halcogenides
TMTSF	**T**etra**M**ethyl**T**etra**S**elena**F**ulvalene
TTF-TCNQ	**T**etra**T**hia**F**ulvene-**T**etra**C**ya**N**o**Q**uinodimethane

PART I

INTRODUCTION

0. INTRODUCTION

This thesis deals with the electronic structure of low dimensional metals in the form of either single layers or bulk. Low dimensional metals were predicted long-time ago to exhibit a distinctive physical behaviour [1, 2] because of the special topology of their Fermi surface, which is prone to sustain different instabilities like charge density waves (CDW) or spin density waves (SDW). A CDW electronic instability is usually coupled with a periodic lattice distortion which opens a gap at the Fermi level thus leading to a metal to insulator transition. This is the well known Peierls distortion [3]. In the case of a SDW it is the spin density which is modulated and in that case the instability is not coupled to a noticeable structural distortion although is also associated with a metal to insulator transition. However, for many years these theoretical predictions could not be tested because of the lack of appropriate materials. The first one-dimensional material for which the Peierls distortion could be well characterized (nature of the structural modulation, occurrence of a Kohn anomaly[1]) was the Krogman salt [4]. This work was very important in calling the attention of the solid state community to low dimensional conductors.

It was during the seventees of the last century that several types of low dimensional metals could be prepared or rediscovered. The seminal work by Wilson, DiSalvo, and Mahajan [5] and by Williams, Parry and Scruby [6] on group IV and V transition metal dichalcogenides, was very important in showing that two-dimensional materials could be the locus of different structural CDW modulations associated with metal to metal and metal to insulator transitions. These modulations were proposed to originate from the so called nesting of the Fermi surface, a generalization of the Peierls mechanism for two-dimensional metals. This

[1]The origin of the Kohn anomaly is discussed in 1.2.

work stimulated a huge activity on inorganic low dimensional metals. Very soon one of the paradigmatic low dimensional metals, $NbSe_3$, exhibiting two successive CDWs was prepared and characterized [7]. $NbSe_3$ and the blue bronzes $A_{0.3}MoO_3$ (A= K, Rb), were the first pseudo-one-dimensional materials exhibiting non-linear trasport [8, 9] as a result of depinning of their CDWs thus confirming one of the theoretical predictions concerning low dimensional metals. Such discovery launched a huge interest on these conductors. Both low dimensional transition metal oxides and chalcogenides were intensely studied trying to unveil the physics of low dimensional metals.

Almost simultaneously another crucial discovery in this field was realized. Although several highly conducting organic donor-acceptor salts had already been prepared, the successful marriage of the TTF donor and TCNQ acceptor in the TTF-TCNQ molecular metal [10, 11] opened the route towards the preparation of highly conducting molecular metals. With a partial charge transfer of $\rho = 0.55$ electrons from TTF to TCNQ, TTF-TCNQ exhibits not only a room temperature conductivity of 500 S$\cdot$ cm^{-1} but also a metallic type behaviour in a large temperature range reaching a 10^4 S$\cdot$ cm^{-1} conductivity around 50 K, just before suffering a drastic drop due to the occurrence of a Peierls metal-to-insulator transition. The discovery of organic superconductivity at the beginning of the 1980s in the $(TMTSF)_2X$ (X= PF_6, ClO_4, NO_3, etc.), Bechgaard salts [12], boosted a whole new area of research. Molecular organic metals are interesting not only due to their superconducting properties but also because of their complex temperature-pressure phase diagrams exhibiting a large number of competing insulating ground states.

Both inorganic and organic low dimensional metals have been intensely studied since then and a plethora of new materials and unusual phenomena have been reported [13]. Recently, with the advent of successful techniques for the manipulation of layered materials it has been possible to prepare thin slabs with a reduced number of layers or even single-layers of these materials [14, 15]. This makes it

possible to study how the reduced electronic screening brought about by lowering the dimensionality from bulk to layers of different thicknesses influences the competition between electronic instabilities like superconductivity, CDW, etc. Layered transition metal chalcogenides have become again the focus of an enormous attention. In particular, the group IV and V transition metal dichalcogenides which played a crucial role in the development of the field have been reexamined as single-layers or a few-layers slabs and remarkable differences with the bulk materials have been reported.

With no doubt, the impressive development concerning low dimensional conductors is partly due to the fact that relatively simple ideas have led to the rationalization of many physical observations. A central role in most of the theoretical approaches is played by the notion that the electronic modulations occurring in these materials originate from Fermi surface nesting. Yet a careful examination of the experimental information casts strong doubts about the appropriateness of such notion for a considerable number of these conductors, including some of those studied since the very beginning of the field. The object of the present thesis is an appraisal of this situation based on the calculation of the Lindhard response function as well as the phonon band structure for a series of low dimensional conductors based on accurate first-principles DFT calculations.

We have studied a large number of systems which exhibit this type of anomalies:

- Single-layers: $TiSe_2$, $TiTe_2$, $NbSe_2$,
- Oxides: Blue Bronzes ($K_{0.3}MoO_3$), Monophospate Tungsten Bronzes, A_nB_nO3n+2, Mo_8O_{23},
- Chalcogenides: NbS_3, $NbSe_3$, TaS_3, $TaTe_4$, Ta_2NiSe_7, T
- Intermetallics: $LaAgSb_2$, $YAgSb_2$, $Y_2Ir_3Si_5$, $Y_5Ir_4SI_10$,
- Molecular Metals: Bechgaard salts, $\alpha-(ET)_2KHg(SCN)_4$.

As we suspected only some of these compounds exhibit density wave instabilities which are clearly related to Fermi surface nesting (e.g. Blue Bronzes, Bechgaard salts, Monophospate Tungsten Bronzes, $\alpha-ET_2KHg(SCN)_4$), while the others are related to phonon mediated mechanisms (e.g. $TiSe_2$, $NbSe_2$, $TaTe_4$, Mo_8O_{23}, $(TaSe_4)_2I$, $Y_2Ir_3Si_5$).

1. THEORETICAL BACKGROUND

1.1 Electronic structure approaches

The starting point for determining the ground state properties of a quantum system is to solve the Schrödinger equation:

$$\hat{H}\Psi = E\Psi, \tag{1.1}$$

where $\hat{H}$ is the Hamilton operator (or most commonly the Hamiltonian), Ψ is the wave-function and E is the energy level of the system.
The type of physical systems that we are going to examine in this thesis consist of electrons and nuclei, and their Hamiltonian can be written as follows:

$$\begin{aligned}\hat{H} = &-\frac{\hbar^2}{2m_e}\sum_{i}^{n}\nabla_i^2 - \frac{\hbar^2}{2}\sum_{j}^{m}\frac{1}{M_j}\nabla_j^2 \\ &+ \frac{1}{2}\sum_{i\neq j}^{n}\frac{e^2}{|\mathbf{r}_i - \mathbf{r}_j|} + \frac{1}{2}\sum_{i\neq j}^{m}\frac{Z_i Z_j e^2}{|\mathbf{R}_i - \mathbf{R}_j|} - \sum_{i,j}^{n,m}\frac{Z_j e^2}{|\mathbf{r}_i - \mathbf{R}_j|} + \hat{V}_{ext} \\ = &\hat{T}_e + \hat{T}_N + \hat{V}_{ee} + \hat{V}_{NN} + \hat{V}_{eN} + \hat{V}_{ext} \end{aligned},$$

where n and m are the number of electrons and nuclei in the system, the first two terms (T_e and T_N) express the kinetic energy of the electrons and the nuclei, respectively, the third term (V_{ee}) is the electron-electron Coulomb repulsion, the fourth term (V_{NN}) is the nuclei-nuclei Coulomb repulsion, the fifth term (V_{eN}) is the electron-nuclei electrostatic attraction and, finally, V_{ext} accounts for other potentials applied externally, like magnetic or electric fields.

The wave-function in solving the Schrödinger equation for the many particle problem is dependent on the position of both electrons and nuclei.

$$\hat{H}\Psi(\vec{r}_1, ..., \vec{r}_n, \vec{R}_1, ..., \vec{R}_m) = E\Psi(\vec{r}_1, ..., \vec{r}_n, \vec{R}_1, ..., \vec{R}_m)$$

The complexity of this equation makes it impossible to obtain the analytical solution of even very simple molecules (considering that we have 3n+3m degrees of freedom, the difficulty rises quickly even for a couple of particles). A very handy approximation was proposed by Born and Oppenheimer[16] where the movement of the nuclei (and implicitly their kinetic energy) is neglected due to the low momentum transfer between nuclei and electrons. In this approximation we can decouple the electronic degrees of freedom from the nuclear ones, and we can express the wave-function of the system as follows:

$$\Psi(\vec{r}_1, ..., \vec{r}_n, \vec{R}_1, ..., \vec{R}_m) = \Phi_e(\vec{r}_1, ..., \vec{r}_n, \{\vec{R}_1, ..., \vec{R}_m\})\phi_N(\vec{R}_1, ..., \vec{R}_m), \tag{1.2}$$

where Φ_e is the electronic wave-function dependent on the electrons positions with the nuclei positions as parameters since they are considered fixed, and ϕ_N represents the nuclear wave-function.
In the Born-Oppenheimer approximation we can rewrite our electronic Hamiltonian as:

$$\hat{H}_e = \hat{T}_e + \hat{V}_{ee} + \hat{V}_{eN} + \hat{V}_{ext} \tag{1.3}$$

with its corresponding Schrödinger equation:

$$\hat{H}_e\Phi_e(\vec{r}_1, ..., \vec{r}_n, \{\vec{R}_1, ..., \vec{R}_m\}) = E_e\Phi_e(\vec{r}_1, ..., \vec{r}_n, \{\vec{R}_1, ..., \vec{R}_m\}), \tag{1.4}$$

The treatment of the nuclear dynamics is another problem in itself which is outside the scope of this thesis, but the nuclear motion is relevant in calculating the phonon dispersion. For this purpose the nuclei are considered to move in an effective potential created by the electrons ($E_e(\{R\})$) and the phonons are calculated by solving the normal modes in the harmonic approximation.

In the past century, there have been several attempts to find the ground state solution to the electronic many body problem. Very early on with the emergence of the quantum theory, an approximate method to the many body wave-function was proposed, namely that the wave-function could be reasonably described by a single Slater determinant, finally reducing the many body problem to a one particle variational problem; this method is called the Hartree-Fock method.[17, 18, 19, 20, 21] Within this method, though, by assuming a one electron in an average non-local electron potential, one neglects the correlation effects between electrons.

In parallel with the Hartree-Fock method, the first density functional method was proposed by Thomas[22] and Fermi[23]. Even though this method had considerable shortcomings, due to neglecting exchange and correlation effects between electrons, it expressed the kinetic energy of the system entirely as a functional of the electronic density. Of course, a density functional based theory was very appealing due to the enormous reduction of degrees of freedom from 3N in the Schrödinger equation to 3 in a density functional based one. A more detailed description of the evolution of the electronic structure theory can be found in R. Martin's book[24].

1.1.1 Density Functional Theory

Hohenberg and Kohn provided a rigorous basis for calculating the exact ground state solution for a system of quantum particles by enunciating the following theorems[25] as put in[24]:

Theorem 1: *For any system of interacting particles in an external potential $v_{ext}(\vec{r})$, the potential $v_{ext}(\vec{r})$ is determined uniquely, except for a constant, by the ground state particle density $n_0(r)$*

Corollary 1: Since the Hamiltonian is thus fully determined, except for

a constant shift of the energy, it follows that the many-body wave function for all states (ground and excited) are determined. Therefore all properties of the system are completely determined given only the ground state density $n_0(\vec{r})$.

Theorem 2: *A universal functional for the energy* $E[n]$ *in terms of the density* $n(r)$ *can be defined, valid for any external potential* $v_{ext}(\vec{r})$. *For any particular* $v_{ext}(\vec{r})$, *the exact ground state energy of the system is the global minimum value of this functional, and the density* $n(r)$ *that minimizes the functional is the exact ground state density* $n_0(r)$.

Corollary 2: The functional $E[n]$ *alone is sufficient to determine the exact ground state energy and density.*

The first theorem basically states that there is a direct mapping between an external potential applied to a system and its ground state density, yet it doesn't provide any explicit direction on how to solve the many body problem. The second theorem calls for knowing the actual functional in order to obtain the exact solution to the ground state. These two theorems constitute the foundational basis of Density Functional Theory(DFT).

Thus we get to the Khon-Sham approach, which provides a practical scheme for exploiting the basic DFT theorems, by assuming a particular representation of the charge density in terms of non-interacting one-particle wave functions. This leads to the replacement of the many body problem by an independent one-particle problem placed in an effective potential that takes into account both exchange and correlation effects.[26]
The Kohn-Sham approach follows two assumptions:
1. The ground state density of an auxiliary system of non-interacting particles can represent the exact ground state, with the charge density given by:

$$\rho(\vec{r}) = \sum_{\sigma} \sum_{i=1}^{N} |\Psi_i^{\sigma}(\vec{r})|^2, \tag{1.5}$$

with $\Psi_i^\sigma(\vec{r})$ - one particle wave functions.

2.The auxiliary Hamiltonian is chosen to act as the usual kinetic operator and provide an effective local potential $v_{KS}(\vec{r})$ acting on an electron of spin σ at point $\vec{r}$.

$$\hat{H}_{aux}^\sigma = -\frac{1}{2}\nabla^2 + v_{KS}^\sigma(\vec{r}), \tag{1.6}$$

with the first term being attributed to the kinetic energy, while the second term to the potential energy that encompasses all the effects in the systems. The kinetic energy term in the Kohn-Sham picture can be written as:

$$T_s = -\frac{1}{2}\sum_\sigma \sum_{i=1}^N \langle \Psi_i^\sigma | \nabla^2 | \Psi_i^\sigma \rangle = \frac{1}{2}\sum_\sigma \sum_{i=1}^N \int d^3r |\nabla \Psi_i^\sigma(\vec{r})|^2 \tag{1.7}$$

and the Kohn-Sham effective potential as:

$$v_{KS}^\sigma = V_{ext} + V_{Hartree} + V_{NN} + V_{XC} \tag{1.8}$$

with V_{ext} coming from the interaction with nuclei and other external fields, V_{NN} is the interaction between nuclei, $V_{Hartree}$ is the self-interacting energy of the electron density and V_{XC} is the exchange-correlation term where all the many-body effects are included. The V_{XC} is the only term that has no known analytical formulation and the predictive power of this method is limited only by the approximations one makes to this term. Finally the ground state energy functional can be written as:

$$E_{KS} = T_s[\rho] + E_{Hartree}[\rho] + E_{NN}[\rho] + E_{XC}[\rho] + \int d\vec{r} V_{ext}(\vec{r})\rho(\vec{r}). \tag{1.9}$$

1.1.2 Approximating the Exchange-Correlation

In treating the exchange-correlation (XC) terms approximations have to be made, since there is no universal functional known for this. There are many approximations available to the XC, such as local density approximation (LDA), generalized-gradient approximation (GGA), hybrid functionals etc. For many purposes LDA and GGA proved to be reliable enough in describing the electronic properties of

many materials, although there are well known defficiencie which, in some cases, can be overcomed by using more sophisticated functionals.

The LDA approximation is based on the idea that the range of the exchange and correlation effects is short, so the XC energy density is assumed to follow the homogeneous electron gas energy density at each point:

$$E_{XC}^{LDA}[\rho(\vec{r})] = \int \rho(\vec{r})\epsilon[\rho(\vec{r})]d\vec{r} \tag{1.10}$$

LDA proved to work well in many situations, especially to those being closer to having a homogeneous electron density, but otherwise it proved to overestimate the binding energy, which in turn could severely underestimate lattice parameters in the case of crystal structures.

GGA comes as a natural step in dealing with the shortcomings of LDA, since in many materials one encounters rapidly varying charge densities. GGA takes into account not only the charge density, but also its gradient:

$$E_{XC}^{GGA}[\rho(\vec{r})] = \int f(\rho(\vec{r}), \nabla\rho(\vec{r}))\epsilon[\rho(\vec{r})]d\vec{r}. \tag{1.11}$$

Even though GGA corrects some parts of LDA, it overestimates the bonding distances. It has to be remarked that both of these XC functionals perform extremely poorly with strongly correlated systems of electrons and for this purpose other methods have to be considered. However these approaches to treating the XC functional proved successful in predicting the fundamental properties for a large number of classes of materials. Throughout this thesis we will resume ourselves to treat DFT mostly within GGA.

1.1.3 The SIESTA method

Apart from the XC treatment and the different approximations considered up so far for treating many body systems, one has to find proper numerical ways to

describe the electronic wave-function in solving the Schrödinger equation. For this purpose there have been many approaches over the past decades, but most common implementations involved either atomic spheres, plane-waves or a linear combination of atomic orbitals. Throughout this thesis we have used the implementation of the self-consistent Kohn-Sham density functional theory available in the SIESTA package.[27, 28]

The SIESTA method involves two further approximations and a slight modification to the standard Kohn-Sham Hamiltonian[27]. The first approximation in the SIESTA code, which is common to many other approaches including the most widely used ones based on plane-waves, is the replacement of the core electrons by an effective potential that acts on the valence electrons and providing an explicit description only for the valence electrons. This method of using a pseudopotential comes very handy in studying problems involving valence electrons and presents several advantages due to the reduction of the number of electrons, such as the reduction of the basis size since we are dealing with states involving only the valence electrons, the use of a uniform spatial grid instead of a logarithmically dense grid closer to the center of the atom that could have been needed due to the acute localization of the core electrons and, most importantly, the replacement of the true wavefunction that contains nodes with a smooth function without nodes. The replacing function gives an exact match of the true wavefunction beyond the pseudopotential cut-off radius r_c, radius that can be fine tuned for each angular channel independently.

The second approximation is to use numerical pseudo-atomic orbitals (NAOs). Since the valence wavefunctions of condensed matter systems retain to a large extent the shape of the atomic wavefunctions (perturbed by the presence of the nearby atoms), atomic orbital bases achieve sufficient accuracy with a finite (and a quite small) number of functions. The NAOs are made up of a numerical radial function and a spherical harmonic, as follows:

$$\phi_{Ilmn}(\vec{r}) = \phi_{Iln}(r_I) Y_{lm}(\hat{r}_I), \tag{1.12}$$

where I is the atoms's index, l is the angular quantum number, m is the magnetic quantum number, n is the principal quantum number and $\hat{r_I} = \vec{r} - \vec{R}_I$ ($\vec{R}_I$ - position of atom I). Inside the SIESTA package one can choose to use between one and multiple radial function for each angular momentum channel. In the case when one uses one radial function for each l-channel, it is referred as a single-ζ function (or basis set), otherwise it is referred as multiple-ζ basis set. To describe the second-,third-,ζ functions, one keeps the same (finite) extent (r_{max}) and the same tail within some range ($r^s \leq r \leq r_{max}$) as the first-ζ function, and below r^s a polynomial behaviour is employed[27].

$$\phi_l^{2\zeta}(r) = \begin{cases} r^l(a_l - b_l r^2) & \text{if } r < r_l^s \\ \phi_l^{1\zeta}(r) & \text{if } r \geq r_l^s. \end{cases} \tag{1.13}$$

Another important aspect in building the basis set is the use of polarization orbitals in order to account for the distortion of the atomic orbitals induced by the bond formation. One can do this in two ways in SIESTA: automatically by including the polarization flag in the basis description, in which case SIESTA will generate a $l + 1$ basis function for the polarized orbital, or manually where one could parametrize and optimize the polarization function included.

The localization and, implicitly, the finite range of the atomic wave-function is preserved by defining a confinement potential. In SIESTA one finds the extent of the radial component of the wave-function by solving the Schrödinger equation for the atom in a box including a soft-confinement potential of the form, as defined in[29]:

$$V(r) = V_0 \frac{e^{-(r_c - r_i)/(r - r_i)}}{r_c - r}, \tag{1.14}$$

with V_0 as a parameter, r_c as the confinement radius where the potential asymptotically tends to infinity and r_i as the starting point for the potential.

1.2 Charge (and Spin) Density Waves

The idea of an electronic instability has its roots in the 1930s when Peierls established that a one dimensional (1D) electron gas would be unstable against a periodic distortion of the the right periodicity leading to a perturbing potential that would produce [1]. The reorganization of electrons, nonetheless, has consequences on the underlying lattice in a real material due to the presence of electron-phonon couplings. The conjunction of the band gap opening around the FL and the periodic lattice distortion (PLD) that sets in as a consequence of the electron-phonon coupling was later determined by Peierls[3] and Fröhlich[2]. In the same decade, Kohn determined that the phonons of an uniform electron gas will experience a sharp frequency variations in dispersion when the phonon wavevector matches the diameter of the (electronic) Fermi sphere[30]; this notion was later referred to as the Kohn anomaly. This cooperative manifestation of the electrons and phonons in metallic systems gave rise to the notion of charge density waves (CDW). Nowadays, after 60 years, the CDW notion has reached broader connotations due to the variety of scenarios that a CDW can be set in different kinds of materials, metallic or otherwise. We will try in this manuscript to describe a comprehensive picture about the CDW manifestation, at least at the level of the studied materials in this thesis.

Let us first start with the reiteration of the CDW manifestation in (quasi-) 1D materials. We refer to materials as being quasi-one dimensional (1D) due to the nature of their electronic structure. Quasi-1D materials present a high energy dispersion along one particular direction around the FL, respectively weak to vanishing energy dispersion along the other directions. Most commonly, quasi-1D materials are prone to a phase transition from their initial metallic state into a CDW state below a certain temperature, T_c. The CDW transition is accompanied by both an electronic density modulation and a PLD, both being dependent on the topology of the Fermi surface (FS). We illustrate, as a case example, the behaviour of an equally spaced 1D linear chain (fig. 1.1.a.I.) which shows a uniform

charge density, ρ_0, throughout the structure, typical for a metallic system. The electronic dispersion at half filling (i.e. 1 e^- per site in this case) has the FL crossing at $k_F = \pm\pi/(2 \cdot a)$ (Fig. 1.1.b.I). The Fermi surface in this case consists of two points at $\pm k_F$ and they could be connected/nested by a wavevector $q = 2k_F$. In a 3D representation, the FS would be a pair of planes perpendicular to the a direction. The translation of Fermi surface states by a unique wavevector q that gives a perfect overlap between these states is called Fermi surface nesting (FS nesting). This scenario is commonly employed in describing the CDW formation in quasi-1D materials. The wavevector that produces such a match is responsible for the CDW formation in materials that present such a FS topology. More often than not, Peierls scenario is misrepresented in the literature. We would like to point out that FS nesting is intimately linked to the Peierls transition and where another mechanism drives the CDW formation, it should be referred to according to its origin.

The FS nesting, as represented in this simple model, allows for the spontaneous breaking of the symmetry in this system, which in turn has two effects: the reorganization of the charge density in a wave-like pattern with a periodicity dictated by the nesting wavevector (Fig. 1.1.a.II) with its corresponding reorganization of the underlying lattice due to the coupling between electrons and phonons, and the opening of a gap at the FL at the edge of the zone boundary of the modulated system (Fig. 1.1.b.II). The gap opening that occurs shows that the energy gain due to the reduction of the energy of the electronic states at the FL is larger than the elastic modulation of the lattice.

Throughout this thesis we have employed calculations of the electronic susceptibility function, also know as the Lindhard response function[31], to check the existence of the FS nesting and the possibility of a Peierls scenario for the CDW formation. We would like to emphasize that the calculations employed in this thesis are based on a first-principles DFT approach and use the detailed crystal structure of the systems, while most of the published body of work on the topic

uses mostly model analytical functions.

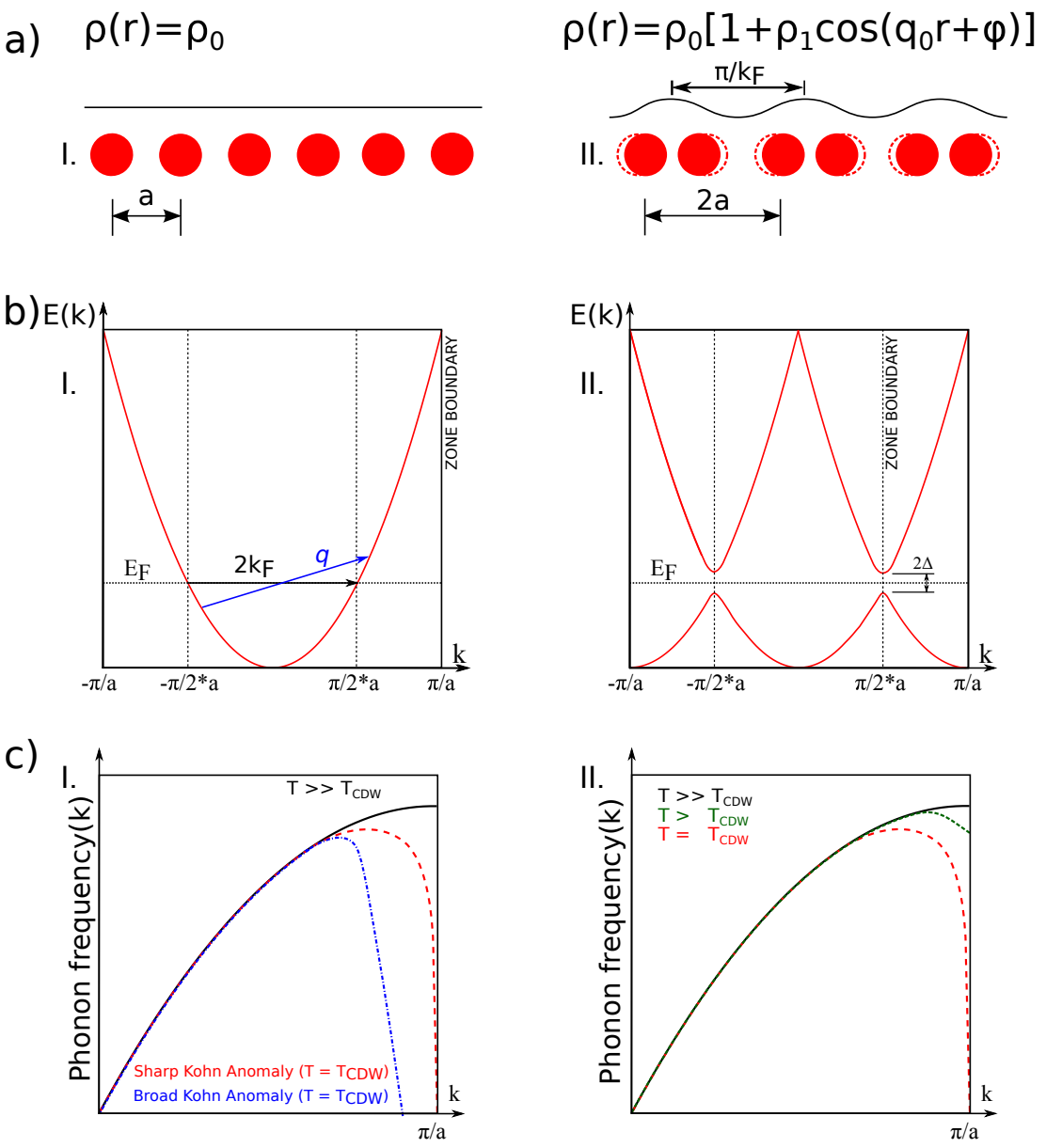

Figure 1.1: Linear metallic chain equally spaced (a.I.) before the phase transition. The chain after the phase transition with the induced lattice distortion and charge density reorganization (a.II.). The band dispersion in the undistorted phase is depicted in b.I.(red line) and one can note that the system is metallic, while in the CDW phase there is forbidden energy region due to a gap opening of 2Δ (b.II. red line). The nesting of the electrons corresponds to a $q = 2k_F$ nesting wavevector. This process is called Fermi surface nesting and it gives rise to a metal-insulator transition. In c.I. we show the two scenarios for the occurrence of the phonon softening in a material at the $T = T_{CDW}$: a sharp or a broad softening around the wave vector responsible for the CDW transition. In c.II we show the development of the phonon softening as we approach the CDW transition temperature.

We would like to reiterate the derivation and approximations considered in the Lindhard response function and we follow Ref. [32, 33] for this purpose. We start by assuming an external potential $\phi^{ext}(\vec{r},\omega)$ as the perturbation to the ideal electron gas; this would lead to an induced density fluctuation $\rho^{ind}(\vec{r},\omega)$ with an induced potential $\phi^{ind}(\vec{r},\omega)$. This perturbative potential would account for the total potential as following:

$$\phi^{tot}(\vec{r},\omega) = \phi^{ext}(\vec{r},\omega) + \phi^{ind}(\vec{r},\omega), \tag{1.15}$$

with $\rho^{ind}(\vec{r},\omega)$ linked to the external potential within a linear response approach:

$$\rho^{ind}(\vec{r},\omega) = e^2 \int d^d r' \chi(\vec{r},\vec{r}\,',\omega)\phi^{tot}(\vec{r}\,',\omega), \tag{1.16}$$

where $\chi(\vec{r},\vec{r}\,',\omega)$ is the electronic response function. This function can be calculated within Random Phase Approximation (RPA) and it can be expressed as $\chi(\vec{q},\vec{q}\,',\omega)$ in momentum space.

$$\chi(\vec{q},\vec{q}\,',\omega) = \lim_{\eta\to 0}\sum_{ij}\frac{f_i - f_j}{\hbar(\omega-\omega_{ij})-i\eta} \times \langle i|e^{i\vec{q}\vec{r}\,'}|j\rangle \ \langle i|e^{i\vec{q}'\vec{r}\,''}|j\rangle\,. \tag{1.17}$$

In the Lindhard approximation, the electron gas is considered non-interacting and the electron-electron correlations are ignored, thus having the Lindhard response function expressed as:

$$\chi(\vec{q},\omega) = \frac{2}{\hbar}\int d\vec{k} f_{\vec{k}}(1-f_{\vec{k}+\vec{q}})\left[\frac{1}{\omega+(\epsilon_{\vec{k}}-\epsilon_{\vec{k}+\vec{q}})+i\eta} - \frac{1}{\omega-(\epsilon_{\vec{k}}-\epsilon_{\vec{k}+\vec{q}})+i\eta}\right], \tag{1.18}$$

with f being the Fermi-Dirac distribution function, ϵ - the electron's energy eigenvalues and ω - the oscillation frequency of the external field.

In the Kohn anomaly picture, the electronic excitations on the Fermi surface require no energy transfer, so we can consider $\omega = 0$ and we are left with the imaginary and real part of Eqn. 1.18 as follows:

$$Im[\chi(\vec{q})] = \frac{1}{2\pi^2}\int_{BZ} d\vec{k}(f_{\vec{k}} - f_{\vec{k}+\vec{q}})\delta(\epsilon_{\vec{k}} - \epsilon_{\vec{k}+\vec{q}}), \tag{1.19}$$

and

$$Re[\chi(\vec{q})] = -\frac{2}{(2\pi)^3}\int_{BZ} d\vec{k}\frac{f_{\vec{k}} - f_{\vec{k}+\vec{q}}}{\epsilon_{\vec{k}} - \epsilon_{\vec{k}+\vec{q}}}. \tag{1.20}$$

The real part of the Lindhard function[1] provides information about the possible nesting vectors and it can also be plugged in to calculate the renormalized phonon mode (i.e. the softening of the vibrational phonon mode) involved in the lattice distortion, in the following way(see for eg. refs. [34, 33]):

$$\omega(\vec{q})^2 = \omega_0(\vec{q})^2 + 2\omega_0(\vec{q})|g(\vec{q})|^2 Re[\chi(\vec{q})], \tag{1.21}$$

where $\omega(\vec{q})$ is the renormalized phonon mode, $\omega_0(\vec{q})$ is the bare phonon mode in the absence of electron-phonon coupling (EPC) and $g(\vec{q})$ is the electron-phonon coupling matrix which most of the time is assumed wavevector independent and simply called the electron-phonon coupling constant. One can already have some intuition over the phonon renormalization from the shape of the Lindhard response function (LRF). If the LRF presents sharp peaks, the renormalized phonon will also present a sharp feature(a sharp dip if one may, see Fig. 1.1.c.I) which in turn would correspond to a weak EPC in the CDW manifestation. When the corresponding renormalization has a broad feature (see Fig. 1.1.c.I); this scenario would correspond to the strong EPC driven CDW formation; in this case there is no FS nesting present.

In Fig. 1.2.a we show the behaviour of the LRF for the ideal one-, two- and three-dimensional free electron gases. In the case of the 2D and 3D free electron gases there is no nesting. Only the 1D case presents a logarithmic discontinuity, indicative of an electronic instability in the system[2]. FS nesting can occur in two possible scenarios. The obvious case would be the one depicted in Fig. 1.2.b where one would have a metallic system with one partially filled band displaying a perfectly parallel pair of Fermi surface sheets. In this case the nesting

[1] We will call it Lindhard reponse function heareafter because throughout this thesis we will calculate only the real part of the Lindhard function.

[2] However,real 2D systems can exhibit partial nesting features which can be responsible for metal to metal anomalies.

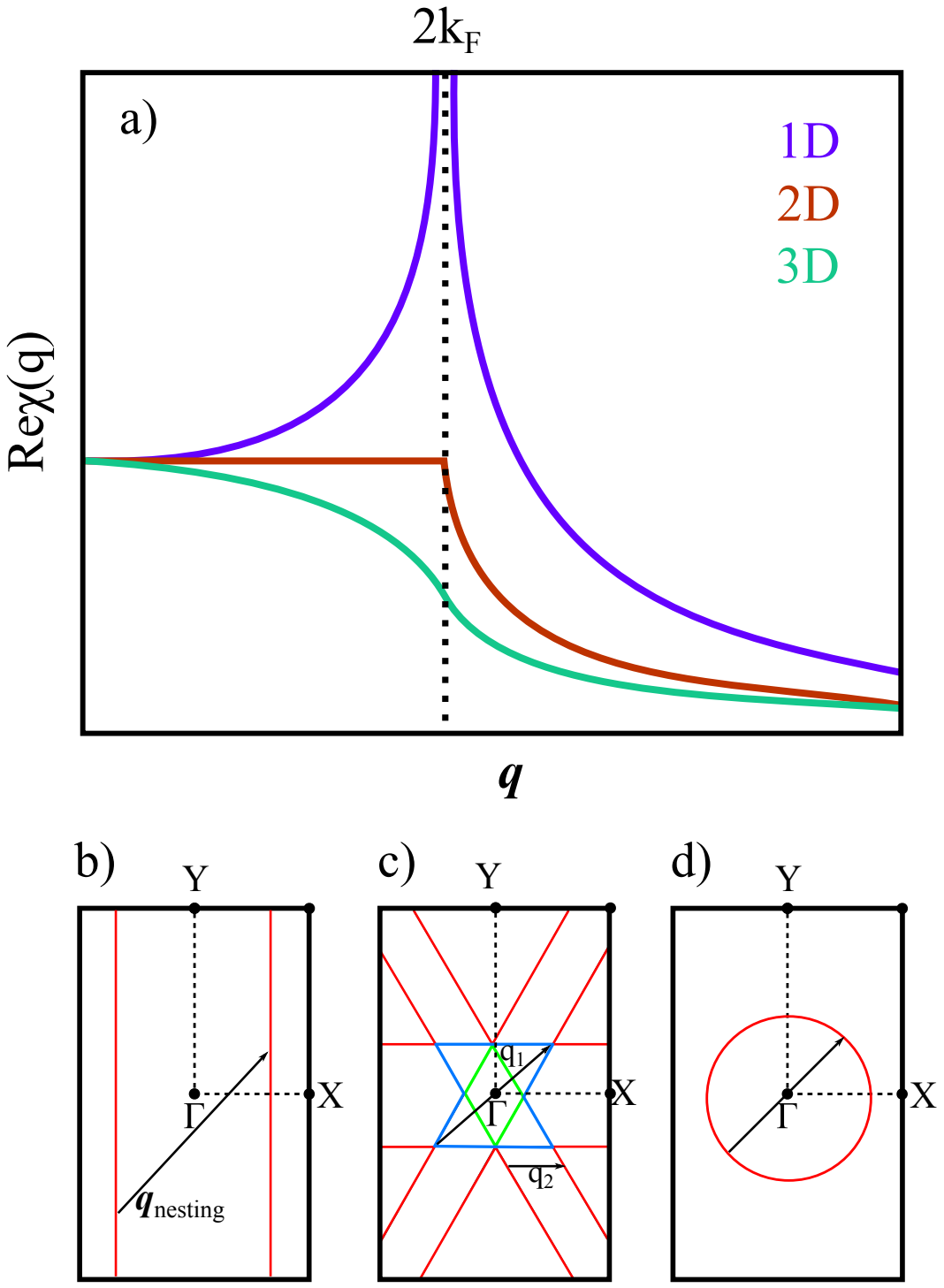

Figure 1.2: Lindhard function representation in reciprocal space for a 1D, 2D or 3D free electron gas at 0 K.(a) Note that only the 1D case shows a logarithmic divergence indicating the presence of an electronic instability. Fermi surface of an ideal metallic system with a partially filled band(b). Fermi surface of a metallic system with 3 partially filled bands(c). Fermi surface of an ideal 2D electron gas(d).

wavevector would be fixed by the Fermi wave vector along X direction, while being independent on the second or third directions components since they are all equally feasible to give raise to FS nesting. A similar behaviour is expected when one would have more than one pair of Fermi surface sheets parallel along the same direction or plane (depending on the dimensionality of system). A more subtle case is when one would deal with pairs of Fermi surface sheets, open or closed, displaying a 2D character each of them coming from a partially filled band, as displayed in Fig. 1.2.c. Here the convolution of all the pairs of Fermi sheets gives rise to parallel segments in the entirety of the Fermi surface, making them suitable for nesting. This behaviour is called hidden Fermi surface nesting due to the apparent inadequacy of the FS for nesting.[35] In comparison with this, in Fig. 1.2.d the 2D nature of the FS doesn't allow for nesting and it would give rise to a plateau up to $2k_F$ followed by a smooth decrease in the LRF rather than a logarithmic discontinuity.

Another situation when the LRF could present a logarithmic discontinuity would be in a system that presents a Spin Density Wave(SDW) instability. Like in the case of CDW, the SDW mechanism involves as well a Fermi surface that favours nesting. The oversimplified interpretation of the LRF in the CDW picture stands for the likelihood of pairing electrons and holes at the Fermi level, i.e. mixing occupied and unoccupied states with the same spin; on the other hand, in the SDW picture, LRF accounts for the mixing of occupied and unoccupied states with opposite spin. Unlike the CDW picture, the driving force in this case is not the (weak) electron-phonon coupling, but the electronic exchange interaction is the one which favours the energy lowering of the system. In fact, in the SDW scenario there is no lattice modulation associated with the phase transition, therefore there is no Kohn anomaly present[36]. The SDW breaks the spin degeneracy and gives rise to different modulations for each spin sub-band in such a way that it leaves the charge density unaffected(this is to say that both spin sub-bands have the same wavevector of the modulation but a π phase difference).[34] In this thesis we have considered a paradigmatic case of these materials: the Bechgaard salts.

In Table 1.1 we show how the CDW manifest in different kinds of materials representative of the classes that they belong to, but also paradigmatic altogether for the study of CDWs. One can notice immediately the common features of a Peierls scenario and in what classes of materials this kind of CDW behaviour prevails. Blue bronzes display a quasi-one dimensional electronic structure, and the driving mechanism in these material would be the Peierls one. In the case of $NbSe_3$, representative of the class of transition metal trichalcogenides, the electronic structure displays a more plentiful FS which contains 4 pairs of (almost) parallel Fermi sheets, but preliminary calculations indicate that current LRF approximations will not suffice. On the opposite side we have the metallic ($NbSe_2$) and semi-metallic ($TiSe_2$) transition metal dichalcogenides, and transition metal tetrachalcogenides($TaTe_4$) where there is no nesting and in which the CDW arises due to the strong electron-phonon coupling mechanism.

	Peierls model	Blue Bronze	$NbSe_3$	$NbSe_2$	$TiSe_2$	$TaTe_4$
Kohn Anomaly	Sharp[30]	Sharp[37]	No[38]	Broad[39]	Broad[40]	Broad[41]
FS nesting	Yes[34]	Yes[42]	Yes[43]	No[44]	No[40]	No[41]
EPC	Weak	Weak[42]	Strong	Strong[45]	Strong[40]	Strong
Gap opening	@FL[1]	@FL[46]	@FL[47]	@BZ[48]	@BZ[40]	@BZ[41]
LRF	Sharp[34]	Sharp[42]	Broad[43]	Broad[44]	Broad[40]	Sharp[41]
Coherence Length	$\gg$ a	$\gg$ a[49]	$\sim$ a[43]	$\sim$ a[50]	$\sim$ a[50]	$\sim$ a[13]
ρ anomaly	Yes	Yes[51]	Yes[47]	No[52]	Yes[53]	NA
Phase transition	M-I[1]	M-I[49]	M-M-M[47]	M-M[52]	SM-SM[53]	M-M[41]

Table 1.1: CDW signs of manifestation in well studied materials representative for the category that they fall into compared to the standard Peierls model. Legend: @FL: at the Fermi level; @BZ: in the whole Brillouin zone; M-I: metal-insulator; M-M: metal-metal; SM-SM: semi-metal to semi-metal.

PART II

STRUCTURAL INSTABILITES IN SINGLE-LAYER MATERIALS

INTRODUCTION

Layered transition-metal dichalcogenides(TMDCs) have been the object of large attention for around four decades because they exhibit a rich variety in physical properties [5, 50]. Most notably, these materials have provided a fertile ground for the study of the competition between several electronic instabilities like commensurate and incommensurate charge-density-waves (CDW), superconductivity (SC), etc. A remarkable aspect is that their layered nature makes the alteration of the band filling and the transport properties possible through chemical intercalation. Very recently, the interest in these materials has experienced a sudden resurgence because of the exciting possibility of preparing and studying thin slabs with a reduced number of layers or even single-layers [14, 15]. This makes it possible to study how the reduced electronic screening brought about by lowering the dimensionality from bulk to layers of different thickness influences the competition between electronic instabilities.

Single-layered materials demonstrate complex phase diagrams and a phenomenological understanding of their behaviour is essential in further advancements of electronic devices at a reduced physical scale. Furthermore the accumulated knowledge can serve as the building block for the next, more complex scenarios of heterostructures built from single-layered materials. It is not intuitively easy to predict what will happen when one combines single-layers that present different phases in specific physical conditions. From the theoretical point of view, these studies can serve as well as a benchmarks for improving our current tools of study. In the next three chapters we will focus on studying the mechanism behind the CDW manifestation in different layered TMDCs. In Chapter 2 we follow the formation of the 3Q CDW and the full gap opening that it is led by said 3Q mechanism in $TiSe_2$. We show that the CDW character in single-layer $TiSe_2$ can be

easily altered under doping with either electrons or holes where the CDW has first a commensurate-incommensurate phase transition followed by a total suppression of the instability and structural recovery of the high temperature symmetry under large enough doping values. We continue with the discussion in Chapter 3 about how well particular ways of describing electron exchange-correlation phenomenon in a physical system can predict the formation of the CDW; in this thesis we report on a rather surprising material: single-layer $TiTe_2$, known for its inability to form a CDW state in bulk, but for which recently has been shown to undergo a CDW instability in the single-layer. We observe that we can enhance the CDW state in single-layer $TiTe_2$ by applying a small amount of strain on the lattice and we successfully predict the appearance of a CDW phase in the few-layers configuration under these conditions. We conclude this part with Chapter 4 by studying the beautiful display of different CDW modulations in $2H$-$NbSe_2$. By correlating theoretical and experimental results we can filter the co-existence down to two 3×3 CDW states in $2H$-$NbSe_2$ out of the 6 theoretically predicted. As a general remark to these 3 chapters, condensation of multiple phonons always leads to the lowest modulated CDW structures. Moreover their manoeuvrability or manipulation depends on the strength of interaction between electrons and their corresponding lattices.

2. NATURE OF THE 2X2 CDW IN SINGLE-LAYER TISE2

2.1 Introduction

$1T$-$TiSe_2$ holds a special position among the conductive layered transition-metal dichalcogenides in that it is formally a d^0 compound, so that its normal state must be either a semimetal or a semiconductor with a very small gap, a feature that has long been debated [5, 50, 54]. This is in contrast with the situation for most of the other CDW-bearing transition metal dichalcogenides which are formally d^1 compounds like $1T$- and $2H$-MX_2 (M = Nb, Ta; X = S, Se) and thus exhibit a partially filled conduction band. In addition, neither bulk $1T$-TiS_2 nor bulk $1T$-$TiTe_2$ exhibit any CDW. However a 2×2 CDW has been reported for single-layer $1T$-$TiTe_2$ whereas no sign of the instability has been found in bilayers or multilayers. [55] On the basis of DFT calculations it has also been reported an incipient stabilization of the CDW in sheets of $1T$-TiS_2 with four or less layers [56].

The bulk structure of $1T$-$TiSe_2$ is built from hexagonal layers of Ti atoms in an octahedral coordination (see Fig. 2.1a) [57]. Short Se-Se contacts occur within the layer but there are also relatively short interlayer Se-Se contacts providing a substantial interlayer coupling. Bulk $1T$-$TiSe_2$ exhibits a CDW transition around 200 K which has been controversial for four decades [5, 50, 54, 58, 59, 60, 61, 62, 63, 64, 65, 66]. It leads to a $2 \times 2 \times 2$ commensurate phase (see Fig. 2.1b) without the occurrence of any intermediate incommensurate phase [53]. In contrast with many of the CDW materials the origin of the instability in bulk $1T$-$TiSe_2$ is not Fermi surface nesting. Both excitonic and phononic type mechanisms have

been suggested and their relative merits are still under discussion.[67] Although $1T$-$TiSe_2$ is not superconducting at low temperature, the CDW may be suppressed either by Cu intercalation [68] or applying pressure [69] and under such circumstances superconductivity may be stabilized (maximum $T_c = 4.15$ K for $Cu_{0.08}TiSe_2$ or 1.8 K at $\sim$ 3 GPa). On the basis of these observations the possible relationship with the phase diagram of electron doped MoS_2 has been considered [70].

The layered nature of the material as well as the above mentioned interplay between SC and CDW orders in the bulk make $1T$-$TiSe_2$ an ideal candidate for studies of the physics associated with these electronic instabilities at the two-dimensional (2D) limit. Recently, a scanning tunneling microscopy (STM) study of single-layer $1T$-$TiSe_2$ provided evidence for the existence of a 1×1 structure at room temperature but a 2×2 superstructure at low temperature [71], although no details about the electronic structure of the single-layers were reported. More recently, two angle-resolved photoemission spectroscopy (ARPES) studies of single-layer $1T$-$TiSe_2$ on bilayer graphene (BLG) terminated SiC(001) provided detailed but somewhat conflicting results about the system. For instance, whereas Sugawara [72] found that the CDW occurs at $\sim$ 200 K, a value very similar to that for bulk $1T$-$TiSe_2$, 202 K, and lower than that for exfoliated films with thickness smaller than 100 nm ($\sim$ 240 K), Chen [73] reported that the CDW temperature is $\sim$ 232 K. The last authors also reported the existence of a small band gap already at room temperature whereas Sugawara [72] observe an electron pocket at the Brillouin zone (BZ) corner above the CDW. It is possible that electron doping of the samples could be at the origin of some of these seemingly conflicting results. The two studies however agree in suggesting that the CDW is more robust in the single-layer than in bulk. Raman spectra studies showed that the CDW transition temperature increases when moving from the bulk to sheets at the nanometer range although it can decrease for very thin ones probably because of surface oxidation or defects [74, 75]. Let us also note that, because of the existence of Se-Se contacts shorter than the sum of the van der Waals radii, the electronic structure near the Fermi level in bulk and single-layers can be somewhat different, which can have

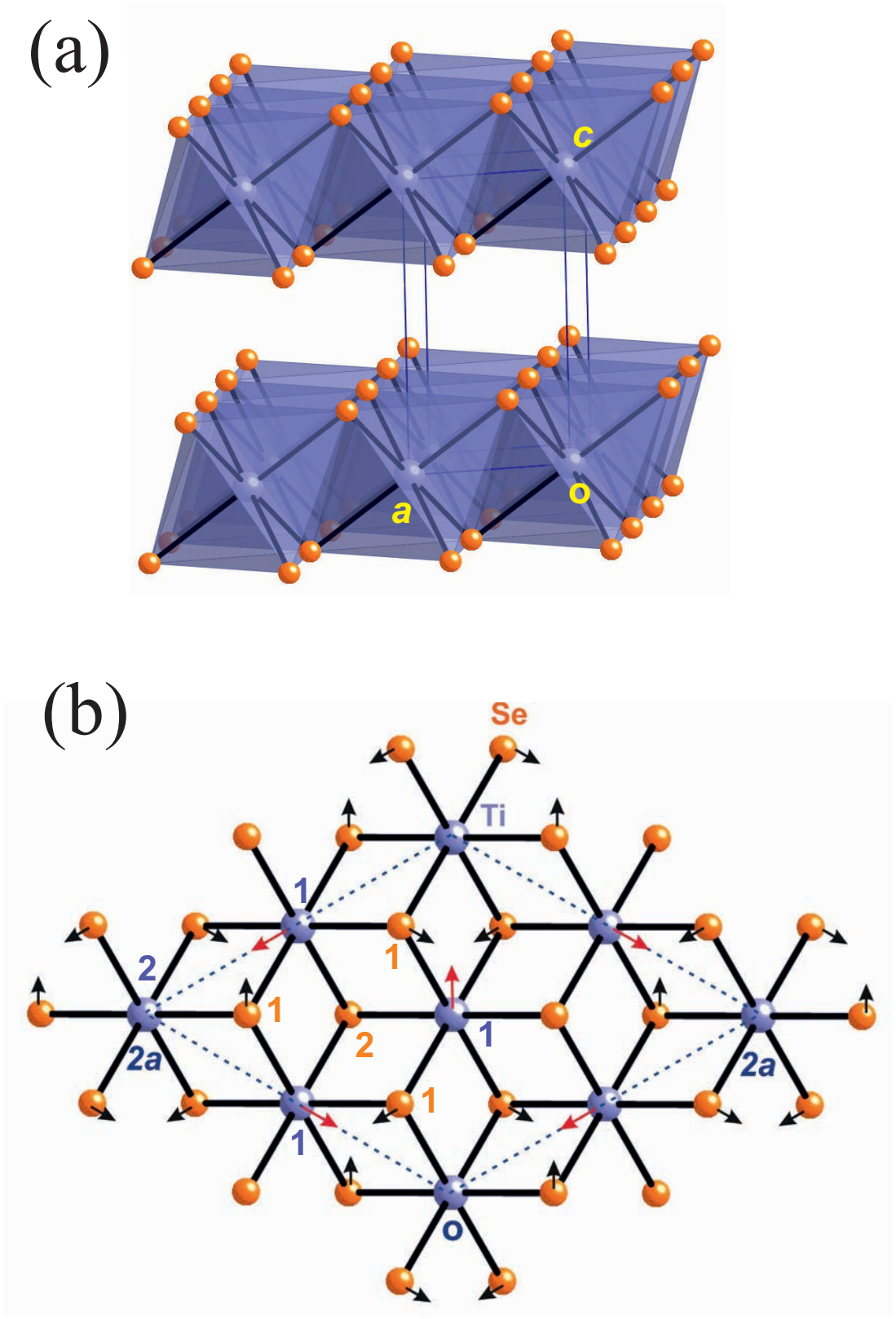

Figure 2.1: (a) Crystal structure of 1T-$TiSe_2$. (b) Schematic representation of the displacements occurring in a single-layer of the 2×2×2 CDW structure of $TiSe_2$.

important consequences for a system with either a small semimetallic overlap or a very small semiconducting gap. For instance, the well-known pancake-like hole pocket occurring in bulk for the related $2H$-$NbSe_2$ [76] does not occur at all in single-layers of the same material [48]. In addition, because of the observation of the suppression of the CDW under Cu intercalation in bulk $1T$-$TiSe_2$, the structural and electronic dependence of the CDW occurrence with the charge-carrier density in single-layers becomes a topic of utmost importance. Recent work with single-crystals of $1T$-$TiSe_2$ with thicknesses less than 10 nm, in which the charge carrier density was modified by means of electric field gating, indeed demonstrated a very remarkable phase diagram [77].

There is a considerable number of theoretical studies of the electronic structure of bulk $1T$-$TiSe_2$, many of them devoted to the discussion of the origin of the CDW [78, 79, 80, 81, 82, 83, 84, 85, 86, 87]. However, only in more recent works [88, 89] the structural dependence of the electronic and vibrational properties were considered in detail. Fu and coworkers [90, 91] analyzed the effect of doping and biaxial strain on the soft phonons giving rise to the CDW in the bulk. For single-layer $1T$-$TiSe_2$ we are aware of only a few theoretical reports. In the earlier one by Fang [82] the electronic structure was discussed on the basis of the room temperature bulk structure without any type of structural relaxation. In the recent work by Sugawara [72] the band structure near the Fermi level was calculated for the normal and CDW phase. More recently, Singh [92] studied the phonon dispersion and showed the presence of an unstable phonon mode but the charge-carrier density dependence of the results was not studied. Yet, in view of the above mentioned recent experimental results the charge-carrier dependence is a truly essential aspect to consider. Chen [93] looked for dimensional effects on the CDW transition by means of ARPES and DFT calculations on sheets with one to six $TiSe_2$ layers.

In order to provide ground for the discussion and rationalization of the recent exciting results concerning the physics of $1T$-$TiSe_2$ at the 2D limit [71, 72, 73, 77],

we report here a detailed first-principles DFT study (see section 2.5 for computational details) of 1T-$TiSe_2$ single-layers. We will consider in detail the subtleties of the CDW mechanism and how the structural, electronic and vibrational features evolve as a function of the charge-carrier density. From now on we will refer to 1T-$TiSe_2$ simply as $TiSe_2$.

2.2 Intrinsic single-layer properties

In this Section we discuss the electronic structure and the CDW instability for the free-standing $TiSe_2$ single layer, in the case where there are no externally induced charge carriers. We will refer to it as the *'intrinsic'* case, in contrast with the one in which we consider the presence of externally induced and controlled charge carriers, which will be refereed to as the *'doped'* case (although the origin of the charge carriers may not necessarily be the presence of dopant impurities, but other external factors such as electric field gating as in Ref. [77]).

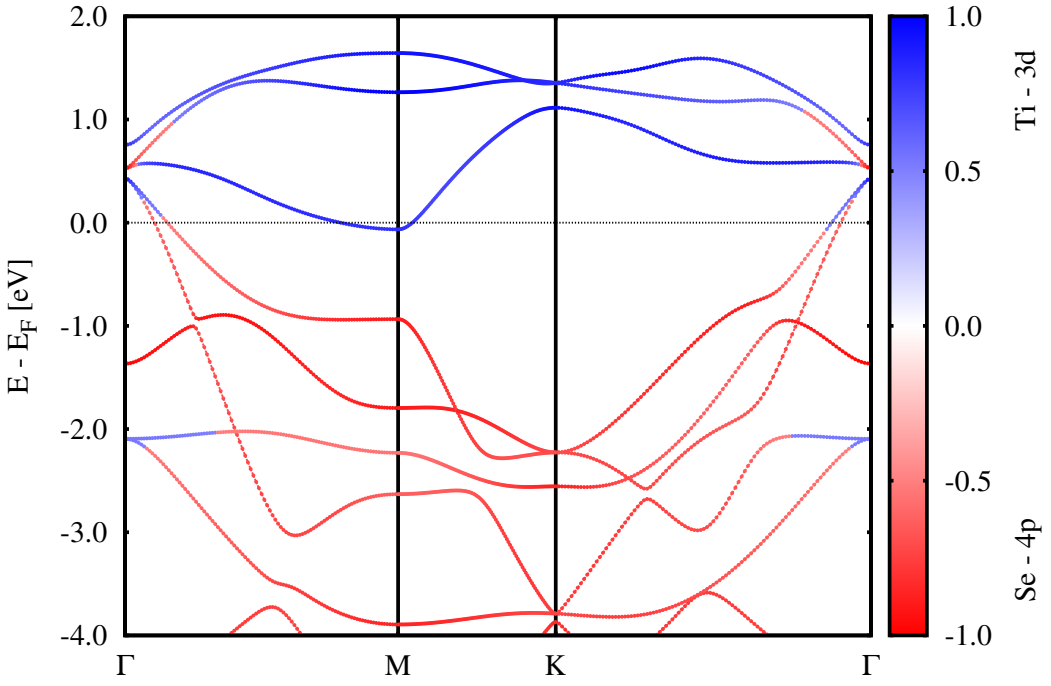

Figure 2.2: Band structure for undistorted, intrinsic, single-layer $TiSe_2$.

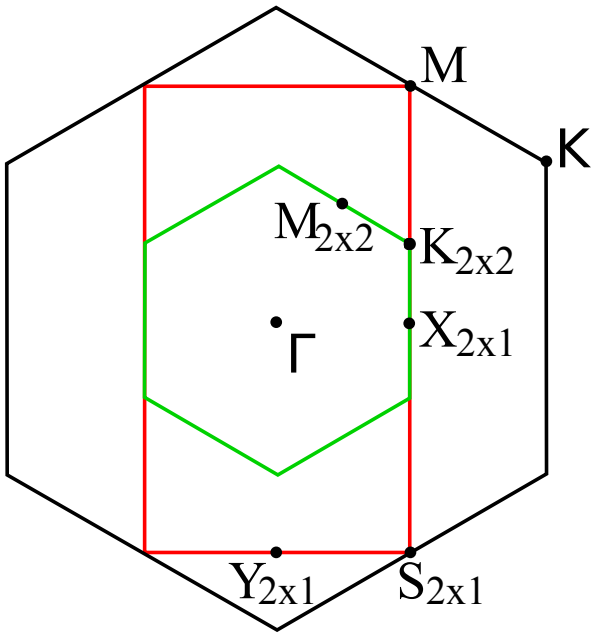

Figure 2.3: Representation of the Brillouin zone of single-layer $TiSe_2$. Black, red and green show the contours of the BZ of the primitive cell and the 2×1 and 2×2 cells, respectively. The notation of the high symmetry points is also indicated.

Fig. 2.2 shows the calculated band structure for the intrinsic, undistorted $TiSe_2$ single-layer. The notation for the high symmetry points (Γ, M and K) of the BZ is indicated in Fig. 2.3. We obtain a semimetallic behavior, with a 'negative gap' of 0.5 eV between the two bands crossing the Fermi level near the Γ point (which are degenerate at that point in the absence of spin-orbit interactions), and the upper band that has its minimum at the M point. These two sets of bands lead to two pockets of holes around the Γ point and a pocket of electrons around each of the M points of the BZ of the undistorted crystal lattice. Our results are consistent with recent calculations for the single-layer by Chen *et al.* [73], although they find a smaller negative gap of 0.2 eV. This is due to the different DFT functionals used in both calculations: while they use a Heyd-Scuseria-Ernzerhof (HSE) hybrid functional [94] (which usually provides gap energies in good agreement to the experimental data), we use a GGA functional, which tends to underestimate the gap energies (leading in this case to a too large overlap between the two bands, and an overestimated negative gap). A second minor difference with the results of Chen *et al.* [73] is the splitting of the bands at Γ induced by the spin-orbit coupling term introduced in their calculations, which is not considered in the results

of Fig. 2.2. Nevertheless, we have checked that introduction of the spin-orbit coupling does not alter in any significant way the results for both the undistorted and CDW distorted structures (see Fig. 2.5) so that from now on we will only report calculations without spin-orbit effects. Effect of the Spin-Orbit (SO) coupling on the band structure and CDW distortion of single-layer $TiSe_2$ in Fig. 2.5 shows the calculated band structure including or not the spin-orbit corrections, both for the undistorted (a) and 2×2 CDW (b) structures of single-layer $TiSe_2$. We have also calculated the energy difference between the undistorted and the 2×2 CDW phases including the SO coupling. We find a value of 6 meV per formula unit, the same as the one obtained without SO coupling.

The band leading to the electron pockets at M is an almost exclusively Ti-based band that, at Γ, is built from one of the three t_{2g} orbitals of Ti (see Fig. 2.2). In this t_{2g} block, located between 0.5 and 1 eV above the Fermi level, two of the bands are degenerate at Γ and the other one is non-degenerate. Assuming a local coordinate system in which the three-fold symmetry axis of the octahedron occurs along the z direction, the non-degenerated band is essentially built from the Ti d_{z^2} orbital which occurs slightly higher in energy than the doubly-degenerate pair because of the slight rhombohedral distortion. The doubly-degenerate set is mainly built from the Ti $d_{x^2-y^2}$ and d_{xy} orbitals which are somewhat tilted because the plane of the Ti atoms is not a symmetry plane. All the way along the Γ-M line (i.e. along the a^* direction), the only symmetry element preserved is the symmetry plane perpendicular to the layer and going along the a^* direction (the plane noted σ in Fig. 2.4a). Although at Γ the symmetry is higher, the two doubly-degenerate levels can be described as symmetric and antisymmetric crystal orbitals with respect to this plane. It is the symmetric one (schematically shown in Fig. 2.4b and Fig. 2.4c for Γ and M, respectively) which leads to the electron pockets at M. At Γ, such crystal orbital is almost exclusively made of slightly tilted Ti $d_{x^2-y^2}$ orbitals, each of which makes antibonding interactions with those of four nearest-neighbor octahedra (shown by red arrows in Fig. 2.4b). From Γ to M the phase changes in such a way that these antibonding interactions turn into

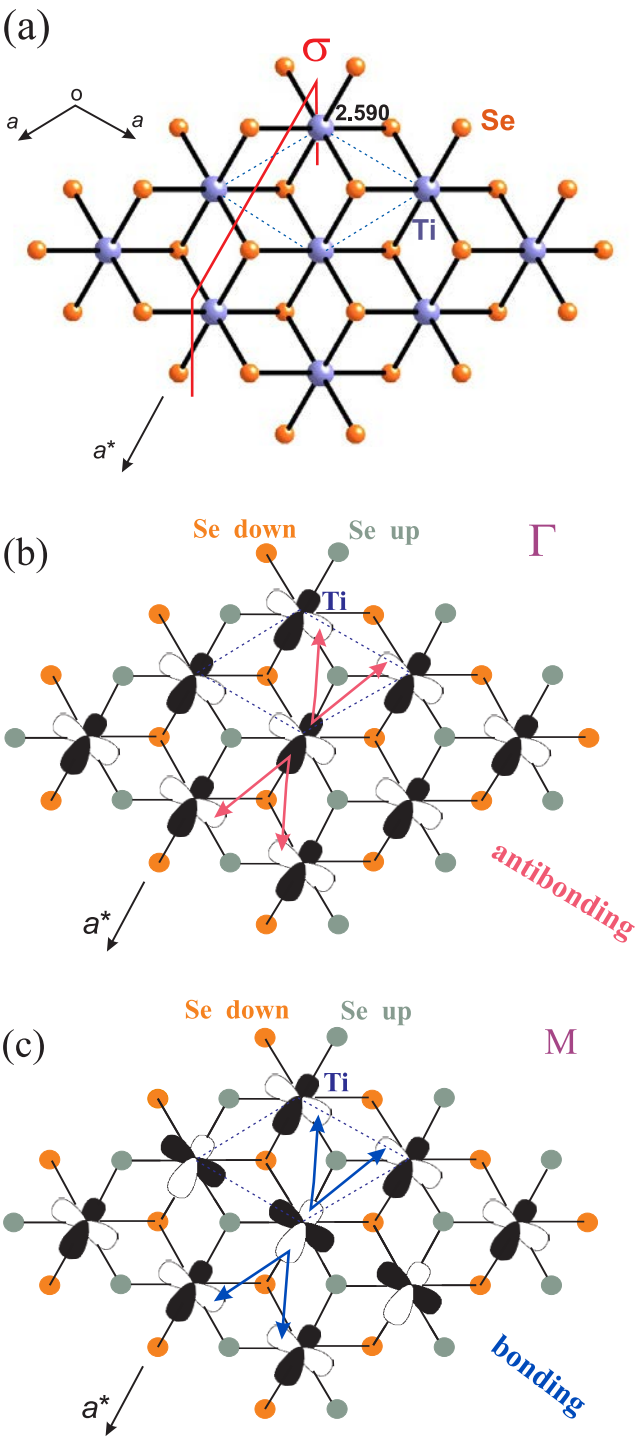

Figure 2.4: (a) Calculated structure of the undistorted single-layer $TiSe_2$. Orange (blue) circles denote Se (Ti) atoms. In (b) and (c) we show a schematic representation of the crystal orbital of the band leading to the electron pockets for the undistorted single-layer $TiSe_2$ at Γ (b) and M (C). Orange (green) circles denote up (down) Se atoms. The red/blue arrows indicate the antibonding/bonding metal-metal interactions changing from Γ to M. In (a), σ denotes the plane of symmetry preserved by those wave-functions along the $\Gamma - M$ line.

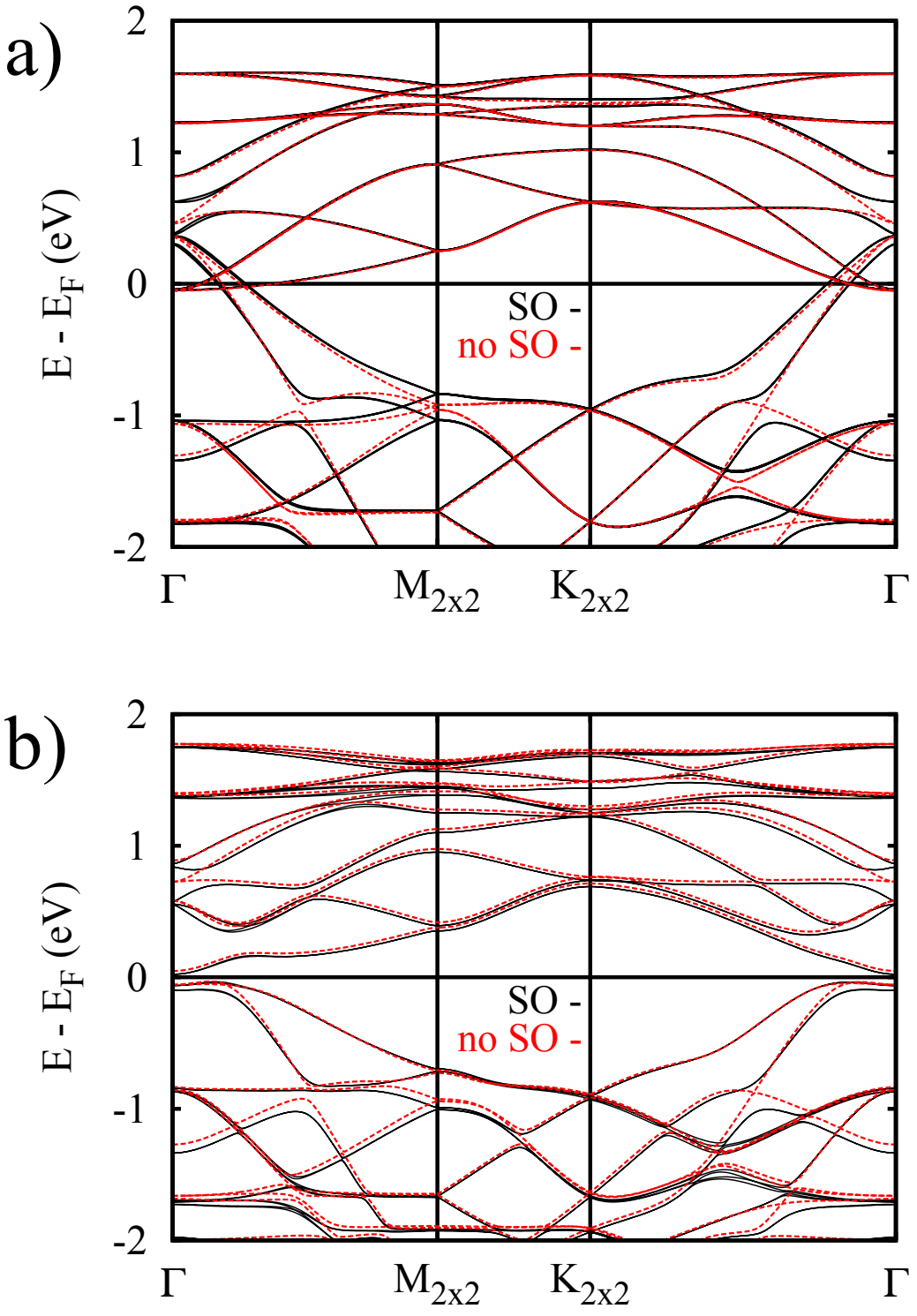

Figure 2.5: Comparison of the calculated band structure including (continuous black lines) and not including (dashed red lines) spin-orbit (SO) corrections for the undistorted (a) and 2×2 CDW (b) structures of single-layer $TiSe_2$. Note that, in both cases, the bands are plotted using the Brillouin zone of the 2×2 cell, to facilitate comparison.

bonding (see Fig. 2.4c) and lead to the band dispersion towards higher binding energies. The metal-metal interactions are then responsible for the semi-metallic character of the material, as the dispersion of the Ti $d_{x^2-y^2}$ band is such that it reaches energies around the M point which are below those of the Se-based valence bands which have their maximum at Γ, thus creating the electron and hole pockets centered at M and Γ, respectively. Of course, the same analysis holds for the other equivalent M points in the BZ, with the appropriate Ti d orbital rotations by 120° and 240° around the three-fold symmetry axis.

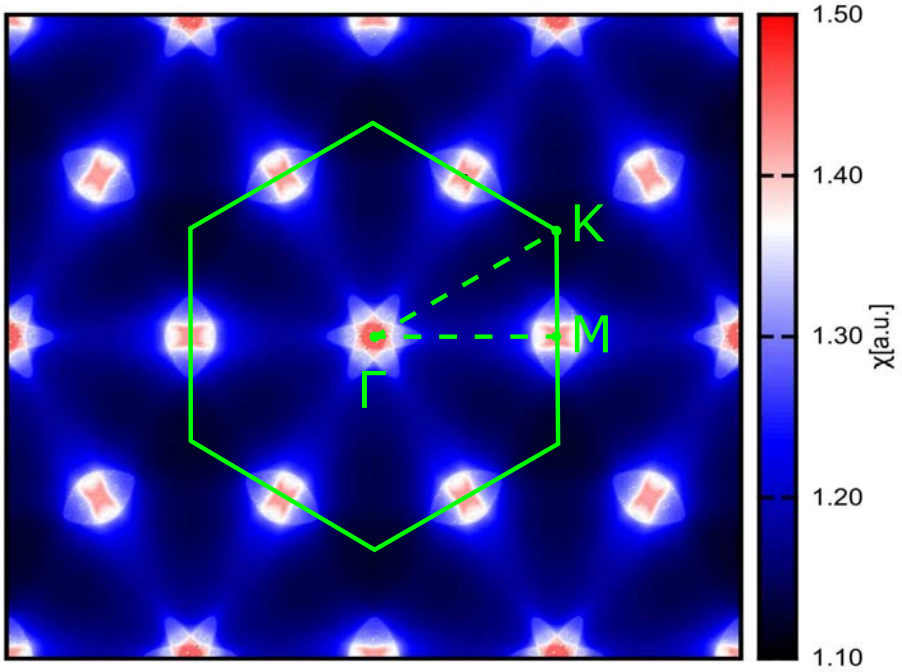

Figure 2.6: $TiSe_2$ single-layer Fermi surface (a) is composed of two closed Fermi sheets around Γ coming from the Se 4p orbitals and one closed Fermi sheet around the middle of the BZ edges originating in Ti 3d orbitals. Lindhard response function (b) for the undistorted, intrinsic, single-layer $TiSe_2$ demonstrates the unfavourable nesting scenario driving the periodic lattice distortion.

In order to study the stability of the single-layer, we have performed calculations for both the Lindhard response function and the phonon band structure for the optimized, undistorted 1×1 structure. The calculated Lindhard response function is shown in Fig. 2.6 next to the correspoding Fermi surface. As it can be noted, there are no sharp maxima around the M points of the BZ which could justify a Fermi surface nesting driven mechanism of the CDW, but rather a shallow regions

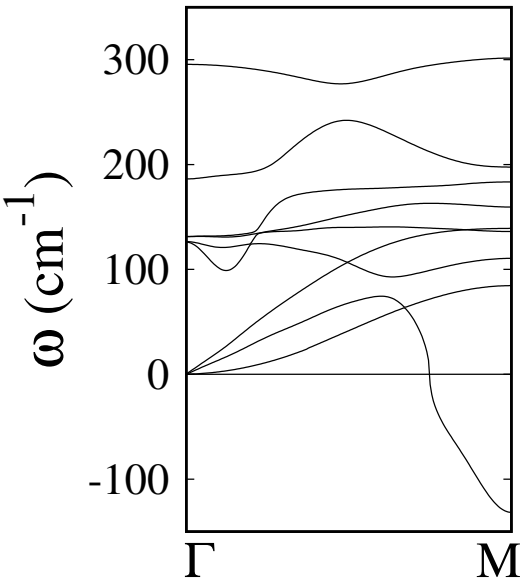

Figure 2.7: Phonon dispersion for the undistorted, intrinsic, single-layer $TiSe_2$ in the $\Gamma - M$ segment of the BZ. Negative phonon frequency refers to imaginary phonon modes.

around the Γ and M points. The phonon calculation results are shown in Fig. 2.7. One of the phonon branches becomes clearly unstable around the M point, similarly to what was found for the bulk crystal [88, 89, 90] for the M and L points of the bulk BZ. The pattern of the distortion associated with the unstable phonon at M is shown schematically in Fig. 2.8. The displacements of the Ti and Se atoms are perpendicular to the phonon wave vector $\mathbf{q}$. We find that the ratio between the Ti and Se displacements is 3.22, in excellent agreement with the value reported in a recent X-ray study of single-layer $TiSe_2$, 3.3 [95]. It is also very close to that found for the bulk CDW experimentally [53] (3.0±0.9) and from DFT [88] (in the range from 2.3 to 2.9, depending on the choice of the functional and lattice constants). The resulting structure has a 2×1 periodicity: single in the direction of the lattice vector perpendicular to the wave vector $\mathbf{q}$, and double in the direction of the other lattice vector.

The presence of phonons with imaginary frequency around the M points indicates that the lattice is unstable against distortions with 2×1 (and symmetry-equivalent) periodicity. This has been confirmed by computing the energy as a function of

the amplitude of the phonon mode in a 2×1 supercell. An energy minimum is found, 3 meV per formula unit lower than the undistorted 1×1 structure. A further relaxation in which the 2×1 periodicity is imposed but the internal degrees of freedom are not constrained to follow the unstable phonon mode, produces a negligible energy gain.

The instability of a single M phonon does not lead by itself to the 2×2 CDW distortion pattern. To understand how does the 2×2 CDW structure develops, we notice that, as in the bulk crystal [79, 88], the combination of the three distortions shown in Fig. 2.8a-c, corresponding to the unstable phonons of the three equivalent M points, leads to a structure with 2×2 periodicity and precisely the same displacement pattern of the 2×2 CDW shown in Fig. 2.1b. The energy gained by this triple-q (or $3Q$) combined distortion is 6 meV per formula unit, which is twice as large as that of each individual, single-q (or $1Q$), M phonon distortion with 2×1 periodicity. This is an interesting result, showing that, as in the bulk, the concerted motion combining the three M phonons leads to an enhanced energy gain, with a displacement pattern similar to that of the experimental 2×2 CDW distortion in the bulk.

Fig. 2.9 shows the relaxed $3Q$, 2×2 distorted single-layer $TiSe_2$ structure, which should be compared with the undistorted 1×1 shown in Fig. 2.4a. In the undistorted structure there is only one type of octahedra, with the six Ti-Se bonds having identical lengths (2.590 Å) and a small rhombohedral distortion. In the 2×2 distorted structure there are two different types of octahedra (one of type I and three of type II per unit cell). Those at the origin of the 2×2 primitive cell plotted in Fig. 2.9 (octahedra I) have the six Ti-Se bonds of identical length (2.593 Å) and very similar to those of the undistorted structure. These bonds are shown in black in Fig. 2.9. Octahedra II have two short, two long and two intermediate Ti-Se bonds which are shown in red, green and blue colors respectively in Fig. 2.9. Along two of the four-fold axes of the octahedra II (the axes passing though the central Ti atom and the two Se atoms on opposite vertices; these are not true

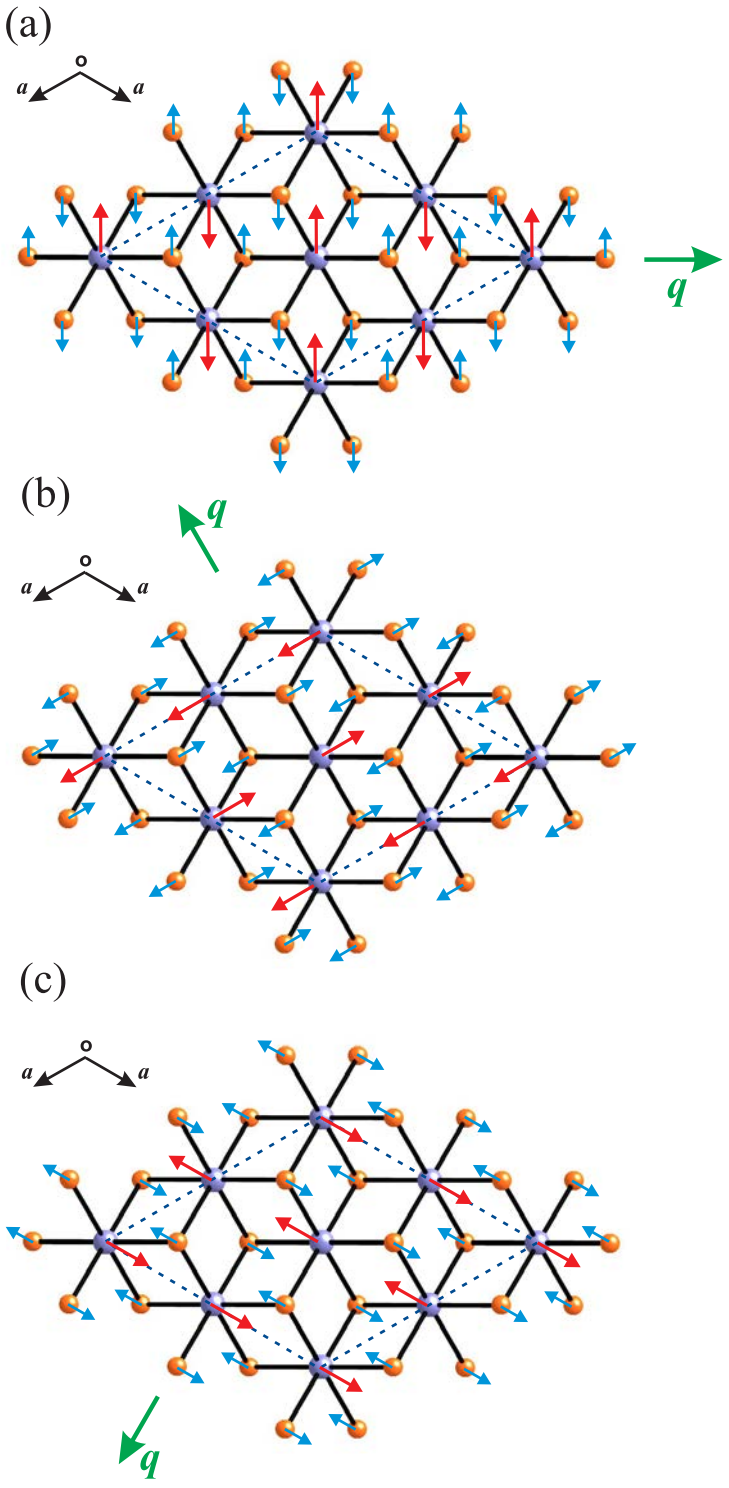

Figure 2.8: Scheme showing the atomic displacements corresponding to the unstable phonon at the M point (see Fig. 2.7) for the intrinsic single-layer $TiSe_2$. Each panel shows the displacement pattern for $\mathbf{q}$ vectors corresponding to the three equivalent M points of the BZ. The combination of the three modes produces the $3Q$ structural distortion of the 2×2 CDW precisely as shown in Fig. 2.1b

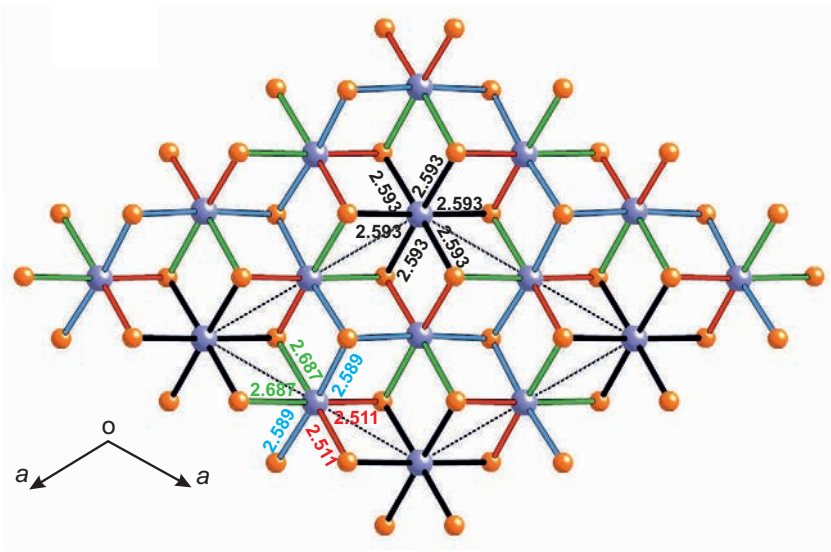

Figure 2.9: Calculated structure for the 2×2 distorted single-layer $TiSe_2$. The Ti-Se bonds of octahedra I are shown in black; the short(long) bonds in octahedra II are shown in red(green) respectively and the two intermediate ones are shown in blue.

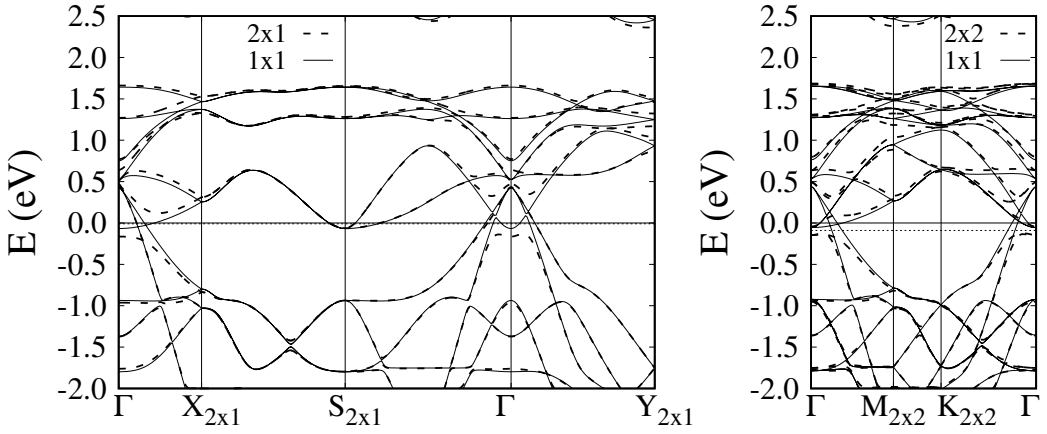

Figure 2.10: Band structure for the intrinsic single-layer $TiSe_2$. Broken lines correspond to the 2×1 structure corresponding to the displacement of the unstable M phonon (left panel), and for the 2×2 CDW structure (right panel). Full lines show the bands of the 1×1 undistorted structures, respectively. The bands are represented in the BZ of the 2×1 (left) and 2×2 structures (right), and therefore are folded with respect to those shown in Fig. 2.2. The origin of the energy scale is the Fermi level of the undistorted phase. The Fermi level of the distorted phases is indicated by the dotted horizontal lines.

symmetry axes because of the small angular distortions, but we use them as simple descriptors) there is a Se-Ti..Se bond alternation with one bond shorter (2.511 Å) and one bond longer (2.687 Å) than those in the undistorted phase (2.590 Å). Along the third four-fold axis the two bonds are identical (2.589 Å), and very similar to that in the undistorted phase. In turn, every regular octahedron of type I is surrounded by six type II octahedra sharing two Se atoms with the central one in such a way that these two Se atoms are making two short (red) or two long (green) Ti-Se bonds. Consequently, the three-fold symmetry axis going through the Ti atom of the octahedra I is preserved, and a hexagonal lattice is also obtained for the 2×2 distorted single-layer $TiSe_2$.

We now analyze the correlation between the structural distortions of the single layer and the changes in the electronic structure, which is ultimately at the origin of the instability of the undistorted phase. Fig. 2.10a shows the change in the electronic band structure induced by a $1Q$ distortion. The bands are compared to those of the undistorted lattice, and shown in the BZ of the 2×1 cell. The M point of the 1×1 cell in the direction of the double periodicity is now folded into the Γ point of the 2×1 supercell, and the corresponding electron pockets can now interact with the hole states from Γ, opening some gaps around the Fermi level. However, the S point of the 2×1 supercell coincides with one of the M points of the undistorted cell, as can be seen in Fig. 2.3 (since one of the original periodicities is maintained), thus still leading to a pocket of electrons at this point of the BZ, and a metallic band crossing the Fermi level near this point (and, correspondingly, a hole pocket and a metallic band at Γ). The $1Q$ distortion therefore reduces the metallic character of the band structure, by splitting some of the bands around the Fermi level, but is not able to open a full gap. This is fully consistent with the symmetry analysis presented above, as the $1Q$ distortion breaks the symmetry with respect to the σ plane. The Ti $d_{x^2-y^2}$ band is practically Ti-Se non-bonding as far as the symmetry plane σ is kept in the structure. However, if the Ti atom moves out of this plane, the symmetry is lost and the Ti and Se orbitals around the Fermi level can effectively mix, thus leading to an energy gain and opening of

a gap. In view of the nature of the Ti d orbitals in Fig. 2.4, the most effective Ti movement to produce such mixing is a displacement perpendicular to the a^* direction, because in that way two Se-Ti..Se bond alternations are produced while leaving the other two Ti-Se bonds barely changed. Such bond alternations are known to be globally stabilizing because the bonding gained in the two red bonds outweighs the bonding lost in the two green ones [81]. This is precisely the type of displacement brought about by the unstable M phonon, as shown in Fig 2.8.

The $3Q$ CDW distortion reduces further the symmetry, as now all the three equivalent M points of the undistorted BZ fold into Γ, and therefore the bands leading to the three electron pockets can interact with those leading to the hole pockets. The result is that a clean gap opens up now, as shown in Fig. 2.10b. The full opening of the gap as several M phonons are combined to form the $3Q$ distortion is the reason for the energy gain of the $3Q$ phase with respect to the single-phonon $1Q$ phase. This can be seen clearly in the electronic density of states (DOS), shown in Fig. 2.11. Comparing the DOS around the Fermi level for the undistorted layer, and for $1Q$, $2Q$ and $3Q$ distortions (i.e., combining one, two and three equivalent M phonons), the DOS around E_F decreases as successive phonons are included in the distortion, until a clean gap develops for the $3Q$ CDW. Also, the position of the Fermi level shifts towards lower energies. Both changes lead to the energy stabilization of the CDW phase. Evolution of the Density of States with the inclusion of unstable phonons in the structure in Fig. 2.11 compares the electronic density of states (DOS) around the Fermi level for the undistorted layer, and for $1Q$, $2Q$ and $3Q$ distortions (i.e., combining one, two and three equivalent M phonons). The DOS around E_F decreases as successive phonons are included in the distortion, until a clean gap develops for the $3Q$ CDW. Also, the position of the Fermi level shifts towards lower energies. Both changes lead to the energy stabilization of the CDW phase.

Both the metal-metal interactions which lower the energy of the Ti $d_{x^2-y^2}$ orbitals from Γ to M, and Ti-Se interactions which lead to the gap opening through

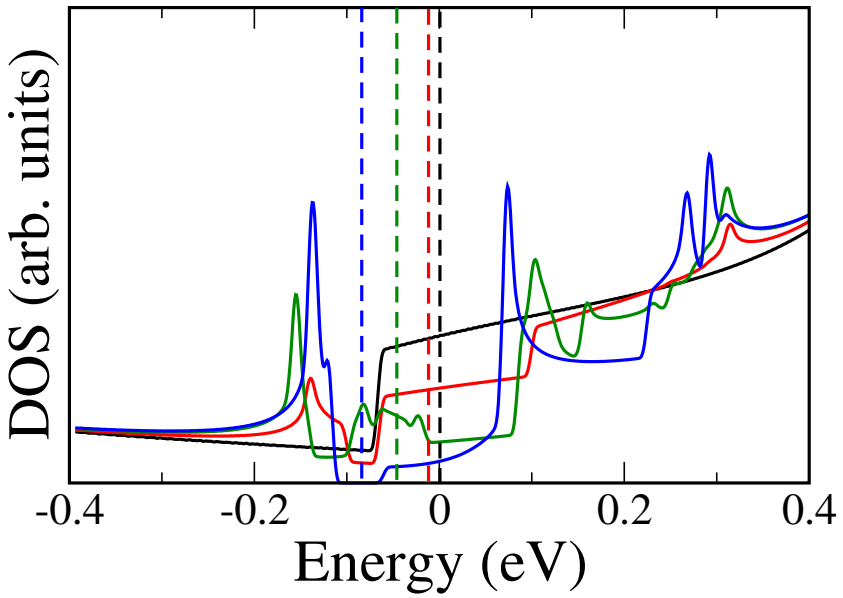

Figure 2.11: Electronic Density of States for single-layer $TiSe_2$, in the vicinity of the Fermi level. The black curve corresponds to the undistorted structure, while the red, green and blue ones to the 1Q, 2Q and 3Q distorted structures, respectively (see text for details). The position of the Fermi level for each case is shown with a vertical dashed line.

the mixing allowed by the symmetry breaking, cooperate in providing the energy stabilization produced by the 2×2 modulated structure. This is in contrast with the case of single-layer 1H-$NbSe_2$ where the driving force for the low temperature 3×3 modulated structure is the optimization of the metal-metal interactions [48]. Note that the mechanism described above relies on the specific movement of Ti atoms so as to create a Se-Ti...Se bond alternation along two of the four-fold axes of type II octahedra. This is the microscopic description of the consequences of the band mixing made possible by the phonon instability and providing the stabilization of the 2×2 modulated structure. It is clear that essentially the same mechanism will stabilize the system even in the case of a small band gap situation.

2.3 Influence of doping

The injection of charges in the $TiSe_2$ single-layer may have important consequences on its structure and physical properties, as shown by the rich phase diagram under chemical [68] and electrostatic [77] doping. Here, we analyze these effects by

introducing extra charges (either positive or negative) explicitly in our DFT calculations. Details are given in section 2.5.

For each value of the doping, we optimize the structure of the undistorted crystal, using the 1×1 periodicity. For the range of doping values considered, we do not see any significant changes in the lattice constant with respect to the undoped case. As a consequence, the positions of the Ti atoms remain unchanged with doping, as well as the in-plane location of the Se atoms. The height of the latter does change with doping, as will be shown below. We then follow the same procedure as for the undoped case, and compute the phonon structure in order to determine the drive towards structural instabilities as a function of doping. The resulting phonon band structures in the Γ-M line are summarized in Fig. 2.12 for electron (top) and hole doping (bottom), respectively.

For small values of the doping, the phonon spectra are qualitatively similar to the undoped case. In particular, the presence of an unstable mode around the M points of the Brillouin zone is observed. However, the imaginary frequency of this mode evolves significantly with the doping level. The evolution is shown in Fig. 2.13a. The phonon at M becomes stable at a certain value of the doping, which is around -0.23 and +0.07 $|e|$ per formula unit for electron and hole doping, respectively. For each value of the doping, we have also performed structural relaxations to obtain the distortion of the 2×2 structure. In all casfes, we obtain a $3Q$ pattern as the one obtained for the intrinsic layer. Fig. 2.13b shows the energy difference between the undistorted 1×1 phase and the 2×2 distorted structure as a function of doping. The 2×2 distortion disappears at the same doping values as those for which the M phonon becomes stable.

Fig. 2.14 presents the variation of the structural distortions associated with the $3Q$, 2×2 phase as a function of doping. The in-plane displacements of the Ti and Se atoms following the pattern of Fig. 2.1b, and the height z of the Se atoms from the plane of the Ti atoms are shown in Figs. 2.14a and 2.14b, respectively.

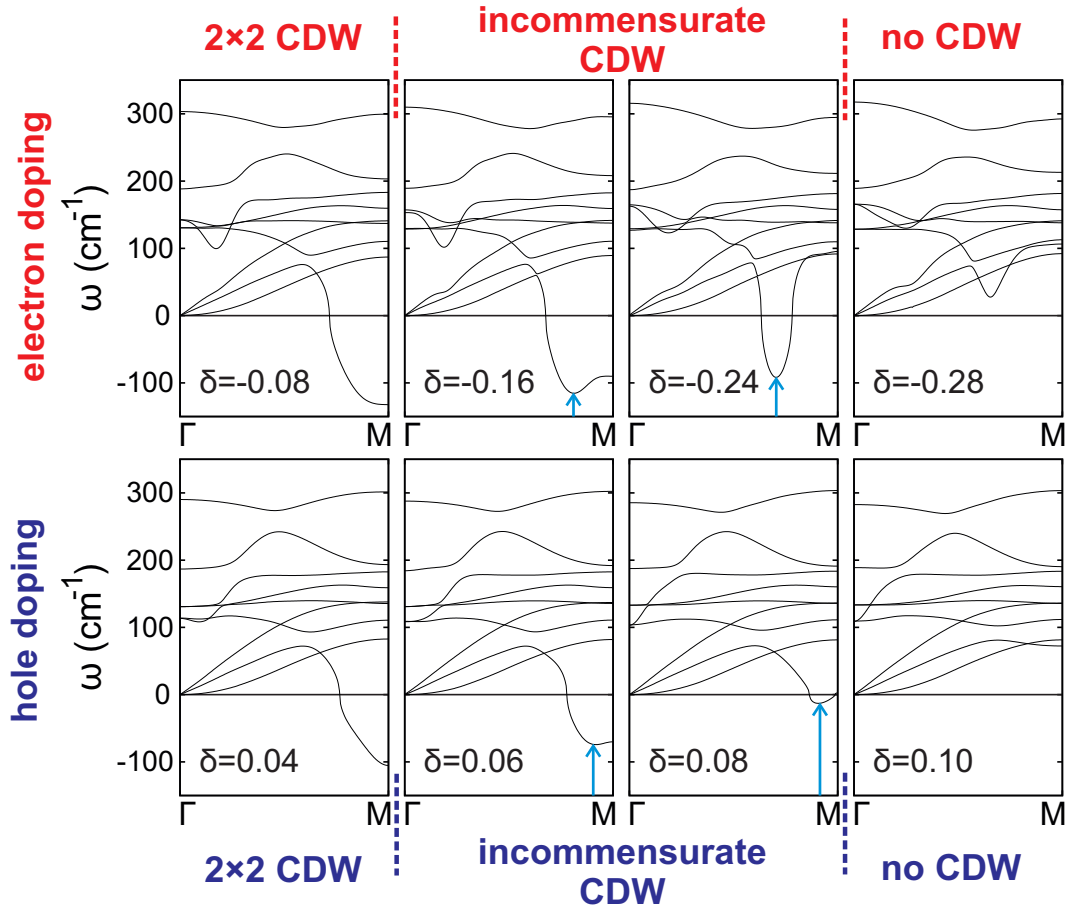

Figure 2.12: Phonon dispersion for the undistorted single-layer $TiSe_2$ in the $\Gamma - M$ segment of the BZ, for different values of doping δ (in electrons per formula unit). The upper (lower) panels correspond to electron (hole) doping. The regions of stability of the 2×2 CDW, incommensurate CDW and no CDW are indicated above and below the panels. The arrows indicate the position of the minimum of the unstable phonon branch for the incommensurate cases.

For reference, we also include the evolution of the Se height for the non-distorted 1×1 phase, and that of the two types of Se atoms in the 2×2 phase. Again, we observe that the distortions away from the 1×1 symmetry disappear at the same values as the instability of the M phonon.

The mechanism for the stabilization of the 2×2 CDW state in the doped case is the same as in the intrinsic one: the hybridization of the hole and electron pockets allowed by the symmetry breaking, and the consequent opening of a significant band gap around the Fermi level. As we showed before, for the intrinsic case, the Fermi level lays within the gap, making the system a semiconductor.

This is imposed by electron counting (as the number of electrons in the system is an integer). For the doped case, the distortion provokes a similar gap in the band structure, but the extra carriers (either electrons or holes) must accommodate within the conduction or valence bands, and the system remains metallic. Nevertheless, for sufficiently small doping values, the distortion still produces a lowering of the energy, driven by the reduction of the DOS near the Fermi level, and the increase of states at lower energies (at the peak defining the band edge). This situation only holds when the doping levels are sufficiently small, so that the Fermi level lays at energies with a significantly modified DOS. A simple model in which the energy gain is estimated from the change of the DOS leads to values of the critical doping for which the 2×2 phase is stable that are quite similar to the ones obtained above, with a difference in a factor of two for the range of stability of electrons and hole doping (not far from the factor of 3 that we obtained in our calculations). As the doping level increases and the Fermi level goes further into the valence or conduction bands, the energy gain due to the distortion is reduced, making the structural distortion progressively less pronounced, until the system recovers the 1×1 periodicity.

It is interesting, however, to realize from Fig. 2.12 that the evolution of the unstable phonons with doping is more complex than the one just described, which took into account only the behaviour of the M phonon. As the doping level increases, the minimum of the unstable phonon frequency displaces from M to smaller values of $\mathbf{q}$, along the $\Gamma - M$ line. This implies that, for such doping values, the CDW would not have 2×2 periodicity, but would be incommensurate, with wavevector corresponding to the position of the minimum of the unstable phonon branch. Also, for values of the doping where the M phonon is already stable, there is still an unstable part of the branch, with a minimum at an incommensurate value of $\mathbf{q}$ along the $\Gamma - M$ line, which evolves with the doping value. Ultimately, for larger values of the doping, the whole branch becomes stable, as shown in the panels with the largest values of both electron and hole doping in

Fig. 2.12. We expect, therefore, that there will be a transition between a commensurate 2×2 and an incommensurate distortion upon increasing the doping of the layer, until the undistorted 1×1 structure is recovered for sufficiently high doping values The wavelength of the incommensurate distortion is expected to increase for increasing doping values, as the minimum of the imaginary frequency of the unstable phonon shifts towards lower momenta. We have checked that this picture is correct, by considering explicitly the case for $\delta = -0.24$ doping, for which the phonon at M is stable, but it is unstable for values of $\mathbf{q}$ around $1/3$ of the $\Gamma - M$ line. Therefore, the 2×2 structure is not stable with respect to the undistorted one, as shown in Fig.2.13b), but one would expect a CDW with an incommensurate modulation close to 3×3. We have explicitly obtained the energy gain for several commensurate modulated structures with periodicity vectors very close to that of the (incommensurate) minimum, and find that they are lower in energy than the undistorted structure by a fraction of a meV per formula unit (see 3 Q phonon pattern in App. A). Therefore, we conclude that, indeed, there should be a range of doping values for which the most stable structure should be incommensurate with a wavevector which varies with the doping value, and with a small energy gain with respect to the 2×2 or the undistorted structures.

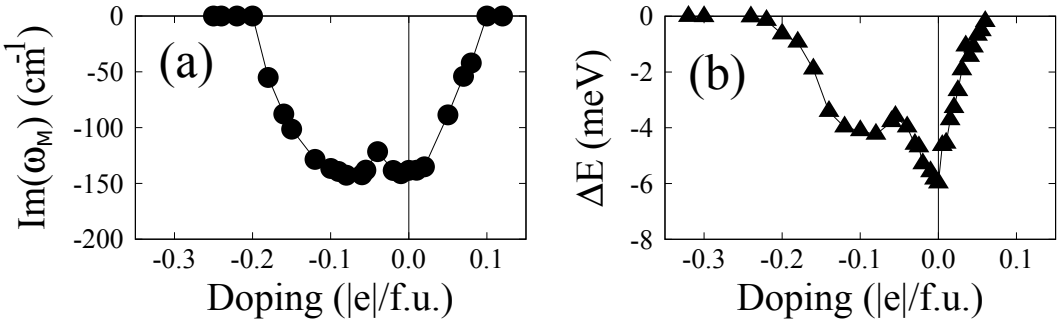

Figure 2.13: Evolution of the (a) imaginary frequency of the unstable mode at M, and (b) the energy decrease (per formula unit) due to the 2×2 distortion as a function of the external doping (in electrons per formula unit; negative values indicate electron doping).

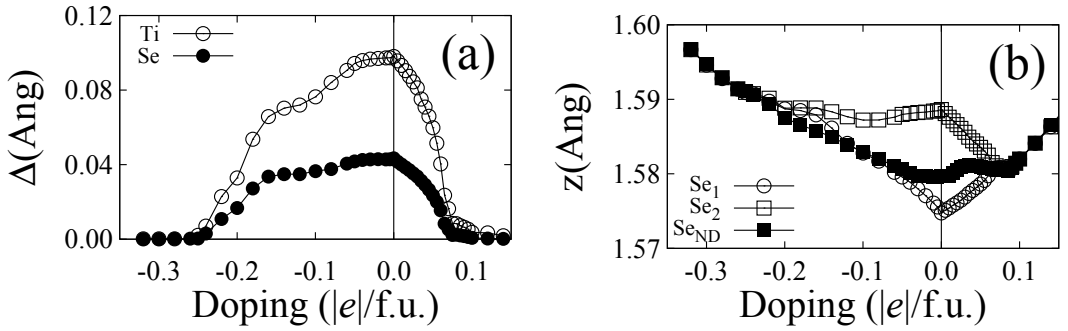

Figure 2.14: (a) Displacement in the plane parallel to the layer for the Ti and Se atoms from their position in the undistorted phase as a function of doping. (b) Height of the Se atoms as a function of doping. Se_1 and Se_2 correspond to the two inequivalent Se atoms in the 2×2 CDW phase, as shown in Fig. 2.1. Se_{ND} corresponds to the undistorted, 1×1 phase.

2.4 Conclusions

In summary, a detailed first principles analysis (using Density Functional Theory) has been carried to identify the origin and characteristics of the CDW distortion in single-layer $TiSe_2$. We identify the origin of the 2×2 CDW from the analysis of a phonon branch that becomes stable around the M point of the Brillouin zone. The atomic displacements of this phonon mode allow the mixing of states at the top of the valence band at the Γ point and the bottom of the conduction band at M (both responsible for the metallicity of the undistorted structure), which leads to partial band gap openings that, in turn, lowers the total energy of the system. The combination of three such phonons for the three equivalent M points allows a full band gap opening and a further energy lowering. This $3Q$ structure has a 2×2 periodicity which closely matches the CDW in-plane distortion of the bulk material. Doping the layer with externally injected charges modifies this picture only slightly for small doping levels: the energy gain due to the structural distortion is reduced when doping is present, as the Fermi level does not fall at the energy gap opened by the distortion. This makes the atomic displacements and the stabilization energy to decrease with increasing doping level, so that the CDW transition temperature is also expected to decrease, as observed experimentally both in the bulk [68] and in samples of thin layers [77]. Furthermore, our calculations show that, for larger doping levels, the phonon band-structure changes

significantly, in such a way that the unstable phonon branch has its minimum at intermediate points of the $\Gamma - M$ segment, while the phonon at M becomes stable. It could therefore be expected that the CDW can become incommensurate for certain values of the doping. Further increase of the doping level makes all the phonon branches to become stable, and therefore the system recovers the undistorted 1×1 structure.

2.5 Computational details

The geometrical optimizations, eletronic and phononic band structures were carried out using a numerical atomic orbitals density functional theory (DFT) [96, 97] approach implemented in the SIESTA code [27, 28]. The Perdew-Burke-Ernzerhof (PBE) functional was used to account for the exchange-correlation energy [98]. The core electrons have been replaced by norm-conserving scalar relativistic pseudopotentials [99] factorized in the Kleinman-Bylander form [100]. We include the $3p$ shell of Ti explicity in the valence, as semicore states. We have used a split-valence double-ζ basis set including polarization functions [101]. The non-linear core-valence exchange-correlation scheme [102] was used for all elements. In the direction normal to the single-layer we chose a vacuum space of 50 Å in order to avoid possible interactions between the layer and its images. In the case of geometrical optimization calculations, the atomic coordinates were relaxed until the forces on them were below 0.004 eV/Å. In all calculations, we use a cutoff of 550 Ry for the real space integrals, and a tolerance of 10^{-5} and 10^{-4} eV on the density matrix ant the total energy, respectively, for the convergence of the SCF cycle. To sample the Brillouin cell for the electronic states, a Monkhorst-Pack [103] k-point grid of 36×36×1 was used for the undistorted minimum cell and it was scaled accordingly where supercell calculations were performed. The phonon band structures were calculated using the finite differences method.

For the geometrical optimization we have relaxed the undistorted and modulated structures in their respective symmetries as described in tables 2.1 and 2.2, i.e.

for the 1×1 cell we have 3 atoms in the unit cell: 1 Ti atom and 2 Se atoms; for which we assign their respective Wyckoff coordinates thus imposing the symmetry constraints. In this particular case only the z-coordinate of the Se atoms is a degree of freedom. For the 2×2 cell we have 12 atoms in the unit cell: 1 immovable Ti (1a Wyckoff position) atom, 3 Ti atoms (3e Wyckoff position) with in-plane degrees of freedom, 2 Se atoms (2d Wyckoff position) with an out-of-plane degree of freedom, respectively 6 Se atoms (6g Wyckoff positions) with both in- and out-of- plane degrees of freedom.

Table 2.1: Wyckoff positions of the space group 164 ($P\bar{3}m1$) used in describing the internal coordinates of the single-layer $TiSe_2$ undistorted structure.

Atom	Multiplicity	Wyckoff letter	Coordinates
Ti	1	a	(0,0,0)
Se	2	d	(1/3,2/3,z) (2/3,1/3,−z)

Table 2.2: Wyckoff positions of the space group 150 (P321) used in describing the internal coordinates of the 2×2 $TiSe_2$ modulated structure.

Atom	Multiplicity	Wyckoff letter	Coordinates		
Ti	1	a	(0,0,0)		
Ti	3	e	(x,0,0)	(0,x,0)	(−x,−x,0)
Se	2	d	(1/3,2/3,z)	(2/3,1/3,−z)	
Se	6	g	(x,y,z) (y,x,−z)	(−y,x−y,z) (x−y,−y,−z)	(−x+y,−x,z) (−x,−x+y,−z)

3. 2X2 CHARGE DENSITY WAVE IN SINGLE-LAYER TITE2

3.1 Introduction

Transition metal dichalcogenides of the groups IV and V rank among the most controversial materials exhibiting charge density wave (CDW) instabilities [50, 104]. The possibility of strong or weak electron-phonon coupling scenarios in group V $2H$-MX_2 (M = Nb, Ta; X = S, Se) and either phonon mediated or excitonic mechanisms in group IV $1T$-$TiSe_2$ have been discussed for decades [50]. Many of these systems also exhibit superconductivity (SC) under certain conditions and the competition between the two instabilities remains an important question still unanswered [105, 76]. These materials are built from MX_2 layers interacting through weak van der Waals forces and thus are easily exfoliated [15]. Consequently, they offer the possibility to examine the above mentioned issues at the two-dimensional (2D) limit as well as by smoothly varying the density of carriers through gate doping. This is at the origin of the huge revival of interest recently raised by these materials [106, 72, 55, 107, 77, 73].

Indeed, intriguing differences of these few-flake or even single-layer materials with their bulk counterparts have been discovered. Recent reports on the existence of a very weak pseudo-gap at the Fermi energy in single-layer $NbSe_2$ [106, 48] or the possible occurrence of incommensurate modulations for slightly electron doped $TiSe_2$ crystals of thicknesses less than 10 nm [77, 40] make clear that we are still far from a full understanding of the physics of CDW materials and more particularly when the screening is reduced.

In this context, the recent report of a 2×2 CDW in single-layer $TiTe_2$ by Chen *et al.* [55] came as a very intriguing surprise. Since long [108, 109, 110] it has been known that bulk 1*T*-$TiTe_2$ does not exhibit the 2×2×2 CDW that occurs in isostructural 1*T*-$TiSe_2$ [53]. In addition, the 2×2 CDW is not observed anymore in pristine multi-layer $TiTe_2$ [55], but the 2×2 CDW phase have been stabilized up to room temperature in multi-layers $TiTe_2$ under applied strain [111]. In contrast, the 2×2 CDW instability is observed in pristine $TiSe_2$ from the single-layer, for ultrathin films with up to six layers [93], and for the bulk crystal [53]. The experimental indication of the occurrence of the CDW in single-layer $TiTe_2$ is even more surprising when considering that first-principles density functional theory (DFT) calculations found that single-layer $TiTe_2$ shows no tendency to distort towards the 2×2 CDW structure at the generalized gradient approximation (GGA) level [55]. Yet, calculations of the same quality successfully predict that the 2×2 CDW structure is more stable than the non-distorted structure for single-layer $TiSe_2$ [93, 92, 40]. Overall, these observations suggested the hypothesis that something really new and challenging is at work in single-layer $TiTe_2$ [55].

However, one should note that the CDW transition occurs at 100 K in single-layer $TiTe_2$ [55] but at a considerably higher temperature, 232 K, in single-layer $TiSe_2$ [73]. Hence, the driving force for the distortion must be considerably weaker in single-layer $TiTe_2$. Before concluding that a new scenario is needed to grasp the origin of the unexpected 2×2 CDW in this material, one should wonder about the appropriateness of the so far successful GGA-type of DFT approaches to the CDW instabilities in single-layer group IV and V dichalcogenides. Such an appraisal is needed because it impinges on very fundamental questions concerning CDW instabilities at the 2D limit. Note that it has been recently shown [87] that GGA-type functionals like PBE [98] overestimate the overlap between the Ti 3*d* and Se 4*p* levels in bulk 1*T*-$TiSe_2$. This can be corrected by using hybrid functionals like HSE06 [94, 112] leading to an improvement of the electronic description of bulk $TiSe_2$ [87]. In the following, we report a DFT study of the likeliness of

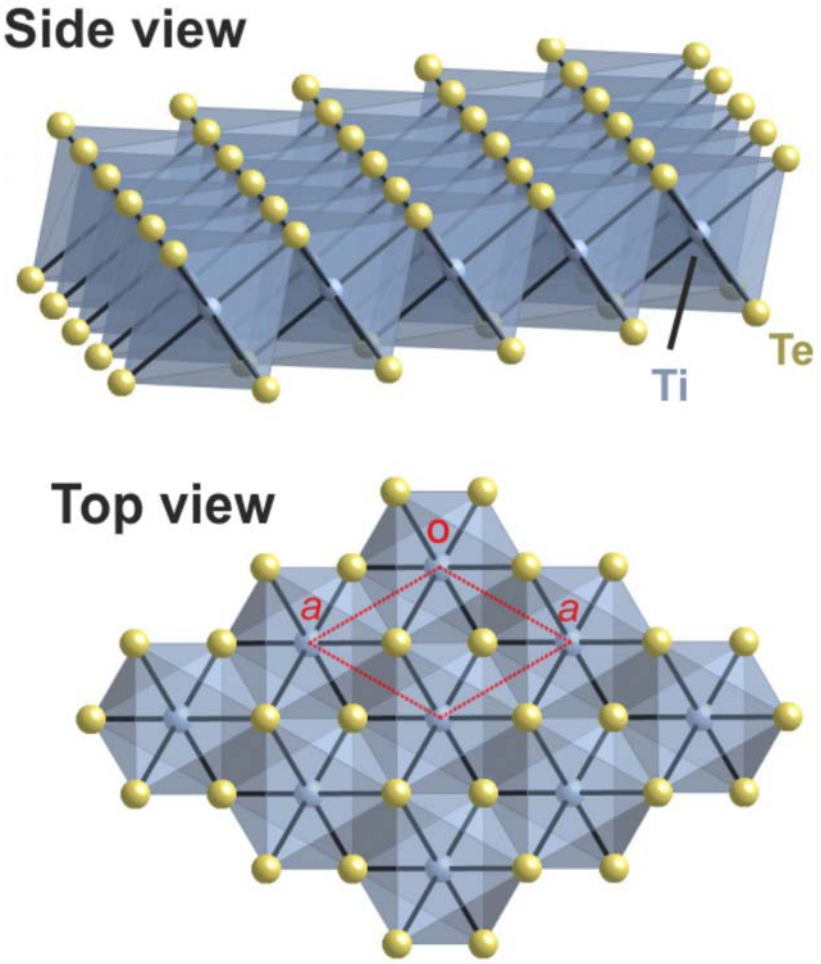

Figure 3.1: Single-layer $TiTe_2$ structure. Side and top views of a layer.

a 2×2 CDW in single-layer $TiTe_2$ employing both PBE and HSE06 functionals which provides useful insight on the origin of the CDW instability in single-layer $TiTe_2$[113].

3.2 Results and Discussion

An isolated layer of 1T-$TiTe_2$ is made of an hexagonal lattice of Ti atoms in an octahedral environment of Te atoms (Fig. 3.1). The repeat unit of the hexagonal bulk crystal structure contains just one of these layers. A detailed description of our calculation method is presented in 3.4. Let us start our analysis by briefly considering the PBE description of the electronic structure. The optimized a cell

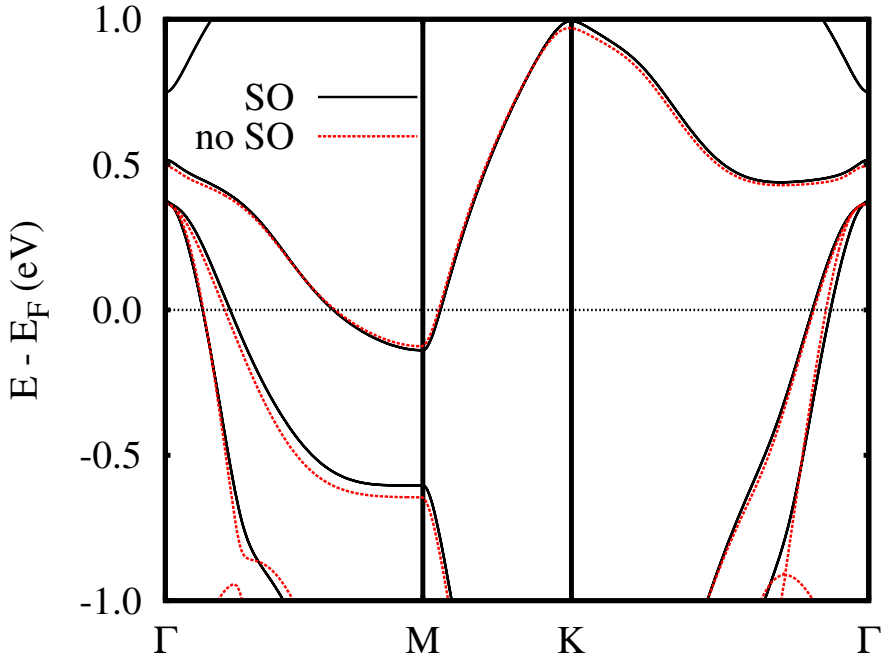

Figure 3.2: Calculated GGA band structure with (black lines) and without (red dots) spin-orbit coupling. Γ = (0, 0, 0), M= (1/2, 0, 0) and K= (1/3, 1/3, 0) in units of the reciprocal hexagonal lattice vectors.

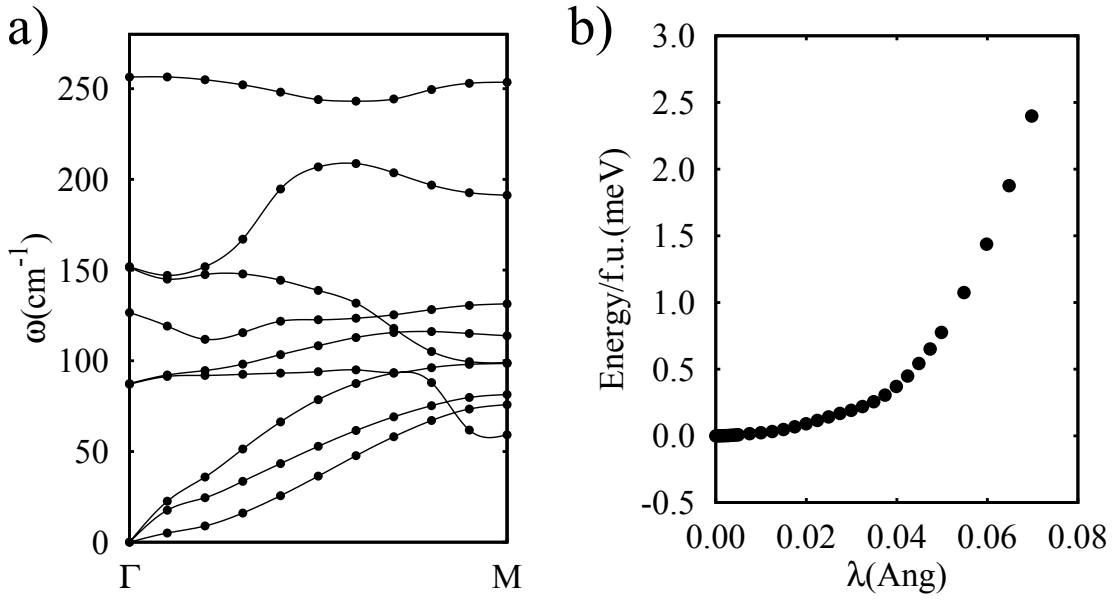

Figure 3.3: (a) GGA phonon dispersion in the Γ - *M* segment of the Brillouin Zone (BZ) for the undistorted structure.(b) Frozen-phonon total energy calculation as a function of the soft phonon mode amplitude at M, calculated with the GGA functional. Energies are given in meV per formula unit relative to the undistorted phase.

parameter is 3.804 Å for the single layer and 3.815 Å for the bulk, in good agreement with the bulk experimental value of 3.777 Å [114]. Within a single-layer there are several Te...Te contacts shorter than the sum of the van der Waals radii so that the valence bands, which have their maximum at Γ and are mostly built from Te $5p$ orbitals, are considerably wide and overlap with the bottom part of the Ti $3d$ bands, which have their minima at the M point (Fig. 3.2). As expected from the fact that in the bulk there are short Te...Te contacts in the direction perpendicular to the layer, the semimetallic overlap is 19% larger in the bulk. Note that, as it is clear from Fig. 3.2, inclusion of spin-orbit coupling effects does not have any noticeable effect and therefore it will not be considered anymore in the following. Thus, according to the PBE calculations single-layer $TiTe_2$ is a semimetal exactly as the bulk. In contrast with the case of single-layer $TiSe_2$, for which the same type of calculations led to a phonon with imaginary frequency at the M point [40], our calculations with the GGA functional for single-layer $TiTe_2$ (Fig. 3.3a) show no phonons with imaginary frequency, in agreement with those of Chen *et al.* [55].

Although there is some remnant of the instability at M (notice the optical branch that disperses downwards and shows the lowest frequency at the M point, reminiscent of the mode that becomes unstable for $TiSe_2$), there is no definite indication of a phonon instability that may lead to the 2×2 distortion of the structure. Detailed structural optimizations of 2×2 supercells confirmed this result. However, as indicated by the frozen-phonon total energy calculation as a function of the soft phonon mode amplitude at M (Fig. 3.3b), the GGA potential energy surface is extremely flat. Under such circumstances, even if strictly speaking the PBE calculations disagree with the experimental results in that no tendency toward the 2×2 CDW distortion is found, the results are somewhat inconclusive and a closer look is needed.

The very flat frozen-phonon energy curve of Fig. 3.3b) suggests that small external perturbations could be able to change the relative stability of the undistorted and 2×2 CDW structures. This could occur, for instance, by the effect of strain. Thus, we studied the evolution of the band structure and the relative stability

Table 3.1: Evolution with tensile strain of: (i) the energy difference between the undistorted structure and the relaxed 2×2 CDW structure, and (ii) displacement of the Ti atoms in the plane parallel to the layer from their position in the undistorted phase. All values obtained using the PBE functional.

Tensile Strain (%)	ΔE (meV/f.u.)	Δ Ti(Å)
0	0.00	0.000
1	-0.001	0.007
2	-0.09	0.057
3	-0.29	0.061
4	-0.47	0.067
5	-0.74	0.080
6	-1.27	0.095
7	-2.04	0.118

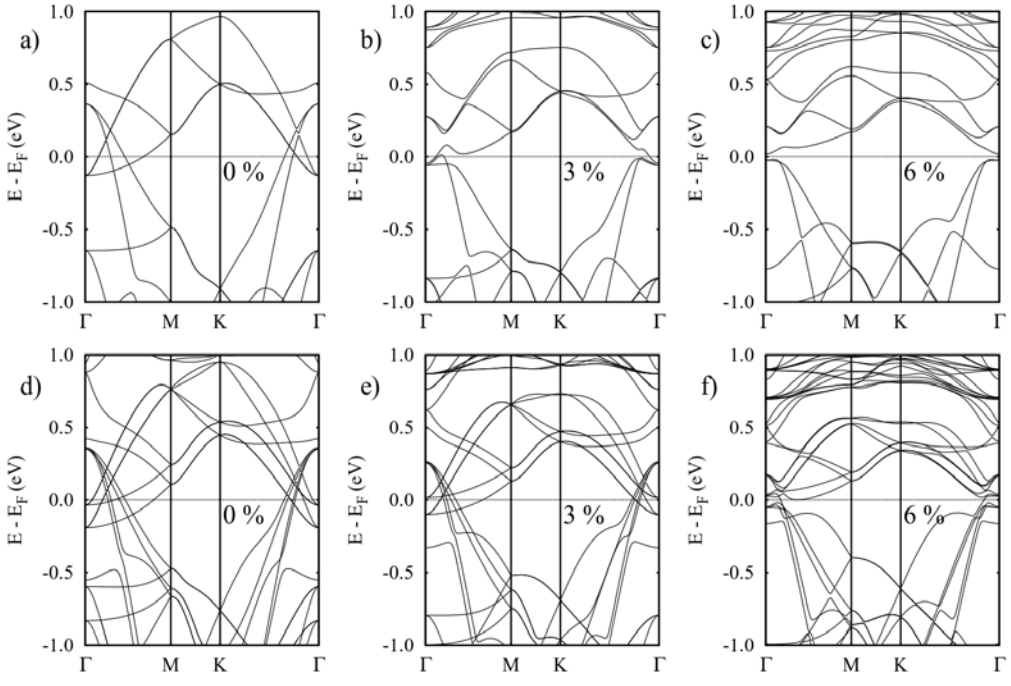

Figure 3.4: Calculated GGA band structures for the stable 2×2 CDW structure of single-layer (a)-(c) and double-layer (d)-(f) $TiTe_2$ under tensile biaxial strain. Γ = (0, 0, 0), M = (1/2, 0, 0) and K = (1/3, 1/3, 0) in units of the reciprocal hexagonal lattice vectors.

of the undistorted 1×1 and 2×2 CDW structures as a function of biaxial tensile strain(allowing the atomic positions to relax for each strain applied). The strain is defined as $s = \delta m/m_0$ where m_0 is the unstrained cell parameter and $m_0 + \delta m$ the strained cell parameter. Thus, positive values correspond to tensile strains. As shown in Table 3.1, a tensile stress as small as 1% is sufficient to make the 2×2 CDW structure slightly more stable than the undistorted one. For strains larger than 2%, the 2×2 CDW is definitely favored. Also we can clearly see the appearance of an imaginary phonon mode with the minimum at the M point in the BZ for the structure under 6% biaxial strain in Fig. 3.5.

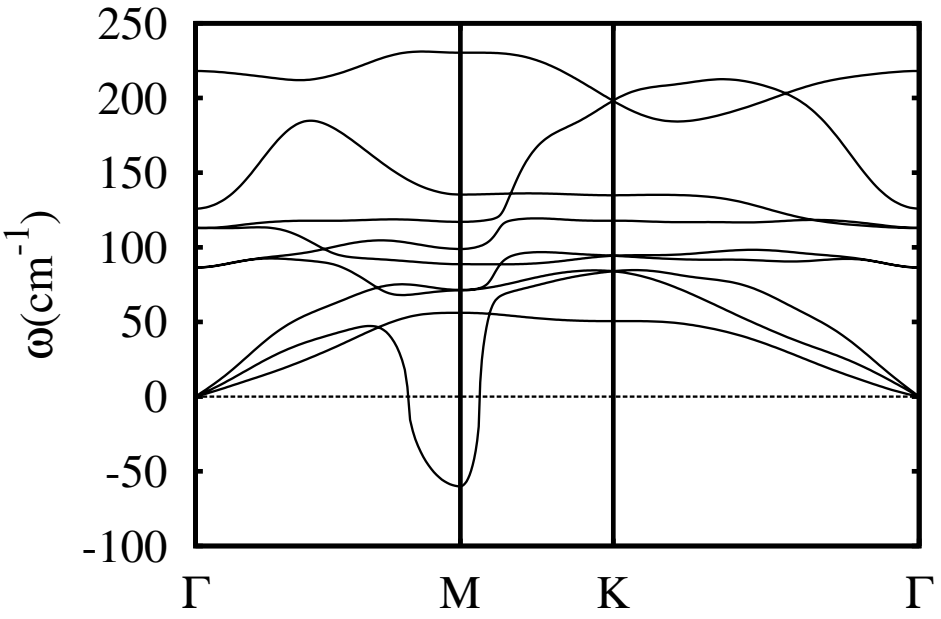

Figure 3.5: GGA phonon dispersion along the high symmetry lines of the Brillouin Zone (BZ) for the 6 % strained structure. Under a large enough bi-axial strain one of the acoustic branches becomes unstable at M indicating an instability of the undistorted structure.

The development of the 2×2 distortion is accompanied with the opening of energy gaps at the crossings between the folded valence and conduction bands. However, as shown in Figs. 3.4a-c, the distorted structure is still semimetallic and only for relatively large tensile strains (between 5 and 6%) a full band gap occurs at the Fermi level. As shown in Fig. 3.4a, in the folded band structure of the initial unstrained layer there is a band crossing slightly below the Fermi level at approximately halfway of the Γ-M line. Under a slight tensile strain, the semimetallic

overlap decreases and this crossing occurs exactly at the Fermi level thus leading to the opening of a gap at that energy. Nevertheless, the second Te-based valence band centered at Γ (the one with a larger effective mass) still crosses the Fermi level: it does hybridize with the M-point bands, but the resulting gap opens about 0.1 eV above the Fermi level. These results are in good agreement with the experimental ARPES data [55], which indicate that the valence band with larger effective mass remains metallic for temperatures below the CDW transition T_c, whereas the band with smaller effective mass does develop a gap at the Fermi level below T_c. The calculated densities of states (DOS) reflect the same result, with a pseudo-gap occurring at the Fermi level for small strains under which the 2×2 CDW structure is already stable (∼2-3%)(see Fig. 3.6) . This also compares favourably with the pseudo-gap observed in the experimental STS spectra (Fig. 4 in [55]), which has a similar width as the one observed in ARPES.

Judging from the comparison of the previous results with the ARPES data of Chen [55] it appears that the GGA-PBE description of single-layer $TiTe_2$ is only consistent with the experimental situation when a slight tensile strain is imposed in the calculation, as the GGA functional overestimates the overlap between conduction and valence bands, which is then compensated by the imposed tensile strain. The main effect of the strain is a decrease of the intralayer Te...Te short contacts which leads to a decrease of the Te 5p bandwidth and, consequently, of the semimetallic overlap. Only when this overlap decreases with respect to the PBE description of the system the 2×2 CDW becomes more stable. This observation is consistent with the fact that, when Te...Te interlayer interactions come into play in the bulk or even in the double-layer, the semimetallic overlap increases and the 2×2 CDW is not observed anymore. As shown in Figs. 3.4 (d)-(f) the semimetallic overlap increases from single- to double-layers. Note that the band structure for the $TiTe_2$ double-layer with ∼6% strain is very similar to that of the single-layer with a 3% strain. These results are reminiscent of the above mentioned work concerning the functional type dependence of the semimetallic overlap of bulk $TiSe_2$ [87] and prompted us to reconsider the stability of the unistorted vs.

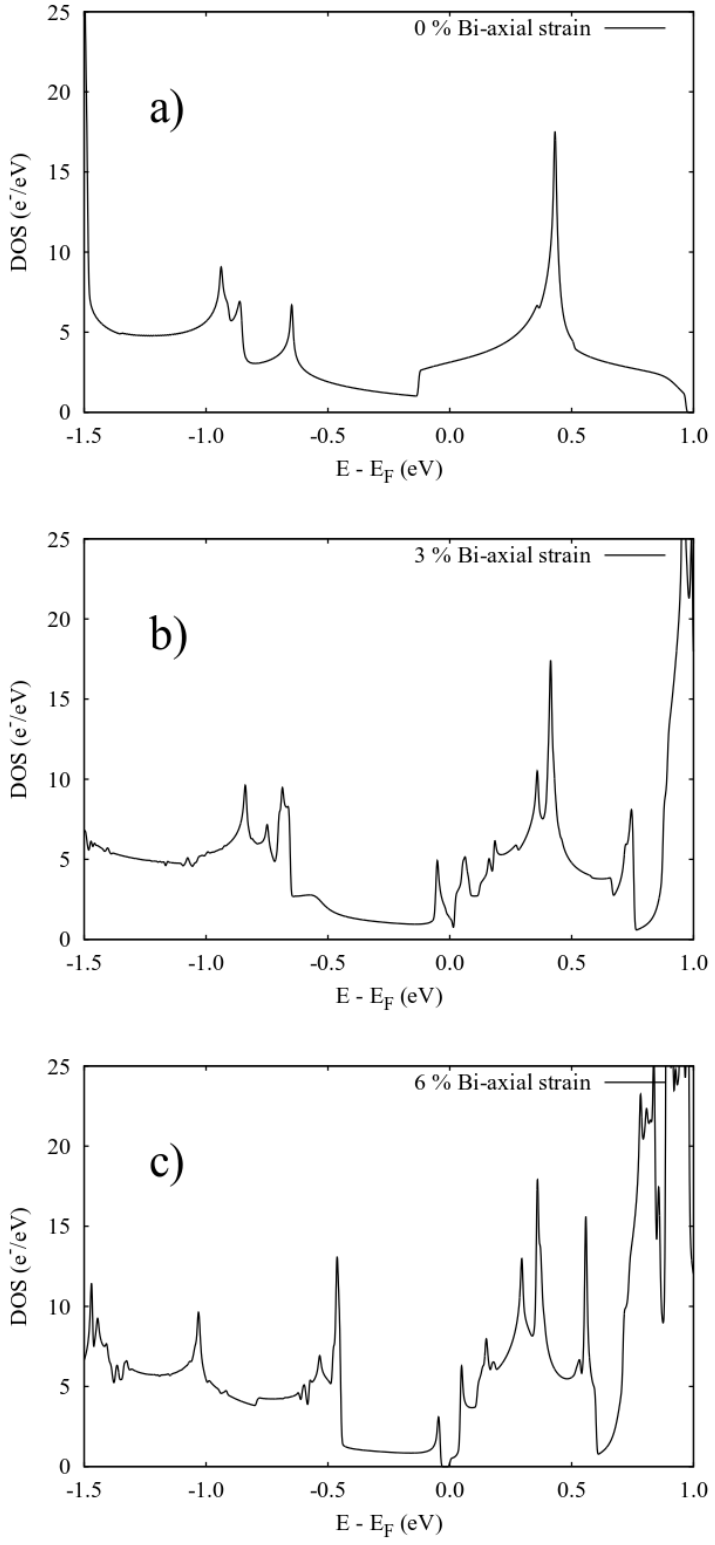

Figure 3.6: Density of states for the 2×2 structure of the single-layer $TiTe_2$ under tensile biaxial strain within PBE functional. A pseudogap at the Fermi level is obtained for a small bi-axial strain (panel b), while a full gap develops for large strain values (panel c).

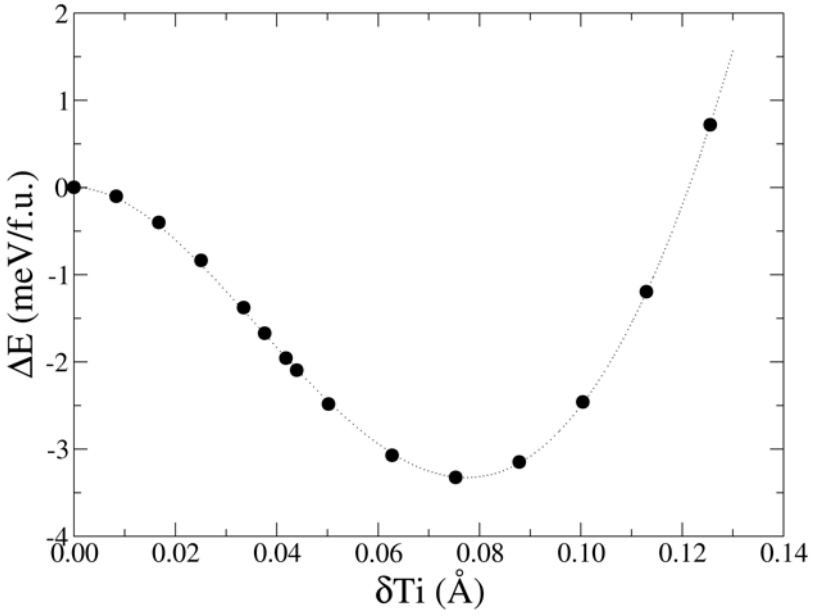

Figure 3.7: Energy difference (in meV per formula unit) between the undistorted and 2×2 CDW structures of an unstrained $TiTe_2$ single-layer according to DFT calculations using the hybrid HSE06 functional.

2×2 CDW structures using the hybrid type functional HSE06 [94, 112]. Shown in Fig. 3.7 is a frozen-phonon calculation of the energy difference between the undistorted structure and the 2×2 CDW structure following the soft phonon mode distortion. The curve clearly shows that, at the HSE06 level, unstrained single-layer $TiTe_2$ is indeed unstable towards the 2×2 CDW distortion. By relaxing the structure around the minimum of the frozen-phonon curve we have obtained an energy gain of 3.8 meV/formula unit. This stabilization energy is much lower than the value obtained for a $TiSe_2$ monolayer using a PBE functional, 6 meV/f.u [40]. Hellgren *et al.* [87] showed that for bulk $TiSe_2$ hybrid functionals predict a much higher stabilization energy than the PBE functional. Thus, it is understandable that according to our PBE type studies single-layer $TiTe_2$ does not tend to experience a 2×2 CDW instability. Overall, our data suggest a weak driving force for the distortion. Since this is a significant result let us consider in more detail the region of the semimetallic overlap. A fatband analysis of the PBE and HSE06 band structures is shown in Figs. 3.8a and b, respectively. A close inspection at the region around Γ points out some clear differences between the results of both functionals. For PBE, above the (partially empty) top of the valence band at Γ

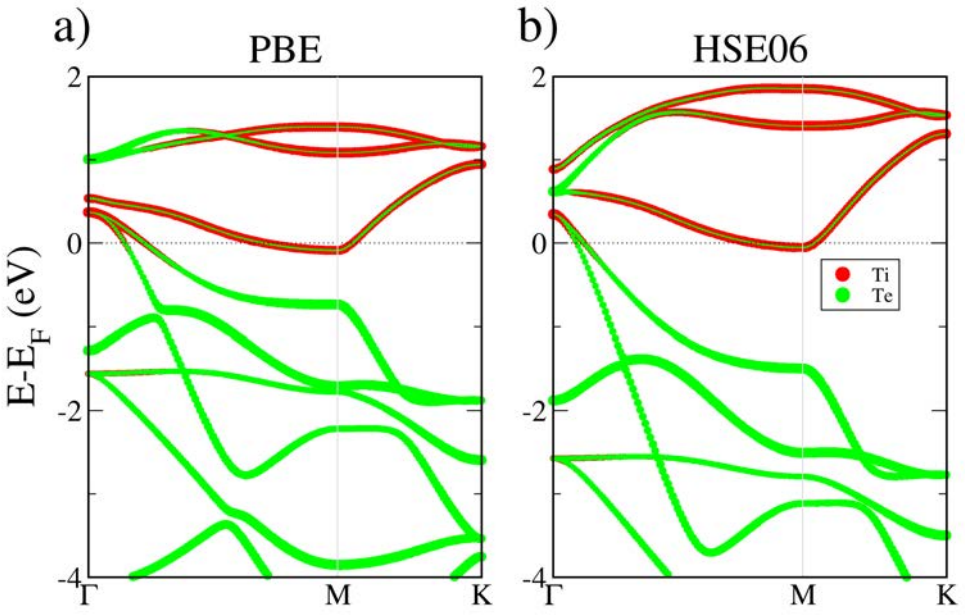

Figure 3.8: Calculated band structure for $TiTe_2$ single-layer using the PBE (a) and hybrid HSE06 (b) functionals. The size of the green and red circles is proportional to the Te and Ti character, respectively.

there is a non-degenerate band and a pair of degenerate bands at a higher energy. The order is the opposite for the HSE06 functional (Fig. 3.8b), for which the two degenerate bands are lower in energy. Around the Fermi level a heavy mixing of the t_{2g} levels of the Ti atom and the $5p$ levels of the Te atoms occurs. Assuming a local coordinate system in which the three-fold symmetry axis of the octahedron occurs along the z direction, the non-degenerate Ti-based band is essentially built from the Ti d_{z^2} orbital, whereas the top of the valence band, which is doubly degenerate at Γ, is mainly built from the Ti $d_{x^2-y^2}$ and d_{xy} orbitals which are somewhat tilted because the plane of the Ti atoms is not a symmetry plane. The single band at Γ is slightly higher in energy than the doubly-degenerate pair because of the slight rhombohedral distortion. The upper, doubly degenerate, Te-based bands are built from the Te p_x and p_y orbitals. Having identified the nature of these levels it is immediately clear that the Te-based doubly degenerate set is higher in energy for the PBE-type calculation. This means that, in the absence of Ti-Te hybridization, the Te p_x/p_y valence bands would raise up to higher energies at Γ than in the HSE06-type calculations. Consequently, when the hybridization

is switched on, a larger number of electron and hole carriers is induced. Indeed, a careful look at the band structures in Fig. 3.8 shows that there is a significantly larger overlap between the top of the valence band around Γ and the bottom of the conduction band at M for the PBE functional than for HSE06. The smaller overlap in the HSE06 band structure is also clear from the decrease of the the area of the constant energy plot at 0.25 eV below the Fermi level [55] for the undistorted $TiTe_2$ single-layer calculated with the HSE06 functional (compare Figs. 3.9 and 3.10). We note that the PBE-type band structure for single-layer $TiSe_2$, which provides a satisfactory description of the relative stability of the undistorted and 2×2 CDW in this system [40, 92], shows exactly the same topology and particularly, the same band ordering as the HSE06 band structure of Fig. 3.8b.

As soon as one moves along the Γ-M line (i.e. along the a^* direction), the only symmetry element preserved is the symmetry plane perpendicular to the layer and going along the a^* direction. One of the two Ti-based doubly degenerate levels at Γ and the Ti d_{z^2} mix and interact with one of the Te p bands near Γ leading to the slowly descending band from Γ-M which is associated with the electron pockets near M. With the local system of axes mentioned above, the crystal orbitals around M are almost exclusively made of tilted Ti $d_{x^2-y^2}$ orbitals (i.e. a mixing of Ti $d_{x^2-y^2}$ and Ti d_{z^2} which leads to the tilting of the orbital) exactly as we have discussed in Sec. 2.2 for the $TiSe_2$ single-layers [40]. We refer the reader to this section for a detailed analysis of the nature of the band structure which entirely applies to the HSE06 one reported in Fig. 3.8b.

The HSE06 band structure and density of states for both the undistorted and the 2×2 CDW structures are reported in Figs. 3.11. As shown in both figures the stabilizing 2×2 CDW distortion opens a gap at the Fermi level. The analysis of the nature and origin of the distortion goes along the same lines presented in detail in the Sec. 2.2 on $TiSe_2$ single-layer and will not be repeated here [40]. However, we note that the non-activated conductivity is kept in single-layer $TiTe_2$ below the CDW transition temperature [55] so that no gap should occur at the

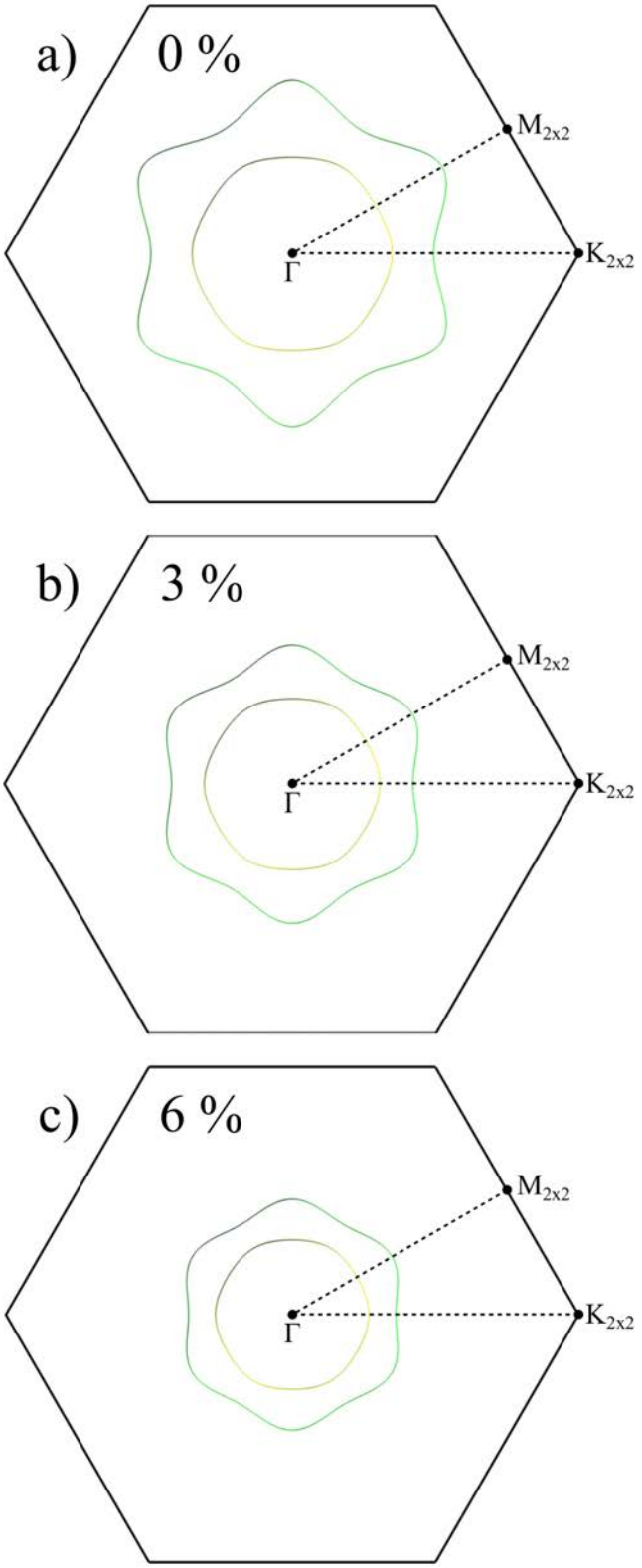

Figure 3.9: Constant energy contour at 0.25 eV below the Fermi level for the 2×2 structure of the single-layer $TiTe_2$ under tensile bi-axial strain. Note that the energy contours calculated within PBE functional are slightly smaller in radius than the experimental one.

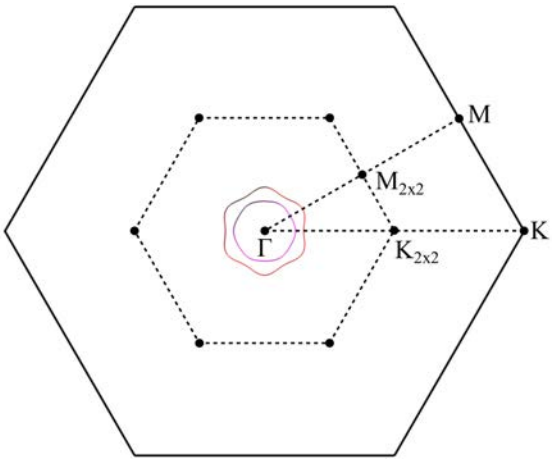

Figure 3.10: Constant energy contour at 0.25 eV below the Fermi level of the single-layer $TiTe_2$ calculated with the hybrid HSE06 functional.

Fermi level. Consequently, the HSE06 calculations exaggerate the tendency towards the transition. As mentioned above, the PBE calculations suggest that under reasonable tensile strain a 2×2 CDW is favored without the development of a band gap. Only when the strain is relatively large (i.e. around 5-6%, see Fig. 3.4) a band gap really opens. The HSE06 band structure of Fig. 3.11a is similar to that in Fig. 3.4c corresponding to a 6% tensile strength. We believe that the HSE06 functional exaggerates the stability of the 2×2 CDW and that the real situation concerning the weaker stabilization of the CDW phase and the lack of a full bandgap opening would rather correspond to that of the PBE functional with a moderate tensile strain. This observation, together with previous results on bulk $TiSe_2$ [87] suggest that a predictive description of these TiX_2 systems is attainable by using the HSE06 functional and tuning the actual contribution of the exact exchange. However, from the viewpoint of the physical origin of the CDW we do not find any noticeable difference with the analysis in Sec. 2.2 of the 2×2 CDW instability of $TiSe_2$ single-layers.

To further assess our conclusion we carried out HSE06 calculations for a $TiTe_2$ double-layer. Two single-layers with the optimized structure were placed with the interlayer bulk distance. The stabilization energy of the 2×2 CDW is reduced to practically one-half the value in the single-layer. Taking into account the small (and exaggerated) value for the single-layer, the driving force for the 2×2 CDW

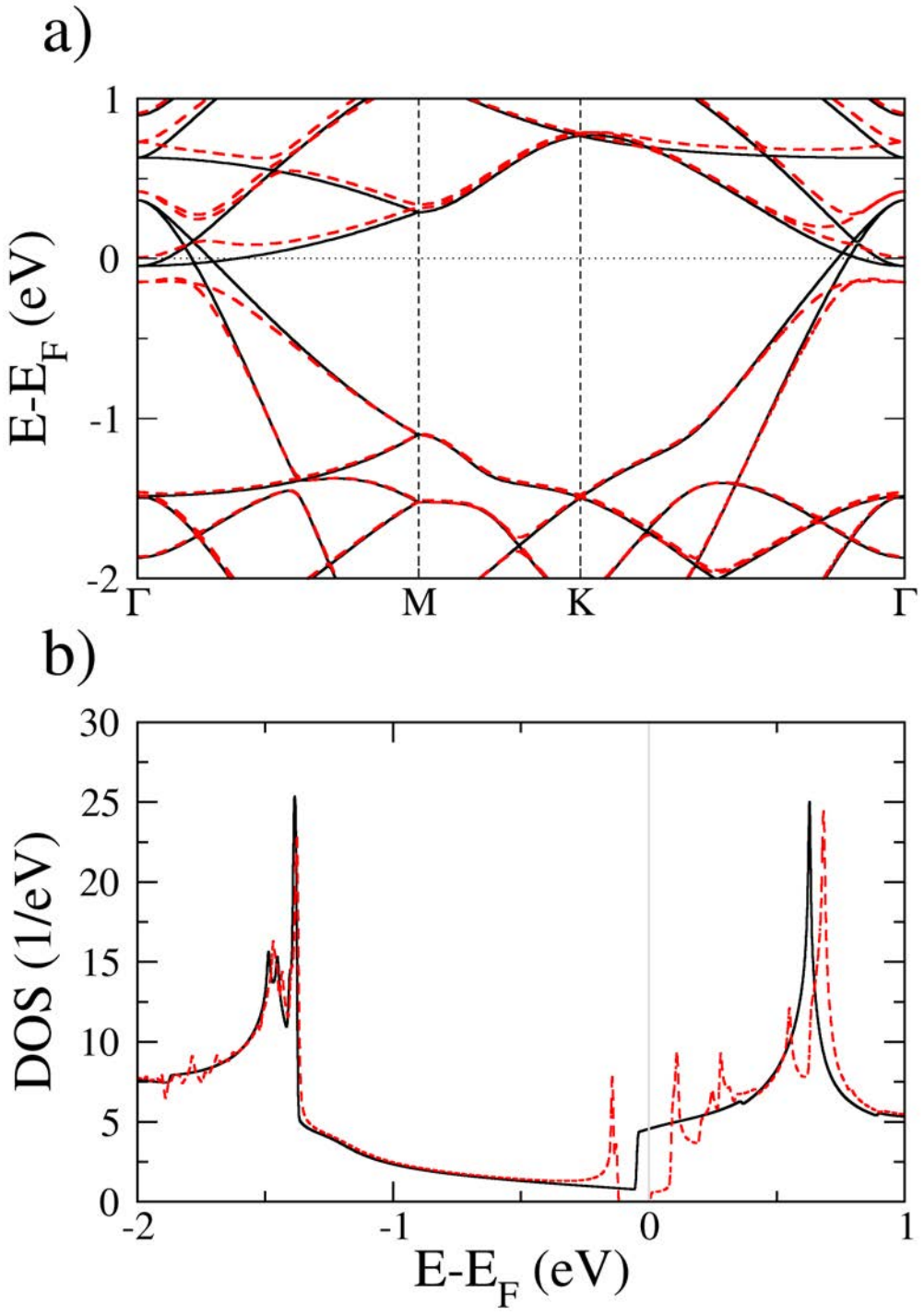

Figure 3.11: HSE06 band structure (a) and Density of States (DOS) (b) for single-layer $TiTe_2$. Broken red lines correspond to the 2×2 CDW structure and black continuous lines to the undistorted structure. The bands are represented in the BZ of the 2×2 structure and therefore are folded with respect to that in Fig. 3.2. The origin of the energy scale is the Fermi level of the undistorted structure.

distortion in the $TiTe_2$ double-layer must be extremely small or most likely nil, as experimentally found.

Our study points out an interesting possibility. Since tensile strain has been found to be a useful technique to induce modifications in single-layer or few-flake materials [115, 116, 117, 118], it is possible that the 2×2 CDW can be induced in double-layers or triple-layers of $TiTe_2$ by using a small tensile strain. [1] This prediction was confirmed shortly after the publication of our study in [111] were the CDW state was stable at room temperature in up to 50 layers under strain. Another useful hint provided by our study is that the 2×2 CDW in single-layer $TiTe_2$ may be more stable and result with a band gap under tensile strain or may be suppressed under a slight compresive strain.

3.3 Conclusions

A density functional theory study concerning the origin of the 2×2 CDW distortion recently reported experimentally for single-layer $TiTe_2$ has been carried out. This report is surprising because neither double-layer nor bulk $TiTe_2$ exhibit the 2×2 distortion and a PBE-based DFT study predicts that the undistorted structure is also more stable for the single-layer. Our study shows that, whereas calculations employing the semi-local functional PBE favor the undistorted structure, the hybrid functional HSE06 correctly predict the 2×2 distortion. However, the HSE06 calculations seem to exaggerate the stability of the distorted phase and, as a consequence, a noticeable band gap of more than 0.1 eV is induced at the Fermi level. This is in contrast with the metallic character of the $TiTe_2$ single-layers below the transition temperature. Interestingly, PBE type calculations for the case where the single-layer is subject to a slight tensile strain also favor the 2×2 distortion while keeping the semimetallic overlap. The study suggests that the magnitude of the semi-metallic overlap is a key factor controlling the tendency

[1] Note that tensile strain has been shown to decrease the semimetallic overlap and eventually lead to a band gap without changing the size of the unit cell both in single-layer [119] and bulk 1*T*-TiS_2) [120].

towards the distortion and consequently only functionals describing such overlap very accurately can provide a truly predictive description of the electronic structure.

According to the present study the mechanism of the CDW instability in single-layer $TiTe_2$ seems to be the same phonon mediated mechanism acting for single-layer $TiSe_2$[40] although now the driving force is smaller and the semimetallic character is kept below the transition temperature. As mentioned above, the magnitude of the semimetallic overlap seems to be one of the key factors in controlling the likeliness of the 2×2 CDW. Taking into account that the overlap should increase in these TiX_2 systems when the number of short Te...Te contacts increase or when they become stronger, the overlap should increase from single-layers to bulk and from X=S to X=Te. Since the instability is not observed in bulk TiS_2 nor in double-layer $TiTe_2$, it seems that only a relatively narrow range of semimetallic overlaps is associated with the instability. In this respect, a significant result of the study is that tensile strain stabilizes the 2×2 CDW distortion in single-layer $TiTe_2$. This could be used to induce the instability in double- or triple-layers of $TiTe_2$ which in the absence of strain remain undistorted, to induce a stronger distortion leading to the creation of a band gap in single-layer $TiTe_2$ or most likely to suppress the 2×2 CDW under a small compression. Such studies could provide useful insight on the CDW mechanism of group IV 1*T*-TiX_2 phases.

3.4 Computational details

The geometrical optimizations, electronic and phononic band structures were carried out using a numerical atomic orbitals density functional theory (DFT) [96, 97] approach implemented in the SIESTA code [27, 28]. The Perdew-Burke-Ernzerhof (PBE) functional was used to account for the exchange-correlation energy [98]. The core electrons have been replaced by norm-conserving scalar relativistic pseudopotentials [99] factorized in the Kleinman-Bylander form [100]. We include the

3p shell of Ti explicity in the valence, as semicore states. We have used a split-valence double-ζ basis set including polarization functions [101]. The non-linear core-valence exchange-correlation scheme [102] was used for all elements. In the direction normal to the single-layer we chose a vacuum space of 50 Å in order to avoid possible interactions between the layer and its images. In the case of geometrical optimization calculations, the atomic coordinates were relaxed until the forces on them were below 10^{-5} eV/Å. In all calculations, we use a cutoff of 2500 Ry for the real space integrals, and a tolerance of 10^{-7} and 10^{-6} eV on the density matrix and the total energy, respectively, for the convergence of the SCF cycle. To sample the Brillouin cell for the electronic states, a Monkhorst-Pack [103] k-point grid of 300×300×1 was used for the undistorted minimum cell and it was scaled accordingly where supercell calculations were performed.

All HSE06 hybrid functional [94, 112] calculations were performed using the VASP code [121]. Core electrons were treated by means of the projector augmented wave method [122, 123] including semicore states for Ti. We used a planewave basis set with an energy cutoff of 330 eV. A Monkhorst-Pack [103] k-point grid of 24×24×1 was used to sample the Brillouin zone.

4. COEXISTENCE OF DIFFERENT MODULATIONS IN THE CDW STATE OF NBSE2 SINGLE-LAYERS

4.1 Introduction

The genuine origin of the charge density wave (CDW) state in $NbSe_2$ has been a matter of continuous debate[50, 124]. Clearing up this point is an unavoidable issue in any attempt to understand the interplay between CDW and superconducting (SC) states in this paradigmatic material[105]. Bulk $2H$-$NbSe_2$ is a room temperature metal which at 33 K undergoes a transition towards an atypical CDW state[104] with practically no resistivity change through the transition. Below 33 K the system exhibits a modulated almost quasi-commensurate 3×3 structure[125] and at 7 K enters into a SC state[126]. It has been recently shown that the CDW order remains intact in single-layer $NbSe_2$ [106]. In contrast with $2H$-$NbSe_2$, the CDW modulation in bulk $2H$-$TaSe_2$ is 3×3 commensurate at low temperature[125]. Dichalcogenides of the $2H$-MX_2 family provide promising playground for the study of competing electronic instabilities in the 2D limit, $2H$-$NbSe_2$ being specially challenging because of the incommensurability of its CDW.

Single-layers of $2H$-$NbSe_2$ (from now on we will refer to them simply as $NbSe_2$) are hexagonal layers of Nb atoms in a trigonal prismatic environment of Se atoms (Fig. 4.1).[127] Although the superlattice periodicity (quasicommensurate 3×3) has been accurately measured by different techniques, the microscopic

structure of the elastic distortion that accompanies the CDW phase still remains elusive. The layers of bulk $2H$-$NbSe_2$ were recently found to exhibit a continuous pattern of overlapping star-shaped Nb atom clusters extending along the layer.[128] More recently, a first-principles DFT study of our group on single-layer $NbSe_2$ assuming a commensurate 3×3 modulation revealed that several structures with nearly equal stability but different distortion patterns are compatible with a 3×3 modulation[48]. This suggests a very flat potential energy surface and a plausible coexistence of the different modulations. This potentiality stimulated two subsequent theoretical works.[129, 130] However, a comprehensive picture of the exact elastic modulations cannot be solved from a purely theoretical DFT approach since (i) the real modulation is strictly non-commensurate, and (ii) the resulting competing modulations have very similar energetic stability. Because of the simultaneous occurrence of these two features, theoretically optimized 3×3 commensurate structures can only be taken as suggestions of different possibilities to be carefully examined by suitable experimental techniques. STM is well suited for this purpose since it can image with atomic resolution the spatial rearrangement of the electronic charge of the CDW phase. Such electronic rearrangements can be compared to those simulated for the different calculated elastic modulations. In this work we have collaborated with the experimental group of Dr. Miguel M. Ugeda (San Sebastián) in order to provide compelling evidence for the coexistence of different modulations in the CDW state of $NbSe_2$. In order to search for the several possible competing phases, we perform total energy minimizations starting from different distorted starting configurations. Some of the structures were only found when a charge doping was initially considered. Once such structures are located for a given doping value, their evolution with doping was also followed. While some of the phases were found for the whole range of doping considered, others were observed for some doping intervals. Doping is therefore used as a practical way to unravel competing structures in our calculations. Nevertheless, we note that our results of the stability of the several structures as a function of doping can also be relevant to experiments where injection of carriers in the

single layers is achieved through electric field gating.[1] We also note again that our commensurate 3×3 structural models are only (close) approximations to the true experimental incommensurate structures.

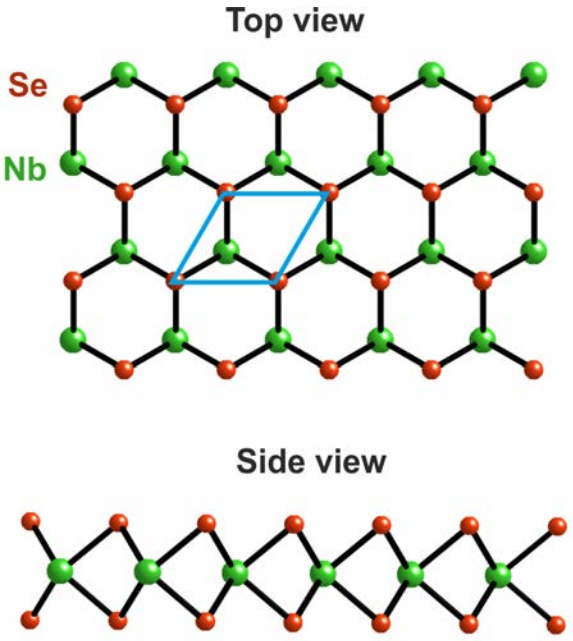

Figure 4.1: Top and side view of a layer of the $2H$-$NbSe_2$ structure.

4.2 Results and discussion

Full optimization of the non-modulated structure of single-layer $NbSe_2$ leads to a lattice constant of 3.48 Å, which is in good agreement with plane-wave type DFT studies,[129] 3.47 Å, and the experimental value for the bulk, 3.44 Å.[127] The band structure and Fermi surface of single-layer $NbSe_2$ in both modulated[48, 129, 130] and non modulated[133, 134, 135] structures have been discussed before. Such Fermi surface contains rounded hexagons and rounded triangles centered at Γ and K points of the Brillouin zone (BZ), respectively (see Fig. 4.2). The calculated Lindhard response function for the optimized non modulated single-layer $NbSe_2$ is shown in Fig. 4.3. As it occurs for the bulk,[136] there are no sharp maxima around

[1] Note that doping of transition metal dichalcogenide single layers can also be achieved by growing the single layers on a Au(111) substrate.[131, 132]

the (a*/3, 0) point and equivalent ones of the BZ which could justify a Fermi surface nesting driven mechanism of the CDW, but a very shallow region around the Γ - M direction. In contrast, as can be seen in the phonon band structure of the optimized non modulated structure shown in Fig. 4.4, one of the phonon branches becomes clearly unstable in a large part of the Γ - M segment of the BZ, with a maximum imaginary frequency near but not exactly at the a*/3 point. The presence of phonons with imaginary frequency around this point indicates that the system is unstable with respect to incommensurate distortions with a periodicity not far from 3×1 (and symmetry equivalent). The combination of the three equivalent distortions (threefold symmetry, i.e. triple-q or 3Q mechanism), leads to an incommensurate structure close to 3×3. We conclude that the modulation of the single-layer $NbSe_2$ is a strong-coupling CDW caused by electron-phonon coupling, as it has been proposed for the bulk[136] and it was previously discussed here for single-layers [48].

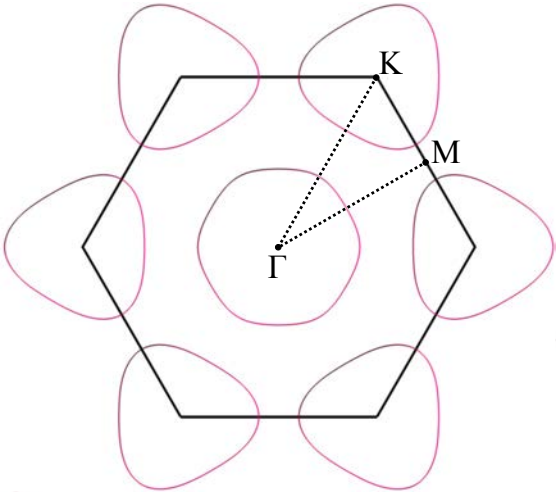

Figure 4.2: Fermi surface of the undistorted single-layer $NbSe_2$.

We then performed structural optimizations imposing a 3×3 periodicity for the pristine as well as for several doping levels of single-layer $NbSe_2$. We also checked that the phonon instability remains under doping. In Fig. 4.5 we show that the effect of doping does not change this picture qualitatively, although the precise shape of the unstable phonon branch and the position of the minimum experience

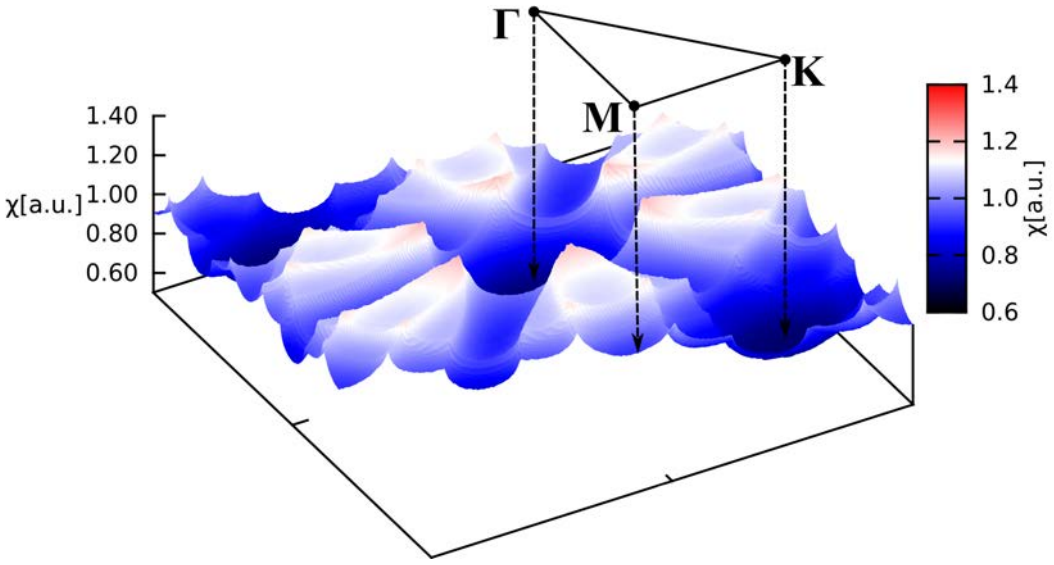

Figure 4.3: Lindhard response function calculated for undistorted single-layer $NbSe_2$.

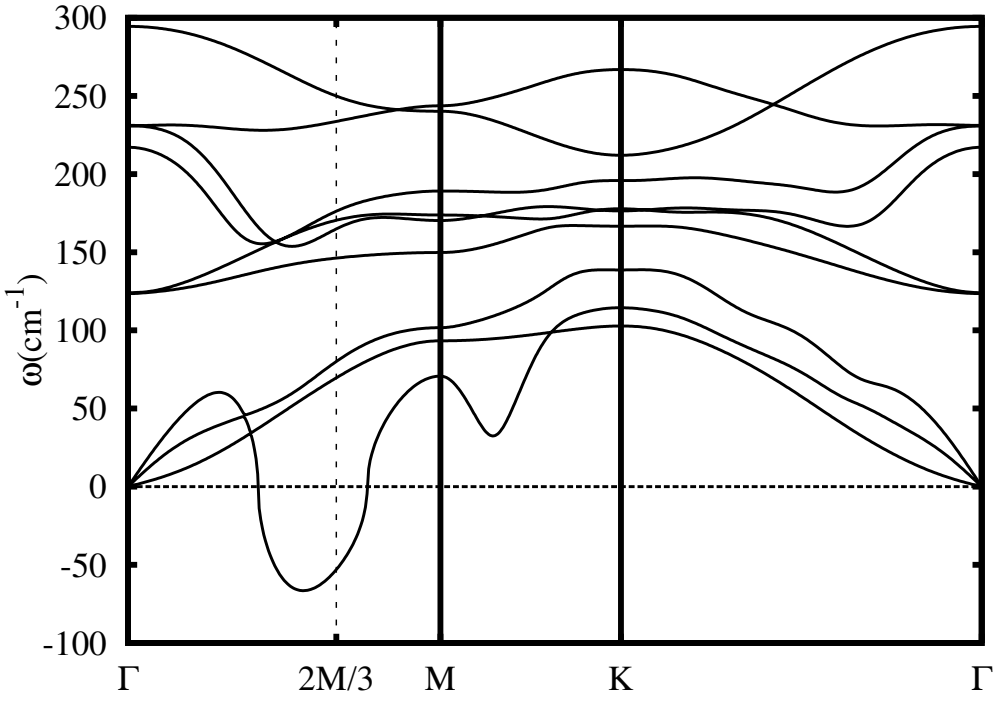

Figure 4.4: Phonon dispersion along the high symmetry lines of the Brillouin zone calculated for the undistorted single-layer $NbSe_2$.

some small changes. A summary of this study is reported in Fig. 4.6. Up to six different modulations compatible with a 3×3 cell were found. One of the structures exhibits centered hexagonal clusters of Nb atoms and single Nb atoms in between (noted Hexagons in Fig. 4.6). Another structure contains a continuous pattern of overlapping star-shaped Nb atom clusters (noted Star in Fig. 4.6) which coincides with the 3×3 modulation reported for the bulk.[128] Two structures contain triangular clusters of 3 and 6 Nb atoms (T1 and T1´ in Fig. 4.6); whereas in T1 the inner triangles of both clusters are centered by two Se atoms above and below the Nb atoms plane, in T1´ they are centered by hollows. Finally, two more structures contain a continuous pattern of overlapping triangular clusters of 6 Nb atoms of two different types, with or without Nb-Nb short distances inside the large triangles (T2 and T2´ in Fig. 4.6). Note that the six structures can be paired in three groups: Hexagons/Star, T1 /T2 and T1/́T2´ so that within each pair the short and long Nb-Nb bonds are interchanged. This suggests that the two structures within each pair may be interconverted as a function of doping. This is indeed the case for the T1 /T2 and T1/́T2´ pairs where a relatively simple gradual change between the two structures is possible. However, the Hexagons/Star pair could not be exchanged due to their complex arrangement. Consequently, for a given carrier-density there are four different structures compatible with a 3×3 modulation. Remarkably, for most doping levels the energy difference between these structures is extremely small (between fractions of a meV and at most 2 meV) so that it is likely that some of the structures experimentally coexist. Let us stress that our calculations are carried out for a commensurate 3×3 CDW structure but the real modulation is incommensurate. As a consequence of this fact and the very small energy differences, the data in Fig. 4.6a should be only taken as suggesting that some of these structures may coexist in real samples and weak changes in doping, strain or internal pressure of the crystal may alter such coexistence.

We have performed the analysis of the stability of the six different structures with 3×3 periodicity by obtaining the Γ phonon frequencies, as shown in Tab. 4.1. As some of the phases are only stable under charge doping, the frequencies

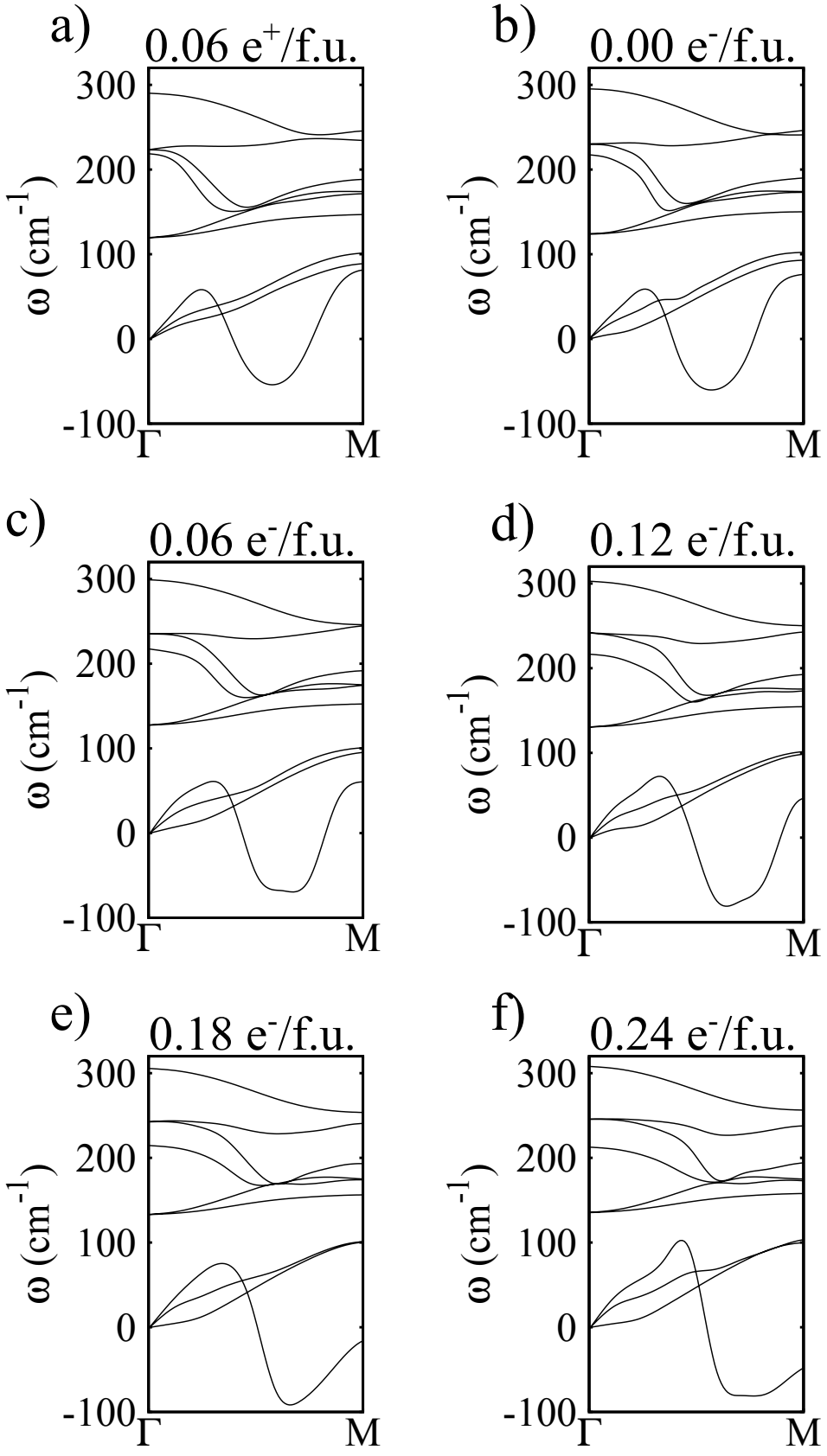

Figure 4.5: Evolution of the phonon dispersion in the Γ-M segment of the BZ for the undistorted $NbSe_2$ single-layer .

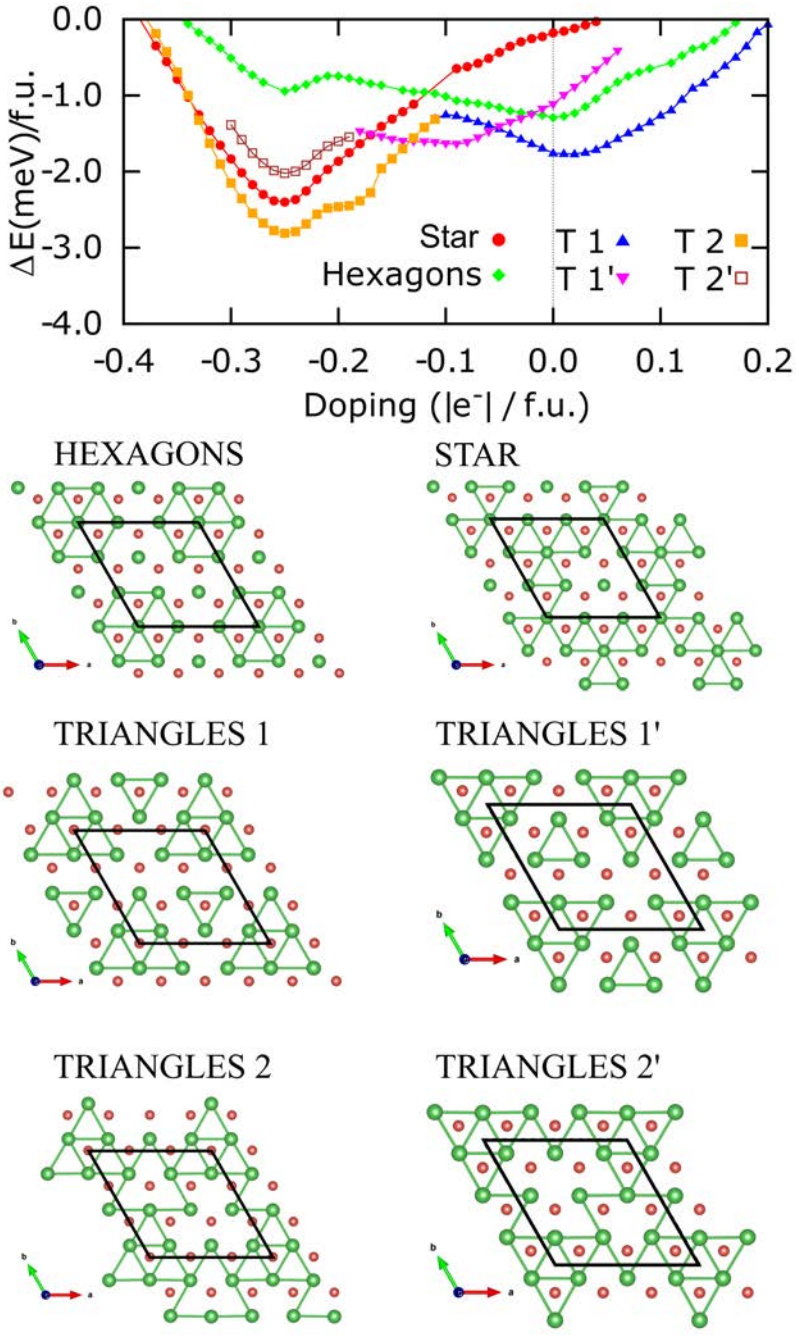

Figure 4.6: Different modulations compatible with a 3×3 periodicity and their relative energies for $NbSe_2$ single-layer as a function of external doping (in electrons per formula unit; negative values indicate electron doping). For a given doping value the energy (in meV per formula unit) is given with respect to the optimized non distorted system for the same doping level. Nb-Nb contacts shorter than in the average structure are those shown in the structural drawings.

were obtained using two doping values: 0 and -0.25 e/f.u.. For the pristine single layer, we find that the Hexagons, T1 and T1´ structures, are stable and show no imaginary frequencies, whereas the star phase does show three imaginary frequencies, which is in agreement with the previous works.[129, 130] For the case of -0.25 e/f.u. doping, we find that this is consistent with the energy ordering of the phases as a function of doping in Fig. 4.6; the phases which are found to have unstable modes are the ones with higher energies (stars for zero doping and Hexagons for -0.25 e/f.u. doping).

Table 4.1: Lowest six Γ-point phonon modes for the 3 × 3 CDW phases in the non-doped case and in the 0.25 $e^-/f.u.$ doped case.

$\omega_\Gamma(cm^{-1})$ Lowest 6 modes							
0.00 e^-/f.u.				0.25 e^-/f.u.			
H	T 1	T 1'	Star	H	T 2	T 2'	Star
0	0	0	-75	-89	0	0	0
0	0	0	-73	-83	0	0	0
0	0	0	-73	-83	0	0	0
6	46	54	0	0	57	28	39
7	49	58	0	0	57	29	39
66	64	61	0	0	70	59	72

In order to determine the possible coexistence from the 6 different calculated phases, it is necessary to compare our simulated STM images with the experimental findings. As mentioned before the experimental study was carried out in the group of Dr. Miguel M. Ugeda. The images were produced by scanning the surface of bulk $2H$-$NbSe_2$ by meants of Scanning Tunneling Microscopy(STM) at T = 1 K. Because both bulk and $NbSe_2$ exhibit a 3×3 CDW phase[106], the experiments were carried out in its bulk fomr due to the much lower density of defects (grain boundaries and domain edges are not present in bulk), which might have altered the energy landscape of the CDW phase. Furthermore, the purely two-dimensional character of the CDW order in $NbSe_2$ allowed for the a direct probing of the existence of the structural phases predicted for the single-layer $NbSe_2$ in the bulk form. The analysis of tens of different regions of bulk $NbSe_2$ led to the identification of two different structural phases.

Upper panel in Fig. 4.7 shows two experimental STM images of a representative region for unoccupied (Fig. 4.7a) and occupied (Fig. 4.7b) states. The STM images reveal the coexistence of two different phases (depicted in blue/yellow) separated by an Å-scale boundary (black dashed line). Although the two phases show the same 3×3 superlattice periodicity at both polarities, the relative intensity of the nine Se atoms of each 3×3 unit cell (blue and yellow cells) vary differently, thus giving rise to a unique pattern in each case. Figures 3c-f show close-up views of these patterns for the two phases at each polarity. Such unique patterns allowed us to compare both structural phases with simulated STM images from the six stable structures, within the Tersoff-Hamann approximation pattern (see Figs. 4.8,4.9 and 4.10 for the images of the Star, T1´ and Hexagons phases not shown in Fig. 4.7).[137] As a first result, the experimental phase labelled in blue can be identified with the theoretical T2´ . Figures 4.7g and 4.7i show the simulated STM images of this phase at ± 0.05 V that compare with the experimental STM images in Figures 4.7c and 4.7e, respectively. The theoretical 3×3 unit cells reproduce the relative intensity of the Se atoms within the unit cells simultaneously for both polarities as well as their relative orientation. Regarding the yellow phase, it can be identified with either the T1 or T2 phases since they exhibit almost the same patterns at both polarities and, therefore, are practically indistinguishable. Figures 4.7h and 4.7j show the simulated STM images for the T1 phase at ± 0.05 V (those for T2 are almost identical) for comparison with the experimental ones in Figures 4.7d and 4.7f, respectively. Here, again, the patterns within the 3×3 unit cells show a good agreement between theory and experiment. We therefore assign the observed blue and yellow phases to the T2´ and T1/T2 phases. Although this is the most likely correspondence between the experimental and theoretical phases, the blue phase can also be identified as the Star phase according to the superlattice. However, this would imply a rotation of 180 deg of the crystal lattice with respect to the T1/T2 phase and, therefore, their mutual coexistence is not compatible in light of the experimental data.

In summary, on the basis of first-principles DFT calculations six different structures are found to be compatible with the 3×3 CDW structure of $NbSe_2$. All these structures are found to coexist in a very narrow energy range of 2-3 meV. Their relative stability can be subtly altered by doping or strain. Imaging the surface of bulk $2H$-$NbSe_2$ with atomic resolution allowed us to identify two of these structures, as anticipated by our theoretical simulations. Intriguingly, these structures differ from the X-ray crystal structure reported for the bulk 3×3 CDW which, in fact, is also one of the six DFT structures located for the single-layer. Preliminary calculations for slabs with a different number of layers suggest that the actual structure stabilized may change from layer to layer, i.e., the energetic preference may depend also on the internal pressure. The coexistence of different structures in $2H$-$NbSe_2$ has far-reaching consequences to fully understand the electronic ground state of $2H$-$NbSe_2$. Thus, experimental work on slabs with different number of layers is encouraged since it may provide important clues to understand the puzzling physics of this correlated material.

4.3 Computational details

The geometrical optimizations, electronic and phononic band structures were carried out using a numerical atomic orbitals density functional theory (DFT) [96, 97] approach implemented in the SIESTA code [27, 28]. We used the Perdew-Burke-Ernzerhof (PBE) functional to account for the exchange-correlation energy [98]. A split-valence double-ζ basis set[101] was used to describe the valence electrons wave function, while the core electrons were replaced by norm-conserving scalar relativistic pseudopotentials[99] factorized in the Kleinman-Bylander form[100]. The 4p shell of Nb is included in the valence explicitly as semicore states. For a good description of the free standing layer, we placed the single layer in a vacuum space of 50 Å to avoid interactions between the layer and its images. We used an energy cutoff of 2500 Ry for the real space integration. A tolerance of 10^{-5} and 10^{-4} on the density matrix and total energy, respectively, was used in order to attain the convergence of the self-consistency cycle. Geometrical optimization

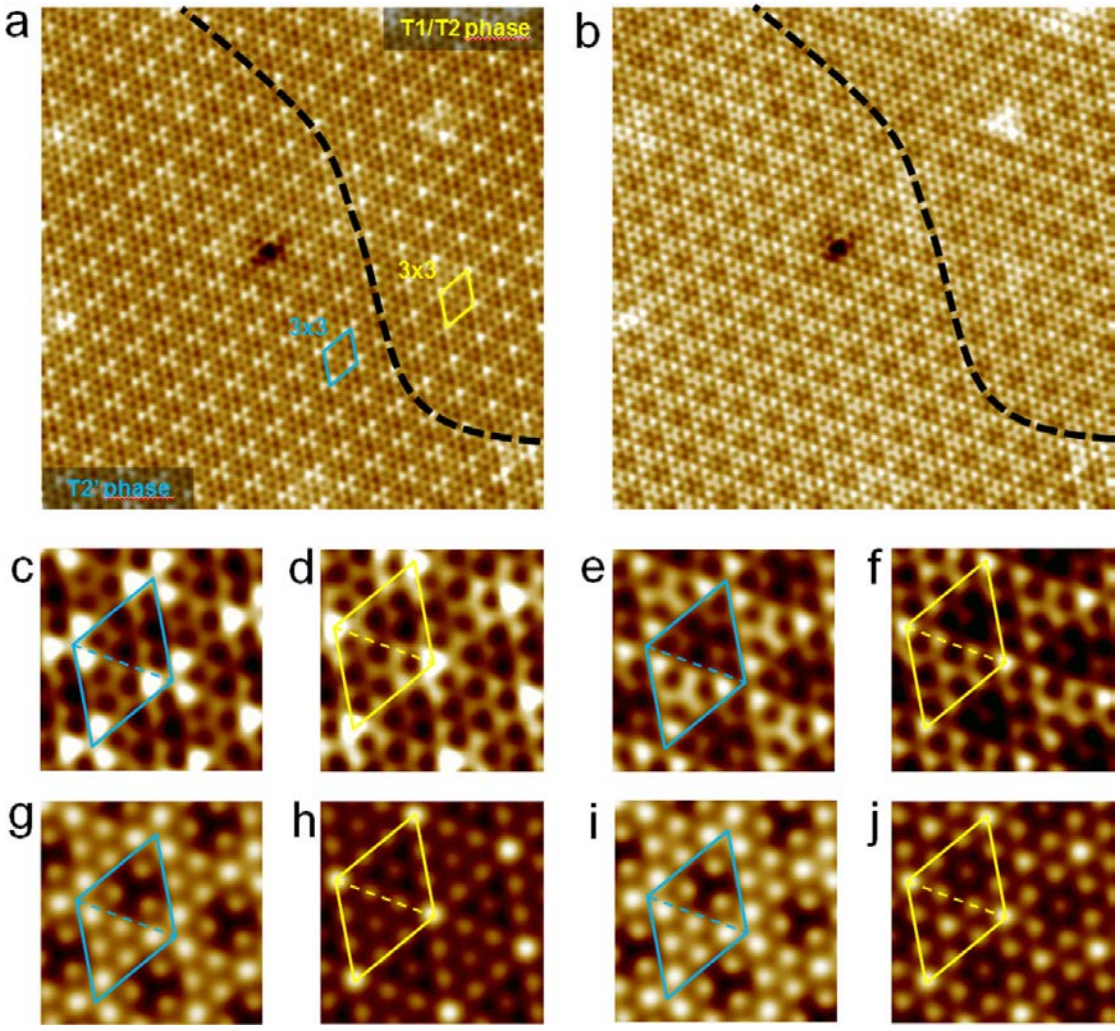

Figure 4.7: Unoccupied (a) and occupied (b) STM images (14 nm x 14 nm) of the same region of bulk $NbSe_2$ showing the coexistence of two structural phases. The black dashed line represents the boundary between them. Parameters: (a) V_S = 50 mV , I = 0.5 nA and (b) V_S = -50 mV , I = 0.5 nA. (c-f) Zoom-in STM images from a and b of the two phases for unoccupied (c,d) and occupied (e,f) states. (g-j) Simulated STM images for both phases and bias polarities ($V_S = \pm$ 50 mV). Reprinted with permission from *Nano Lett.,2019,19,5,3027-3032*[138]. Copyright 2019 American Chemical Society.

calculations were performed to ensure a maximum interatomic force of 4×10^{-3} eV/Å^{-1}. A Monkhorst-Pack[103] k-point grid of 72×72×1 was used to account for the sampling of the Brillouin zone of the minimum unit cell and it was scaled accordingly where supercell calculations were performed. Phonon calculations were done using the finite difference method. In the case of the phonon band structure calculations, a k-point grid of 120×120×1 per minimum unit cell and a 5×10^{-3} eV Fermi-Dirac smearing were used.

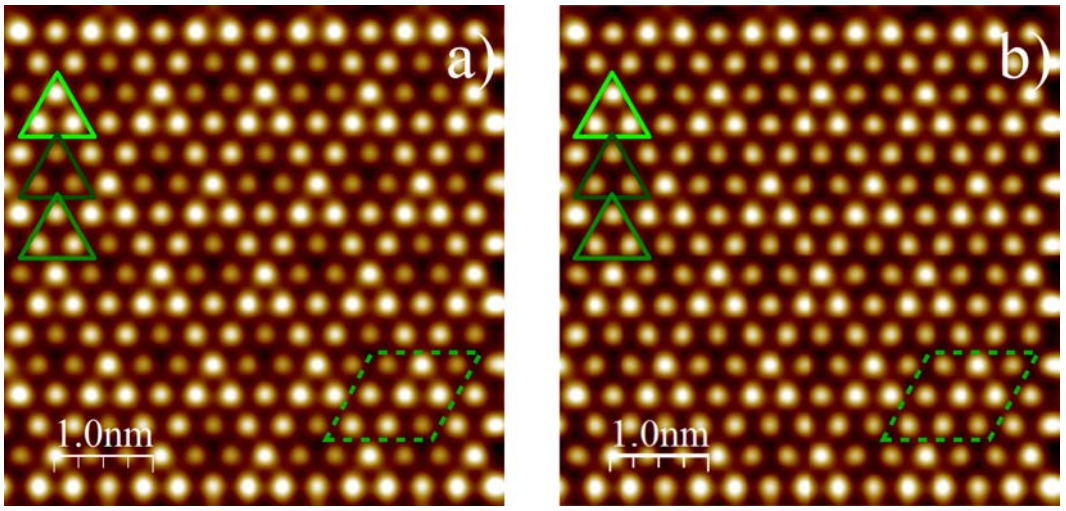

Figure 4.8: Unoccupied (a) and occupied (b) simulated STM images of the Star structure for bias polarities ± 50meV. Note the incompatible pairing at both polarities with the experimental results.

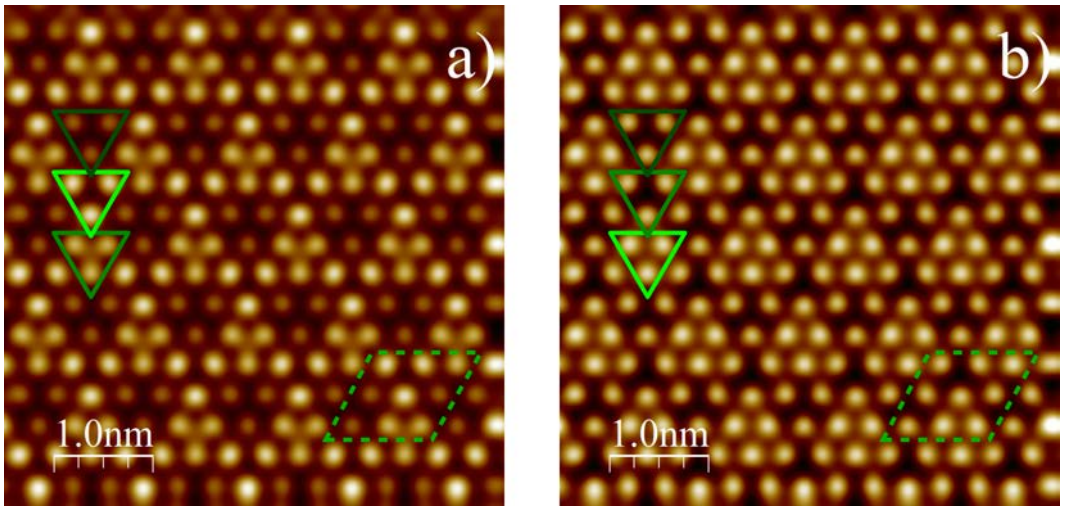

Figure 4.9: Unoccupied (a) and occupied (b) simulated STM images of the T1' structure for bias polarities ± 50meV. Note the incompatible pairing at both polarities with the experimental results. Also note the incompatible phase change(180 deg rotation) from one polarity to the other even though the image looks similar with T1 structure simulated images.

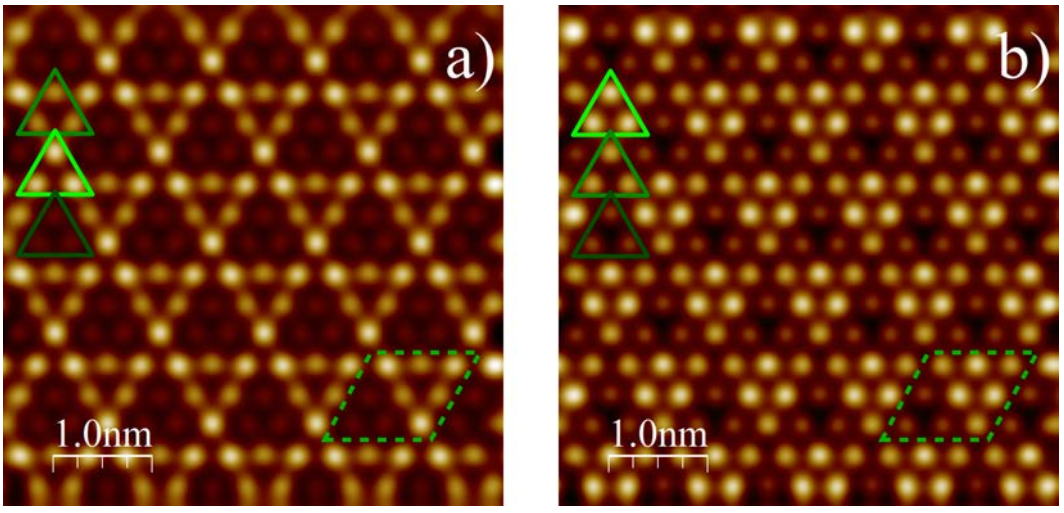

Figure 4.10: Unoccupied (a) and occupied (b) simulated STM images of the Hexagons structure for bias polarities ± 50meV. Note the incompatible pairing at both polarities with the experimental results.

PART III

IS FERMI SURFACE NESTING THE DRIVING FORCE FOR THE ELECTRONIC INSTABILITIES OF LOW-DIMENSIONAL METALS?

INTRODUCTION

In the following chapters we will approach the family of bulk low-dimensional metallic systems and their propensity towards electronic and structural instabilities below certain temperatures. We refer to low dimensional materials in both of its forms: crystal and electronic. Crystal-wise, low dimensional materials present a covalent bonding in one or two crystallographic directions. They form chain-like structures (like in the case of $(NbSe_4)_2I$, $TaTe_4$), respectively slabs (like in the case of $ZrTe_3$ or Bechgaard salts) that are weakly coupled in the other direction(s) by van der Waals forces. The electronic structure naturally inherits the anisotropy of the crystal structure. However, there are also systems which are 3D in terms of the structure yet they exhibit a low-dimensional behaviour in terms of the transport properties. Mo_8O_{23} or $Li_{0.9}Mo_6O_17$ are two examples. The dimensional contraction of the electrons' degrees of freedom down to one has a strong impact on the physical properties. It was predicted by Peierls[1] that a one dimensional electron gas on a lattice would be unstable under a small perturbation, leading the system into a metal-insulator phase transition due to its electron-hole pairing at the Fermi level at 0 K. This model that implies a certain topology of the Fermi surface, i.e. large portions of the Fermi sheets that can be connected by the same wave-vector, can very well describe the manifestation of the charge density wave in some of these low dimensional metals. But what can we learn from where this scenario fails? In the previous chapters we have seen that $TiSe_2$, $TiTe_2$ and $NbSe_2$ single layers are room temperature low dimensional metals which undergo some kind of low temperature structural modulation associated with anomalies in the transport properties and, yet, none of them originates from a Peierls like instability.

Our main focus in the next chapters is to determine what stands at the origin of the modulation(s) in different classes of bulk low-dimensional metals. Our main

tool will be the calculation of the Lindhard response function. When Fermi surface nesting is at the origin of the CDW modulation, the Lindhard response function exhibits a sharp maximum for a wave vector which coincides or is very near to that of the CDW modulation, which results from the coupling of the CDW instability with a periodic lattice distortion (the Peierls scenario). Fig. 4.11 clearly illustrates this point. Whereas the Lindhard function of single layer $NbSe_2$ does not exhibit sharp maxima but plateaus, that of the blue bronze exhibits said sharp maxima. As discussed in chapter 2, the CDW of the first one does not originate from a Fermi surface instability, but as it will be discussed in the following chapter, the metal to insulator transition of the Blue Bronze is a perfect example of a CDW following the Peierls scenario.

Altogether we have studied from the first principles calculations standpoint the following classes of materials: oxides (blue bronze, monophosphate tungsten bronzes, layered perovskite-related $A_nB_nO_{3n+2}$ niobates and titanates, Magnéli phases Mo_4O_{11} and Mo_8O_{23}), transition metal trichalcogenides(NbS_3, $NbSe_3$, TaS_3, $ZrTe_3$) and tetrachalcogenides ($TaTe_4$, $(TaSe_2)_4I$), Bechgaards salts ($(TMTSF)_2X$ with X = ClO_4, NO_3, PF_6) and rare earth intermetallics ($LaAgSb_2$). However, we will only report here our results for three of these materials: the Blue Bronzes, the Bechgaard salts and $TaTe_4$, which illustrate very clearly the diversity of phenomena exhibited by low dimensional metals.

We will begin our incursion with the prototypical example of the blue bronze ($K_{0.3}MoO_3$) which provides a perfect example of a pseudo-1D metal exhibiting a CDW formation as a result of a Fermi surface nesting instability. As it will be seen in the next chapter, our calculations provide compelling evidence that the CDW formation follows the weak electron-phonon coupling scenario in the adiabatic approximation, something that had not yet been proved on the basis of first-principles calculations for a real material. Then we will report our results for three Bechgaard sals, $(TMTSF)_2PF_6$, $(TMTSF)_2ClO_4$ and $(TMTSF)_2NO_3$, which undergo SDW instabilities at low temperature. In that case, the analysis of the

variation of the wave vector and temperature dependence of the Lindhard function leads to a rationalization of the electronic dimensional crossover and spin density wave instability in these salts. In the case of $(TMTSF)_2ClO_4$ and $(TMTSF)_2NO_3$ the situation is even more complex because of the conccurrence of an anion ordering transition. Finally we will consider the case of $TaTe_4$, a room temperature metal exhibiting structural modulations which have been ascribed to a Peierls type mechanism, an interpretation challenged by our calculations.

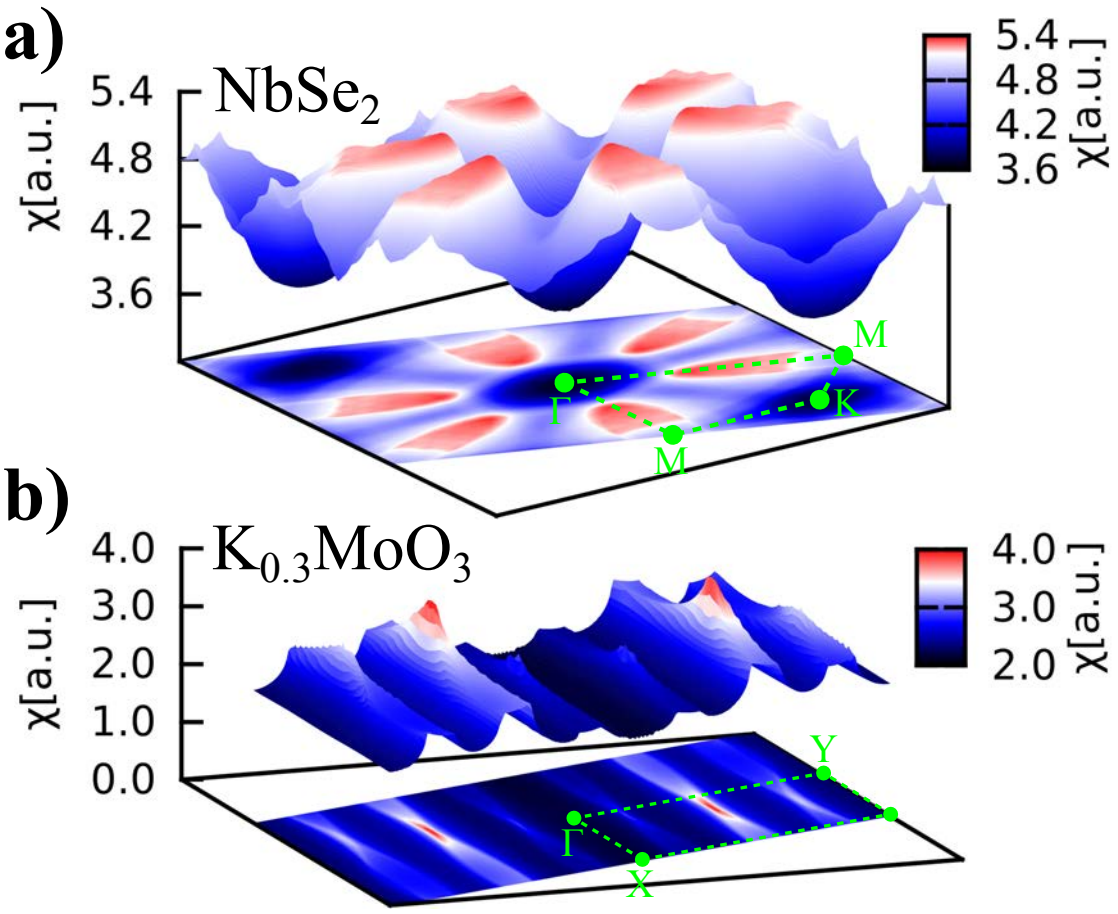

Figure 4.11: Comparison between the Lindhard function for the layered $NbSe_2$ (a) and the $K_{0.3}MoO_3$, Blue Bronze (b).

5. A PARADIGMATIC CASE: THE BLUE BRONZE K0.3MOO3

5.1 Introduction

Many low dimensional metallic systems exhibit a charge density wave (CDW) ground state where the electronic density is modulated with a wave number related to the shape of their Fermi surface [139, 140, 141]. In experimental situations reported in the literature, the electronic modulation is stabilized by a periodic lattice distortion (PLD) [142]. Thus, electronic and lattice degrees of freedom are coupled by the electron-phonon coupling [143, 144]. The electronic energy gain is caused by the fact that the new periodicity of the PLD opens a full gap in the band structure for 1D electronic systems or partial gaps in electronic systems of higher dimension [145]. In the case of 1D systems, the CDW/PLD modulation is accompanied by a metal-insulator transition (i.e. Peierls transition in the literature) and the modulation wave vector, $2k_F$, is simply twice the Fermi wave vector [146].

In the standard description of the Peierls transition [146] the electron-phonon coupling is assumed to be small so that the electronic wave functions are weakly perturbed by the lattice vibrations. In this limit, which relies on a PLD of small amplitude, the instability towards the formation of electron-hole pairs is driven by the thermal divergence at a well defined critical wave vector ($q_c = 2k_F$ in the 1D case) of a sharp electron-hole (i.e. Lindhard [31]) response function of the

non-perturbed electron gas. This response can be written as

$$\chi(q) = -\sum_{i,j}\sum_{k}\frac{f_F(\epsilon_i(k)) - f_F(\epsilon_j(k+q))}{\epsilon_i(k) - \epsilon_j(k+q)}, \tag{5.1}$$

where f_F is the Fermi function and $\epsilon_i(k)$ are the band eigenvalues.

In the weak electron-phonon coupling limit and within the adiabatic approximation where $\Omega_0\tau_{eh} < 1$ (Ω_0 being the frequency of the bare critical phonon Kohn anomaly and τ_{eh} the lifetime of the electron-hole pair), the electron-hole pairs fluctuate so fastly during the phonon oscillation period that they screen the coupling between the atoms. This leads to a phonon softening around q_c (i.e. to the occurrence of a Kohn anomaly) for lattice modes whose frozen displacements stabilize the PLD below the Peierls transition. In the adiabatic approximation, the critical lattice dynamics is of the displacive type with a progressive softening of the frequency of the Kohn anomaly when approaching the Peierls transition, following the thermal divergence of the electron-hole response [146]. In this limit the width of the dispersion of the Kohn anomaly is related to the width of the electron-hole response around q_c ($2/\xi_{eh}$, where ξ_{eh} is the coherence length of the electron-hole pair). Finally, in the standard theory of the Peierls transition, the entropy of the critical phonon mode is neglected, an approximation valid if the Kohn anomaly involves only a small fraction of the Brillouin zone (i.e. if $\xi_{eh}2k_F >> 1$ in 1D). In the weak coupling limit, the theory of the Peierls transition is of the BCS type [146]. Note that in the presence of a broad electron-hole response spreading over a sizeable fraction of the Brillouin zone (i.e. if $\xi_{eh}2k_F \sim 1$ in 1D) the phonon entropy cannot be neglected [147]. In that case it is needed to go beyond the weak coupling BCS formalism to describe the Peierls instability and theoretical treatments suggest more likely strong electron-phonon coupling scenarios.

In the non-adiabatic approximation ($\Omega_0\tau_{eh} > 1$) the critical q_c phonon fluctuates very fastly during the lifetime of the electron-hole pairs so that phonon modes cannot efficiently couple with the electron-hole condensate. There is no screening and thus no critical softening of a phonon branch. The long-living electron-hole

condensate induces, via the electron-phonon coupling, a quasi-static local PLD quite well decoupled from the phonon spectrum. The critical lattice dynamics of the Peierls transition is thus of relaxation or order-disorder type [148]. Note that such dynamics is also found in the strong electron-phonon coupling limit [149] where the PLD fluctuations are of large amplitude.

The largest contribution of the Lindhard function (Eq. 5.1) originates from electronic energies leading to a vanishing denominator. This occurs for electronic states located at the Fermi level such that

$$E_F(k+q) = E_F(k) \tag{5.2}$$

Eq. (2) defines k states of the Fermi surface (FS) which coincide with other states of the FS after application of a q translation. If there are large portions of the FS exhibiting such a property the nesting of the FS by q will dominantly contribute to $\chi(q)$ [145]. Such nesting process can simply account for the maxima of $\chi(q)$ and provide a simple explanation for the occurrence of charge and spin density wave instabilities found in many experimental systems [150]. For example, in 1D systems where the FS is made of two planes at the $+k_F$ and -k_F wave vectors, the translation wave vectors $q = \pm 2k_F$ nest completely the FS leading to a divergence of $\chi(q)$ and to the stabilization of a CDW-Peierls ground state [146]. However, at finite T, because of the Fermi-Dirac distribution spreading over several k_BT on each side of E_F, the contributions to the Lindhard function are not restricted to the Fermi level. This is the case for a single band dispersion where FS nesting connecting also electronic states with opposite Fermi velocities preserves the divergence.

However, for a more complex band structure with different Fermi velocities, FS nesting is not a sufficient condition to obtain a maximum of $\chi(q)$. We illustrate this statement using a simple model for a 1D metal with two conduction bands having the Fermi wave vector $\pm k_F^I$ and $\pm k_F^{II}$. If the dispersion of the two bands is

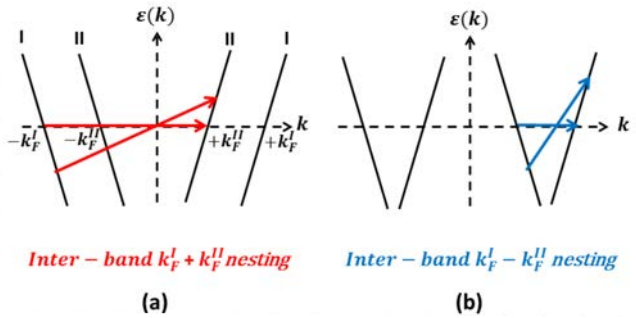

Figure 5.1: Schematic illustration of why for a 1D system with two partially filled bands with different Fermi velocities only certain inter-band nestings may be effective.

parallel, the nesting process linking band dispersions with opposite Fermi velocities leads to maxima of $\chi(q)$ for $q = 2k_F^I$, $2k_F^{II}$ and $k_F^I + k_F^{II}$ but not for $k_F^I - k_F^{II}$ (Fig. 5.1a). This situation is relevant for the blue bronze considered below [151]. If the dispersion of the two bands is inverted, the nesting process linking band dispersions with opposite Fermi velocities leads to maxima of $\chi(q)$ for $q = 2k_F^I$, $2k_F^{II}$ and $k_F^I - k_F^{II}$ but not for $k_F^I + k_F^{II}$ (Fig. 5.1b). This situation is relevant for the charge transfer salts of the TTF-TCNQ family [152]. In conclusion, the sign of the Fermi velocity of the different bands connected by the nesting process determines the type of inter-band contribution leading to maxima of the Lindhard function. With more complex band structures it has been also reported that maxima of $\chi(q)$ could differ from the best FS nesting condition [153]. It is thus necessary to go beyond the simple consideration of the nesting properties of the FS and to perform the direct calculation of the Lindhard function to obtain the critical wave vectors of the CDW instability. In the case of the blue bronze, the CDW-Peierls instability has been proposed to be caused by the inter-band $k_F^I + k_F^{II}$ nesting proces [151, 49].

The Mo blue bronze $A_{0.3}MoO_3$, where A= K, Rb or Tl is a monovalent atom, exhibits a complex C-type centred monoclinic structure [154]. Fig. 5.2a shows that this structure is built from (b, a+2c) layers of MoO_6 octahedra. In the perpendicular interlayer 2a*-c* direction vacancies incorporate an ordered sub-lattice of A atoms. The essential building blocks of the layers are the clusters of ten MoO_6 octahedra highlighted in Fig. 5.2b (see Sect. 5.2 for a detailed structural discussion). Both tight binding [151] and Density Functional Theory (DFT) [155]

electronic structure calculations as well as ARPES measurements [156] show that the blue bronze exhibits a quasi-1D band structure with two parallel conduction bands leading to a slightly warped double sheet open Fermi surface. The repeat unit of the crystal structure in the 1D direction is the cluster of ten octahedra. As monovalent A atoms provide 3 electrons per cluster, the two bands are partially filled with ρ= 3 electrons. The blue bronze is a 1D metal with a sizeable RT conductivity of $\sigma_b \sim 10^3$ S/cm and an anisotropy of conductivity [157] which follows the structural anisotropy $\sigma_b : \sigma_{a+2c} : \sigma_{2a*-c*} \sim 1{:}10^{-2}{:}10^{-3}$. Polarized reflectance measurements show that the blue bronze is a true 1D metal exhibiting a metallic Drude behaviour only if the light is polarized in the chain direction [158]. At T_p= 180 K the blue bronze exhibits a Peierls metal-insulator transition accompanied by the setting of a CDW/PLD modulation of critical wave vector q_c= (0, 1-($k_F^I + k_F^{II}$), 0.5) or equivalently, within a reciprocal wave vector, of q_c= (1, $k_F^I + k_F^{II}$, 0.5). At low temperature, the value of $k_F^I + k_F^{II}$ is $\approx$ 0.75 [157]. It exhibits a very sizeable regime of quasi-1D CDW fluctuations [49] above T_p and the occurrence of a Kohn anomaly in the phonon spectrum whose frequency continuously softens as T_p is approached [159, 37].

In this work we confirm the interband $k_F^I + k_F^{II}$ nesting mechanism by a direct calculation of the Lindhard function using the real DFT band structure for the undistorted, high-temperature metallic phase of $K_{0.3}MoO_3$. Our calculation of the thermal dependence of the shape and width of the peaks of the Lindhard function for the metallic phase allows to *quantitatively* account for the standard weak coupling scenario of the Peierls transition. Our results do not provide direct insight on the CDW phase, such as the lattice distortions or the specific displacements of the phonon mode exhibiting the Kohn anomaly, but on the driving mechanism for the Peierls transition originating from the instability of the electron gas, and the physical regime of weak electron-phonon coupling and adiabatic limit. To the best of our knowledge, this type of validation of the weak coupling scenario based on actual data for a real material has never been reported in the literature.

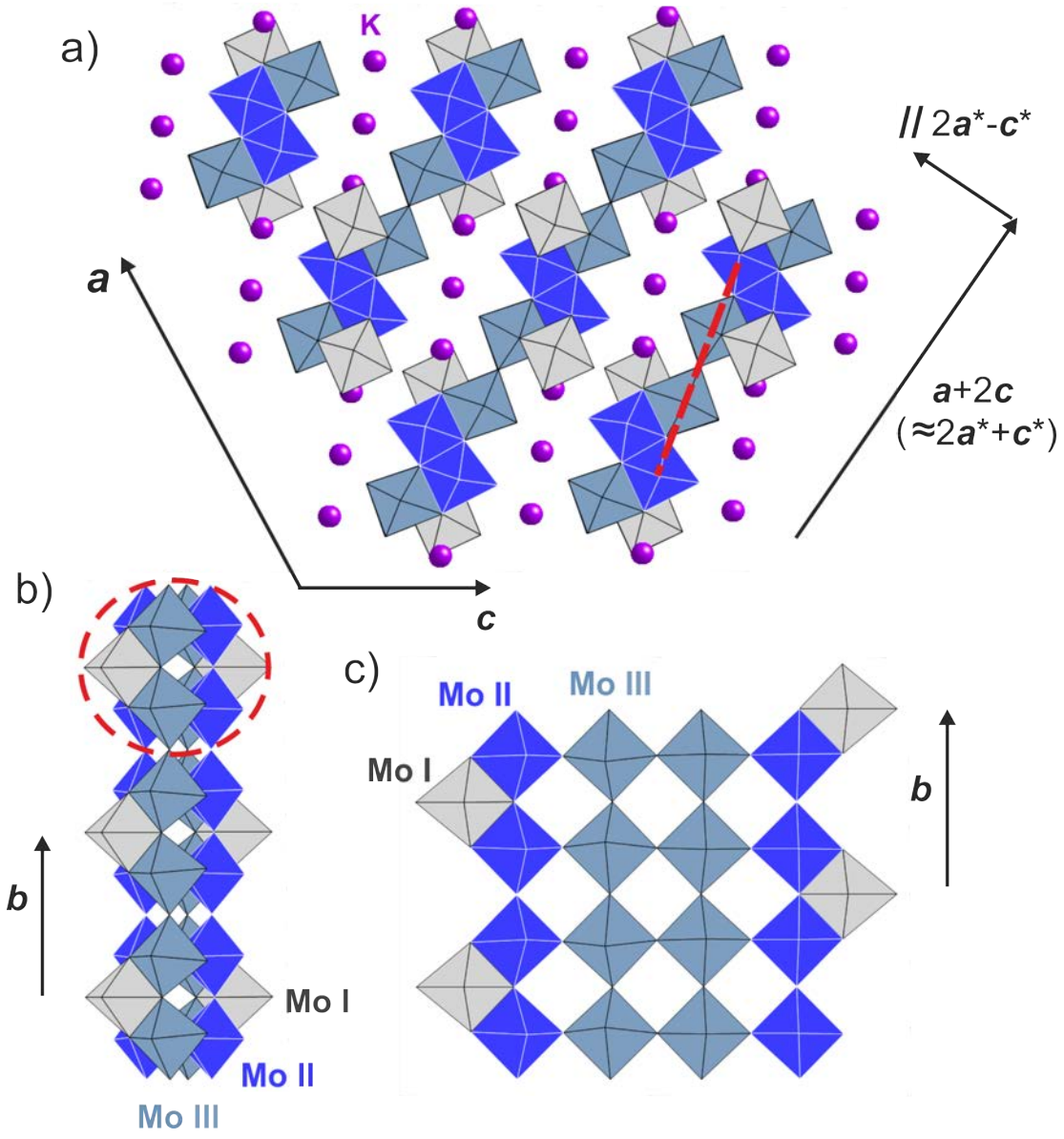

Figure 5.2: Crystal structure of the blue bronzes. The lattice vectors shown in (a) are those of the C-centered cell of Graham and Wadsley[154]. The three different types of MoO_6 octahedra are shown with different colors. The elementary building block of the structure (i.e. a cluster of ten octahedra) and the octahedral chains it generates along the b direction are shown in (b). An alternative description of the octahedral chains associated with the red dashed line in (a) and the hump octahedra is shown in (c).

5.2 Electronic structure of K0.3MoO3

$K_{0.3}MoO_3$ crystallizes in a centered monoclinic structure and contains twenty formula units per unit cell, i.e. $K_6Mo_{20}O_{60}$ (Fig. 5.2)[154, 160]. In our DFT calculations we used a half-sized unit cell based on the centrosymmetric nature of the crystal where the lattice parameters used are $a' = 1/2(a+b)+c$, $b' = b$ and $c' = c$ where a, b and c are the lattice constants reported by Graham and Wadley.[154] The crystal structure consists of slabs of MoO_6 octahedra with the alkali metal atoms in between these slabs. As mentioned, the structure contains three inequivalent Mo atoms and thus three different types of MoO_6 octahedra (see Fig. 5.2). Although the structure of the blue bronzes is usually discussed on the basis of the clusters of ten octahedra shown in Fig. 5.2b, an alternative description is more convenient in order to understand the nature of the electronic structure [161] (Fig. 5.2c). The Mo II and Mo III type octahedra form units of four corner-shared octahedra (marked with a dashed red segment in Fig. 5.2a) which lead to quadruple chains along the b axis by further corner-sharing along this direction. The Mo I hump octahedra fill one every two outer holes of these quadrupole chains in an zigzag way sharing two edges with Mo II octahedra (Fig. 5.2c). Consequently, the chains along b are really built from a repeat unit of ten octahedra: two rows of the four octahedral units and two type I hump octahedra. The cluster of ten Mo octahedra which is the repeat unit of this chain is structurally equivalent to that highlighted in Fig. 5.2b. The layers of the blue bronze result from the condensation of these chains along the a+2c direction through edge-sharing of octahedra of the different chains.

The calculated band structure of $K_{0.3}MoO_3$ along the three main directions of the Brillouin zone is shown in Fig. 5.3a. The Fermi level cuts two bands dispersive along $\Gamma-Y'$ (i.e. not far from the intra-chain b direction, Γ-Y) but only slightly dispersive along Γ-X' (i.e. the inter-chain direction) and with a nil dispersion along $\Gamma-Z'$ (i.e. the inter-layer direction). The band structure of Fig. 5.3a is in very good agreement with the results of previous DFT calculations [155, 162] and

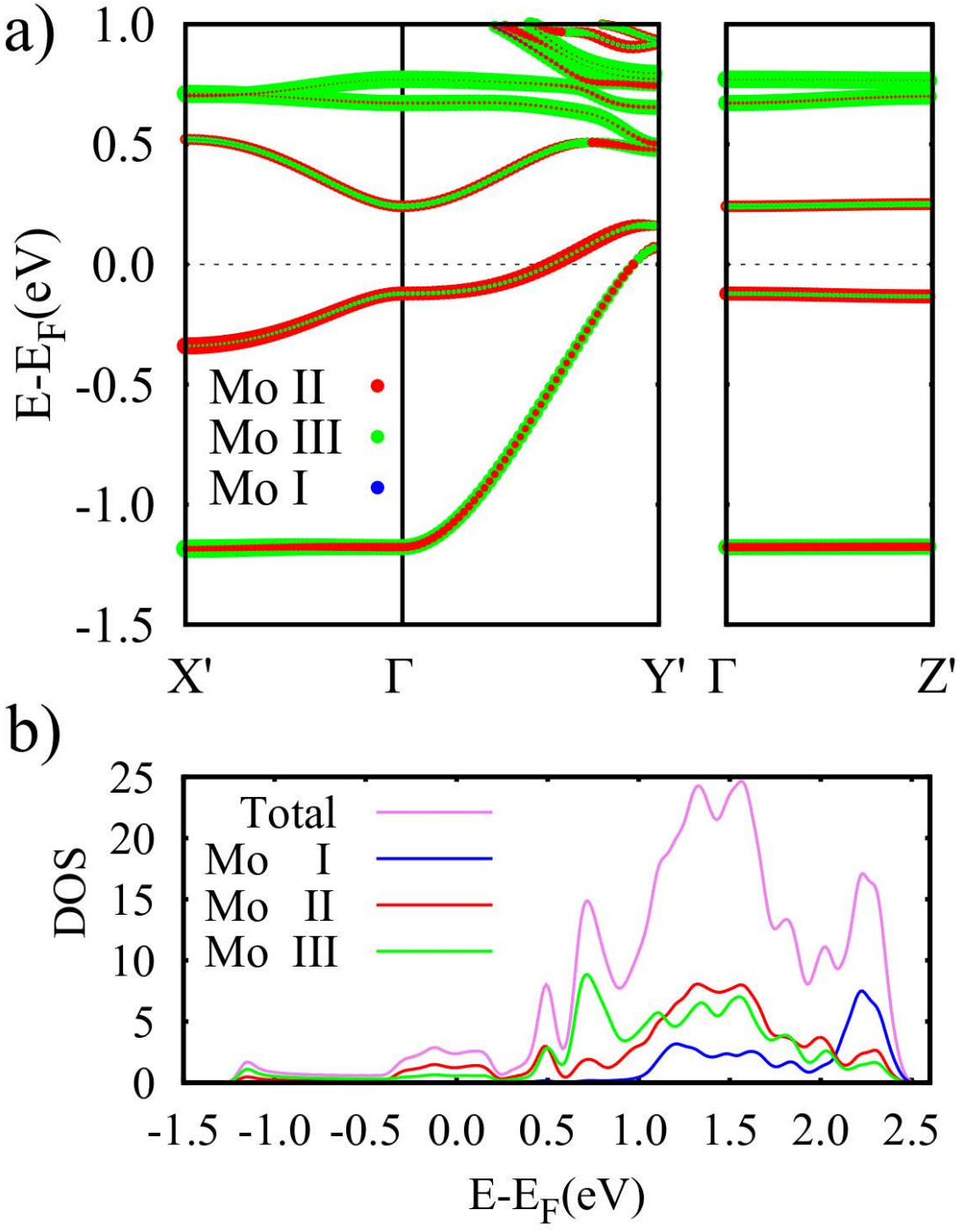

Figure 5.3: DFT band structure (a) and density of states (DOS) (b) for $K_{0.3}MoO_3$. In (a) the size of the blue, red and green dots are proportional to the Mo I, Mo II and Mo III character. respectively. Γ= (0, 0, 0), X′= (1/2, 0, 0), Y′= (0, 1/2, 0) and Z′=(0, 0, 1/2) in units of the a'^*, b'^* and c'^* reciprocal lattice vectors (see beginning of Sect. 5.2 and Fig. 5.4). (b) In (b) the total DOS and Mo I, Mo II and Mo III projected DOS are shown. The DOS is given in units of states per eV per unit cell of 10 Mo and per spin direction.

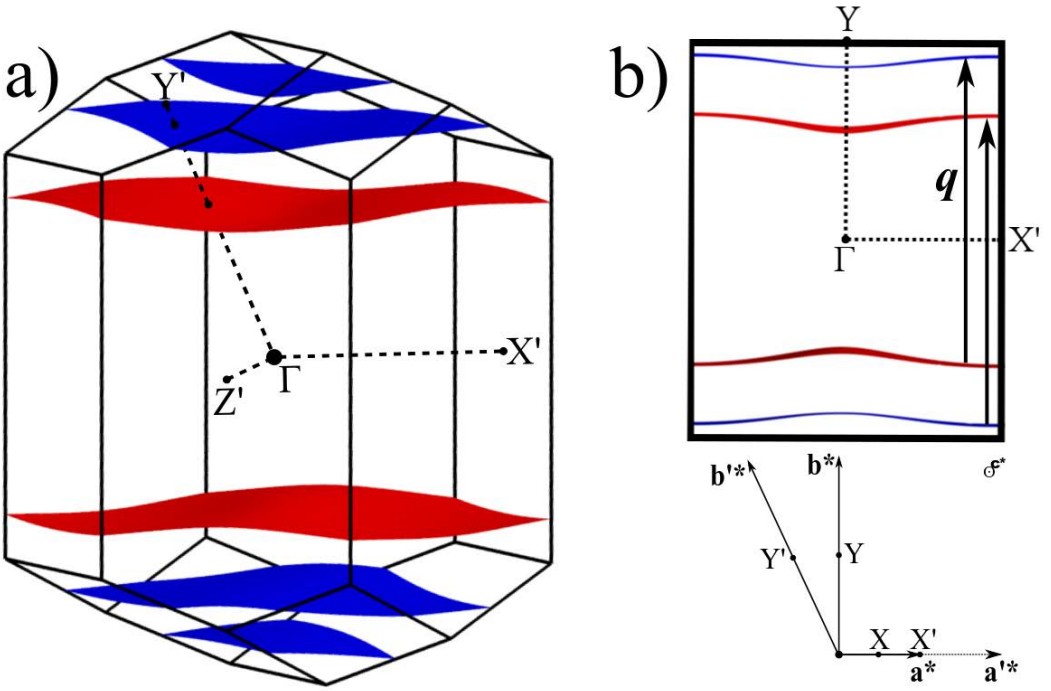

Figure 5.4: DFT Fermi surface for $K_{0.3}MoO_3$: (a) Representation using the rhombohedral Brillouin zone, and (b) View along the perpendicular to the (a^*,b^*) plane.

different ARPES studies [156, 163, 164, 165, 166, 167, 168, 169, 170]. For instance, the calculated values of the k_F^I and k_F^{II} Fermi wave vectors are found to be $0.59\pi/b$ and $0.91\pi/b$ respectively, which are within the range of values determined in different ARPES studies: between 0.55 and 0.69 for k_F^I and between 0.86 and 0.97 for k_F^{II} [156, 163, 164, 165, 166, 167, 168, 169, 170]. In addition, the two calculated band dispersions are also in good agreement with the ARPES studies. The ratio of the calculated Fermi velocities of the two bands in the Γ-Y direction is ≈ 4.5 which compares well with the more recent ARPES studies, ≈ 4.6 [170]. Note also that in the Peierls theory of inter-band nesting [49] an effective Fermi velocity can be defined as $v_F = 2v_F^1 v_F^2/(v_F^1 + v_F^2)$, where $v_F^{1(2)}$ is the Fermi velocity of band 1 (2). Using the ARPES results of reference [170] one obtains $v_F \approx 1.9$ eV.Å, which is in nice agreement with the $v_F \approx 2$ eV.Å value that we calculate from the slope of the thermal dependence of the electron-hole inverse coherence length (see Fig.5.7). Thus, in contrast with earlier tight-binding calculations [151], which led to a pair of bands with similar and considerably smaller dispersion, DFT provides a sound picture of the electronic structure of the blue bronzes. Also shown in Fig. 5.3a

is the contribution of the three different Mo atoms to the different bands. Mo I does not contribute to the two partially filled bands. In fact the orbitals of Mo I only participate in levels between 1.0 and 2.5 eV higher than the Fermi level (see Fig. 5.3b). The reason is that the Mo I octahedra exhibit *two* strong O-Mo...O short/long bond alternations in the basal plane as a consequence of the fact that half of the octahedron shares edges with Mo II and Mo III octahedra whereas the other half does not share any edge, thus leading to a strong distortion. This structural feature leads to a strong destabilization of the three t_{2g} orbitals of the Mo I atom [161]. Consequently, the carriers associated with the two partially filled bands of $K_{0.3}MoO_3$ are confined within the quadruple chains of Mo II and Mo III octahedra. This is in agreement with the fact that the participation of the Mo I atoms in the structural modulation of the blue bronzes was found to be practically nil in the X-ray study of Schutte and De Boer [171]. It is however remarkable that, as discussed in detail by Machado-Charry *et al.* [172], using DFT calculations very similar to the present ones, the brightest spots of the scanning tunneling microscope images of the modulated blue bronzes originate from oxygen atoms of these Mo I octahedra. These atoms are the uppermost oxygen atoms of the surface and the STM experiment is mostly measuring the differences in the local density of states of these O atoms as a result of the CDW.

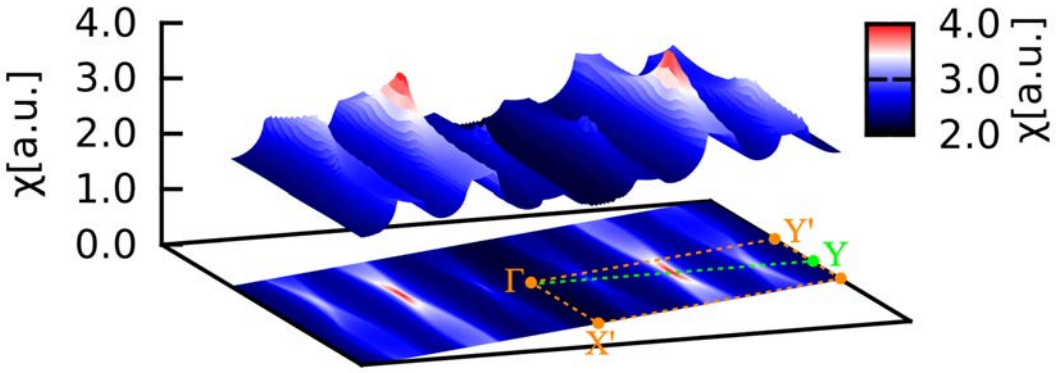

Figure 5.5: DFT Lindhard response function for $K_{0.3}MoO_3$ at 10 K

The two partially filled bands result from the mixing of the Mo II and Mo III orbitals (as well as the associated O p orbitals), although Mo III dominates in the

lower band whereas Mo II dominates in the upper one. These bands are almost exclusively built from the Mo d_{xz} orbitals (here we assume a local system of axis with z along the chain b direction and x along the dashed red line in Fig. 5.2a). This feature originates from the local distortions of the Mo II and Mo III octahedra, which lead to *one* strong O-Mo...O alternation in the basal plane of the octahedra along the inter-layer direction. Such alternation strongly destabilizes the Mo d_{yz} and $d_{x^2-y^2}$ orbitals but does not noticeably affect the d_{xz} orbital. The reason is that the Mo d_{yz} and $d_{x^2-y^2}$ orbitals make π-type antibonding interactions with the O p_z and p_y orbitals, respectively, and the destabilizing effect due to the short Mo-O distance largely outweights the stabilizing effect of the long Mo-O distance [161]. The inner Mo III octahedra dominate in the lower band because the octahedral distortion is weaker than in Mo II octahedra. The d_{xz} orbitals of the more distorted Mo II octahedra dominate in the upper partially filled band. $K_{0.3}MoO_3$ is thus a pseudo-1D metal because the d_{xz} orbitals of the Mo II and Mo III quadruple units undergo strong antibonding π-type interactions with the O p_x orbitals along the chain direction but only weak inter-chain interactions as a result of the unfavourable orientation of the d_{xz} in different chains.

The calculated Fermi surface for $K_{0.3}MoO_3$ is reported in Fig. 5.4. It contains two pairs of slightly warped sheets perpendicular to the b quadruple chains direction. The red sheets, originating from the Mo II octahedra are found to be slightly more warped. The computed Fermi surface compares very well with those determined by ARPES [167, 170] which exhibit a weak but definite warping. In fact, as it will be shown in the next section, the warping is practically irrelevant around the temperature of the metal to insulator transition, T_p= 180 K [157] so that the four sheets may be nested by a single inter-band nesting vector, q. The calculated Lindhard response function associated with the two partially filled bands is shown in Fig. 5.5 where a clear cusp occurs for q= 0.25b^* (note that the chain direction is along Γ-Y, the green dashed line in Fig. 5.5). Two weaker maxima are also visible along the Γ-Y line. In the next sections we discuss in detail the significance of these results to understand the workings of the CDW/PLD modulation at the

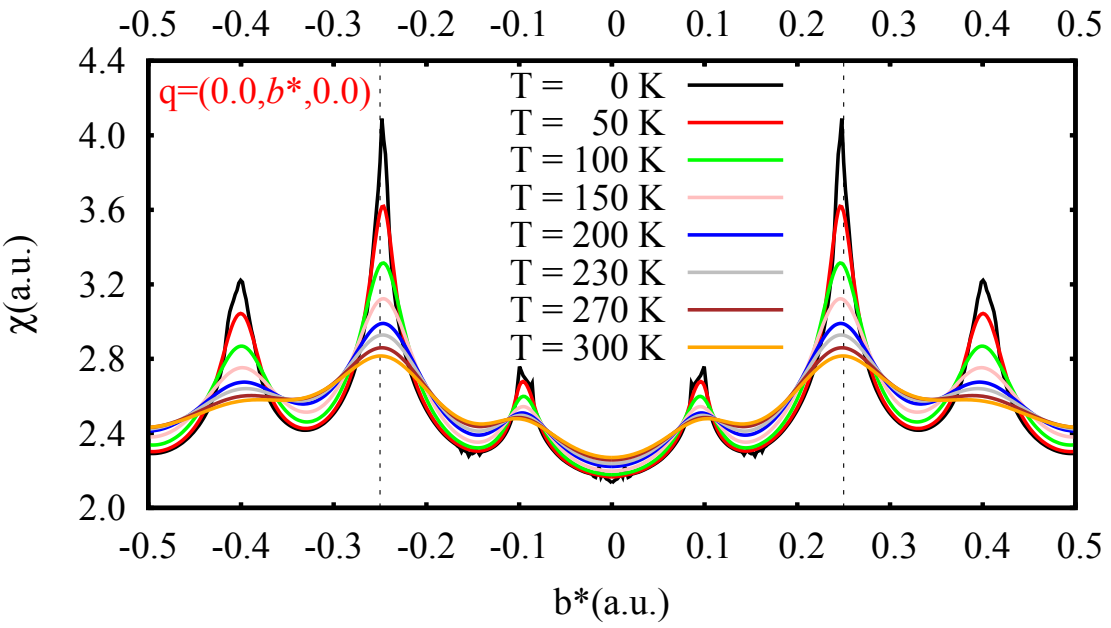

Figure 5.6: Scans of the Lindhard response function along the Γ-Y chain direction for different temperatures. This figure clearly shows the individual responses of the three Fermi surface nesting processes (i), (ii) and (iii) defined in the text.

origin of the metal to insulator transition of $K_{0.3}MoO_3$.

5.3 Quantitative analysis of the Lindhard function

5.3.1 The three individual responses

The Lindhard function (Fig. 5.5) is made of three responses corresponding to three different nesting processes between the four sets of open Fermi surfaces. Scans along the b^* chain direction (see Fig. 5.6) show (using the labelling of Fig. 5.1a) three peaks at:

- 1-$2k_F^{II}$= $0.09b^*$ corresponding to the intra-band nesting of the blue FS,
- 1-$2k_F^{I}$= $0.41b^*$ corresponding to the intra-band nesting of the red FS and
- 1-$(k_F^I + k_F^{II})$ = $0.25b^*$ corresponding to the inter-band FS nesting.

The strongest response is for the inter-band FS nesting. This nesting process achieves the Peierls transition of the blue bronze. With a single modulation all

four FS sheets can be connected and thus a gap opens on the entire FS. The intra-band I response is stronger than the intra-band II response, which agrees with a lesser degree of warping of the corresponding FS. Upon cooling the intensity of these responses increases but does not diverge at low T. Divergence is predicted in the case of nested planar FS [145]. Here, the formation of residual pockets in the nesting process between warped FS stops the divergence. Because of the presence of nesting breaking pockets, the three responses exhibit a slightly anisotropic profile at low T. The $k_F^I + k_F^{II}$ inter-band response exhibits a cusp anomaly whereas a shoulder is exhibited by the $2k_F^I$ response and a tilted plateau by the $2k_F^{II}$ response (see Figs. 5.5 and 5.6). The maximum of the inter-band response occurs for $k_F^I + k_F^{II} = 0.75b^*$, which corresponds to the intra-chain component of the experimental modulation wave vector measured at low T [49]. However, the experimental intra-chain component decreases significantly by a few percent upon heating [49] while Fig. 5.6 shows that the maximum of the Lindhard function stays constant at $0.25b^*$ for whole temperature range considered. Thus, our calculation shows that the experimental decrease of $k_F^I + k_F^{II}$ is not due to a shift of the q dependence of the Lindhard function induced by thermal population effects of the curved conduction bands, as previously suggested [173]. This point will be further considered at the end of section 5.3.3.

5.3.2 Electronic parameters of the inter-band nesting process and validation of the weak coupling scenario

Except at very low T when nesting breaking effects are relevant, each individual Lindhard component exhibits a lorentzian profile in q. The half-width at half-maximum (HWHM) of the Lorentzian in the chain direction gives the inverse coherence length of the fluctuating 1D electron-hole pair, $1/\xi_{eh\parallel}(T)$, which depends on the temperature T and on the microscopic parameters of the 1D electron gas [174]. Fig. 5.7 gives the thermal dependence of $1/\xi_{eh\parallel}(T)$ for the inter-band response component. This quantity increases linearly with the temperature, but does not vanish at 0 K, as expected for planar nested FS. The intercept, which

amounts to $1/\xi^0_{eh\|} = 0.015\text{Å}^{-1} = 1.8\%b^*$, represents the longitudinal size of the pocket due to imperfect longitudinal nesting. One thus has

$$1/\xi_{eh\|}(T) = 1/\xi^0_{eh\|} + 1/\xi^T_{eh\|} \tag{5.3}$$

where $1/\xi^T_{eh\|}$ is the thermal length associated with the broadening of the FS at T. According to the microscopic theory of refs. [174, 175]

$$\xi^T_{eh\|} = \hbar v_F/\pi k_B T. \tag{5.4}$$

For the inter-band nesting process v_F is an effective Fermi velocity defined in ref [49]. Dividing Eq. 5.3 by $<k_F> = (k^I_F + k^{II}_F)/2$ ($= 0.31$ Å^{-1}) leads to the dimensionless expression

$$1/[< k_F > \xi_{eh\|}(T)] = 1/[< k_F > \xi^0_{eh\|}] + T/T_{eff} \tag{5.5}$$

which, according to the data of Fig 5.7, gives a $T_{eff} \approx 2400$ K.

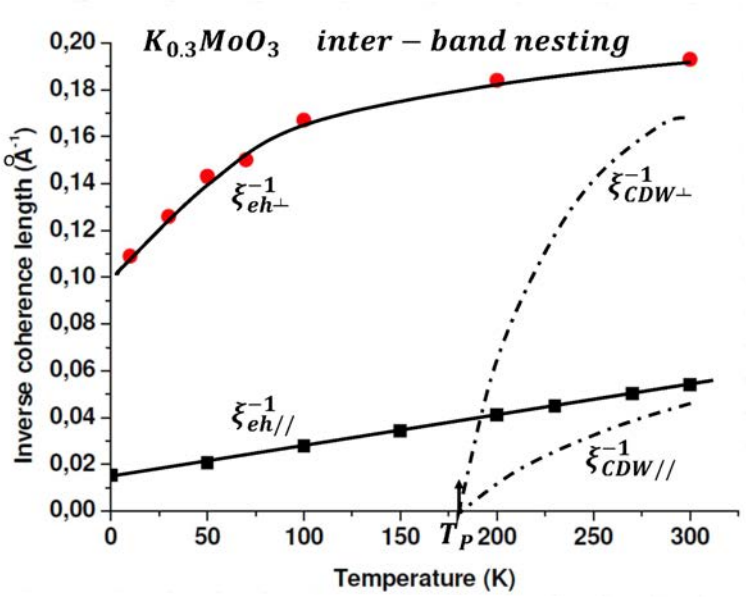

Figure 5.7: Thermal dependence of the inverse coherence lenghts along the chain (‖) and the intra-layer (⊥) directions. These quantities are compared (dashed dotted lines) with the inverse experimental CDW correlation lengths reported in ref[176]

Using the data of Fig. 5.7 it is found that above T_P the value of $< 2k_F > \xi_{eh\|}(T)$ is ≈ 16 at T_P and ≈ 11 at room temperature (RT). Thus, only a very small fraction of the Brillouin zone is affected by the Peierls critical instability. This justifies the criteria for which the phonon entropy change can be neglected at the Peierls transition. Consequently the weak coupling theory of the Peierls transition should apply to the blue bronzes. Using T_{eff} the cut-off energy ($E_{cut-off}$) entering the standard theory of the Peierls transition can be obtained as [145, 152, 175]

$$\pi k_B T_{eff} = \hbar v_F < k_F >= 0.65\ eV \tag{5.6}$$

This energy is comparable to the average Fermi energy of the two conduction bands determined by DFT calculation (see Fig. 5.3) and ARPES measurements [156]. Eq. 5.6 gives an effective Fermi velocity of $v_F \approx 2$ eV·Å.

For a 1D free electron gas with perfect longitudinal $2k_F$ nesting, the Lindhard function should thermally diverge as [175]

$$\chi(2k_F) = N(E_F) \ln(E_{cut-off}/\pi k_B T) \tag{5.7}$$

where $N(E_F)$ is the density of states at the Fermi level and where the cut-off energy E_{cutoff} is of the order of E_F, as given by Eq. 5.6. This divergence does not really occur at low T in the blue bronze because of the presence of residual pockets due to the imperfect longitudinal nesting. Under such conditions it is better to use $1/\xi_{eh\|}(T)$, as given by Eq. 5.3, instead of the scaling variable T. This leads to

$$\chi(2k_F) \propto \ln[k_F \xi_{eh\|}(T)] \tag{5.8}$$

and, as shown in Fig. 5.8, this logarithmic dependence is fulfilled by the peak intensity of the inter-band Lindhard function of the blue bronze for all the temperature range.

The BCS weak coupling relationship relates the Peierls gap at 0 K, $2\Delta_0$, with

the reduced electron-phonon coupling constant λ [145, 152, 175]. For a parabolic band dispersion agreeing with the DFT calculation (see Fig 5.3a) and ARPES measurements [156] it is found that

$$\Delta_0 = 4E_F e^{-1/\lambda} \tag{5.9}$$

Then, using the half-optical direct gap in the Peierls ground state [158], Δ_0= 75 meV, and $E_F \approx 0.65$ eV (Eq. 5.6), a value of $\lambda \approx 0.28$ is obtained. Using the explicit expression for the reduced electron-phonon coupling [145]

$$\lambda = 2g^2 N(E_F)/\hbar\Omega_0, \tag{5.10}$$

one can obtain, using the DFT density of states at the Fermi level, $N(E_F)$= 2.36 eV^{-1} per cluster and spin direction (see Fig. 5.3b), together with a bare critical phonon frequency of Ω_0= 1.7 THz (determined in Fig. 5.9), g = 20 meV. This quantity is more than twice larger than the electron-phonon coupling g determined by the same method for molecular conductors [177].

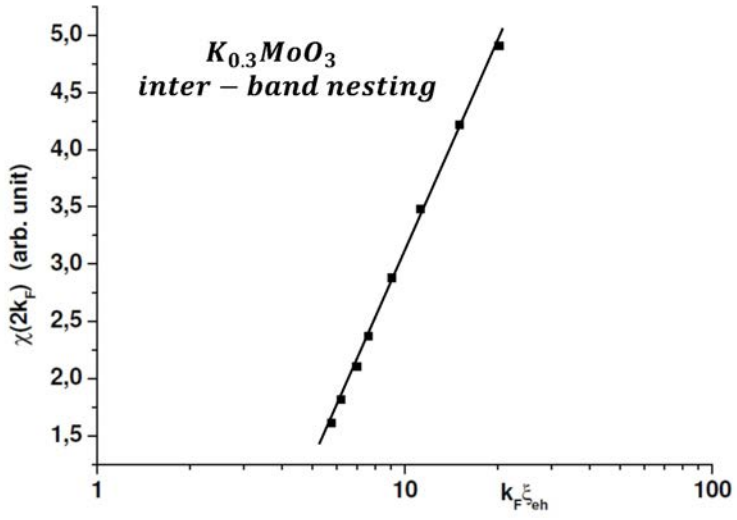

Figure 5.8: Logarithmic dependence of the electron-hole response for the inter-band nesting process of the blue bronze according to Eq. 5.8.

The finding of λ<1 and of $\Delta_0 << E_F$ sustains the weak coupling approximation

for the blue bronze. Fig. 5.7 compares the thermal dependence of the electron-hole coherence length ($\xi_{eh\|}(T)$) with the longitudinal CDW structural correlation length ($\xi_{CDW\|}(T)$) measured by X-ray scattering [49, 157, 176] and whose divergence drives the Peierls transition at T_P. The CDW/PLD fluctuation divergence is driven by the coupling of the 1D electron gas with the critical phonon modes via the electron-phonon coupling g [178, 179]. More precisely, Fig. 5.7 shows that at high temperature (i.e. above RT) $\xi_{CDW\|}(T)$ tends asymptotically towards $\xi_{eh\|}(T)$. Thus, above $\sim 2\ T_P$, when the coupling to the lattice is not yet critical, the length scale of the CDW fluctuations amount to the electron-hole coherence length, as expected in the weak coupling scenario of the Peierls transition.

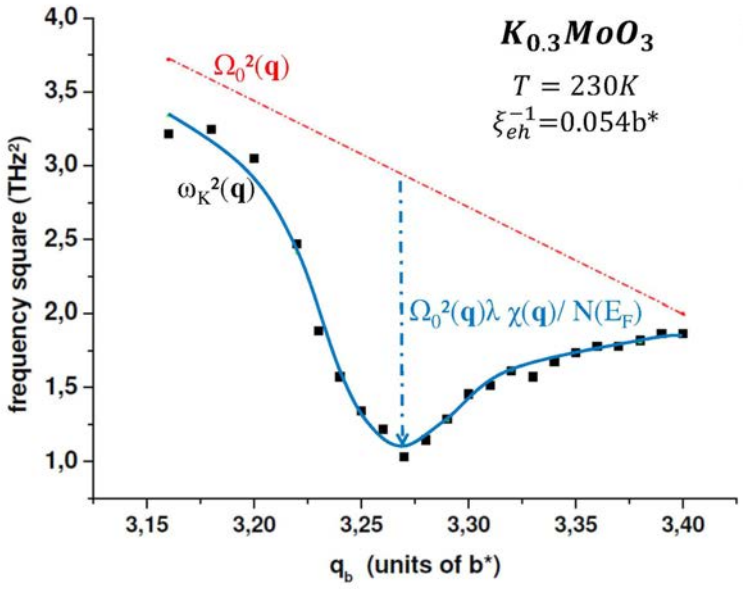

Figure 5.9: Fitting of the square of the frequency of the Kohn anomaly measured at 230 K in ref [37] (see also Fig. 5.13a) with the calculated Lindhard function. The best fit allows to determine the base line corresponding to the square of the bare critical phonon mode $\Omega_0^2(q)$.

5.3.3 Relation with the dynamics of the Peierls transition

Using the relation

$$\xi_{eh\|} = v_F \tau_{eh}, \tag{5.11}$$

it is possible to obtain the lifetime of the electron-pair. It amounts to $\tau_{eh} \approx 10^{-16}$s at room temperature. Thus with Ω_0= 1.7 THz, a very small dimensionless quantity $\Omega_0\tau_{eh} \approx 1.7{\cdot}10^{-4} << 1$ is obtained. This means that the electron-hole pairs fluctuate so fastly during the phonon oscillation period that they are able to screen the coupling constant between the atoms. The Peierls transition of the blue bronze is thus located in the adiabatic limit where the screening effects lead to the formation of a well defined Kohn anomaly in the vicinity of $2k_F$. Such a phonon anomaly is experimentally observed [37]. With the screening effects treated in the RPA approximation the square of the Kohn anomaly frequency is given as [146]

$$\omega_K^2(q,T) = \Omega_0^2(q)[1 - \lambda\chi(q,T)/N(E_F)], \tag{5.12}$$

which involves the Lindhard function $\chi(q,T)$. In Eq. 5.12 we have explicitly included the 3D dependence of the Kohn anomaly (with q= ($q_\parallel$, $q_\perp$)). Fig. 5.9 shows that Eq. 5.12 quantitatively accounts for the $q_\parallel$ dependence of the Kohn anomaly of the blue bronze in the chain direction at 230 K using the Lindhard function calculated with DFT. Note that the best fit of the experimental data with the calculated Lindhard function shown in Fig. 5.9, allows the determination of the square of the bare critical phonon frequency, $\Omega_0^2(q)$. It is found that $\Omega_0(k_F^I + k_F^{II}) \approx 1.7$ THz, which coincides with the frequency of the amplitude mode at low T[37, 46].

Note that in the fit of Fig. 5.9, the q_b values of the Lindhard response function have been shifted by about -0.02b*. The reason is the following: whereas the computed electron-hole response function exhibits a maximum at 0.25b* for the whole temperature range (Fig. 5.6) because the total number of electrons filling the two conduction bands in the calculation remains constant, the wave vector of the experimental minimum frequency of the Kohn anomaly or the q_b maximum of the CDW fluctuations [49] continuously increases upon cooling to reach 0.25b* at low temperature. The origin of such a wave vector shift is unclear. Beside the simple yet unlikely explanation that, for some unknown reason, the total number

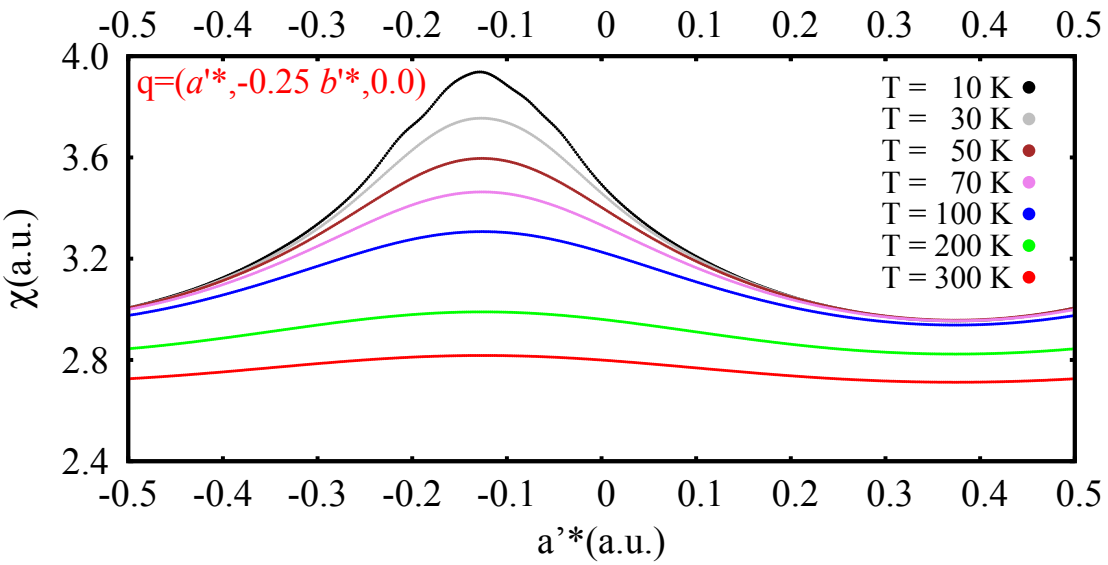

Figure 5.10: Scans of the Lindhard response function along the intra-layer transverse direction for different temperatures. Note that the maxima at about $0.12a$'* corresponds to $0a$*.

of electrons is changing with temperature, it is possible that the reduced electron phonon coupling λ in Eq. 5.12 depends upon q_b. According to Eq. 5.10, λ should vary if the bare phonon frequency Ω_0 and/or the electron-phonon coupling constant g change with q_b. The fit in Fig. 5.9 shows that this is indeed the case for Ω_0. The other possibility, a variation of g with q_b, should also be seriously considered because, as shown by Fig. 5.13 and discussed in Sec. 5.4, the Kohn anomaly develops in a phonon branch resulting from a strong hybridization between the transverse acoustic TA_2 branch and a low frequency optical branch. The two vibration modes certainly involve different atomic displacements so that these lattice deformations should lead to a different electron-phonon coupling. Thus, with a mode mixture changing substantially with q_b in the vicinity of $k_F^I + k_F^{II}$, one should expect that the electron-phonon coupling g should exhibit a strong q_b dependence.

5.3.4 Inter-chain coupling

In a purely 1D electron-phonon coupled system the intra-chain correlation length diverges at 0 K because the structural fluctuations prevent any ordering at finite

temperature [178, 179]. The observation of a Peierls transition at finite T is due to the inter-chain coupling between the CDW fluctuations [179]. In general inter-chain coupling can occur through three different mechanisms [179, 148]:

- A transverse nesting of the FS. In that case the Lindhard function should exhibit an inter-chain wave vector dependence (i.e. $q_\perp$) along which direction the FS is warped,
- An inter-chain Coulomb coupling between CDW's, since each individual CDW exhibits a charge modulation, or
- A transverse wave vector, $q_\perp$, dependence of the bare critical phonon $\Omega_0(q)$.

It is worth considering the likeliness of the three coupling mechanisms for the blue bronze. Let us start with mechanism (i). Fig. 5.10 presents thermal scans of the Lindhard function along the $a + 2c \approx 2a^* + c^*$ intra-layer transverse direction (see Fig. 5.2). It exhibits a very broad response centered at $q_\perp = 0$ (in the a^*,b^* frame defined in Fig. 5.4b) corresponding to an inter-chain coupling in-phase along the $a+2c$ direction. This wave vector achieves the best FS nesting of band I to band II, as outlined in previous band structure calculations [151, 155]. Note however that mechanisms (b) and (c), which will be considered below, give a similar phasing. However the present calculation shows that the transverse response of the Lindhard function is quite broad. From its HWHM on gets an inverse inter-chain electron-hole coherence length $\xi_{eh\perp}^{-1} \approx 0.19$ Å^{-1} at RT which very slightly decreases upon cooling (Fig 5.7), reaching 0.18 Å^{-1} at T_P. The inverse of this quantity leads to a coherence length of ∼5.5 Å which is about the distance between the two outer Mo III of the cluster but twice smaller than the distance (12 Å) between the two outer Mo II of the segment defined in Fig. 5.2c. $\xi_{eh\perp}^{-1}$ is larger than the inverse CDW structural correlation length $\xi_{CDW\perp}^{-1} \sim$ 0.14-0.17 Å^{-1} measured along the $2a^* + c^*$ direction at RT [49, 176]. In addition, the non-detection of a transverse plasma edge for light polarized in the transverse direction [176] shows that the warping effect of the FS is not thermally relevant above T_P. The blue bronze thus remains a true 1D metal in the CDW fluctuating regime above T_P. We thus

conclude that mechanism (i) is not relevant for the blue bronze and we must concentrate on the other two mechanisms.

Let us first consider mechanism (ii) which was previously discussed in ref. [148]. According to the structural refinement of the modulated structure of the blue bronze below T_P [171] there is basically a longitudinal displacement of the Mo atoms in the direction of each linear segment of four corner-sharing MoO_6 octahedra (see Fig. 5.2c). This in-phase displacement induces a ferroelectric polarization of the segment, and the CDW modulates along b the amplitude of polarization of linear segments with the $2k_F = 0.75b^*$ wave number. In this scenario, the inter-chain electrostatic coupling mechanism occurs between dipolar CDW. Such a coupling is quite anisotropic and as shown in Fig. 5.11:

- the intra-layer coupling along a+2c between polar CDWs in the dipole direction, $W_{\parallel}$, leads to a uniform inter-chain CDW order,
- the inter-layer coupling along 2a^*-c^* between polar layers of CDWs in the perpendicular direction, $W_{\perp}$, leads to a staggered inter-layer CDW order.

From the anisotropy of inter- and intra-layer transverse correlation lengths [142] one gets an anisotropy of couplings of $W_{\parallel} \approx 8W_{\perp}$ (see Fig. 5.11). Finally, let us consider mechanism (iii) above T_P. This mechanism is compatible with mechanism (ii) below T_P. Mechanism (iii) relies on the presence of an incipient anisotropic valley of low frequency phonons whose bare frequency $\Omega_0(q)$ sizably varies with q. In the blue bronze such an anisotropic dispersion along $q_{\perp}$ is observed for the acoustic phonon branch polarized along a+2c mixed with a polar optical branch (see Sec. 5.4 for experimental evidence taken from the phonon spectrum). This composite mode involves optical-like uniform off-center Mo displacements within the four MoO_6 octahedra of each segment. The correlated Mo displacement between neighboring corner-sharing octahedra should induce a local polarization (Fig. 5.12a). When the correlated Mo displacements are in-phase between neighboring overlapping segments of four octahedra separated by $a/2$+c (see Fig. 5.2a),

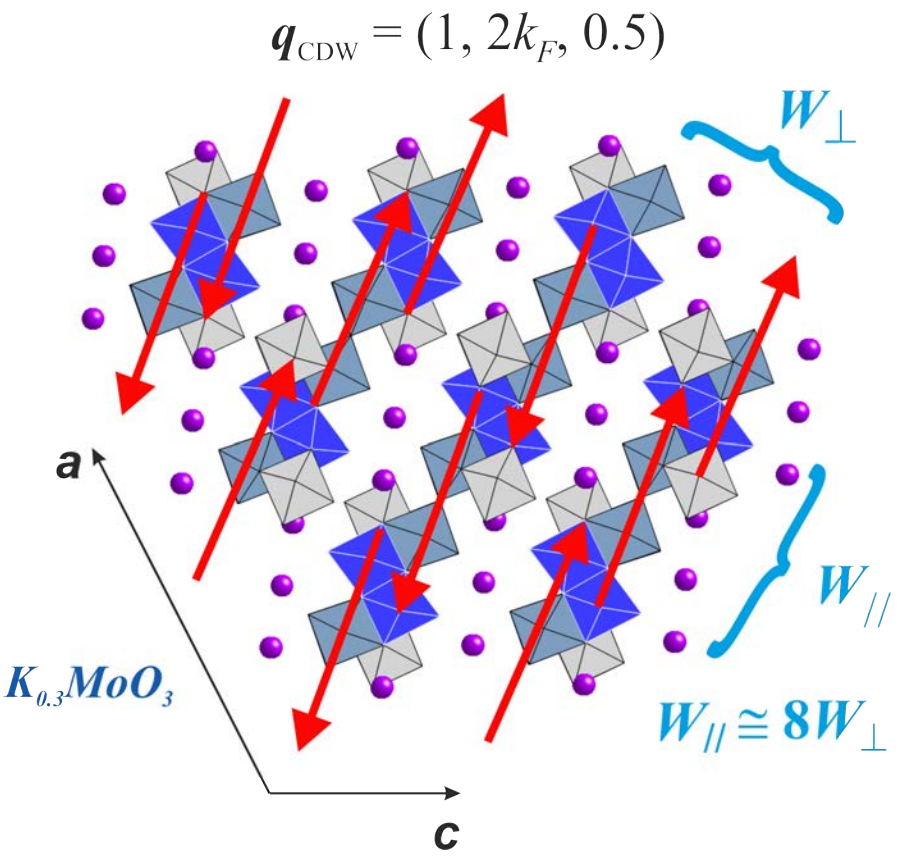

Figure 5.11: Lateral phasing of the dipolar CDWs in $K_{0.3}MoO_3$.

a frequency softening of the composite acoustic/optical phonon branch should occur. This softening persists along the b^* and $2a^*$-c^* perpendicular propagating wave vectors starting from each $2\pi/\mid a/2 + c \mid$ reciprocal position. In reciprocal space this should give rise to a sheet of low frequency phonons perpendicular to the polar segment direction (Fig. 5.12c). The trace of such sheet of low frequency phonons leads to an enhanced X-ray planar diffuse scattering (Fig. 5.12b) which has been detected in the blue bronze at RT (see ref. [157, 148]). The CDW/-PLD instability and the associated Kohn anomaly develop inside this valley of soft phonons. Such a preexisting valley imposes the intra-layer CDW component $q_\perp = 0$. We thus suggest that mechanisms (ii) and (iii) are strongly intermingled and are at the origin of the inter-chain coupling in the blue bronzes.

Similar low frequency planar valleys of mixed acoustic/polar phonons are observed in ferroelectric perovskites such as $BaTiO_3$ $KNbO_3$ and $KTaO_3$ [180, 181, 182] or the chain-like ferroelectric SbSi [183]. Note that features similar to those

of the blue bronze are observed in the CDW monophosphate tungsten bronzes, $(PO_2)_4(WO_3)_{2m}$, which are built from segments of m corner-sharing WO_6 octahedra and which exhibit a tendency to ferroelectricity. Note that WO_3, which corresponds to the limit of this family when $m \to \infty$ is an antiferroelectric. The CDW/PLD instability in the monophosphate tungsten bronzes develops inside a planar valley of low frequency phonons also perpendicular to the segment directions [184, 185]. The possible link between the CDW/PLD instabilities of the blue bronzes, $\gamma-$ and $\eta-Mo_4O_{11}$ Magnéli phases and monophosphate tungsten bronzes suggested by our discussion is thus a challenging issue in the quest for a full understanding of microscopic origin of the CDW instabilities in oxides and bronzes.

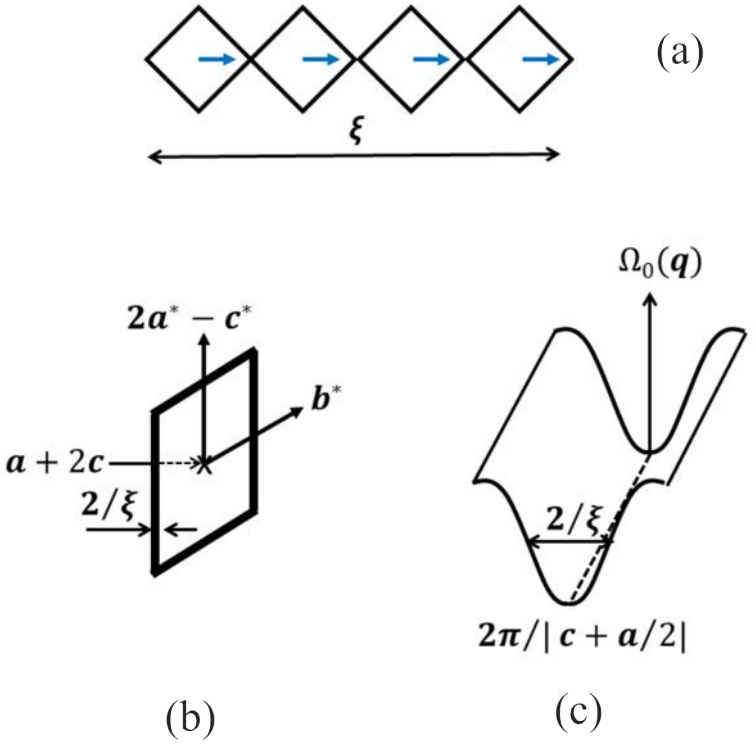

Figure 5.12: Illustration of the low-frequency phonon coupling mechanism for inter-chain coupling in the blue bronze and its detection. (a) Local polarization induced by the correlated Mo displacements in neighboring corner sharing octahedra. (b) Planar diffuse scattering developed in X-ray scatering measurements due to (c) a sheet of low-frequency phonons perpendicular to the polarization direction when the correlated Mo displacements are in-phase between neighboring segments.

5.4 Critical low frequency phonon branches of $K_{0.3}MoO_3$

The phonon spectrum of $K_{0.3}MoO_3$ is quite complex because it contains many optical branches of low frequency which hybridize with acoustic branches. Figure 5.13a shows the dispersion of some of these branches measured by inelastic neutron scattering between 225 K and RT along the reciprocal directions defined in Figs. 5.13b and 5.13c [37, 186]. Since previous neutron scattering studies focused on the dynamics of the Kohn anomaly, the phonon spectrum of the blue bronze has never been analyzed. In this respect the true polarization of the critical phonon branch has never been considered.

Let us first consider the acoustic branches. The orthogonal frame used to label the acoustic modes is based on the structural anisotropy (see Fig. 5.2a) according to the decrease in the bonding strength:

- the monoclinic b direction: label 1,
- the [102] direction: label 2,
- the perpendicular to the (-201) layer of MoO_6 octahedra: label 3.

Using the slope of the acoustic branch one obtains the elastic constants given in Table 5.1. The relative C_{ij} values follow the structural anisotropy:

- for the compression deformation: $C_{22} > C_{11} \gg C_{33}$, the deformation energy of the chain of clusters is stronger than that between clusters along the [102] direction of the layer and much stronger than that in the inter-layer direction incorporating alkaline atoms.
- for the shear deformation: $C_{66} > C_{44} \approx C_{55}$, the shear deformation energy of the (-201) layer of octahedra is stronger than that associated with their relative shift.

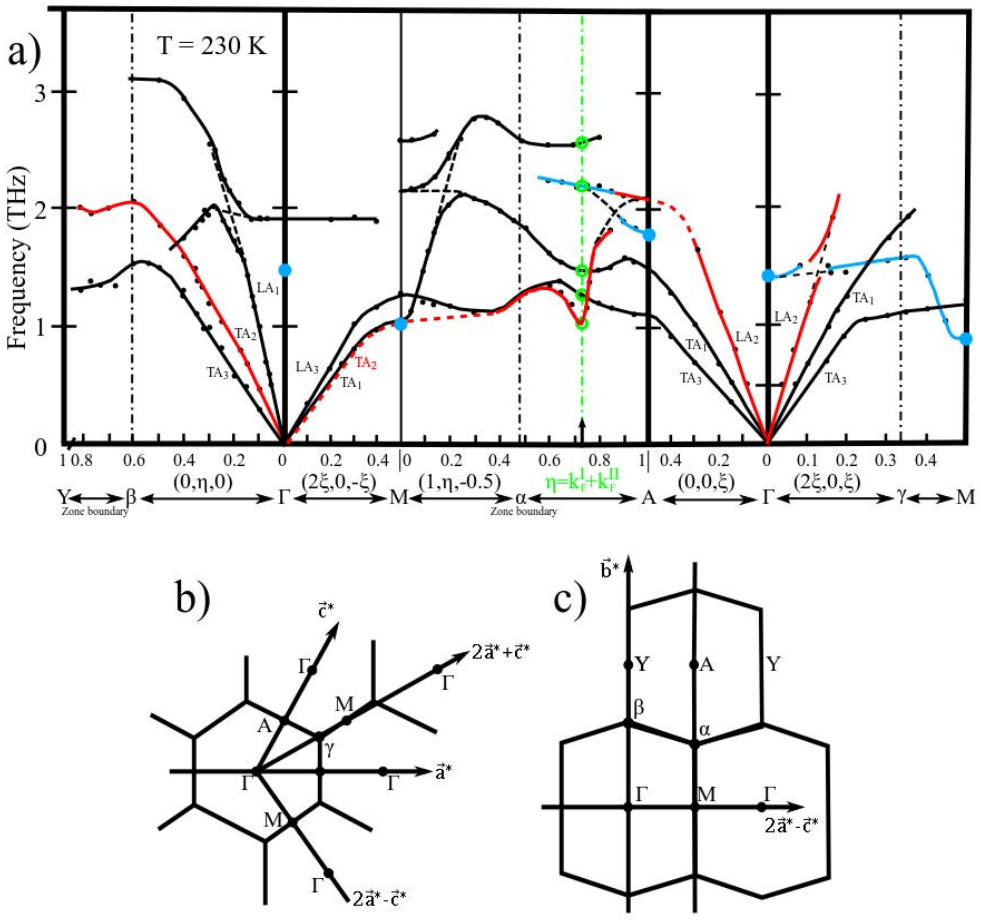

Figure 5.13: (a) Dispersion of the low-lying phonon branches of the blue bronze measured between 225 and 295 K. The acoustic branches are labelled according to their polarization defined in the text. The hybridized phonon branches involved in the Peierls instability are colored in red and blue for the acoustic and optic counterparts respectively. The empty green circles outline the phonon modes in the vicinity of the Kohn anomaly drawn at 230 K. (b) and (c): Sections of the Brillouin zone scanned during the inelastic scattering investigations (adapted from refs. [157, 186]).

The dispersion of the phonon branch bearing the Kohn anomaly is not straightforward to analyze because it results from the hybridization of the acoustic mode polarized in the segment direction (label 2 and red lines in Fig. 5.13a) with a low lying optical phonon mode (blue lines in Fig. 5.13a) whose frequency is 1.4 THz at the Γ point and 1.8 THz at the A point (blue empty circles in Fig. 5.13a; the Γ and A points are defined in Figs. 5.13b and c). Although not measured from a $(2\xi, 0, -\xi)$ scan along ΓM, the TA_2 branch should be very close to the TA_1 branch because $C_{44} \approx C_{55}$ (see Table 5.1). At the zone boundary M point one expects a

mixing of the TA_2 branch with the above mentioned optical branch reaching 0.9 THz at the M point along a different (2ξ, 0, ξ) scan (see Fig. 5.13a). Another mixing between the two modes occurs near the A point, very close to the position of the Kohn anomaly. As a result, the low frequency phonon branch sustaining the Kohn anomaly should be strongly hybridized in the MA direction. The (2ξ, 0, ξ) scan clearly shows an avoided crossing near the Γ point between the bare LA_2 and the 1.4 THz optical branches. Beyond this crossing point the frequency of the optical branch stays nearly constant until the γ zone boundary crossing point. Then, the γM scan shows that its frequency drastically decreases to reach 0.9 THz at the M point (where it should mix with the TA_2 branch). Such dispersion, which recalls that depicted in Fig. 5.12c, is the cut of a preexisting valley of soft phonons discussed in the main text, where the frequency softening should be associated to correlated 1D Mo displacements, ξ. From the inverse of the half-width of the wave vector softening along γM it can be inferred a correlated Mo displacement on $\xi \approx 9$ Å, which is about the distance between two neighboring clusters in the transverse layer direction (Fig. 5.2a).The dispersion along MA of the bottom of the valley of soft acoustic/optic phonon is represented in Fig. 5.13a. Note that this dispersion exhibits an extra screening with the 1D electron gas near $2k_F$, which leads to the formation of a Kohn anomaly in the phonon spectrum.

Another difficulty to analyze the Peierls lattice instability resides in the presence of four additional low-lying phonon modes at the position of the Kohn anomaly (empty green circles in Fig. 5.13a).

5.5 Comparison with other charge density wave systems

The present study shows that the CDW instability and the Peierls transition of the blue bronze can be quantitatively understood within the weak electron-phonon coupling scenario. As a consequence, there is a clear softening above T_P of a sharp

Table 5.1: Elastic constants obtained from the dispersion of the acoustic branches shown in Fig. 5.13a. The direction of propagation q and the polarization e of the acoustic branch used for each determination are indicated. The accuracy of the determination is estimated to be of 5%. A comparison between our C_{ij} values and other measurements in the literature can be found in ref [187]

Elastic constant	q direction	e direction	$C_{ij}(10^2$ GPa)
C_{11}	2	2	1.5
C_{22}	1	1	2.25
C_{33}	3	3	0.31
C_{44}	3/1	1/3	0.21
C_{55}	2	3	0.22
C_{66}	1/2	2/1	0.52

Kohn anomaly driven by the divergence of the electron-hole response function (Fig. 5.9). This well pronounced Kohn anomaly leads to the emergence below T_P of two collective excitations of the amplitude and phase of the incommensurate CDW modulation whose dispersion has been clearly measured by inelastic scattering [37, 188, 189]. The phase excitation mode whose frequency tends to zero at the $2k_F$ wave vector and which stiffening of the linear dispersion increases upon cooling [188, 189], is a basic ingredient allowing to understand the sliding of the CDW of the blue bronze under electric fields [139, 140, 141]. This situation should be contrasted with the case of $NbSe_3$ where analogous CDW sliding effects have been reported [13]. Two differences are worth noting. First, the Lindhard function of the blue bronze shows a well decoupled $2k_F$ sharp response for the different intra- and inter-band FS nesting processes (Fig. 5.6) while $NbSe_3$ shows a broad electron-hole response in the chain direction where the different intra- and inter-band FS nesting processes are superposed [42]. Second, up to now no Kohn anomaly has been detected in $NbSe_3$ by neutron and X-ray inelastic scattering methods [190]. Such absence of Kohn anomaly has been interpreted as providing evidence for a strong coupling scenario of the Peierls transition [190]. Note however that these measurements report an anomalous drop of the frequency of the longitudinal acoustic (LA) branch for wave vectors tending to the zone boundary. Thus, it is expected that in the next Brillouin zone the LA branch transforms into an longitudinal optical (LO) branch. This LO branch, which has the right

symmetry to achieve the out-of-phase longitudinal deformation of first neighbor coupled $NbSe_3$ chains required to form a π shifted CDW [191], could exhibit a soft frequency on a large intra-chain wave vector range around the CDW critical wave number. In this respect note that, in agreement with this hypothesis, both the Lindhard function calculation [42] and the measurement of the intra-chain CDW correlation length [192] give a small $\xi_{eh} \sim$ 5-10 Å at RT which leads to a product $2k_F\xi_{eh} \sim$ 2-4, more than three times smaller than $2k_F\xi_{eh} \approx 11$, estimated here for the blue bronze. This indicates that the phonon entropy should certainly not be neglected when considering the mechanism of the Peierls transition of $NbSe_3$. In this respect, $NbSe_3$ could bear a resemblance to the 2D CDW systems which will be considered below.

It is also interesting to compare these findings to those for 2D CDW systems such as the RTe_3 (where R is a rare earth atom) tellurides and the transition metal dichalcogenides. In $TbTe_3$, the CDW lattice instability is revealed by the formation of a broad Kohn anomaly in an optical branch where frequency softens and damping increases at the critical CDW wave number when approaching the Peierls transition (T_P= 330 K) [193]. Furthermore, below T_P the CDW modulation develops with a critical wave vector slightly off the best nesting FS wave vector [153, 193]. It is thus proposed [193] that a wave vector dependent electron-phonon coupling could be responsible for this effect.

Controversial interpretations have been proposed during many years concerning the mechanism of the CDW instability of the layered transition metal dichalcogenides. According to a recent review [50], predictions based on the mean-field model agree only semi-quantitatively with experimental data and it appears that generally there is no real dominant factor favoring the CDW formation. A recent inelastic X-ray investigation of $2H$-$NbSe_2$ evidences the formation of a broad and damped Kohn anomaly in a longitudinal acoustic branch whose frequency critically softens at the CDW wave number when reaching T_P= 33 K (contrary to earlier neutron scattering investigations) with a damping diverging at the CDW

transition [64]. As it is the case for $TbTe_3$ [193], it was proposed [64] that in the presence of a broad electron-phonon response, which does not really select a particular FS nesting mechanism [153], the q-dependent electron-phonon coupling should be incorporated into the explanation of the CDW instability.

Compared to $NbSe_3$, rare-earth tellurides and transition metal dichalcogenides, the blue bronze, which exhibits a CDW instability that can be accounted for by the standard (weak electron-phonon coupling) Peierls scenario, appears to be unique. This is due to the fact that it exhibits a sharp $2k_F$ electron-hole response, due to a simple FS nesting mechanism, which drives the formation of a sharp Kohn anomaly which softening drives the Peierls/CDW instability. In rare-earth tellurides and transition metal dichalcogenides, the electron-hole response is broad and leads to the formation of a broad Kohn anomaly. In the latter 2D CDW metals the way by which the critical CDW wave vector is selected remains unclear. It has been recently proposed that a wave vector dependent electron-coupling is essential for that purpose [64]. Another important question concerns the mechanism of the CDW/Peierls instability. In the presence of a broad Kohn anomaly, where the softening involves a large number of wave vectors of the Brillouin zone, the lattice degrees of freedom play a more important role (in particular through its entropy) than that assigned in the standard theory of the Peierls transition, where only the elastic energy cost is considered. A full account of lattice effects, considered earlier by McMillan [147], should invalidate the BCS-type theory for the Peierls transition and should lead to strong coupling scenarios.

Finally, let us mention that other 2D transition metal Mo and W metallic oxides and bronzes exhibit a succession of CDW instabilities [141, 139]. In contrast with the transition metal dichalcogenides, the electronic structure of these oxides can be described by a 2D lattice of interpenetrating and differently oriented chains [194]. As a consequence, their Lindhard function, which is dominated by the $2k_F$ FS nesting processes of individual chains, exhibits in reciprocal space a collection of differently oriented and well-defined chain-like electron-hole responses similar to

that calculated for the blue bronze [195, 196]. The CDW instability occurs at the crossing point of the differently oriented chain responses, whose associated 1D-like CDW fluctuations have been detected by X-ray diffuse scattering methods [197]. The CDW transition of these materials thus presents a Peierls character [185]. However since inelastic scattering measurements have not been performed, the CDW lattice dynamics is still unknown.

5.6 Concluding Remarks

The wave vector and temperature dependencies of the electron-hole (i.e. Lindhard) response function of the blue bronze $K_{0.3}MoO_3$ have been calculated on the basis of its *first-principles* DFT electronic structure. This response has three components corresponding to three possible nesting processes of its warped double sheet quasi-1D FS. We have quantitatively analyzed the $k_F^I + k_F^{II}$ inter-band electron-hole component which is responsible for the Peierls instability of the blue bronze. We have shown that the electron-hole coherence length of this response determines the length scale of the experimental intra-chain CDW correlations. In addition, the intra-chain $q_{\|}$ dependence of such response also determines the shape of the Kohn anomaly experimentally measured. All these features prove that the Peierls transition of the blue bronze can be well accounted for by the weak electron-phonon coupling theory of this transition in the adiabatic approximation. To the best of our knowledge this is the first time that such theory, already established in the 1970s, is quantitatively verified. Finally, the calculation of the intra-layer transverse $q_{\perp}$ dependence of this response shows that the warping effect of the FS above T_P does not provide a pertinent mechanism for the CDW interchain coupling. We propose that such inter-chain coupling is achieved through the Coulomb coupling between dipolar CDWs. Furthermore, we show that the dipolar nature of the CDW modulation is due to the condensation at T_P of a critical phonon mode resulting from the hybridization of an acoustic branch polarized in the MoO_6 intra-layer segment direction, and an optical polar branch

similar to those found in ferroelectric perovskites. We suggest that such an interchain coupling mechanism also occurs in CDW oxides and bronzes such as the monophosphate tungsten bronzes.

5.7 Computational details

DFT calculations [96, 97] were carried out using a numerical atomic orbitals approach, which was developed for efficient calculations in large systems and implemented in the SIESTA code [27, 28]. We have used the generalized gradient approximation (GGA) to DFT and, in particular, the functional of Perdew, Burke and Ernzerhof [98]. Only the valence electrons are considered in the calculation, with the core being replaced by norm-conserving scalar relativistic pseudopotentials [99] factorized in the Kleinman-Bylander form [100]. The non-linear core-valence exchange-correlation scheme [102] was used for all elements. We have used a split-valence double-ζ basis set including polarization functions [101]. The energy cutoff of the real space integration mesh was 350 Ry. To build the charge density, the Brillouin zone (BZ) was sampled with the Monkhorst-Pack scheme [103] using grids of (21×45×21) k-points. The Lindhard response function (Eq. 5.1) was obtained from the computed DFT values of the band eigenvalues $\epsilon_i(k)$. The integral over k-points of the BZ was approximated by a direct summation over a dense, regular grid of points. As the Lindhard function is more sensitive to the accuracy of the BZ integration than the total energy, especially in very anisotropic systems, and/or in the presence of hot spots in the band structure (e.g. saddle points with the corresponding van Hove singularity in the DOS), the k-points grid used for its calculation must be more dense than in the standard self-consistent determination of the charge density and Kohn-Sham energy. The calculations are done, nevertheless, using the eigenvalues obtained in the DFT calculation for the coarser grid, and interpolating their values in the denser grid, using a post-processing utility available within the SIESTA package. In this work, for the calculation of the Lindhard response function, the BZ was sampled using a grid of (256×256×16) k-points. The two partially filled bands were those taken into account in the calculations.

6. ELECTRONIC DIMENSIONAL CROSSOVER AND FERMI SURFACE NESTING INSTABILITIES IN THE BECHGAARD SALTS REVEALED BY THE LINDHARD RESPONSE FUNCTION

6.1 Introduction

The study of one dimensional (1D) systems was initially developed to obtain exact quantum and thermodynamic solutions for the many body problem in interacting magnetic and electronic systems [198]. However, it was only during the 1970s that became possible experimental studies of solids built from a collection of weakly coupled magnetic or conducting chains in order to test the theoretical predictions (at least for the temperature range where thermal fluctuations overcome the inter-chain coupling energy). Thus, in order to rationalize the data obtained from 1D thermal and/or quantum fluctuations in real anisotropic or quasi-1D systems it was necessary to evaluate the anisotropy of the inter-chain vs. intra-chain couplings since the former drives the system towards a three dimensional (3D) ground state at finite temperature. This feature contrasts with exact theoretical results stipulating that a 1D system cannot exhibit a phase transition at finite temperature (only a phase transition at 0 K is possible for the classical chain and no phase

transition at all for the quantum chain).

The chain coupling is achieved by inter-chain exchange coupling in magnetic systems [199] and by inter-chain tunnelling and/or Coulomb coupling in metallic systems [200]. Note that in quasi-1D metals the presence of various types of 1D fluctuations with different kinds of inter-chain couplings generally leads to complex phase diagrams including competing ground states which could end into a quantum critical point. One of the best examples of this situation can be found among the isostructural Fabre $(TMTTF)_2X$ and Bechgaard $(TMTSF)_2X$ 1D organic salts [TMTTF is tetramethyltetrathiafulvalene, TMTSF is tetramethyltetraselenafulvalene and X is a monovalent anion such as PF_6^-, ClO_4^- and NO_3^-] whose 3D ground state evolves upon changing the TMTTF donor by TMTSF and/or by increasing pressure from a spin-Peierls to an antiferromagnetic ground state, then to a $2k_F$ spin density wave (SDW) where $2k_F$ is the Fermi wave vector of the 1D electron gas, and finally to a superconducting state (see Fig. 6.1) [201].

Among the different inter-chain interactions occurring in anisotropic metals an essential role is played by the inter-chain transfer integrals, $t_\perp$. Earlier studies have clearly pointed out the difference between inter-chain diffusive electron transfer and coherent electron transfer mechanisms [200, 203]. In the first case there is no coherence between Bloch functions located on neighbouring chains. Thus, one has a true 1D metal where the warping of the Fermi surface (FS) is not relevant and there is no transverse plasma edge detected by optics. In the second case, the electronic wave function is 2D or 3D delocalized over several chains and $t_\perp$ is a relevant interaction. More precisely, for a non-interacting electron gas the coherent regime occurs for $k_B T < t_\perp/\pi = k_B T_{CO}$, where T_{CO} is the 1D to 2D/3D crossover temperature [203, 204]. Below T_{CO} a transverse plasma edge should be detected. It has been predicted [205, 206] that the crossover transition T_{CO} between the diffusive and coherent regimes decreases in the presence of sizeable intra-chain Coulomb repulsion because the latter interaction tends to localize the electron wave pockets so that the effective inter-chain tunnelling process should

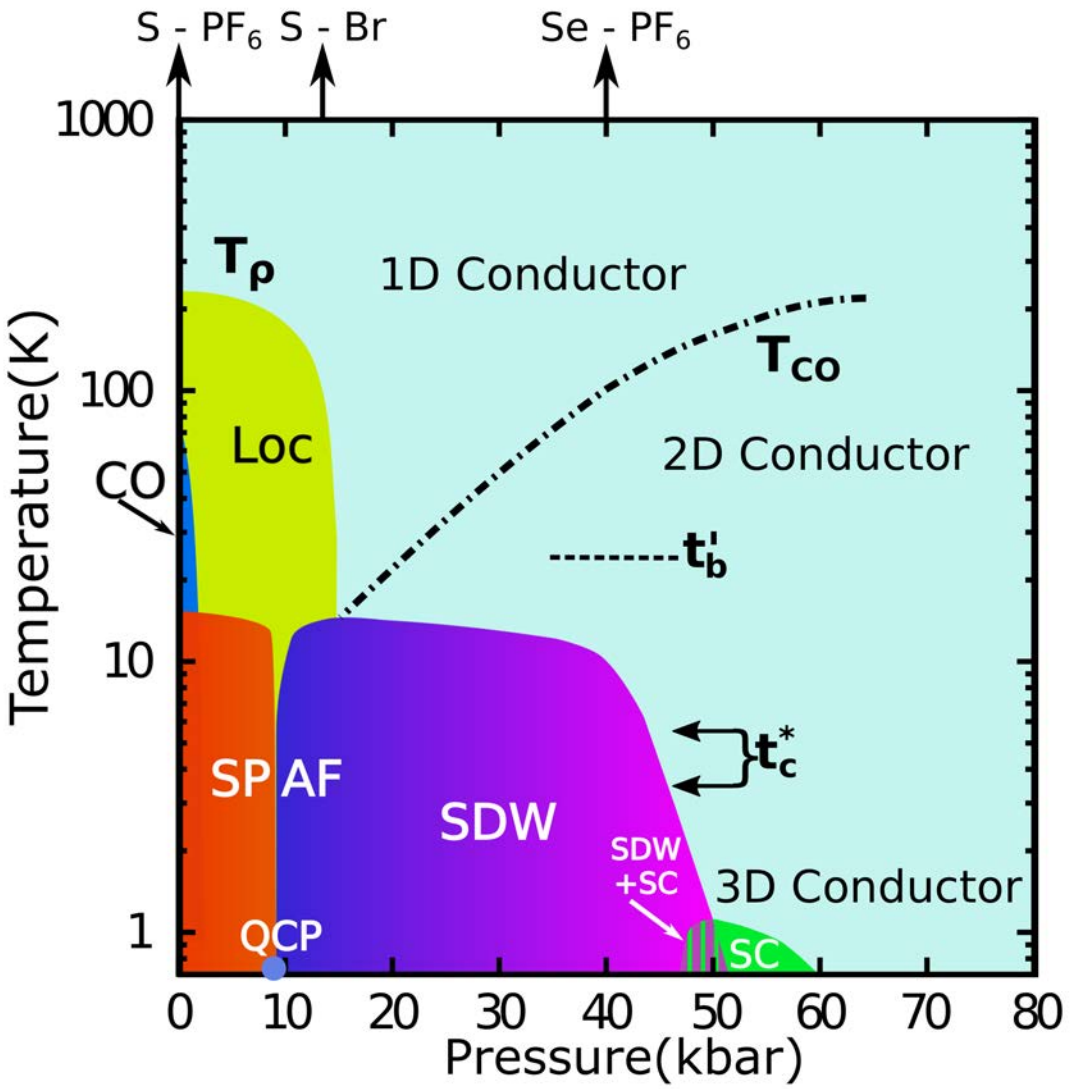

Figure 6.1: Generalized phase diagram for Fabre (S-X) and Bechgaard (Se-X) salts where X is a centrosymmetrical anion. The pressure scale corresponds to $(TMTTF)_2PF_6$. Vertical arrows place $(TMTTF)_2Br$ and $(TMTSF)_2PF_6$ at atmospheric pressure in the phase diagram. CO, SP, AF, SDW and SC refer to charge ordered, Spin-Peierls, antiferromagnetic and superconducting ground states. QCP is a quantum critical point between the SP and AF ground states. T_ρ indicates the onset temperature for charge localization (Loc in the Figure) as detected in the conductivity measurements. T_{CO} is the crossover temperature from a 1D (in the stack direction, a) to a 2D (in the (a,b) donor layer) delocalized electron gas according to ref [202]. On the right hand scale there is also a crossover to a 3D delocalization regime along c through the anion cavities at a temperature of the order of t_{c*}. The nesting breaking term $t_b{}'$ introduced in the text is also indicated.

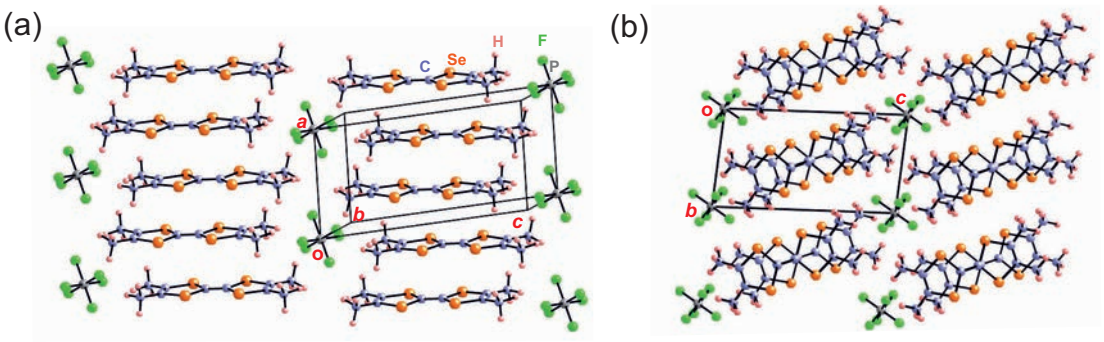

Figure 6.2: Crystal structure of the $(TMTSF)_2PF_6$ Bechgaard salt: (a) Quasi-planar organic molecules stack along the a axis and are separated along the c^* direction by PF_6^- anions. (b) Projection of the $(TMTSF)_2PF_6$ structure along the stack direction.

be reduced. This leads to a renormalized T_{CO} where there is a deconfinement transition from a 1D Luttinger liquid to a 2D or 3D Fermi Liquid [207]. However beyond this qualitative picture many important theoretical questions remain to be solved in order to quantitatively describe the deconfinement transition [208]. These considerations should particularly apply to organic conductors. For instance, in TTF-TCNQ(F-Q) NMR experiments lead to the estimation of $t_\perp \sim 5$ mev [200], sizeably smaller than $t^c_{QQ} \sim 17$ meV and $t^{a\pm c}_{QF} \sim 12$ meV according to DFT calculations [209]. Thus, the Peierls transition of TTF-TCNQ (T_Q= 52 K) occurs in the diffusive regime above $T_{CO} \sim 20$ K [200] so that the inter-chain coupling should be due to Coulomb interactions between charge density waves (CDW) located on different chains. In the present work we will consider in detail the situation in the Bechgaard salts.

The structure of a typical Bechgaard salt, $(TMTSF)_2PF_6$, is shown in Fig. 6.2 [210] where slightly dimerized zig-zag stacks of the TMTSF donor molecules run along the a direction. Organic stacks form (a,b) layers which delimitate cavities along c^* filled by monovalent (X^-) anions. According to the present DFT calculations the transfer integrals for the PF_6 salt at 300 K are $t_a \approx 210$ meV, $t_b^{eff} \approx 28$ meV and $t_{c*} \approx 0.8$ meV along the a, b and c^* directions, respectively. As expected from the crystal structure, these values imply a highly anisotropic system. The temperature-pressure (T-P) phase diagram of $(TMTSF)_2PF_6$ is shown in Fig. 6.1. At ambient pressure this salt exhibits a SDW insulating ground state below T_{SDW}

= 12 K. However, T_{SDW} significantly decreases under pressure. When the metallic state is restored above $\sim$ 9.5 kbar, $(TMTSF)_2PF_6$ becomes a superconductor at $T_S \approx 1.2$ K. In $(TMTSF)_2PF_6$ the 1D to 2D deconfinement temperature T_{CO} is measured to be around 100 K at ambient pressure from the change (from an activated behaviour to a metallic dependence) of the transverse electrical conductivity along c^* [211] and from the detection of a transverse plasma edge when an electric field is applied along b^* [202]. This crossover temperature sizeably increases under pressure (see Fig. 6.1). Note that the ambient pressure $T_{CO} \sim 100$ K compares nicely with our estimation of $\sim t_b^{eff}/\pi$. When pressurized, $(TMTSF)_2PF_6$ becomes metallic and as shown in Fig. 6.1 there is a lower 2D-3D temperature crossover estimated to occur around $t_c* \sim$ 3-5 K (see Fermi surface warping in App. C) obtained from DFT calculations with different 4 K crystal structures (this work). In contrast, the Fabre salt $(TMTTF)_2PF_6$ despite having quite similar transfer integrals ($t_a \approx 180$ meV, $t_b^{eff} \approx 24$ meV and $t_c^* \approx 0.5$ meV at 300K) exhibits a very different phase diagram whose main difference is the occurrence within the 1D electronic regime of a high temperature $4k_F$ hole localisation on the bonds of the donor zig-zag chains. This effect is due to the intra-stack Coulomb repulsions assisted by an enhanced interaction with the $4k_F$ potential of the anion sublattice (for a recent review see [177]). The charge localization, which is apparent from the occurrence of an activated intra-chain conductivity below $T_\rho \sim 230$ K [212], leads to a spin-charge decoupling. Due to the charge localization phenomenon T_{CO} is renormalized to 0 K [201].

Below T_{CO}, $(TMTSF)_2PF_6$ exhibits a SDW ground state at T_{SDW}= 12 K whose " $2k_F$" instability has been interpreted, due to the coincidence of the SDW critical wave vector measured by NMR [213, 214] with the best nesting vector of its warped FS [215], as resulting from a FS nesting process. However, since a closer inspection of the FS shows that there is a wide range of possible nesting vectors, in what follows we determine the best nesting condition by a direct calculation of the Lindhard response function using the DFT band structure of $(TMTSF)_2PF_6$. We will also study the thermal and wave vector dependence of this electron-hole

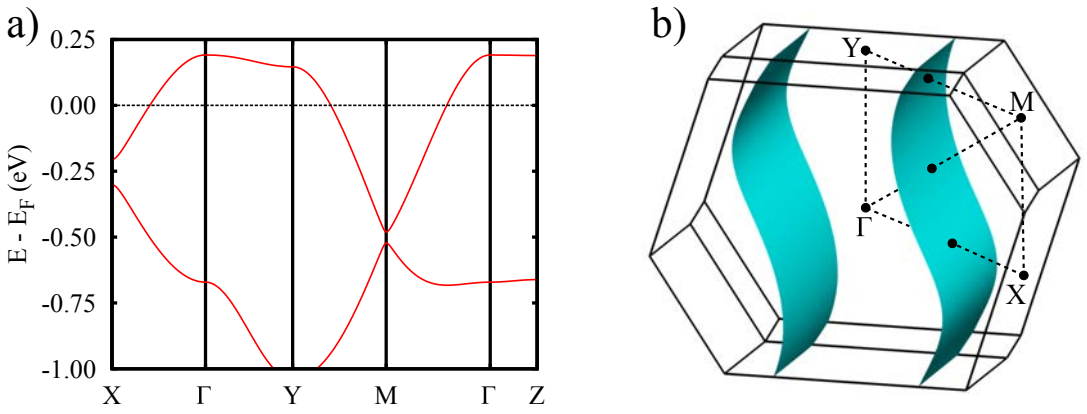

Figure 6.3: Calculated band structure (a) and Fermi surface (b) for $(TMTSF)_2PF_6$ using the 4 K crystal structure.The energy zero corresponds to the Fermi level. Γ = (0, 0, 0), X = (1/2, 0, 0), Y = (0, 1/2, 0), Z = (0, 0, 1/2) and M = (1/2, 1/2, 0) in units of the triclinic reciprocal lattice vectors.

response through the various crossover temperatures previously considered.

The Lindhard response function for two other salts, $(TMTSF)_2NO_3$ and $(TMTSF)_2ClO_4$, which exhibit a SDW ground state under different conditions will also be calculated and analyzed. $(TMTSF)_2NO_3$ exhibits a SDW ground state below T_{SDW}= 9 K after a (1/2, 0, 0) anion ordering (AO) transition occurring at $T_{AO} \approx$ 43 K, which is not believed to sizeably affect the nesting properties of the FS. $(TMTSF)_2ClO_4$ exhibits a SDW ground state below $T_{SDW} \approx$ 6.5 K when samples are quenched through the T_{AO}= 24 K (0, 1/2, 0) AO transition with the result that the absence of long range AO leaves intact the FS nesting properties. In complete contrast, when the (0, 1/2, 0) AO is fully achieved in the relaxed samples, the SDW ground state is replaced by superconductivity. This effect is interpreted as being due to the killing of the SDW instability by nesting breaking terms in the reconstructed FS caused by the onset of new AO periodicities in the system. Although the reconstructed FS due to AO in $(TMTSF)_2NO_3$ and $(TMTSF)_2ClO_4$ have been recently reported by some of us [216], we present here a more quantitative estimation of their nesting properties through the calculation of the Lindhard function in their respective AO ground states.

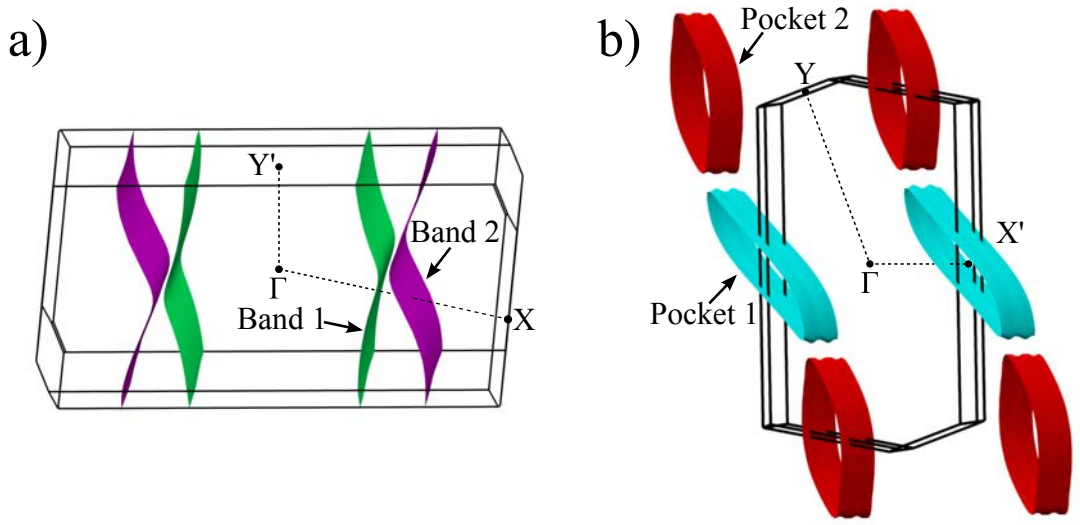

Figure 6.4: Calculated Fermi surface for: (a) $(TMTSF)_2ClO_4$ in the (0, 1/2, 0) AO phase , and (b) $(TMTSF)_2NO_3$ in the (1/2, 0, 0) AO phase. In (a) Y' refers to (0, 1/2, 0) in units of the triclinic reciprocal lattice vectors of the $a \times 2b \times c$ superlattice. In (b) X' refers to (1/2, 0, 0) in units of the triclinic reciprocal lattice vectors of the $2a \times b \times c$ superlattice.

6.2 Electronic Structure

The calculated band structure near the Fermi level for the 4 K crystal structure of $(TMTSF)_2PF_6$ is shown in Fig. 6.3a. The two bands are almost exclusively built from the HOMO of TMTSF and because of the stoichiometry they contain one hole so that the upper band is half-filled. The total dispersion of these bands is 1.23 eV and the dimerization gap at X is 96 meV. The two bands exhibit quite different dispersion along the b^* interchain direction, the upper one being considerably flatter. These features are very similar to previously reported band structures, both the first-principles and extended Hückel ones [217, 215, 218, 219]. Fitting the DFT results to the tight-binding model of Yamaji [220, 221] leads to the following values of the transfer integrals for the PF_6 salt at 300 K: $t_a \approx 210$ meV, $t_b^{eff} \approx 28$ meV and $t_{c^*} \approx 0.8$ meV along the a, b and c^* directions, respectively. Thermal contraction up to 4 K leads to increases of 23% and 33 % for t_a and t_b^{eff} and a decrease of 37% for t_{c^*}, respectively. For the same temperature range the variation is considerably smaller in the isostructural $(TMTTF)_2PF_6$ Fabre salt: 13% and 11% increase for t_a and t_b^{eff} respectively, and 5% decrease for t_{c^*}. In understanding

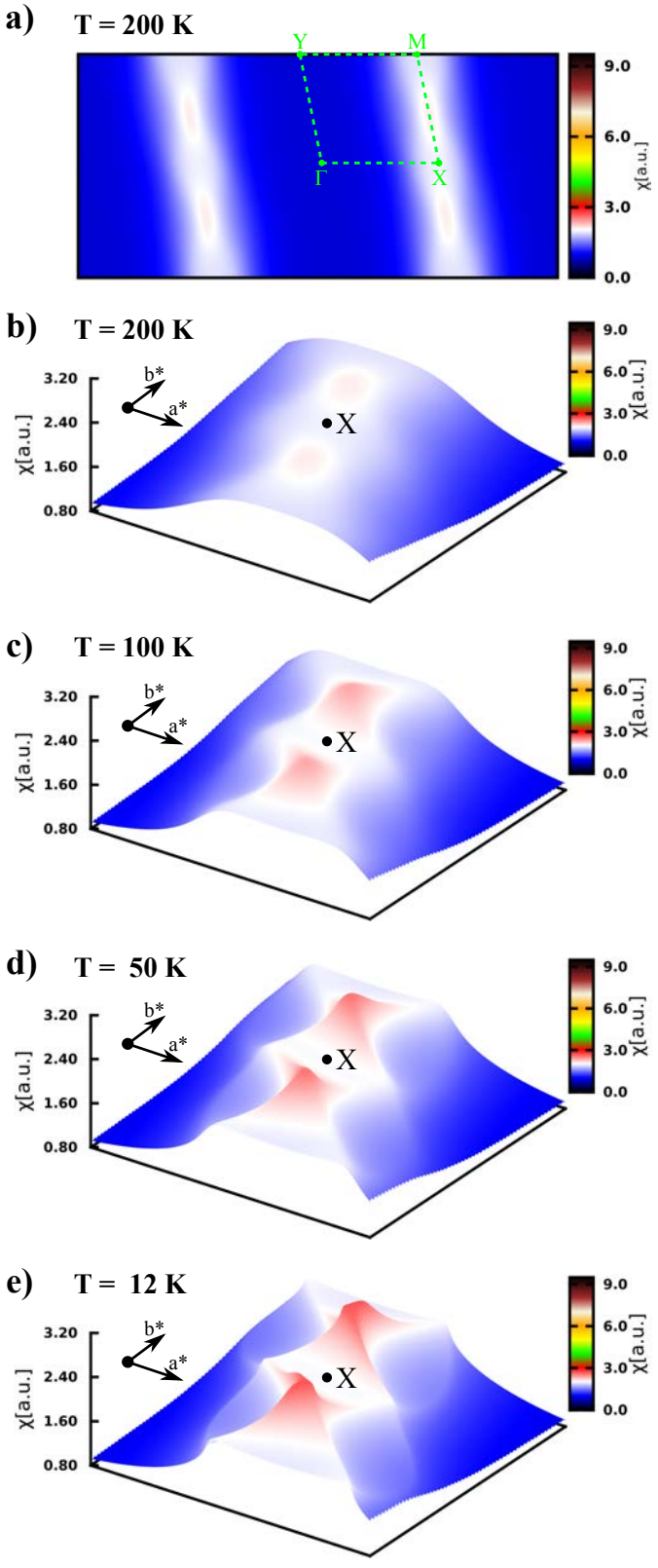

Figure 6.5: 2D (a) and 3D (b) plots of the Lindhard function of $(TMTSF)_2PF_6$ in the (a*,b*) reciprocal plane at 200 K. (c)-(e) 3D plots at 100 K, 50 K and T_{SDW} = 12 K, respectively.

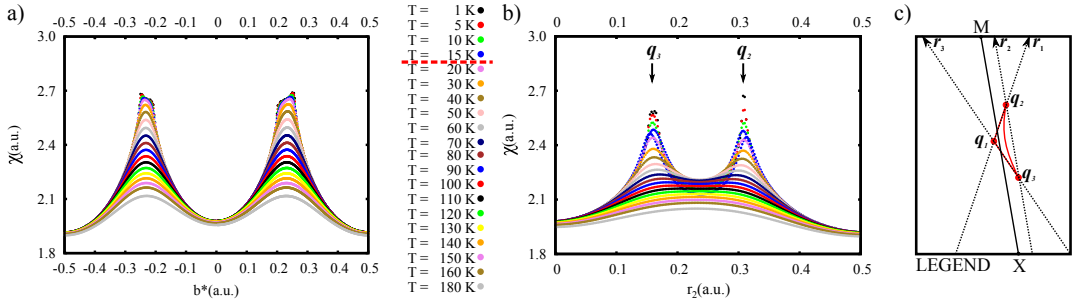

Figure 6.6: Thermal dependence of the transverse b^* scans across the Lindhard function of $(TMTSF)_2PF_6$ at $0.5a^*$ [i.e. $(0.5a^*, b^*)$ scans] (a) and transverse tilted q scans along the q_2-q_3 line defined in part (c). The red dashed line in the temperature scale indicates the temperature at which the single maximum leads to a tilted segment of maxima in (a). Note in (b) the progressive development of a double maxima below about 100 K. In c) we present a legend for the scans directions where $\vec{r}_2 = -(1 + \tan(|\vec{q}_3 - \vec{q}_2|))a^* + b^*$. Positive values are designated for q points above the Γ-X direction.

the T-P phase diagram of the Bechgaard salts an important parameter is the so-called unnesting (or nesting breaking) parameter [221, 220, 222],

$$t'_b = \frac{1}{2\sqrt{2}} \frac{t_b^2}{t_a} \tag{6.1}$$

which measures how much the actual FS differs from the perfect nesting condition within Yamaji's tight-binding model. For $(TMTSF)_2PF_6$ t'_b is estimated from the above transfer integrals to be -21.7 K, which compares well with the value estimated ($4t'_b \sim 75$ K), from the difference between the direct optical (100 K [223]) and indirect thermal (25-30 K [200]) SDW gaps. As mentioned above, the present calculations also provide an excellent estimation of the T_{CO} crossover temperature for $(TMTSF)_2PF_6$. Elsewhere we have discussed in detail the evolution of the transfer integrals of the $(TMTSF)_2ClO_4$ and $(TMTSF)_2NO_3$ salts with temperature and pressure based on DFT calculations [216]. The calculated anion ordering gap and the SDW transverse component for both salts were shown to be in very good agreement with experimental results. We thus conclude that DFT seems to provide a reasonable description of the main interactions influencing the electronic structure of these Bechgaard salts.

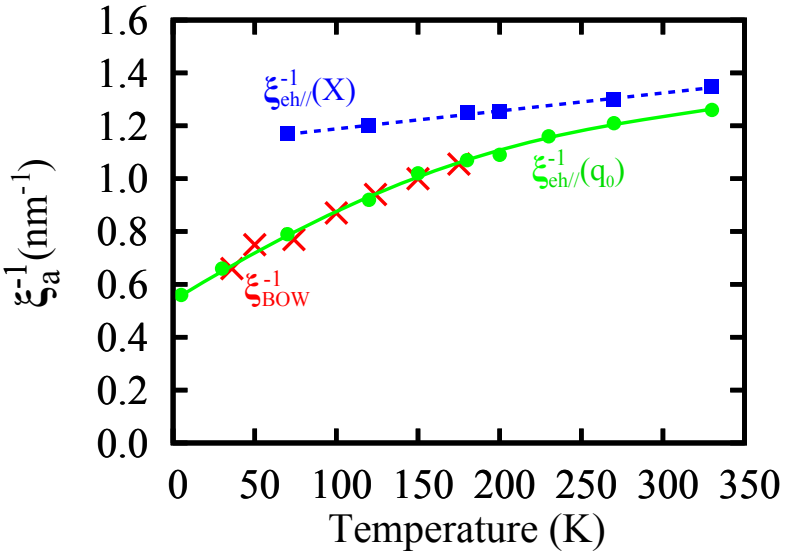

Figure 6.7: Comparison of the thermal dependence of the inverse electron-hole coherence length $\xi^{-1}_{eh\|}$ calculated at the q_0 and X points with the BOW correlation length ξ^{-1}_{BOW} of $(TMTSF)_2PF_6$ measured in ref. [224].

The calculated FS for $(TMTSF)_2PF_6$ at 4 K is shown in Fig. 6.3b. The shape of this FS is common to all Bechgaard salts which only differ in subtle details of the warping. However such subtle differences have strong consequences for their low temperature behaviour since, as discussed in Sect. 6.3 on the basis of the calculated Lindhard function, such warping influences the FS nesting vector. The two salts $(TMTSF)_2ClO_4$ and $(TMTSF)_2NO_3$ with non-centrosymmetrical anions exhibit however an AO transition doubling the periodicity of the cell along different directions, i.e. b for the first but a for the second. Consequently their appropriate FSs below the AO transition essentially result from the folding and hybridization of a FS like that of Fig. 6.3b. Since the folding occurs along different crystallographic directions the calculated DFT Fermi surfaces exhibit different shapes (see Fig. 6.4). The DFT AO gaps (Δ_0) are calculated to be 14 and 8.9 meV for $(TMTSF)_2ClO_4$ and $(TMTSF)_2NO_3$, respectively. The different directions of the AO leads to the development of AO gaps at different zones of the original FS, a feature that has important consequences for the physical behavior of these salts below T_{AO}. For instance, the FS after AO for $(TMTSF)_2ClO_4$ is made of a series of warped planes separated by small AO gaps (Fig. 6.4a) which develop at the regions of the original FS with better nesting. In contrast, for $(TMTSF)_2NO_3$ after AO the FS is made of a series of elongated cylinders (Fig. 6.4b) such that

the AO gaps develop at regions of the original FS where the nesting is not very good so that the AO exerts a considerably smaller influence on the nature of the SDW of this salt.

6.3 Analysis of the Lindhard function

In this section we will first study the temperature and wave vector dependencies of the Lindhard function calculated for the high-temperature metallic phase of the Bechgaard salts $(TMTSF)_2X$ with X = PF_6, ClO_4 and NO_3. Later on we will consider the response for the ClO_4^- and NO_3^- salts in their AO phase, i.e. below T_{AO} = 41 K for the (1/2, 0, 0) AO phase of $(TMTSF)_2NO_3$ [225] and below T_{AO} = 24 K for the (0, 1/2, 0) AO phase of $(TMTSF)_2ClO_4$ [226].

6.3.1 $(TMTSF)_2PF_6$

Shown in Fig. 6.5 are the intensity plots of the Lindhard function for $(TMTSF)_2PF_6$ in the (a^*, b^*) reciprocal plane calculated at 200 K, 100 K, 50 K and 12 K (T_{SDW}). Let us note that the Lindhard response does not vary with the interlayer c^* wave vector component. At 200 K (Fig. 6.5a) there is a broad response centered at around q_{1D} = 0.5 a^* in the chain direction, which corresponds to the $2k_F$ wave number of the quasi-1D electron gas. This response, which is slightly modulated along b^* exhibits a broad maximum at $\sim$ 0.23 b^* (Fig. 6.5a).

Upon cooling the modulation of the Lindhard response along b^* increases. Fig. 6.6a shows that the intensity of the broad maximum at q_0 = (0.5, 0.23) increases. When T decreases the shape of the Lindhard response becomes sinusoidally modulated along a^* (Fig. 6.5b). As a consequence, the response along a^* becomes broader at the X (0.5, 0) and M points (0.5, 0.5) than in-between, near q_0 (0.5, 0.25). This is quantitatively illustrated in Fig. 6.7 by the thermal dependence of the intra-chain inverse electron-hole coherence length $\xi_{eh\|}^{-1}$, measured by the half-width at half-maximum (HWHM) of the response along a^* at the X and q_0 points. These

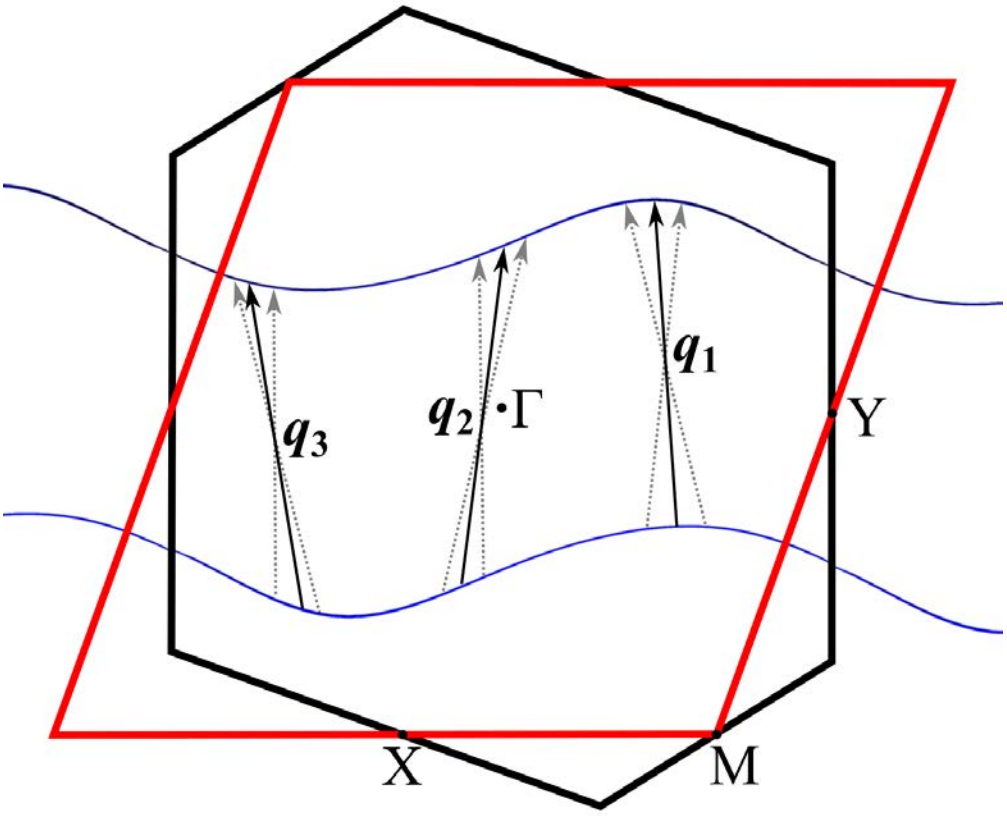

Figure 6.8: Schematic illustration of the three nesting vectors at the origin of the arcs of the Lindhard function.

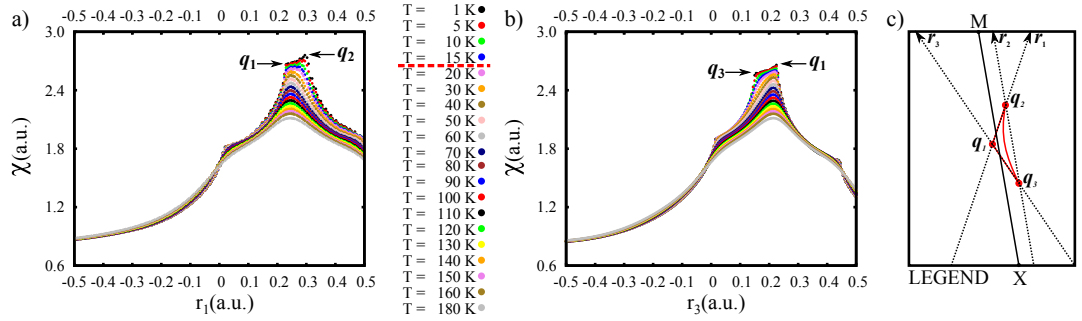

Figure 6.9: Thermal dependence of the scans across q_1-q_2(a) and q_3-q_1(b) lines of the Lindhard function for $(TMTSF)_2PF_6$. Note the tilted plateau which continuously develops upon cooling. The red dashed line in the temperature scale indicates the temperature at which the single maximum leads to a tilted segment of maxima. The kinks observed for q_1-$q_2 \sim 0$ and q_3-$q_1 \sim 0$ and 0.4 correspond to the crossing of singularity lines mentioned in the text which separate the light blue to dark blue regions in Fig. 6.10b. In c) we present a legend for the scans directions where $\vec{r}_1 = (1-\tan(|\vec{q}_1 - \vec{q}_2|))a^* + b^*$, respectively $\vec{r}_3 = -(1+\tan(|\vec{q}_3 - \vec{q}_2|))a^* + b^*$. Positive values are designated for q points above the Γ-X direction.

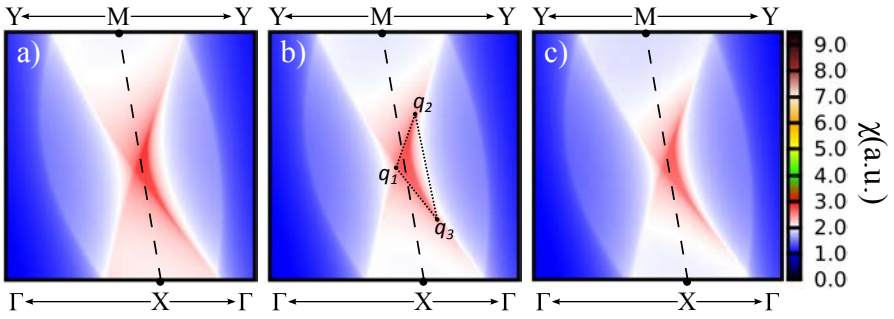

Figure 6.10: Magnified section of the Lindhard functions at 5 K for 98% deuterated $(TMTSF)_2PF_6$-D_{12} at P_{atm} (a), protonated $(TMTSF)_2PF_6$-H_{12} at P_{atm} (b), and 7 kbar pressure (c). The X→ Γ and M→Y arrows are only used to indicate the associate directions. In (b) the q_1, q_2 and q_3 points used in the text are labelled.

quantities slightly decrease upon cooling, but do not vanish. This effect is due to the onset of FS nesting breaking terms which prevent the divergence of the electron-hole response (see below). Note also that the HWHM of the q dependence of the Lindhard function along b^* (Fig. 6.6a) gives an inter-stack transverse electronic length $\xi_{eh\perp}$ of the order of b which means that there is no sizable inter-chain coupling, so that one can consider the electron-hole divergence as being essentially 1D. However, this picture remains only valid until about 100 K because below this temperature the shape of the Lindhard function is modified.

Fig. 6.5d shows a 3D plot of the intensity of the Lindhard function at 50 K, where arcs of intensity maxima can be clearly distinguished. The formation of arcs is revealed by a transverse scan slightly off the $0.5a^*$ wave vector. In the scans shown in Fig. 6.6b crossing the extremities of the arc, i.e. between q_2 and q_3 defined in Fig. 6.10c, one clearly observes the passage for a temperature about 90 K from a high temperature broad maximum at 0.23 b^* toward two stronger and narrower maxima around ∼ 0.30 b^* and ∼ 0.14 b^* for lower temperatures. Also below 100 K the q_0 maximum progressively shifts to q_1= (0.48, 0.23). The origin of these arcs can be understood on the basis of a plot of the (a^*, b^*) section of the FS for a triclinic lattice. As schematically illustrated in Fig. 6.8 which is based on our calculations for the $(TMTSF)_2PF_6$, three different nesting processes are possible. Those associated with q_2 and q_3 nest the zones around the inflection points of the warped lines. Because of the triclinic geometry q_2 and q_3 are different and

since these zones around the inflection points are relatively flat they both lead to a linear segment with high values of the Lindhard function with opposite slope (and varying intensity). The crossing point of these two linear fragments corresponds to the third nesting process, q_1. Since none of these nestings is perfect so that different small pockets are left in any of the three nesting processes, the Lindhard response intensity can vary with temperature.

Upon further cooling, the b^* scan of Fig. 6.6a shows that in fact a tilted segment of maxima develops at low temperature. More precisely, the 3D plot of the intensity of the Lindhard function at T_{SDW}= 12 K (Fig. 6.5) reveals the presence of a tilted triangular plateau of maxima. This plateau which has more likely the shape of a boomerang is limited by the q_1-q_2 and q_1-q_3 segments and the q_2-q_3 arc previously described, and whose peak coordinates, as indicated in Fig. 6.10b, are q_1 = (0.48, 0.23), close to q_0, q_2 = (0.52, 0.30) and q_3 = (0.53, 0.14). Fig. 6.9 shows more precisely by means of q_1-q_2 and q_1-q_3 scans that the plateau develops slightly above T_{SDW} around $\sim$ 15-20 K. Fig. 6.6b shows that the q_2 and q_3 peak intensities grow sharply upon cooling and Fig. 6.9 shows that concurrently with this growth a continuum of intensity develops with the q_1 peak. At low temperature the absolute maximum of the Lindhard response is not located at $q_1 \approx q_0$, as expected from the temperature extrapolation of the high temperature data, but at q_2 which exhibits the strongest low temperature divergence (Fig. 6.9). However at T_{SDW}= 12 K the q_1 and q_2 responses are of similar intensity. This triangular shaped maxima of the Lindhard function was first predicted for an electronic dispersion in the presence of a single nesting breaking term t'_b for an orthorhombic lattice [227]. It has also been recently calculated in ref. [228] for a triclinic lattice with several nesting breaking terms more relevant to describe the case of the Bechgaard salts. Finally, note that the low temperature plateau is delimited by several sinusoidal lines of singularities calculated in ref.[229] which are visible in Figs. 6.5d and e and Fig. 6.10. Along these lines there is a continuous sliding of the two sheets of the FS on onto another. Note that q_1, q_2 and q_3 belong to these sinusoidal lines.

An unexpected result of our study is provided by the low temperature calculation of the Lindhard response in $(TMTSF)_2PF_6$-H_{12} under a pressure of 7 kbar (where there is a strong reduction of T_{SDW} to $\sim$ 4 K and the onset of coexistence between the SDW modulation and the superconductivity [230]) and in 98 % deuterated $(TMTSF)_2PF_6$-D_{12} (corresponding to a *negative* pressure of 5 kbar with respect to $(TMTSF)_2PF_6$-H_{12} at atmospheric pressure, P_{atm}, [231]). Fig. 6.10 compares the section of the Lindhard function at 5 K for these two salts (Figs. 6.10c and a, respectively) as well as for $(TMTSF)_2PF_6$-H_{12} at P_{atm} (Fig. 6.10b). It is clear that the shape of the triangular maximum of the Lindhard function is not changing appreciably when the effective pressure increases (from (Fig. 6.10a to b and c).

6.3.2 $(TMTSF)_2NO_3$ in the absence of AO transition

The shape of the Lindhard function for $(TMTSF)_2NO_3$ bears a resemblance with that of $(TMTSF)_2PF_6$. Fig. 6.11a shows the 3D plot of the Lindhard function at 120 K. $2k_F$ scans along b^* show the existence of a broad maximum for q_0 = (0.5, 0.27) which grows in intensity when temperature decreases (Fig. 6.12). This maximum is slightly shifted with respect to that of $(TMTSF)_2PF_6$.

The shape of the maximum changes into arcs below $\sim$ 70 K. Fig. 6.11b reports the 3D plot of the Lindhard function at 40 K, close to the (1/2, 0, 0) AO critical temperature (T_{AO} = 41 K) of the $(TMTSF)_2NO_3$ salt [225]. It is interesting to remark that the AO critical wave vector corresponds to the X point of the Brillouin zone where the Lindhard function exhibits a minimum (Fig. 6.12). In consequence, the response of the organic salt to the (1/2, 0, 0) AO potential should be weak. Thus, one does not expect a strong $2k_F$ stack distortion below T_{AO} = 41 K, which agrees with the structural refinement of the AO superstructure [232].

Upon fast cooling the AO superstructure does not develop at T_{AO} for kinetic reasons [232]. In that case the appropriate plot of the Lindhard function is that of

Fig. 6.11e. As for $(TMTSF)_2PF_6$ a triangular shaped maximum of the Lindhard function also appears between 15 and 20 K although for slightly different q_i values: $q_1 = q_0 = (0.50, 0.27)$, $q_2 = (0.52, 0.29)$ (strongest maximum) and $q_3 = (0.52, 0.24)$. However, upon further cooling the triangular plateau is subtly modified. The calculated Lindhard function at 1 K is shown in Fig. 6.13a. Although at first sight it may look almost unchanged with respect to that at 40 K this is not so. As shown in Fig. 6.13b where we plot the overlap of two sections of the Lindhard function, those for the q_{c*} components of 0.0 and 0.5, in the region of q_3 there are two well separated contributions marked with white arrows. The inner of these contributions corresponds to the plane with $q_{c*}= 0.$ and the outer, which is more elongated, to that with $q_{c*}= 0.5$. In the region around q_2 the two contributions remain on top of each other. These changes originate from the 3D interactions, i.e. the weak warping of the FS along c^* in the region leading to the triangles. This warping varies along the FS and is non-negligible for quenched $(TMTSF)_2NO_3$ in the regions leading to the q_3 nesting but much less in the regions leading to the q_2 nesting. The result is that the region of the triangular plateau around q_3 is spread along the direction of the initial linear component of the arc whereas that around q_2 does not. Consequently, the triangular plateau spreads somewhat in this direction and becomes more inclined. Thus, the prevalence of q_2 at low temperatures is enhanced by the interlayer interactions. This effect starts to be visible in our calculations around 12-15 K. Of course, in the full calculation of the Lindhard function of Fig. 6.13a these effects are not easy to see because the effect of the interlayer interactions is smmoth. This feature was not accounted for in the model study of refs. [229, 228] because 3D effects were neglected. Interestingly, we do not find this feature in our calculations for $(TMTSF)_2PF_6$. In that case the warping of the FS affecting the region of the triangles is around three times smaller than in quenched $(TMTSF)_2NO_3$ so that the effect becomes practically undetectable and the triangular plateau is not affected by the interlayer interactions.

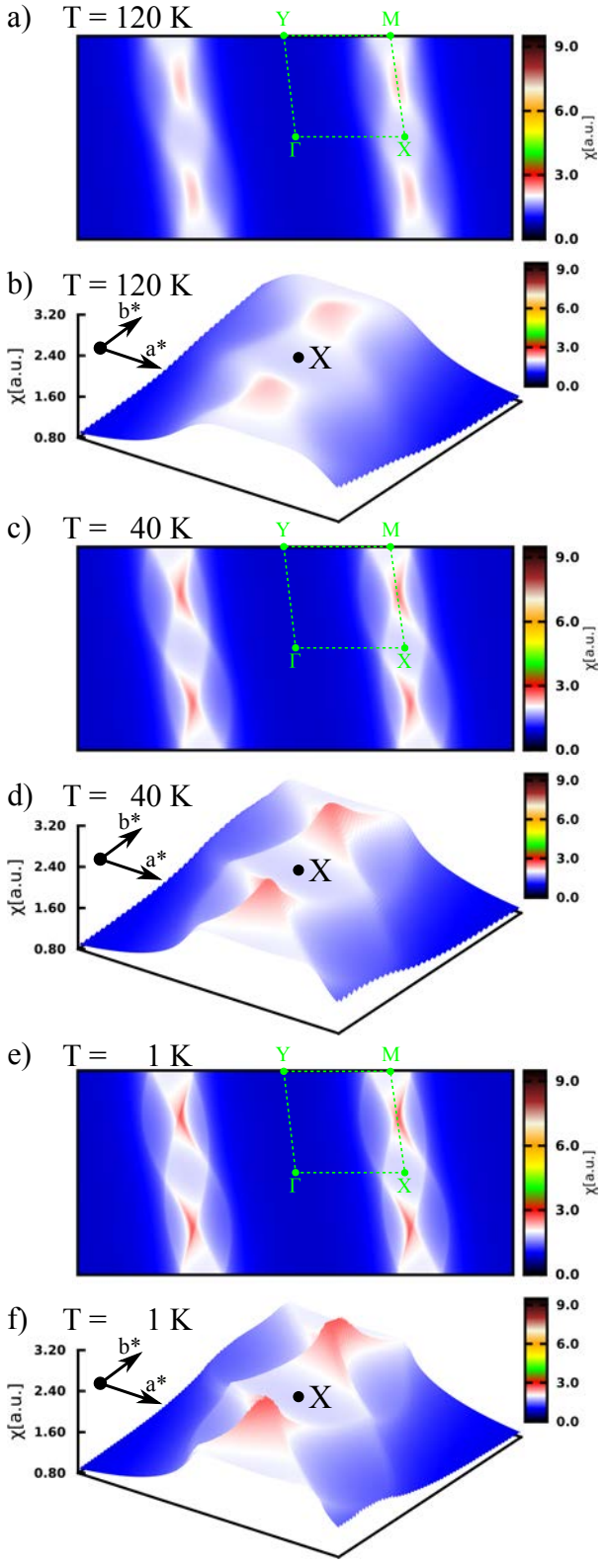

Figure 6.11: 2D plot of the Lindhard function of $(TMTSF)_2NO_3$ in the (a^*,b^*) reciprocal plane at 120 K (a), 40 K (c) and 1 K (e). 3D sections of the Lindhard function of $(TMTSF)_2NO_3$ around the X-M direction at 120 K (b), 40 K (d) and 1 K (f).

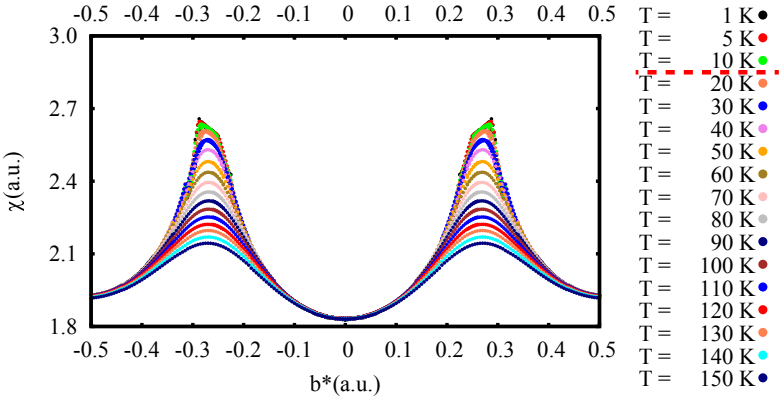

Figure 6.12: Thermal dependence of the transverse b^* scans across the Lindhard function of $(TMTSF)_2NO_3$ at 0.5 a^*. The red dashed line in the temperature scale indicates the temperature at which the single maximum leads to a tilted segment of maxima.

6.3.3 $(TMTSF)_2ClO_4$ in the absence of AO transition

The Lindhard function of $(TMTSF)_2ClO_4$ slightly differs from that of $(TMTSF)_2PF_6$. Figs. 6.14a and b show this response at 200 K. It exhibits a broad maximum around the X point. This is well illustrated by the b^* transverse scan for $2k_F = 0.5a^*$ (Figs. 6.15). This figure shows that the broad maximum splits into two sharper maxima at $q_0 = (0.5, \pm 0.14)$ around 130 K. Around 100 K the maxima become an arc as previously found for the $(TMTSF)_2PF_6$ and $(TMTSF)_2NO_3$ salts. Figs. 6.14c and d show plots of the Lindhard function at 50 K. The minimum of response remains at the M point for all the temperature range. Fig. 6.14 shows that the Lindhard function is more sinusoidally modulated along b^* in $(TMTSF)_2ClO_4$ than in $(TMTSF)_2PF_6$ (compare also Figs. 6.17 and 6.7). The HWHM of the Lindhard function along a^* gives the inverse electron-hole coherence length $\xi^{-1}_{eh\|}$. The calculated values at the X and q_0 points (see Fig. 6.17) weakly decrease upon cooling from ~ 0.1 Å^{-1} at 200 K to ~ 0.07 Å^{-1} at 15 K. These values are comparable to those found for $\xi^{-1}_{eh\|}$ in $(TMTSF)_2PF_6$ (Fig. 6.7), but are much smaller than $\xi^{-1}_{eh\|} \sim 0.14$ Å^{-1} measured at the M point.

For quenched samples preventing the establishment of the (0, 1/2, 0) AO superstructure, a triangular plateau begins to form below about 20-30 K (see Fig. 6.15) which is close to T_{AO}. This is clearly illustrated in Fig. 6.16a showing a 2D plot of

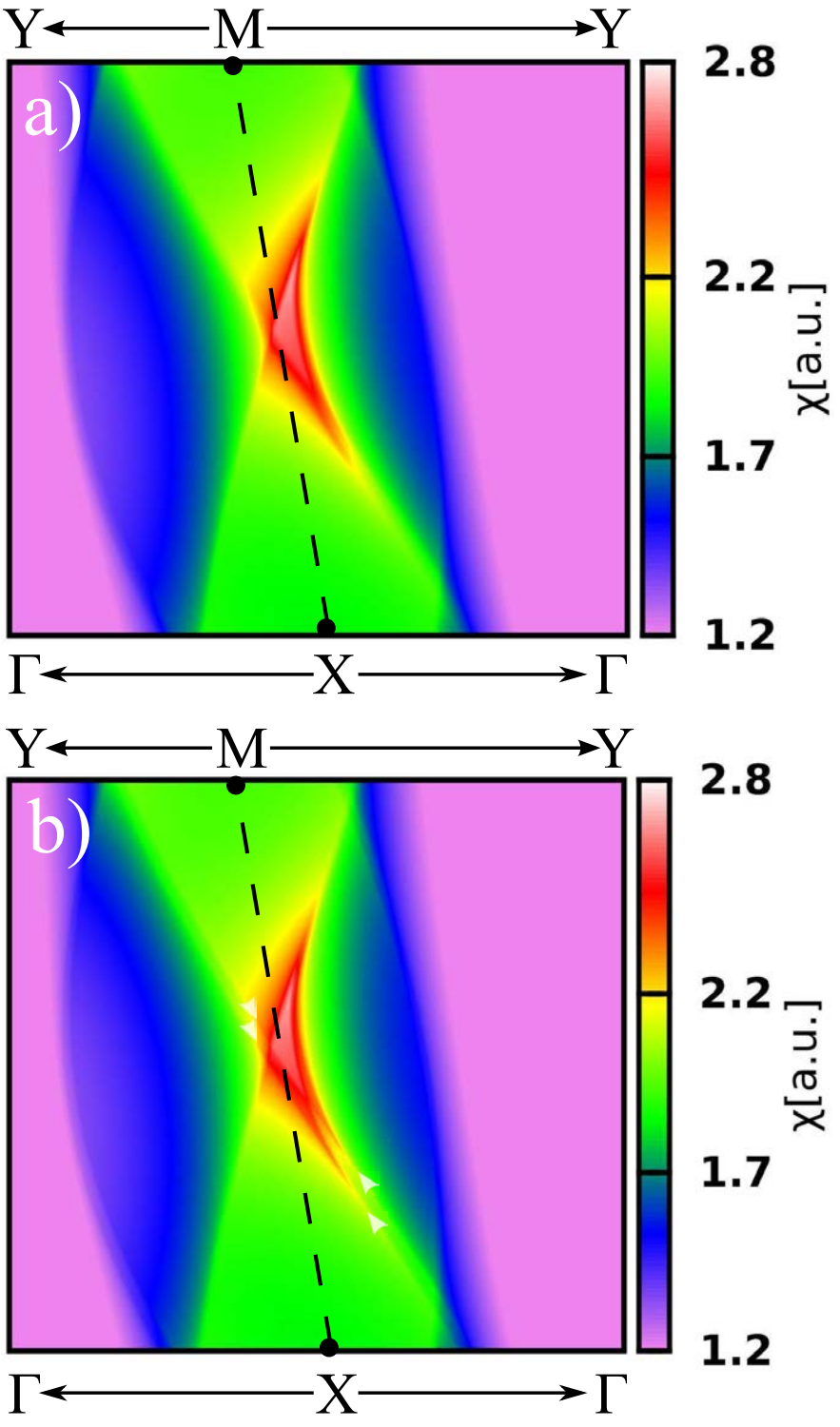

Figure 6.13: Magnified section of the Lindhard function for $(TMTSF)_2NO_3$ without AO at 1 K (a). Overlap of the Lindhard response function sections calculated at planes parallel with (a^*,b^*) for $q_{c^*}= 0$ and $q_{c^*}= 0.5$ at 1 K in the non-ordered phase (b) of $(TMTSF)_2NO_3$. Note the white arrows indicating the effect of 3D interactions.

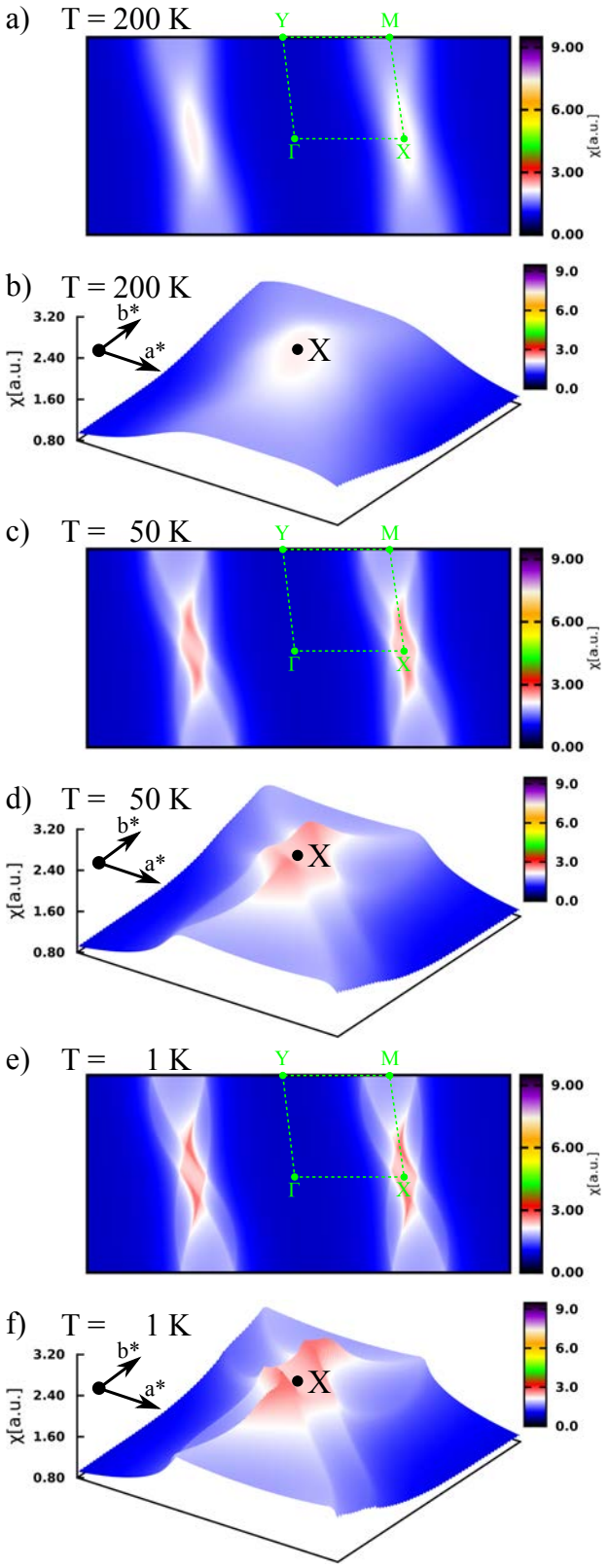

Figure 6.14: 2D plot of the Lindhard function of $(TMTSF)_2ClO_4$ in the (a^*,b^*) reciprocal plane at 200 K (a), 50 K (c) and 1 K (e). 3D sections of the Lindhard function of $(TMTSF)_2ClO_4$ around the X-M direction at 200 K (b), 50 K (d) and 1 K (f).

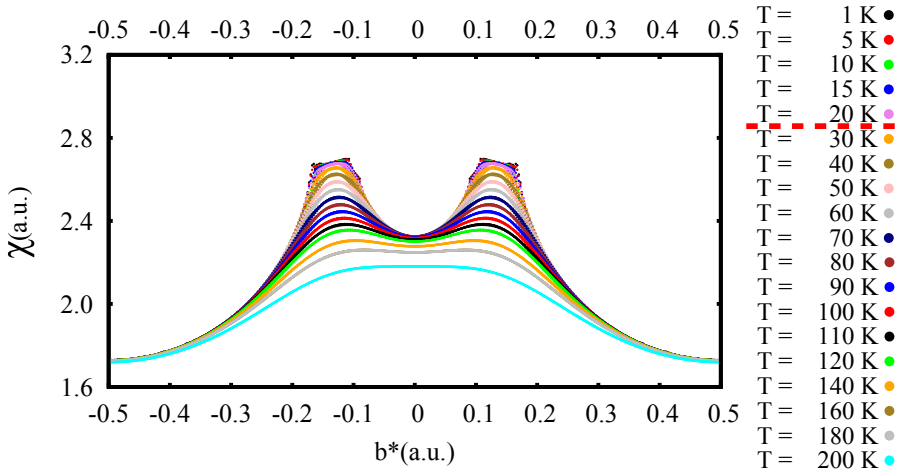

Figure 6.15: Thermal dependence of the transverse b^* scans across the Lindhard function of $(TMTSF)_2ClO_4$ at 0.5 a^*.

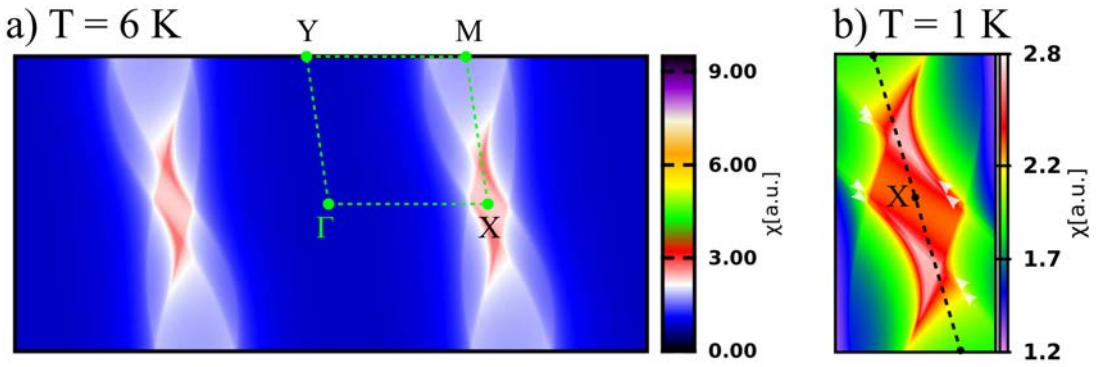

Figure 6.16: Section of the Lindhard function in quenched $(TMTSF)_2ClO_4$ in the (a^*,b^*) reciprocal space plane at T_{SDW} = 6 K (a). Overlap of the Lindhard response function sections calculated at planes parallel with (a^*,b^*) for q_{c^*}= 0 and q_{c^*}= 0.5 at 1 K (b).

the Lindhard function at 6 K. The plateau is spanned between maxima located in $q_1 = q_0 = (0.5, 0.14)$, $q_2 = (0.56, 0.21)$ and $q_3 = (0.57, 0.07)$ (strongest maximum). Note that the 1 K Lindhard function also exhibits the 3D features discussed for $(TMTSF)_2NO_3$ (see Fig. 6.16b) although slightly weaker. The warping of the FS in the region of the triangles is found to be in between that of $(TMTSF)_2NO_3$, for which the effect was clearly visible, and that of $(TMTSF)_2PF_6$, for which we could not detect it.

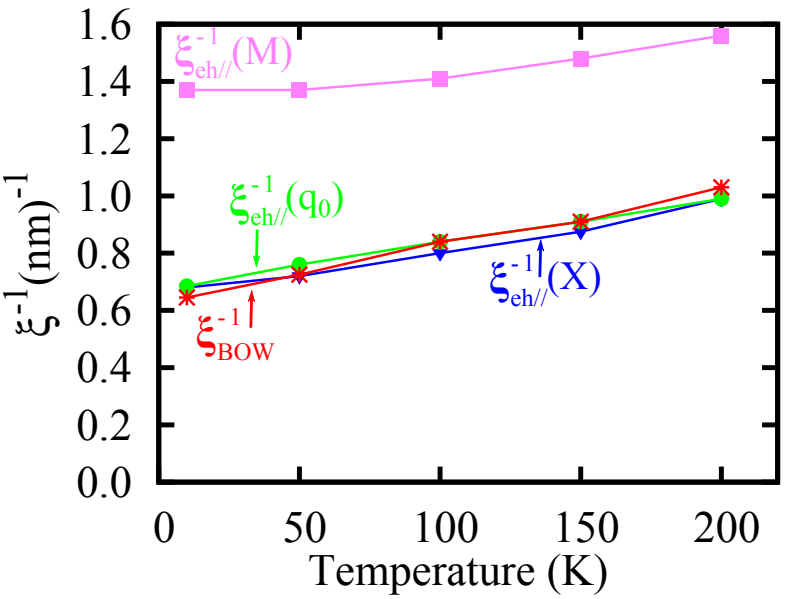

Figure 6.17: Comparison of the thermal dependence of the inverse electron-hole coherence length $\xi^{-1}_{eh\|}$ calculated at the q_0, X and M points with the BOW correlation length ξ^{-1}_{BOW} of $(TMTSF)_2ClO_4$ obtained from the data in ref. [233]

6.3.4 $(TMTSF)_2NO_3$ in the AO phase

At the (1/2, 0, 0) AO transition, the electronic structure of $(TMTSF)_2NO_3$ is modified. Such structural transition is accompanied by a metal to semi-metal transition with the formation of an electron pocket (red pocket in Fig. 6.4b) and a hole pocket (blue pocket in Fig. 6.4b) per unit cell [216]. As a consequence, the Lindhard response function must change. However, since the stack modulation is quite weak the Lindhard function of the semi-metallic phase (Figs. 6.18a and b) bears some resemblance with that of the metallic phase (Fig. 6.11). In Fig. 6.18c to e the total Lindhard response is decomposed into the inter-pocket and two intra-pocket components. Only the inter-pocket component (a 3D plot is also shown in Fig. 6.19) exhibits a strong response under the form of an intensity modulated warped line at $q_{1D} = 0a'^*$ (note that the AO unit cell with a doubling of the a parameter is used here so that $a'^* \approx a^*/2$). In contrast with the Lindhard response in the absence of AO, the maximum in the triangular plateau has been transformed into a sharp maximum at (0.01, 0.29) which wave vector is close to q_1 of the metallic phase. Because of the folding and gap opening as a result of the AO there is a further thickening of the walls of the triangular plateau.

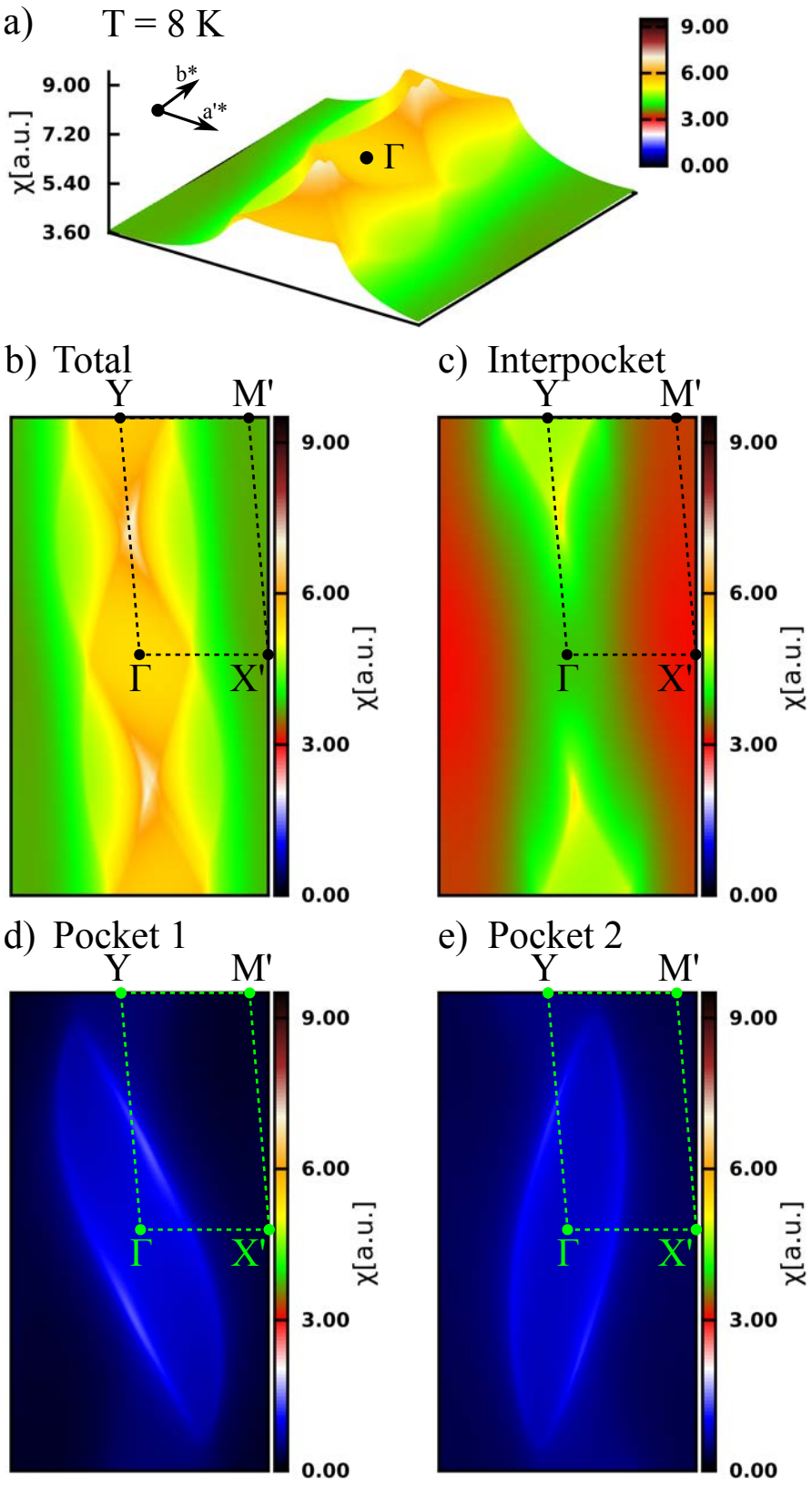

Figure 6.18: 3D plot of the Lindhard response of $(TMTSF)_2NO_3$ in its AO phase at 8 K (=T_{SDW}) (a). 2D plots of the decomposition of this Lindhard function (b) into its interpocket (c), pocket 1 (d) and pocket 2 (e) components. See Fig. 6.4b.

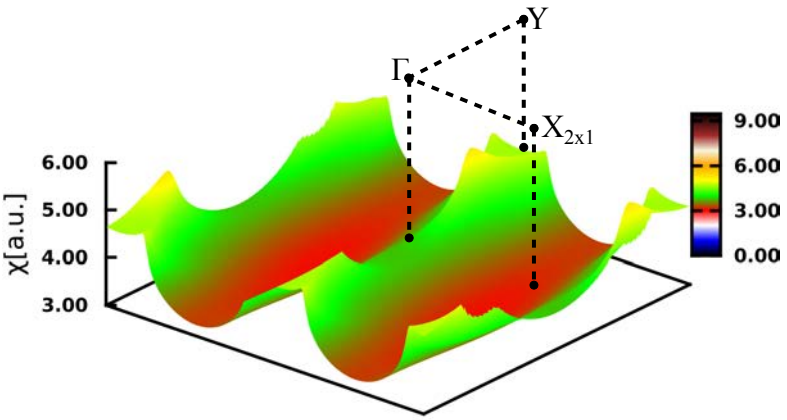

Figure 6.19: 3D plot of the inter-pocket Lindhard function of $(TMTSF)_2NO_3$ in its AO phase at 8 K (=T_{SDW}). The maximum response occurs at (0.01,0.29)

Note that there is accumulating evidence that the (1/2, 0, 0) AO superstructure changes into a (0,1/2, ?) one by application of $\sim 7.5 \pm 1$ Kbar in $(TMTSF)_2NO_3$ [234]. In which case the Lindhard function should drastically change under pressure. If the (0, 1/2, 0) AO superstructure is stabilized, one should expect the formation of two non-equivalent donor stacks along b. By analogy with the results obtained in the AO phase of $(TMTSF)_2ClO_4$ (see Sect. 6.3.5), one should also expect the occurrence of a quasi-1D Lindhard response. If the (0, 1/2, 1/2) AO superstructure is stabilized as in pressurized $(TMTSF)_2ReO_4$ [235], all the donor stacks must remain equivalent and the Lindhard function should be different from those considered in the present work. Magnetotransport measurements performed in pressurized $(TMTSF)_2NO_3$ suggest the occurrence of a quasi-1D FS. [234].

6.3.5 $(TMTSF)_2ClO_4$ in the AO phase

At the (0, 1/2,0) AO transition the electronic structure of $(TMTSF)_2ClO_4$ is modified. There are two differently modulated donor stacks per unit cell and an anion gap opens at the zone boundary [216]. Fig. 6.20 shows that the Lindhard function is considerably modified. The 3D (a) and 2D (b) plots show that this response is more similar to that of a 1D system with a broad line of maxima for $q_{1D} = 0.5a^*$. Along this line two broad maxima leading to an arc can be distinguished around $\pm$

$0.3b^*$. This Lindhard response does not look like that modelled in ref. [228] where only the anion gap has been considered. Since the major modification induced by the AO concerns the electronic structure of the stack, the Lindhard function is modified via the introduction of new nesting processes between the two quasi-1D bands of the unit cell. This is quantitatively illustrated by parts (b) to (e) of Fig. 6.20 where a decomposition of the total Lindhard function into two intra-band and one inter-band components is shown. The intra-band components of the response are the typical ones for a nesting process between warped FSs. The best nesting conditions within the same set of bands give rise to broad maxima with the shape of arcs. However these arcs of maximum intensity are located at quite different position in the Brillouin zone; namely around (0.6, 0.5) and (0.4, 0.3) for the two types of bands in the (a^*, b'^*) reciprocal plane (note that the AO unit cell with a doubling of the b parameter is used here so that $b'^* \approx b^*/2$). It is the inter-band nesting process which exhibits the strongest response under the form of a $q_{1D}= 0.5a^*$ line of maxima resembling that of the Lindhard response of a 1D system such as the blue bronze [42]. This response can be fitted along b^* by two broad Lorentzians centered at +/- $0.29b'^*$. This maximum is completely different from that exhibited by the Lindhard function in the non AO phase (see Fig. 6.16). The HWHM of the inter-band response along a^* and b'^* leads to electron-hole correlation lengths of 17 Å and 9 Å along a and b respectively. Finally note that the inter-band response does not vary with temperature between 24 K (T_{AO}) and 1K.

6.4 Discussion

6.4.1 Electronic dimensional crossover and detailed structure of the Fermi surface

The main result of the present investigation is the finding of a Lindhard response with a shape varying substantially with temperature. Such variation should be

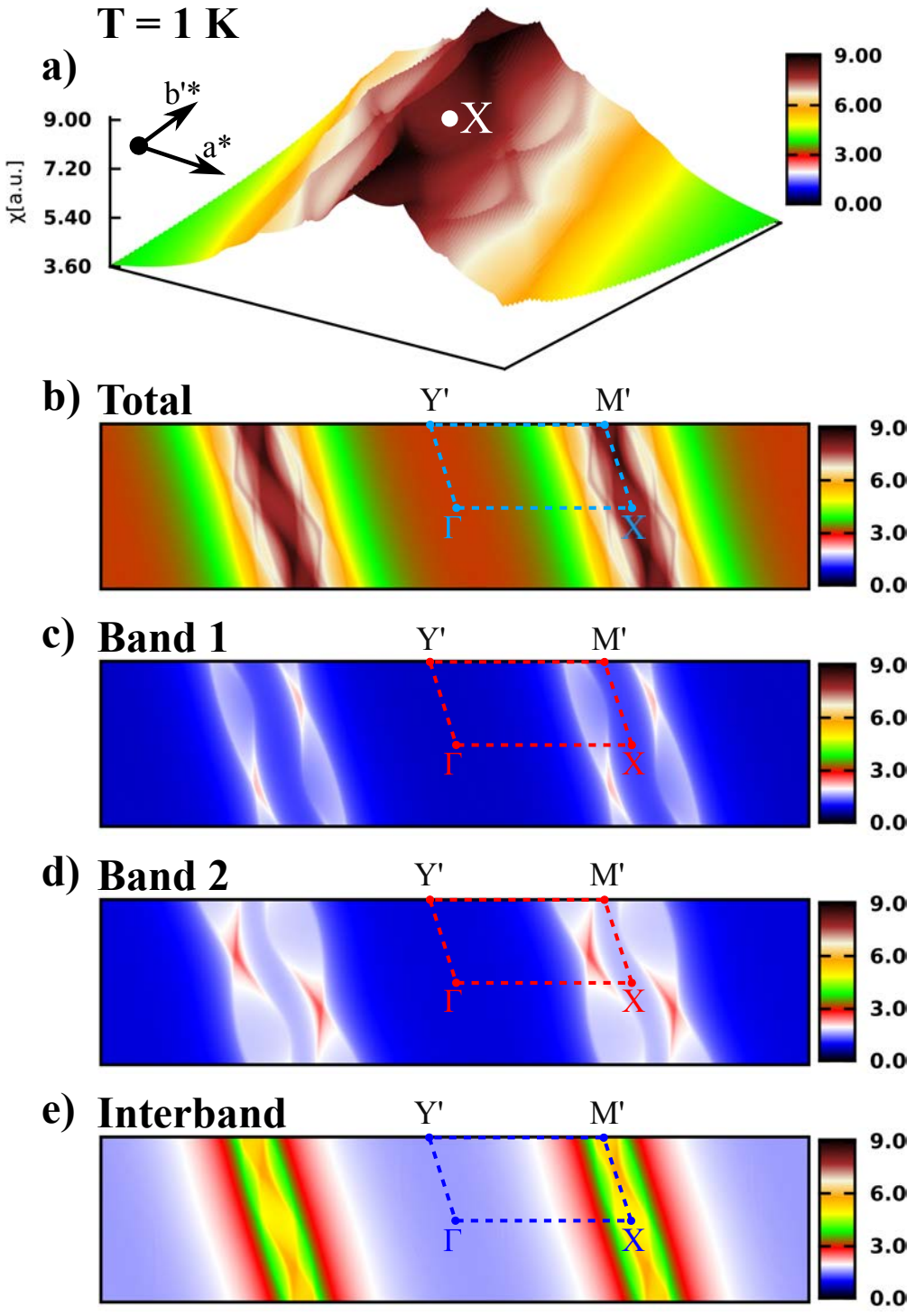

Figure 6.20: 3D plot of the Lindhard function of the $(TMTSF)_2ClO_4$ in its AO phase at 1 K ($\sim T_S$) (a). 2D plots of the decomposition of this Lindhard function (b) into the first band (c), second band (d) and interband (e) contributions.

associated with a change of dimensionality of the electron gas located on the donor stacks. At high temperature (i.e. above 100 K) the Lindhard function shows a line maximum at $q_{1D} = 0.5a^*$ which corresponds to the $2k_F$ critical wave vector of the quasi-1D band structure. This line, which is slightly modulated in intensity, exhibits a broad maximum at q_0. Such maximum corresponds to the best nesting wave vector of the thermally warped high temperature Fermi surface. Below around 90-100 K (70 K in the $(TMTSF)_2NO_3$ salt) the line of maxima transforms progressively into an arc limited by the q_2 and q_3 wave vectors which are outside the q_{1D} line and q_0 shifts to q_1 in $(TMTSF)_2PF_6$. The q_2 - q_1 - q_3 arc of maxima should correspond to a broad range of good nesting wave vectors of the warped FS (Fig. 6.8. The change of shape occurs at the 1D to 2D crossover temperature, T_{CO} (see Fig. 6.1 of the electron gas detected by the observation of a transverse plasma edge when the electric field is applied along the inter-stack direction b [202] and by the change of the nature of electron transport along c^* [211]. At T_{CO} the transverse warping of the FS becomes relevant for a large range of q_i wave vectors. Upon cooling below T_{CO} the arc broadens and transforms into a boomerang. Then, the intensity of the q_2 and q_3 maxima of the Lindhard response increases substantially, which means that FS nesting processes other than q_0 become prominent. Below 15-20 K a line of maxima links q_2 to $q_1 \approx q_0$ and q_3 to $q_1 \approx q_0$. This leads to a tilted triangular plateau limited by a q_2 - q_3 arc. Such a triangular shape of maxima has been analytically calculated when nesting breaking terms are included in the FS dispersion [227, 229, 228].

As mentioned in Sect. 6.2, the magnitude of the FS nesting breaking transverse integral t'_b can be estimated for a quarter-field band modeled by an orthorhombic thigh-binding band dispersion with two t_a and t_b transfer integrals as in Eq. 6.1 [221]. Note that in the real triclinic structure of the Bechgaard salts, because of the lower symmetry, there are several other transverse transfer integrals [228] and thus, more FS breaking terms are required. Nevertheless, in a simplified model with t_b = 36.8 meV and t_a= 256 meV, issued from our parametrization of the DFT band structure at 4K, one can estimate a t'_b value of

1.87 meV ≈ 21.7 K, which nicely corresponds to the temperature below which the triangular shaped maximum of the Lindhard function is observed.

It is worth noting the finding of very similar triangular maxima for the Lindhard function in $(TMTSF)_2PF_6$ at atmospheric pressure (P_{atm}) and under 7 Kbar (where there is a strong reduction of $T_{SDW} \sim 4$ K and the onset of coexistence between the SDW modulation and superconductivity [230]) as well as in 98 % deuterated $(TMTSF)_2PF_6$-D_{12} (corresponding to a negative pressure of 5 Kbar with respect to $(TMTSF)_2PF_6$-H_{12} at P_{atm} [231]). Since, according to ref. [229], the triangular shape is controlled by the presence of different nesting breaking effects, the finding of the same area of the triangular maxima and of the limiting q_i wave vectors (Fig. 6.10) means that nesting breaking effects are not varying significantly in pressurized $(TMTSF)_2PF_6$. In connection with this note that our DFT electronic structure calculations reveal only a very small increase of the effective inter-stack transfer integral t_b from 35.6 meV to 36.8 meV and to 37.3 meV in $(TMTSF)_2PF_6$-D_{12}, $(TMTSF)_2PF_6$-H_{12} at P_{atm} and 7 Kbar, respectively. More quantitatively, using Eq. 6.1 one gets a negligible increase of t'_b from 1.87 meV to 1.88 meV by applying 7 Kbar to $(TMTSF)_2PF_6$. This finding contradicts the explanation generally admitted in the literature [221] that the SDW ground state vanishes under pressure because of the enhancement of nesting breaking terms. Thus the vanishing of the SDW ground state under pressure (Fig. 6.1) could be more likely ascribed to a decrease of the direct SDW gap, related to effective Coulomb repulsions, under pressure.

6.4.2 Relationship with the density wave instability

When a $2k_F$ maxima of the electron-hole Lindhard response function occurs, a quasi-1D electron gas can be driven towards a $2k_F$ density wave electronic instability. When the electron-phonon coupling is non-negligible a charge density wave (CDW) instability should generally occur accompanied by a bond order wave (BOW) instability where the phonon field modulates the bond distances. In the

presence of sizeable electron-electron exchange interactions, a spin density wave (SDW) should occur. At high temperature the Bechgaard salts exhibit both kinds of instabilities. Pretransitional SDW fluctuations have been detected by NMR below 200 K in $(TMTSF)_2PF_6$ and $(TMTSF)_2ClO_4$ salts. For the former salt the SDW fluctuations diverge critically below $\sim$ 21 K when approaching the 12 K SDW transition [236].

Quasi-1D $2k_F$ BOW fluctuations are detected by diffuse scattering methods below 200-175 K in the PF_6 [233], AsF_6 [237] and ClO_4 [233] salts. Furthermore, the intra-chain correlation lengths of these BOW fluctuations nicely corresponds to the electron-hole coherence length $\xi_{eh\|}$ deduced from the width of the Lindhard function at the q_0 point (see Figs. 6.7 and 6.17). However, the correlation length of the BOW fluctuations, ξ_{BOW}, only follow the evolution of $\xi_{eh\|}$ with temperature. They are not enhanced upon cooling as it happens for electron-phonon driven Peierls systems such as the blue bronze [42]. This means that, although occurring, the CDW fluctuations are not critical in the Bechgaard salts. Furthermore, the BOW fluctuations vanish below $\sim$ 50K in the PF_6 and AsF_6 salts probably when the lattice becomes more rigid because of the enhancement of the donor-anion hydrogen bond linkage [177, 231]. Such a rigidity does not occur in the ClO_4 salt whose anions remain free to order in a superstructure at a lower temperature T_{AO}= 24 K, so that the BOW fluctuations remain present [233, 224, 238]. CDW fluctuations have also been detected at low temperature in the ClO_4 salt by optical means [239].

Finally it is interesting to recall that in spite of the opening of an anion gap in sections of the well nested parts of the high temperature FS, $(TMTSF)_2ClO_4$ exhibits below T_{AO} a well pronounced $2k_F$ quasi-1D inter-band response. This is a surprising result which also questions the reason for which a density wave instability does not develop instead of supercondivity in relaxed $(TMTSF)_2ClO_4$. Tentatively, the H-bond linkage of anions to donor stacks could prevent a lattice instability and the inter-stack charge transfer of about 0.04 holes [216] could disfavor the onset of a charge or spin density wave instability involving neighboring

stacks along b. Note also that the inter-band Lindhard function was found to be independent of the temperature in the AO phase.

6.4.3 Relationship with the SDW modulated ground state

In the weak coupling limit and the random phase approximation (RPA) the maximum of the Lindhard function should select the critical SDW wave vector which develops at T_{SDW}. This criterium is partly validated by our *first-principles* calculations. The SDW modulation wave vector has been experimentally determined by fitting the NMR line-shape assuming that the a^* component of the modulation is q_{1D} =$2k_F$ = 0.5 a^*. With this assumption it is found that the q_b transverse SDW modulation wave vector in $(TMTSF)_2PF_6$ should be in the range 0.20 ± 0.05b^* [213] or 0.24 ± 0.03b^* [214]. Within experimental errors these wave vectors nicely correspond to the calculated q_1 = (0.48, 0.23) wave vector. In quenched $(TMTSF)_2ClO_4$, NMR studies give a q_b transverse SDW modulation wave vector of 0.12 b^* [240, 241] close to the calculated q_0= (0.5, 0.14). Finally, in the AO phase of $(TMTSF)_2NO_3$ it is found by NMR that $q_b \sim 0.25\ b^*$ [242, 243], which approximate value is close to the calculated q_0 = (0.5, 0.27) for the non-AO phase and (0.01, 0.29) for the AO superstructure. However, the calculation of the Lindhard function brings more information than expected. Indeed, for temperatures below 20-15 K, slightly above T_{SDW}, the Lindhard response of $(TMTSF)_2PF_6$ and quenched $(TMTSF)_2ClO_4$ exhibit a sizable triangular q_2 - q_0/q_1 - q_3 maximum, where one of the summits is the q_0 maximum determined by NMR. Furthermore, the absolute maximum is associated with the doubly incommensurate wave vector q_2 in $(TMTSF)_2PF_6$ and q_3 in quenched $(TMTSF)_2ClO_4$. It is only in the AO phase of $(TMTSF)_2NO_3$ that the Lindhard function exhibits a single maximum.

Our calculation of the Lindhard response in $(TMTSF)_2PF_6$ and quenched $(TMTSF)_2ClO_4$ leaves the possibility that the SDW modulation could occur with any wave vector inside the q_2 - q_0/q_1 - q_3 triangle. Thus, this modulation could be doubly incommensurate. The presence of an incommensurate a^* component makes easier the

sliding of the SDW which is at the origin of a non-linear conductivity when the electric field is applied along a [244]. Another possibility could be that, in a doubly incommensurate situation, the SDW wave vector varies with temperature. Also, the presence of a wide range of maxima means that different sets of modulation waves could be simultaneously established without any prohibitive cost in energy. In other words, the SDW ground state could be very fallible. This could explain the glassy behavior observed inside the SDW ground state [13]. In relation with recent NMR results [245], note that the commensurate SDW wave vector (1/2, 1/4), which is located inside the triangular maximum of $(TMTSF)_2PF_6$ can be locally stabilized in the 4 K sub-SDW phase. It should be remarked that in the presence of a continuum of triangular shaped electron-hole instabilities it is not clear how a single SDW modulation wave vector can be selected at T_{SDW}. This seems to be particularly the case of $(TMTSF)_2PF_6$ where at T_{SDW} the Lindhard function presents two maxima at q_1 and q_2. This should involve a mechanism which goes beyond the standard Peierls-like scenario describing the metal-insulator transition due to the divergence of a single $2k_F$ electron-hole instability (see for example [221, 244]). A more elaborate mechanism taking into account the q_2-q_1-q_3 triangular set of fluctuations could be responsible of the first order order nature of the SDW transition of $(TMTSF)_2PF_6$ [246] since it is known that enhanced fluctuations induce a first order transition [247, 248]. Another possibility could be a lock-in of the modulation at the commensurate $q_{1D} = a^*/2$ component which differs from the incommensurate one entering in the $q_2 = (0.52,\ 0.30)$ modulation wave vector for which the Lindhard function exhibits an absolute maximum. The lock-in process could be facilitated by the coupling of the SDW with the lattice which exhibits (within experimental errors) q_0 and $2q_0$ charge density wave modulations [249].

6.4.4 Relationship with the mechanism of superconductivity

The mechanism of superconductivity in organic conductors is still the object of a long debate [250]. In the case of Bechgaard salts experimental evidence has been accumulated in favor of a pairing mechanism due to incipient SDW fluctuations [251]. Theoretical analysis has recently pointed out that superconductivity should emerge from an extended quantum critical region of the phase diagram which is a function of nesting deviation of the FS [252]. In this framework the shape of the electron-hole instability in the P-T region near the superconducting transition T_S, together with its relationship with the FS nesting properties, could be of key importance. The q-dependent Lindhard function calculated at 1 K corresponding to T_S in relaxed $(TMTSF)_2ClO_4$ is shown in Fig. 6.20. This figure should be compared to the q-dependent Lindhard function in pressurized $(TMTSF)_2PF_6$ at 7 kbar (Fig. 6.10c) where SDW and superconductivity coexist [230]. The Lindhard function of these two salts exhibits a broad maximum for a sizeable number of q wave vectors which should favor the existence of a sizable mixture of q-dependent SDW fluctuations. However, since the maximum of the Lindhard function has a quasi-1D shape in relaxed $(TMTSF)_2ClO_4$ while it has a triangular shape for a large range of pressures in the case of $(TMTSF)_2PF_6$, the SDW fluctuations near T_S should significantly differ in their anisotropy. Such difference, related to a substantially different electronic structure, is pointed out for the first time by the present Lindhard function calculations. How an anisotropy variation of the SDW fluctuations could modify the superconducting pairing mechanism is another challenging question to answer.

6.4.5 Relationship with the Field Induced and Magneto-transport Phenomena

Nesting breaking effects play an important role in the reorganization of the FS in the presence of a modulation. They are at the origin of magnetic quantum oscillations in quasi-1D conductors. In this respect Bechgaard salts offer a large range of possibilities which can be probed by the so-called rapid magnetic oscillation phenomena. Such effects have been recently reviewed and analyzed for the case of an orthorhombic energy dispersion approach for which the nesting deviations are well modeled [251]. Our calculation of the Lindhard function shows that the real triclinic structure offers a larger possibility of different nesting effects (see Fig. 6.8 attested by the finding of a large range of q wave vectors (forming a triangular plateau) presenting equally good nesting conditions. How such an effect can modify the present theory of rapid magnetic oscillations is another challenging question.

In addition nesting breaking terms are a key ingredient in the theory of field induced SDW (FISDW) phases of Bechgaard salts [221]. Nesting breaking effects control the maxima of the Lindhard function in the presence of a magnetic field as considered in ref. [227] for an orthorhombic lattice with one nesting breaking term t'_b and in ref. [229] for a triclinic lattice with several nesting breaking terms. Here our calculations give the true shape of the Lindhard function of the Bechgaard salts at zero magnetic field from which the field effects should be included in order to construct the FISDW phase diagram. The relative value of the different nesting breaking components accounts also for subtle low temperature effects such as the sign reversal of the quantum Hall effect [253].

6.5 Conclusions

In this study we have performed a high-q resolution *first-principles* DFT study of the electron-hole Lindhard response function for the $(TMTSF)_2PF_6$, $(TMTSF)_2NO_3$

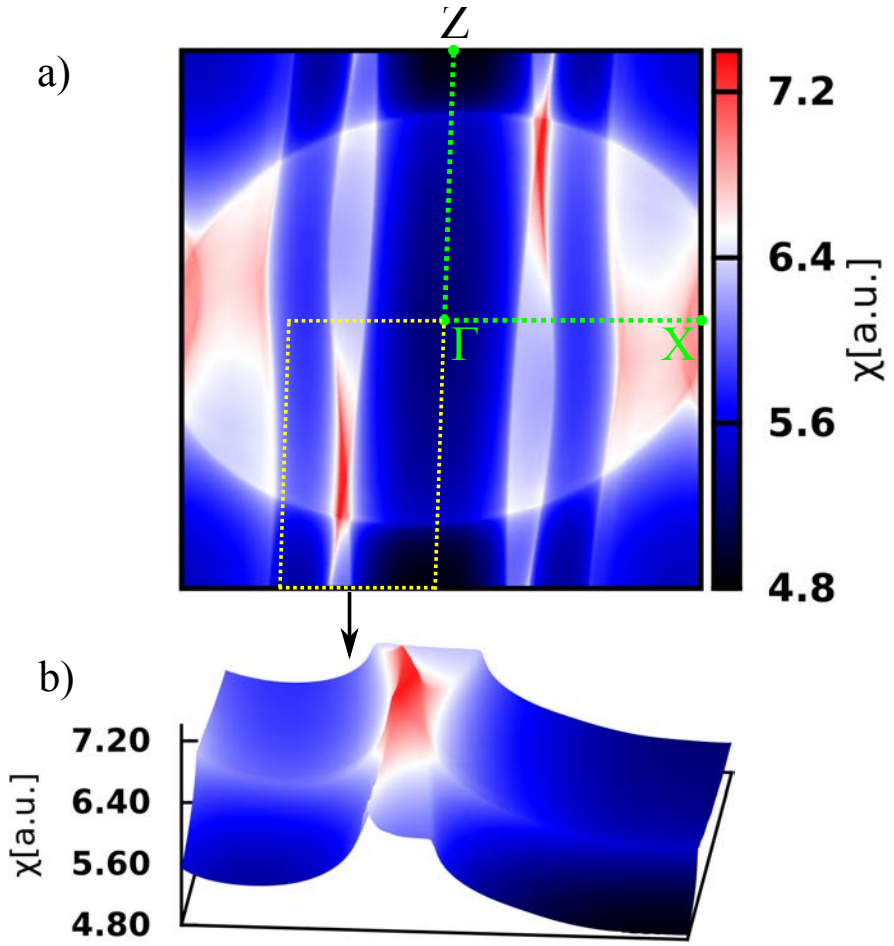

Figure 6.21: 2D plot of the Lindhard function of the α-(BEDT-TTF)$_2$KHg(SCN)$_4$ in the (a*, c*) reciprocal plane at 10 K (a). 3D plot of the region around the maxima of the Lindhard function.

and (TMTSF)$_2$ClO$_4$ Bechgaard salts both in their metallic phase and their different AO superstructures. These calculations allowed us to relate the variation of shape of the response function to the change from 1D to 2D delocalized regimes around T$_{CO}$ and, at very low temperature, to the crossover toward the 3D delocalized regime around t_{c^*}. Our calculation shows unexpectedly that the electron-hole response function exhibits a broad triangular maxima at temperatures just above the SDW transition whose features have been related to multiple nesting conditions of the warped FS. This feature should have important consequences for the analysis of the physical properties of the SDW ground states. Our calculation also shows that minute modifications of the electronic dispersion upon crossing the AO critical line lead to considerable modifications of the Lindhard function. In particular, an unexpected result is the finding of a 2k$_F$ quasi-1D inter-band response

for relaxed and superconducting $(TMTSF)_2ClO_4$.

Our calculations have been performed assuming that the DFT electronic structure calculation accounts for the band dispersion of the Bechgaard salts. In particular our calculations assume that there is no reduction of the inter-chain coupling due to sizable intra-stack Coulomb repulsions. In their presence one expects a reduction of transverse inter-chain hopping which should reduce the FS warping and the magnitude of the FS nesting breaking terms. However, the fact that our calculations correctly account for the experimental 1D to 2D T_{CO} crossover temperature, the experimental determination of the effective nesting breaking term t'_b and the thermal dependence of the BOW correlation length, ξ^{-1}_{BOW}, of the $(TMTSF)_2PF_6$ and $(TMTSF)_2ClO_4$ salts (Figs. 6.7 and 6.17) casts some doubt on the relevance of renormalization effects of the transverse integrals in the Bechgaard salts.

Some of the unexpected features reported here for the Lindhard function response due to the presence of nesting breaking terms in the FS nesting process are in fact quite general. One thus expects to obtain somewhat similar plateaus of maxima of the Lindhard response for systems exhibiting open and sizably warped FSs. As an example, we show in Fig. 6.21 the intensity-wave vector plot of the Lindhard response of the 2D α-$(BEDT\text{-}TTF)_2KHg(SCN)_4$ organic metal which contains both open and close FS sheets. Comparison of the Lindhard response with X-ray diffuse scatering results for this salt proved the FS nesting origin of its low temperature resistivity anomaly [254]. The present calculation of the Lindhard function with a better resolution clearly shows that the quasi-1D $2k_F \sim 0.17a^*$ maxima of the electron-hole response associated to the warped open FS, exhibits indeed a curved triangular-like shape implying also the presence of a set of good FS nesting wave vectors with transverse components between 0.1 and 0.4 c^*.

6.6 Computational details

DFT calculations [96, 97] were carried out using a numerical atomic orbitals approach, which was developed for efficient calculations in large systems and implemented in the SIESTA code [27, 28]. We have used the generalized gradient approximation (GGA) to DFT and, in particular, the functional of Perdew, Burke and Ernzerhof [98]. Only the valence electrons are considered in the calculation, with the core being replaced by norm-conserving scalar relativistic pseudopotentials [99] factorized in the Kleinman-Bylander form [100]. The non-linear core-valence exchange-correlation scheme [102] was used for all elements. We have used a split-valence double-ζ basis set including polarization functions [101]. The energy cutoff of the real space integration mesh was 350 Ry. To build the charge density, the Brillouin zone (BZ) was sampled with the Monkhorst-Pack scheme [103] using grids of (45×45×18) k-points in the non-anion ordered phases and (31×15×15) k-points in the anion ordered phases. The Lindhard response function,

$$\chi(q) = -\sum_{i,j}\sum_{k} \frac{f_F(\epsilon_i(k)) - f_F(\epsilon_j(k+q))}{\epsilon_i(k) - \epsilon_j(k+q)}, \tag{6.2}$$

where f_F is the Fermi function and $\epsilon_i(k)$ are the band eigenvalues, was obtained from the computed DFT values of the band eigenvalues $\epsilon_i(k)$. The integral over k-points of the BZ was approximated by a direct summation over a dense, regular grid of points. As the Lindhard function is more sensitive to the accuracy of the BZ integration than the total energy, especially in very anisotropic systems, and/or in the presence of hot spots in the band structure (e.g. saddle points with the corresponding van Hove singularity in the DOS), the k-points grid used for its calculation must be more dense than in the standard self-consistent determination of the charge density and Kohn-Sham energy. The calculations are done, nevertheless, using the eigenvalues obtained in the DFT calculation for the coarser grid, and interpolating their values in the denser grid, using a post-processing utility available within the SIESTA package. In this work, for the calculation of the Lindhard

response function, the BZ was sampled using a grid of (400×400×16) k-points. The partially filled bands were those taken into account in the calculations.

7. ORIGIN OF THE CDW IN $TaTe_4$

7.1 Introduction

Transition metal tellurides usually exhibit crystal structures and transport properties noticeably different from those of the corresponding selenides or sulphides [255]. The tellurium valence p orbitals are considerably more diffuse than those of selenium or sulphur and they are able to interact with other tellurium atoms which are considerably farther away. As a result the filled tellurium p bands are wider than those of selenides or sulphides and may overlap substantially with the bottom part of the transition metal based d bands causing a non-negligible electron transfer from tellurium to the transition metal [256]. In other cases, the result of this overlap between Te difuse p orbitals may lead to the opposite effect. For instance, when the Te sublattice contains Te_2 dimers, the Te-Te empty antibonding levels can interact and spread into wide bands so that their bottom part overlaps with filled transition metal levels leading to a reverse electron transfer from the transition metal to tellurium. A consequence of these electron transfers is that the formal electron counting for the tellurium atoms and fragments of transition metal tellurides is sometimes not quite obvious [257, 258], a problem that does not generally occur in transition metal sulphides and selenides. As a consequence of these transfers the anion sublattice of transition metal tellurides often contains tellurium fragments larger than dimers and even large polianionic units [259, 258]. These electron transfers have strong implications for their structural and, consequently, transport properties.

Recently, the transition metal teratellurides $NbTe_4$ [260] and $TaTe_4$ [261] have been the object of considerable attention in the context of the search for materials

with high magnetoresistance and the competition between CDWs and superconductivity [262, 263, 264, 265]. Structural modulations towards a $2a \times 2a \times 3c$ commensurate phase occur in both Ta and Nb tetratellurides. $TaTe_4$ has a direct transition to the commensurate phase at around 450 K [266], while its isostructural counterpart, $NbTe_4$, crosses several incommensurate phases before locking into the final commensurate one at 50 K [267, 268]. Because of the presence of chains of transition metal atoms coordinated with Te atoms and the metallic character, these modulations have been attributed to CDW formation as in other pseudo-1D metals [269, 270, 271]. In contrast with other pseudo-one-dimensional chalcogenides exhibiting structural modulations like $NbSe_3$ or monoclinic-TaS_3 [255], the resistivity change when the structural modulation occurs is small. Thus, the usual Fermi surface driven mechanism behind the CDW formation may not be at work here as it was the case in 2H-$NbSe_2$ (see Chapter 2.3). The origin of the CDW in these tetratellurides has been discussed for longtime but to the best of our knowledge there have not been detailed first-principles studies of their Fermi surface and Lindhard response function. In this section we present a first-principles DFT study of the origin of the CDW state in $TaTe_4$. We focus in $TaTe_4$ for practical reasons because of the commensurate nature of the structural modulation although very similar arguments should also apply for $NbTe_4$.

7.2 Crystal Structure and Electron Counting

7.2.1 Crystal Structure

$TaTe_4$ crystallizes in a tetragonal structure with Ta atoms coordinated by 8 Te atoms in a chain like fashion. The Ta atoms are located in the center of a square antiprism of Te atoms, where the two Te_4 square units are rotated 45° with respect to each other as shown in Fig. 7.1. The crystal structure of $TaTe_4$ is a tetragonal

array of chains of this type (Fig. 7.2). The space group symmetry has been determined by Bjerkelund and Kjeskus [261] to be P4/mcc for the average structure[1] with the experimentally found lattice parameters a= 6.514 Å and c= 6.809 Å. Their corresponding Wyckoff positions are 2a for Ta atoms situated in (0, 0, 1/4) and (0, 0, 3/4) in fractional units, respectively 8m for Te atoms situated in (x, y, 0) and its equivalent positions, where $x = 0.1440$ and $y = 0.3280$. We carried out a relaxation of the internal coordinates while forcing the space group symmetry giving us $x = 0.1501$ and $y = 0.3296$, values which are in good agreement with the experimental ones. The structure of the $2a \times 2a \times 3c$ commensurately modulated phase was solved by Bronsema et al. [266]. Let us note that weak superlattice reflections at (1/2, 0, 1/3), (0, 1/2, 1/3), and very weak ones at (0, 0, 1/3) were also observed [269, 266] although the last ones are most likely second harmonics satellites.

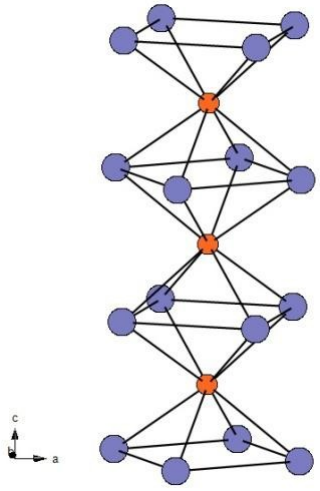

Figure 7.1: Lateral view of a chain in $TaTe_4$. Ta atoms are represented in orange and Te in blue.

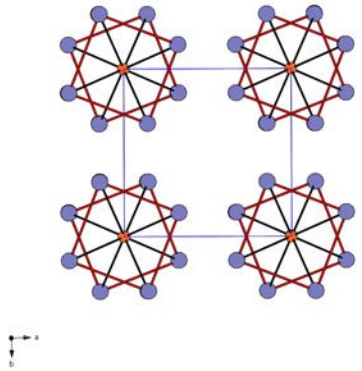

Figure 7.2: Top view of $TaTe_4$. Red lines represent Te-Te bonds.

[1]The denomination of average structure comes from the fact that the measurements were performed at room temperature when the structure is already modulated in its $2a \times 2a \times 3c$ phase. Thus, since superlattice reflections were not taken into account, information can be provided only for a subcell (here our average structure) of the already modulated structure in order to understand the characteristics of an undistorted structure.

7.2.2 Electron counting

For a better understanding of both the crystal and electronic structure, we need to determine how many electrons fill the Ta-based bands. The first thing to do is to look at the Te−Te distances. Those within a Te_4 square unit (3.29 Å) are shorther than the sum of the van der Waals radii of Te (4.12 Å), but too long to be considered as a real Te-Te bond (2.7 - 2.9 Å). At a careful inspection of the structure we can observe that the shorter Te-Te contacts are not those in the Te_4 square units but those connecting the squares of neighbouring chains (red bonds in Fig. 7.3: 2.93 Å), which are of the same order as many Te-Te single bonds. Under these considerations the structure should be viewed as a 3D lattice of Ta-Te and Te-Te bonds as shown in Fig. 7.3, in contrast with the usual description of this structure as a tetragonal array of $TaTe_4$ chains (see Fig. 7.2).

Because of the occurrence of Te-Te bonds the tellurium atoms should be considered as $(Te_2)^{2-}$, which means that only one electron is left to fill Ta-based bands (i.e. Ta atoms are formally d^1). Thus only the bottom Ta d based bands may be partially filled. The d orbitals of a transition metal in this coordination environment are such that the lowest energy orbital is a d_{z^2} orbital and slightly higher in energy there are the two d_{xy} and $d_{x^2-y^2}$ orbitals. These two orbitals will be very weakly dispersive along the Ta chains direction whereas the d_{z^2} orbital creates strong interactions and will thus lead to a wide band. Consequently, the bottom Ta-based band will be a dispersive d_{z^2} band. Since there is just one electron to fill this band, the bottom part of the Ta based bands will be most likely a half-filled Ta d_{z^2} band.

On the basis of this formal electron counting we can predict that if the solid behaves as a 1D system around the Fermi level, it should be unstable to some kind of dimerization that would open a gap at the Fermi level. However, this is in conflict with the experimental observations. To begin with the modulated structure is metallic. Moreover the observed superlattice spots all have a 1/3 component along the c-direction (the direction of the Ta chains). Thus, if the system can be treated

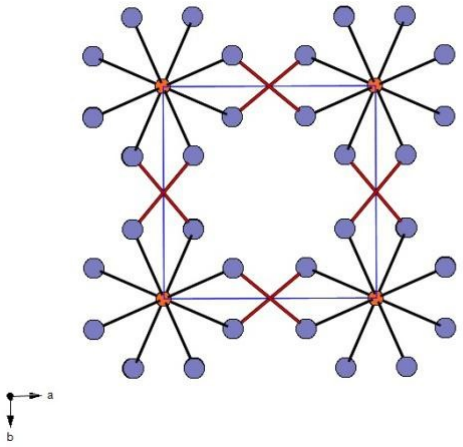

Figure 7.3: Top view of $TaTe_4$. Red lines represent the shorter Te-Te bonds of the structure

as electronically 1D, the Ta band should not be half-filled but 1/3rd or 2/3rds filled. The second possibility can be easily understood; it simply means that there is some electron transfer from the Te valence band towards the Ta d_{z^2} band. This is indeed likely because of the short Te... Te contacts between the Te_2 units which may raise the top of the Te valence band. Thus, the top of the valence band may end up being higher than the Fermi level. At first sight the second possibility may appear to be unlikely because according to the occurrence of $(Te_2)^{2-}$ units the Te valence band is already full. Consequently, to acquire some electrons from the Ta atoms some of the Te-Te bonds should be broken, which is not the case according to the crystal structure [266]. However, let us remind that although the Te...Te contacts of the Te_4 squares are longer than those between the squares, they are considerably shorter than the sum of the van der Waals radii. Taking into account both types of Te...Te contacts, one can see that one plane of Te atoms is made of a series of orthogonal almost linear Te_4 units. Thus there must be very strong Te...Te interactions along the layer so that the bottom of a very wide band built from the interchain antibonding σ^* Te-Te levels could overlap with the filled d levels and result with a Ta to Te electron transfer that would lead to a less than half-filled Ta d_{z^2} band.

The previous considerations raise some serious questions: do the Te-Te short interchain contacts confer the electronic structure around the Fermi level with a 2D or 3D character? In that case the probability to have good Fermi surface nesting vectors is unlikely. In that case the CDW would not be Fermi surface nesting driven. In addition, it is doubtful that the electronic transfer leads to a commensurate filling of the d_{z^2} band. This objection can be somewhat dismissed by noting that the isostructural and isoelectronic $NbTe_4$ undergoes a series of incommensurate modulations along the *c*-direction before becoming commensurate at low temperature. Thus, maybe in $TaTe_4$ (but not in $NbTe_4$) the electron transfer is very near the commensurability. Note also that whatever it is the sense of the electron transfer, even if the Ta-based bands lead to a Fermi surface nesting driven CDW and thus to the opening of a gap at the Fermi level, the Te-based bands may not be necessarily affected so that the metallic character of the bands can be kept after the CDW sets in the material, as it is in fact observed. Thus, it is not at all clear from simple electron counting arguments that the modulation exhibited by $TaTe_4$ originates from a Fermi surface nesting phenomena, as in many low-dimensional materials, or from a phonon driven instability, as for instance in single-layers of 2H-$NbSe_2$ (see Chapter 2.3)

7.3 Electronic structure of the average structure

The only electronic structure calculations available at the moment of writing were performed by Bullet [272] and Whangbo and Gressier [270]. Bullet argues that the strong interchain Te-Te interaction confers a 3D character to the electronic structure, argument which naturally applies for both Nb- and Ta- tetratellurides. A more detailed theoretical band structure calculation using the extended Hückel method was done by Whangbo and Gressier whom argument lies in Te-Te interchain distances conferring a 3D character to the structure. They also argue that the CDW formation originates in the Fermi surface nesting, yet with a shorter wave vector component along the metallic atoms chain (calculated 1/4 c^* compared to experimental $\sim$1/3 c^* for $NbTe_4$). The work of Zwick et al. [273] presents the

ARPES spectra which exhibit a combination of 1D and 3D Fermi surface components. The experiment doesn't clarify though if there are two decoupled Fermi surface components, nor if the Fermi surface nesting plays a role in the structural modulation. To make some progress we decided to carry out a first-principles DFT study for the average and modulated structures of $TaTe_4$.

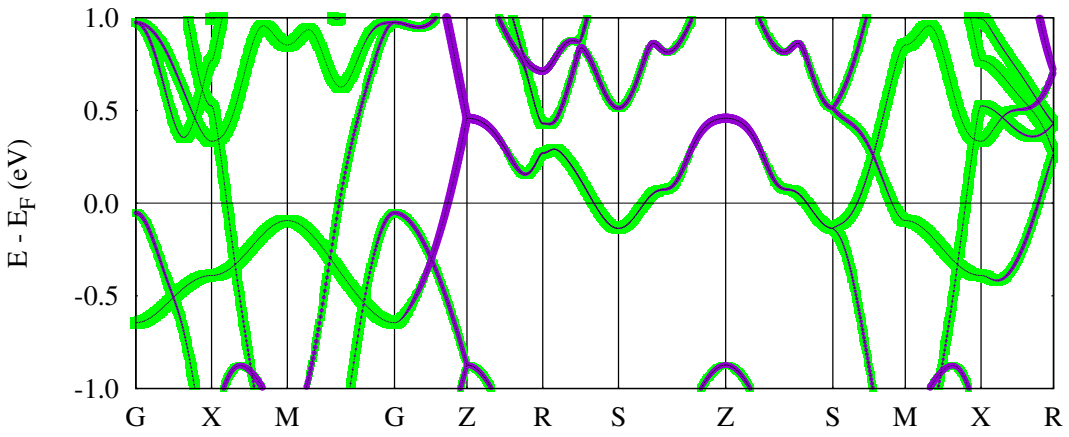

Figure 7.4: Fatband structure of $TaTe_4$ (see Fig. 7.5d for the labeling of the special points). The red and blue full circles are associated with the Te p and Ta d_{z^2} contributions.

The weighted band dispersion calculation of the $TaTe_4$ average structure (Fig. 7.4) reveals that there are essentially two types of bands crossing the Fermi level. The band crossing from Γ to Z is dominated by Ta d_{z^2} orbitals and it is actually a folded band because there are two Ta atoms along the *c* direction in the unit cell related by a screw axis. Since the lower component is only partially filled it appears that the formal electron count for Ta is lower than d^1. Note also that the Te content of this pair of bands is quite sizeable and in several lines of Fig. 7.4 even seems to dominate. However this is due to the 1:4 stoichiometry which increases the total weight of the Te orbitals. What is however quite clear is that whereas these Ta d_{z^2} bands are strongly dispersive along the *c* direction they are also engaged in interchain interactions (see for instance the Γ-M and X-M lines in Fig. 7.4) because of the short interchain Te-Te contacts highlighted in Fig. 7.3. This band should thus have a strong memory of the 1D type interactions associated with the Ta d_{z^2}-Ta d_{z^2} interactions along the chain but exhibit a non-negligible warping due to the

interchain interactions. There is a second band crossing the Fermi level which is mostly based on p Te orbitals exhibiting a large dispersion on both directions, perpendicular (see Γ-M and M-X in Fig. 7.4) and parallel (see M-S in Fig. 7.4) to the $TaTe_4$ chains. This mostly Te-based band should thus have a 3D character. In fact, the two bands overlap and interact quite strongly, thus interchanging character, along different parts of the Brillouin zone (see for instance the Z-S line in Fig. 7.3). Thus, one should expect a relatively complex Fermi surface resulting from the interaction between the Ta d_{z^2} and Te based bands for non-modulated $TaTe_4$.

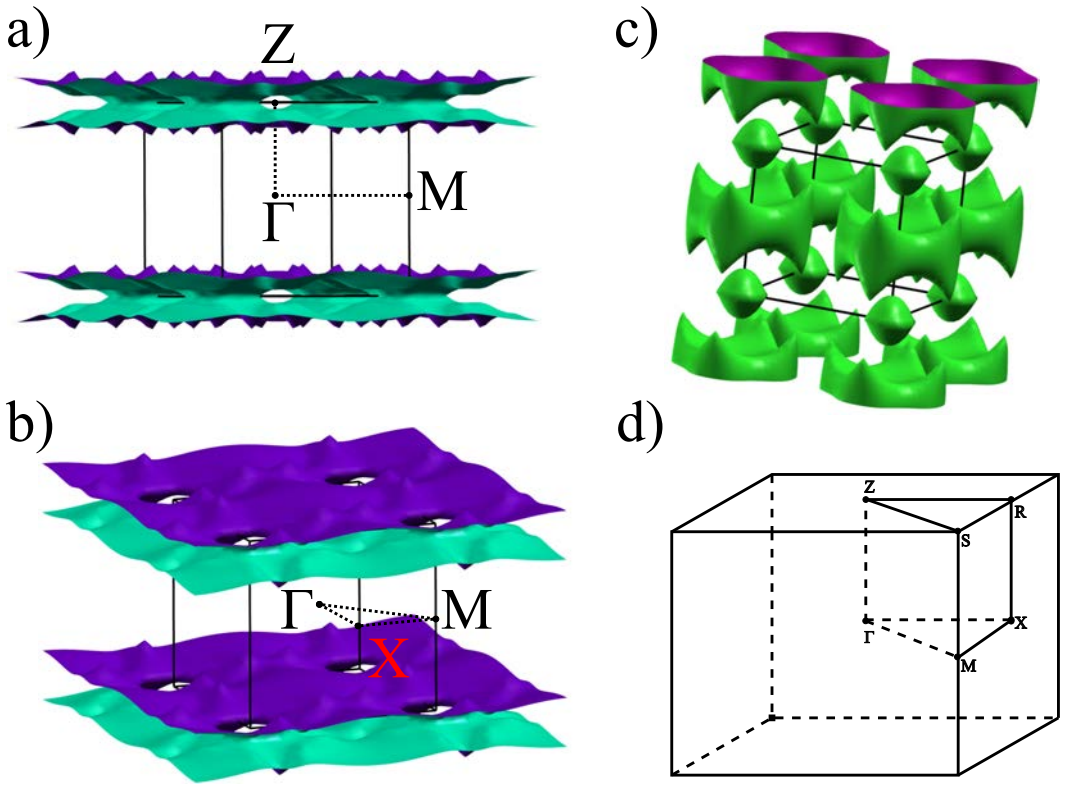

Figure 7.5: Fermi surface of the $TaTe_4$ average structure. a) and b) are two views of the component mostly originating in the Ta d_z^2 orbitals. c) Component originating in the Te p orbitals. d) Brillouin zone representation of a tetragonal lattice. The high symmetry points have the following coordinates: $\Gamma = (0,0,0), X = (0.5,0,0), M = (0.5,0.5,0), Z = (0,0,0.5), R = (0.5,0,0.5), S = (0.5,0.5,0.5)$ in units of the reciprocal lattice vectors.d)

The Fermi surface of $TaTe_4$ is shown in Fig. 7.5. It is made of two different contributions originating from the two different types of bands crossing the Fermi level. As expected, one of the components is relatively flat (Figs. 7.5a and b)

although bearing a very substantial degree of warping and even holes. In fact, the two sheets making this portion of the Fermi surface touch at many points of the Brillouin zone thus making a complex slab with holes and closed empty regions inside. Coming to the second component of the Fermi surface, we notice that it has a multi-dimensional topology since the band generating this Fermi surface component crosses the Fermi level in several directions like Γ-M, M-X, but also along M-S where the band mixes with the Ta band. In fact, because of the degeneracy of the bands in the outer plane of the Brillouin zone (see the traject Z-R-S-Z in Fig. 7.4) there is a third band crossing the Fermi level leading to the closed almost sperical pockets around the corners of the Brillouin zone (point S) in Fig. 7.5c.

The warped Fermi surface of Fig. 7.5a is associated with less than 2 electrons per unit cell which is the filling associated with Ta atoms with an electron counting of d^1. This result confirms that, in contrast with the usual situation in many transition metal tellurides, there has been a formal electron transfer from the Ta to the Te sublattices (i.e. the formal electron counting for Ta is $d^{1-\delta}$) with $\delta \sim 0.2$, in between those of a one-third field ($\delta = 2/3$) and half-filled ($\delta = 0$). It is because of this transfer than the "double pillow" pockets of Fig. 7.5c are created.

In order to clarify if the structural modulation originates in a Fermi surface nesting phenomena we have performed Lindhard function calculations across several planes in both a^*-a^* and a^*-c^*. According to the experimental findings, we should find sharp maxima in the Lindhard function calculations for $1/2a^*$ and $1/3c^*$ components, i.e. in the corners of Fig. 7.6b. However, this is not the case. In the a^*-a^* plane where we vary the q_{c^*} component (Fig. 7.6), the maximum in the Lindhard function occurs for a $q_{c^*} = 1/2$ and not $1/3$. Even so, the occurring maximum is not a typical logarithmic dispersion for a Fermi surface nesting driven instability, but it covers a rather broad region of suitable nesting vectors for the q_{a^*} in the $[0.1 : 0.5]$ interval. It could be argued that the $1/2$ components of the modulation along the interchain directions originate from Coulomb coupling between intrachain modulations. However, in the case where we calculate the Lindhard

function in the a^*-c^* plane and vary the second q_{a^*} component (Fig. 7.6), we find that the maximum response is given by $q = (0, 0, 0.4)$. Again, this is not a proper nesting vector to explain the modulation mechanism. Let us note that this wave vector does not correspond to the $2k_F$ value of a folded d_{z^2} band for Ta $\sim d^{0.8}$. In fact, this wave vector is associated with an interband nesting. We thus conclude that the Lindhard function does not contain maxima with a (1/3) c^* component so that we may dismiss the possibility of a Fermi surface driven instability that leads to the structural modulation manifested in $TaTe_4$.

7.4 Structural modulation

The next step we considered in our analysis of the origin of the modulation was calculating the phonon dispersion. We found imaginary phonon modes with 1/2 a^* and 1/3 c^* components, matching the experimental results, and another one with a 1/4 c^* component and no a^* contribution. These calculations suggest that trimerizations of the Ta chains coupled with a dimerization along one or two interchain directions, presumably to relieve the strain generated in the Te network connecting these chains, or tetramerizations of the Ta chains which apparently can occur without generating much strain in the Te network can stabilize the system.[2]. However, as surprising as this might be, this is not necessarily conflicting with the experimental results, but it indicates the possible existence of another modulated phase of $TaTe_4$.

Assuming no prior knowledge of the modulated structure of this material, the clear-cut answer of phase stability/ordering, whichever they might be, is provided by the energy gain of each phase with respect to the undistorted structure. We have performed internal coordinates relaxation of each of the possible phases and the lowest energy state we obtained was the $2a \times 2a \times 3c$ phase. All the other stable

[2]As a general note on the behaviour of the phonons, the broad imaginary phonon bands are also an indicator that the modulation is driven by a collection of wave vectors instead of one single wave vector as it is the case of Fermi surface nesting, dismissing once again Fermi surface nesting driven instability for this material.

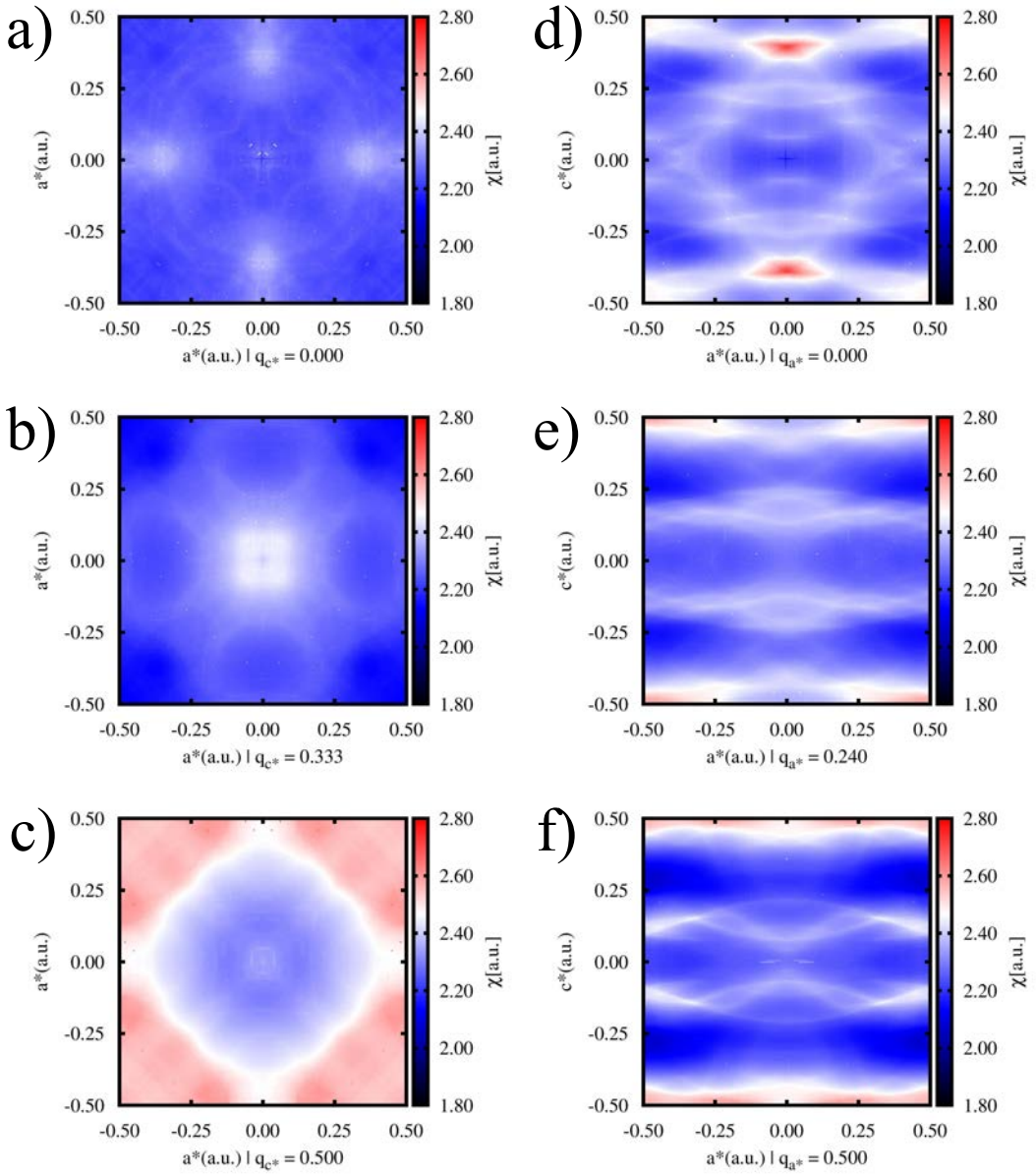

Figure 7.6: 2D mapping of the calculated Lindhard function of $TaTe_4$ in the a*-a* plane for different q_{c^*} components(a-c), respectively in the a^*-c^* plane for different secondary q_{a^*} components (d-f). The bars represent the Lindhard function value in arbitrary units.

phases were higher in energy than the a $2a\times2a\times3c$ phase as presented in Table 7.1.

One possible reason for which the $1a\times1a\times4c$ phase is not observed in experiments is due to the establishing of $2a\times2a\times3c$ phase at a much higher temperature. Although we did not find an unstable phonon with $1a\times1a\times3c$ wave vector we checked that an optimization for this phase leads to the average structure. We can infer from these calculations that the charge density wave modulation of $TaTe_4$ is electron-phonon coupling based.

Table 7.1: Energy gain of each phase (as indicated by the imaginary phonon mode minimums) with respect to the $TaTe_4$ average structure.

Periodicity	Energy gain(meV/f.u.)
$1a\times1a\times4c$	-13
$2a\times1a\times3c$	-38
$2a\times2a\times3c$	-57

7.4.1 Modulated structure

The charge density wave structure and lattice symmetry have been determined experimentally by van Smaalen, Bronsema and coworkers.[266] It was later restated by Corbett et al.[274] that the modulated structure symmetry is indeed P4/ncc. We present in Table 7.2 a comparison between the experimental structure and our calculated structure of the lowest energy state. The calculated structure is in excellent agreement with the experimental one.

The calculated $2a\times2a\times3c$ phase as well as the $2a\times1a\times3c$ one can be described on the basis of Fig. 7.7. The unit cell of both phases contains two different $TaTe_4$ chains with different trimerization patterns labelled A and B. In chain A (Fig. 7.7b) three different Ta-Ta distances are generated (see Table 7.3); two are shorter than in the average structure and one is longer whereas in chain B (Fig. 7.7c) there are only two different distances; the two shorter Ta-Ta distances are identical in that case but different in chain A. The average value of the two shorter distances in chain A (3.128 Å) is very similar to the short distance in chain B (3.133 Å).

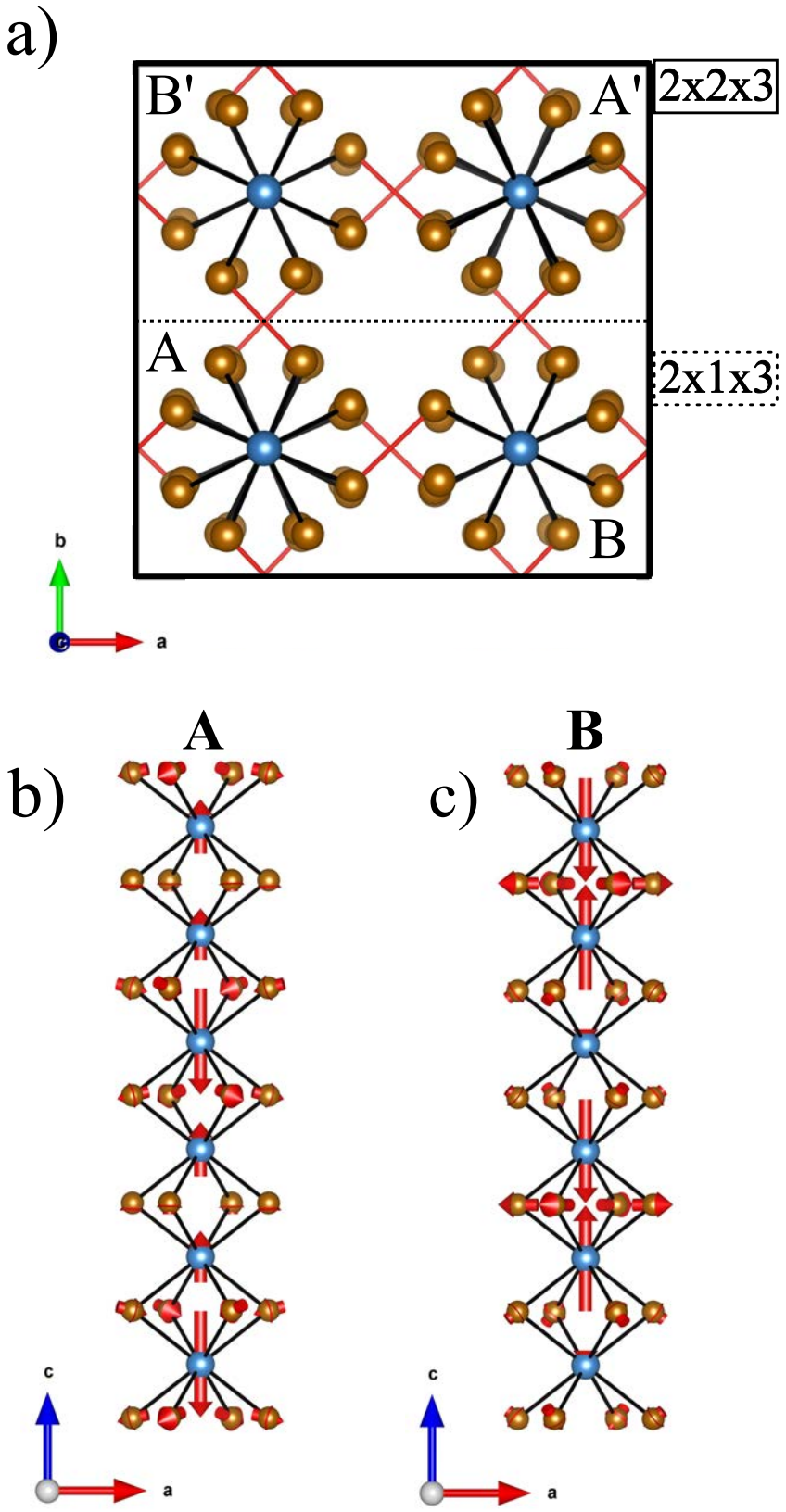

Figure 7.7: Unstable phonon modes correspondence to each chain type in the 2×2×3 and 2×1×3 $TaTe_4$ supercells.

Table 7.2: Comparison between the experimental coordinates (taken from [266]) and those calculated for the $TaTe_4$ modulated structure in its $2a\times2a\times3c$ phase.

		Experimental			Calculated		
Atom type	Wyckoff Position	x	y	z	x	y	z
Ta 1	8e	0.0000	0.0000	0.09652	0.0000	0.0000	0.09668
Ta 2	4a	0.0000	0.0000	0.25000	0.0000	0.000	0.25000
Ta 3	4c	0.0000	0.5000	0.41827	0.0000	0.5000	0.41828
Ta 4	4c	0.0000	0.5000	0.26351	0.0000	0.5000	0.26385
Ta 5	4c	0.0000	0.5000	0.07030	0.0000	0.5000	0.07005
Te 1	16g	0.0611	0.1579	-0.00300	0.0832	0.1653	-0.00176
Te 2	16g	0.5802	0.1655	0.00170	0.5911	0.1874	-0.00049
Te 3	16g	0.1656	0.0789	0.16860	0.1828	0.0933	0.16734
Te 4	16g	0.6665	0.5747	0.16970	0.6774	0.5796	0.16336
Te 5	16g	0.6687	0.0700	0.16330	0.6673	0.0827	0.16871
Te 6	16g	0.1561	0.5648	0.16750	0.1717	0.5817	0.16943

Table 7.3: Ta-Ta contacts in the average structure and in the two types of chains in the modulated structure. Please note that the distortion is allowed within the experimental lattice parameters. Refer to Fig. 7.8 for labels.

d(Å)	Average	Type A	Type B	#
Ta-Ta	3.406	3.156	3.952	(a)
		3.101	3.133	(b)
		3.960	3.133	(c)

Table 7.4: Te-Te contacts in the average structure and in the two types of chains in the modulated structure. Both the interchain and the intrachain distances are included. A particular case represents chain type B where the square symmetry is broken and we have two types of distances within the rectangle. Moreover the planes containing these two consecutive rectangles are rotated by 90° with respect to each other (Thus the order of writing in the table). Note that the distortion is allowed within the experimental lattice parameters. Refer to Fig. 7.8 for labels.

d(Å)	Average	Interchain	Average	Square in A	Square in B	#
Te-Te	2.959	2.974	3.337	3.143	3.389 - 3.471	S_a
		2.965		3.414	3.471 - 3.389	S_b
		2.929		3.447	3.146	S_c

Table 7.5: Ta-Te contacts in the average structure and in the two types of chains in the modulated structure. Note that the distortion is allowed within the experimental lattice parameters. Refer to Fig. 7.8 for labels.

d(Å)	Average	Type A	Type B	#
Ta-Te	2.910	2.845	2.969	1
		2.982	2.843	2
		2.971	2.945	3
		2.836	2.926	4
		2.935	2.839	5
		2.934	2.982	6

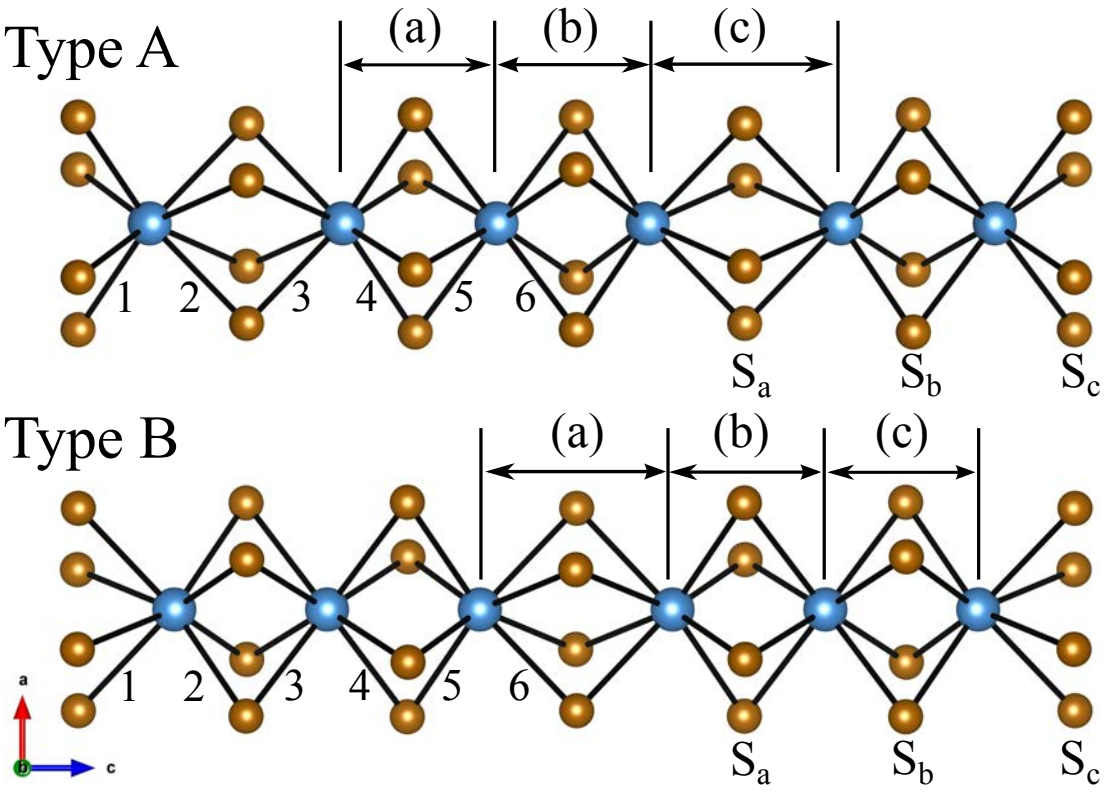

Figure 7.8: Distances labels in the different chains.

Trimerized units or clusters are thus formed in every chain.

Although as shown in Figs. 7.7b and c the structural variations are strongly located on the Ta sublattice, the occurrence of these triplets induces a response of the Te sublattice. There are two different types of Te squares (they are really squares in chain A but rectangles in chain B): one-third of them have shorter Te...Te contacts whereas two-thirds have longer Te...Te contacts (see Table 7.4). Those being contracted are those in between Ta atoms which have moved apart;

this is easy to understand since the $TaTe_4$ chains tend to keep the Ta-Te bonding. The variation of these Te...Te distances is considerably larger (one order of magnitude) than the variation of the Te-Te interchain bonds (see Table 7.4). Thus, it is clear that the system tries to keep the Te-Te bonds as stable as possible. The rotations and shifts undergone by the Te atoms under the modulation have this purpose. The variation of the Ta-Te bonds (Table 7.5) can be analyzed in the same way. All structural variations noted for the optimized structures mirror those of the experimental ones. In summary it appears that optimization of the metal-metal bonding subject to inducing the minimum alteration of the Te sublattice is the driving force for the CDW irrespective of the nature of the Fermi surface.

Using this structure we have calculated the band structure of the CDW phase. As it was also found experimentally, the modulated phase is clearly metallic as one can see in Fig. 7.9. The extensive folding leads to the four components of the Fermi surface shown in Fig. 7.10. It is clear from this Fermi surface that $TaTe_4$ in the CDW structure is a 3D metal, in agreement with the experimental observation of $\rho_c/\rho_a \sim 1$ [271]. Since $TaTe_4$ is already in the modulated phase at room temperature it is not possible to know the resistivity change when the transition occurs. However, for $NbTe_4$ which is structurally and electronically very similar, the change in the resistivity is very small without variation of the anisotropy [271]. This is also consistent with the 3D character of the Fermi surfaces calculated for the average and modulated structures of $TaTe_4$. The different components of the Fermi surface in Fig. 7.10 contain numerous closed circuits which are consistent with recent studies reporting a very large magnetoresistance for $TaTe_4$ in the CDW state.

7.5 Conclusions

We have discussed the possible character of the electronic structure of $TaTe_4$ and argued that it has a 3D behaviour. This behaviour comes primarily from the adjacent interchain coupling due to Te atoms. The Te atoms distances are of the order

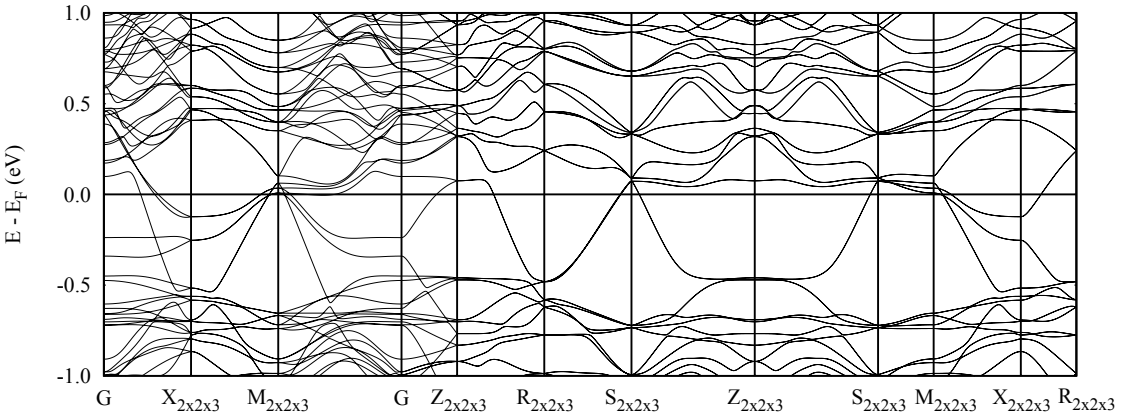

Figure 7.9: Band structure for the $2a\times2a\times3c$ modulated $TaTe_4$ structure

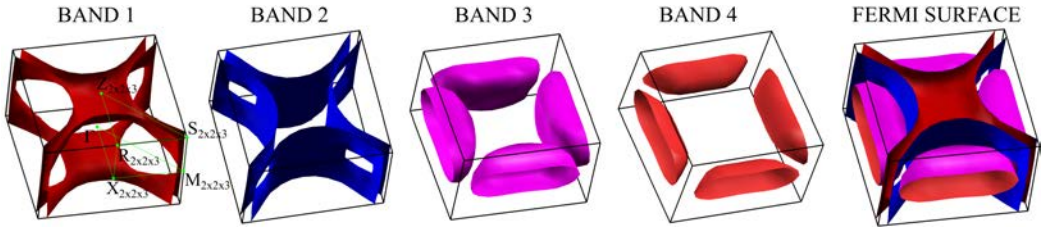

Figure 7.10: Calculated Fermi surface for the $2a\times2a\times3c$ modulated $TaTe_4$ structure

of most Te-Te bonds in this compound. Secondly we have dismissed the Fermi surface driven instability as origin of the modulated structure based on our Lindhard function calculations. We have calculated the phonon dispersion and described the ordering of the possible modulated phases. The optimized $2a\times2a\times3c$ structure is found to be the more stable in agreement with the experimental observations. The nature of the distortions with respect to the average structure suggest that the driving force for the distortion is the maximization of Ta metal-metal bonding subject to inducing the minimum decrease in bonding of the Te sublatice. Thus, as it was the case for 2H-$NbSe_2$, the CDW in $TaTe_4$ does not originate from an instability of the Fermi surface.

7.6 Computational details

The eletronic band structure calculations were carried out using a numerical atomic orbitals density functional theory (DFT) [96, 97] approach implemented in the

SIESTA code [27, 28]. The Perdew-Burke-Ernzerhof (PBE) functional was used to account for the exchange-correlation energy [98]. The core electrons have been replaced by norm-conserving scalar relativistic pseudopotentials [99] factorized in the Kleinman-Bylander form [100]. We have used a split-valence double-ζ basis set including polarization functions [101]. In all calculations, we use a cutoff of 800 Ry for the real space integrals, and a tolerance of 10^{-4} and 10^{-3} eV on the density matrix and the total energy, respectively, for the convergence of the SCF cycle. To sample the Brillouin cell for the electronic states, a Monkhorst-Pack [103] k-point grid of $32\times32\times30$ was used for the undistorted unit cell and scaled accordingly to the supercell calculations.

PART IV

CONCLUSIONS

8. CONCLUSIONS

In this thesis we have considered low dimensional materials both in single-layers (part 2) and bulk (part 3). Some of the materials considered like the blue bronzes, the Bechgaard salts, $TiSe_2$ or $NbSe_2$ rank among the more studied and controversial materials of this type. The main conclusions of this work are the following:

1) The origin of the 2×2 CDW of $TiSe_2$ is construed from the analysis of a phonon branch which becomes unstable around the M point of the Brillouin zone. The atomic displacements of this phonon mode allow the mixing of states at the top of the valence band at the Γ point and the bottom of the conduction band at M (both responsible for the metallicity of the undistorted structure). The combination of three such phonons for the three inequivalent M points allows a full band gap opening. This $3Q$ structure has a 2×2 periodicity which closely matches the CDW in-plane distortion of the bulk material. Doping the layer with externally injected charges modifies this picture only slightly for small doping levels. However, for larger doping levels, the phonon band structure changes significantly, in such a way that the unstable phonon branch has its minimum at intermediate points of the $\Gamma - M$ segment, while the phonon at M becomes stable. It could therefore be expected that the CDW can become incommensurate for certain values of the doping. Further increase of the doping level makes all the phonon branches to become stable, and therefore the system recovers the undistorted 1×1 structure.

2) The mechanism of the unexpected CDW instability in single-layer $TiTe_2$ seems to be the same phonon mediated mechanism acting for single-layer $TiSe_2$ although the driving force is smaller and the semimetallic character is kept below the transition temperature. The magnitude of the semimetallic overlap is one of the key factors in controlling the likeliness of the 2×2 CDW. It has been shown that tensile

strain stabilizes the 2×2 CDW distortion in single-layer $TiTe_2$. We propose that this fact could be used to induce the instability in double- or triple-layers of $TiTe_2$ which in the absence of strain remain undistorted, to induce a stronger distortion leading to the creation of a band gap in single-layer $TiTe_2$ or most likely to suppress the 2×2 CDW under a small compression. The first of these predictions was experimentally verified after the publication of our results.

3) We have found six different structures compatible with the 3×3 CDW structure of $NbSe_2$. All these structures are found to coexist in a very narrow energy range of 2-3 meV so that their relative stability can be subtly altered by doping or strain. Imaging the surface of bulk $2H$-$NbSe_2$ with atomic resolution and comparison with the STM images calculated for the different structures allowed the experimental group of Dr. M. Ugeda (San Sebastián) to identify two of these structures. Intriguingly, these structures differ from the X-ray crystal structure reported for the bulk 3×3 CDW which, in fact, is also one of the six DFT structures located for the single-layer. Preliminary calculations for slabs with a different number of layers suggest that the actual structure stabilized may change from layer to layer, i.e., the energetic preference may depend also on the internal pressure. The coexistence of different structures in $2H$-$NbSe_2$ has far-reaching consequences to fully understand the electronic ground state of $2H$-$NbSe_2$.

4) The wave vector and temperature dependencies of the electron-hole (i.e. Lindhard) response function of the blue bronze $K_{0.3}MoO_3$ has three components corresponding to three possible nesting processes of its warped double sheet quasi-1D FS. We have quantitatively analyzed the $k_F^I + k_F^{II}$ inter-band electron-hole component which is responsible for the Peierls instability. We have shown that the electron-hole coherence length of this response determines the length scale of the experimental intra-chain CDW correlations and the intra-chain $q_{\|}$ dependence of such response also determines the shape of the Kohn anomaly experimentally measured. All these features prove that the Peierls transition of the blue bronze can be well accounted for by the weak electron-phonon coupling theory of this transition

in the adiabatic approximation. This is the first time that such theory, already established in the 1970s, is quantitatively verified on the basis of first-principles calculations for a real material. In addition, we propose that the inter-chain coupling is achieved through Coulomb coupling between dipolar CDWs.

5) We have studied the electron-hole Lindhard response function for three Bechgaard salts $(TMTSF)_2PF_6$, $(TMTSF)_2NO_3$ and $(TMTSF)_2ClO_4$ both in the metallic and anion ordered phases. The Lindhard response is found to change considerably with temperature and these changes are clearly associated with dimensional crossovers. Near the spin density wave instability it has the shape of a broad triangular plateau as a result of the multiple nesting associated with the warped quasi-one-dimensional Fermi surface. The thermal dependence of the inverse electron-hole coherence length based on these calculations compares very well with the thermal evolution of the $2k_F$ Bond Order Wave correlation lengths measured for the $(TMTSF)_2PF_6$ and $(TMTSF)_2ClO_4$ salts. The existence of a triangular plateau of maxima in the low temperature Lindhard response of these salts should favor a substantial mixing of q-dependent fluctuations which can have important consequences in understanding the nature of the spin density wave transition, the mechanism of superconductivity and the magneto-transport of these paradigmatic quasi-one-dimensional materials.

6) Secondly we have dismissed a Fermi surface driven instability as the origin of the $2a\times2a\times3c$ modulated structure of $TaTe_4$ based on the Lindhard function calculation. We have calculated the phonon dispersion and described the ordering of the possible modulated phases. The optimized $2a\times2a\times3c$ structure is found to be the more stable in agreement with the experimental observations. The nature of the distortions with respect to the average structure suggests that the driving force for the distortion is the maximization of Ta metal-metal bonding subject to inducing the minimum decrease in bonding of the Te sublatice. The band structure both in the average and modulated phases is found to exhibit an extensive mixing

of the Ta d_{z^2} and Te p bands, in contrast with the usual situation in transition metal sulphides and selenides.

7) The results of this study pave the way for future studies on low-dimensional metals as for instance: (i) the generalization of the inter-chain coupling mechanism proposed for the blue bronze to other CDW oxides and bronzes such as the monophosphate tungsten bronzes, (ii) the extension of the work concerning the implications of the existence of a triangular plateau of maxima to other molecular conductors with warped open Fermi surfaces, and (iii) since our work suggests that transition metal chalcogenides have a weaker tendency than transition metal oxides and bronzes to exhibit Fermi surface nesting driven instabilities, the origin of the CDWs occurring in low dimensional transition metal chalcogenides should be reconsidered.

A. PHONON PATTERN OF DOPED $TISE_2$ SINGLE-LAYERS NEXT TO THE INCOMMENSURATE PHASE

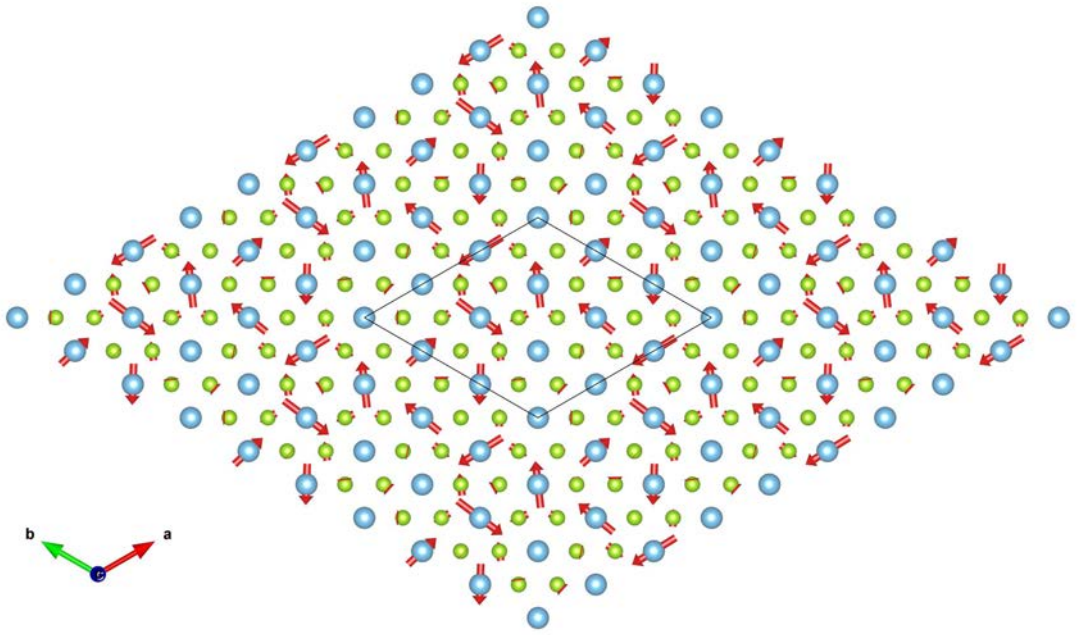

Figure A.1: 3×3 approximation to the incommensurate CDW phase of $TiSe_2$ single-layers doped with 0.24 e^-/f.u. In the figure above we present the $3Q$ phonon displacement pattern which further lowers the energy of the 3×3 supercell.

B. STM IMAGE COMPARISON OF $TITE_2$

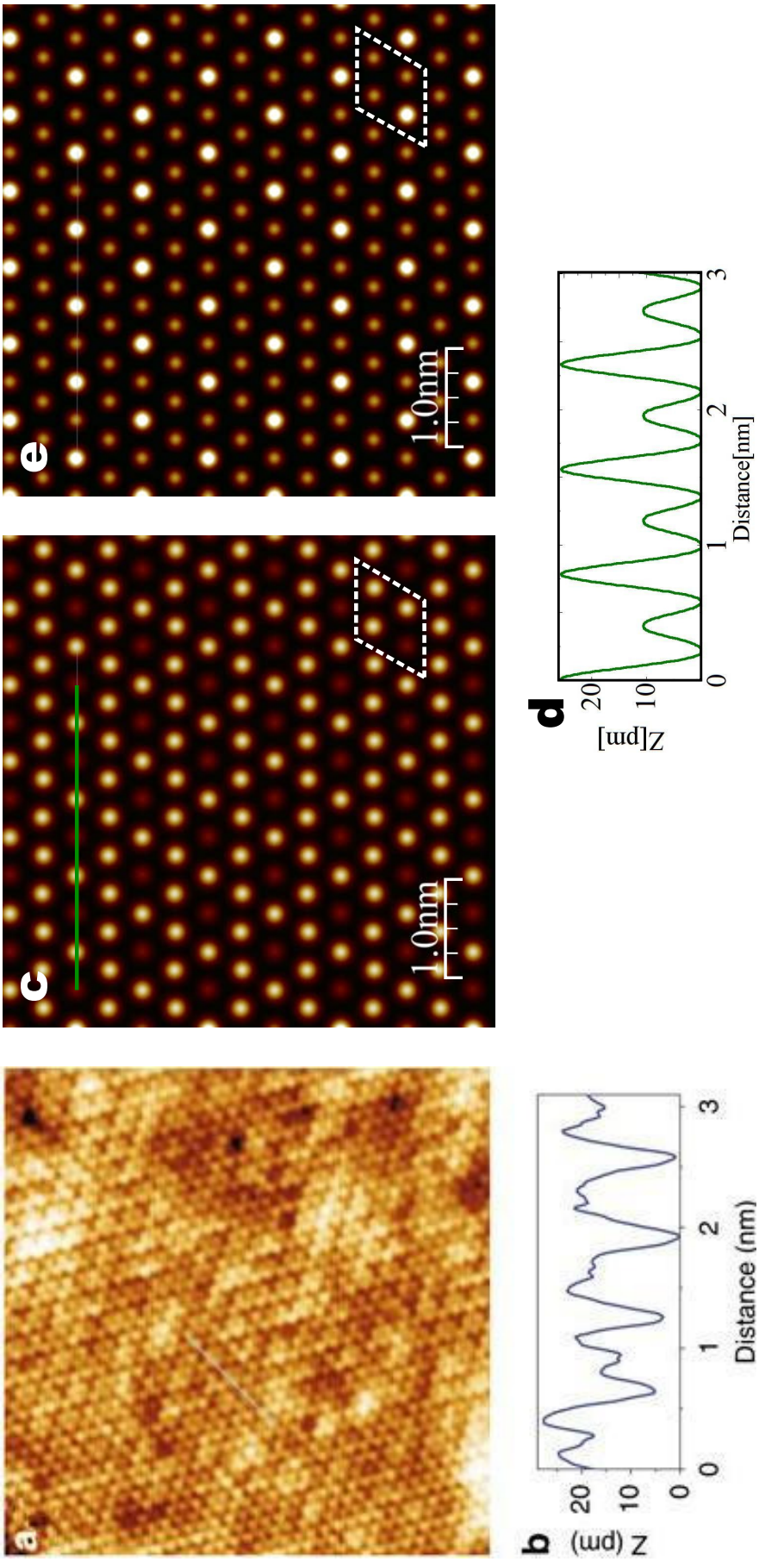

Figure B.1: Experimental STM image (a) for the single-layer $TiTe_2$ taken and adapted from [55] under Creative Commons Attribution 4.0 International License. The experimental image has a 12×12 nm, a sample bias of 105 mV and a tunneling current of 1.0 nA [55]. Experimental height profile (b) shows a modulation as low as 5 nm.[55]. Occupied (c) simulated STM images of the distorted structure under 2% bi-axial strain for bias polarity +100 meV. Unoccupied (e) simulated STM images of the distorted structure under 2% bi-axial strain for bias polarity +100 meV. Calculated topographic profile (d) along the chain of strongly modulated atoms shows a clear doubling in the periodicity of the structure.

C. FERMI SURFACE WARPING OF BECHGAARD SALTS

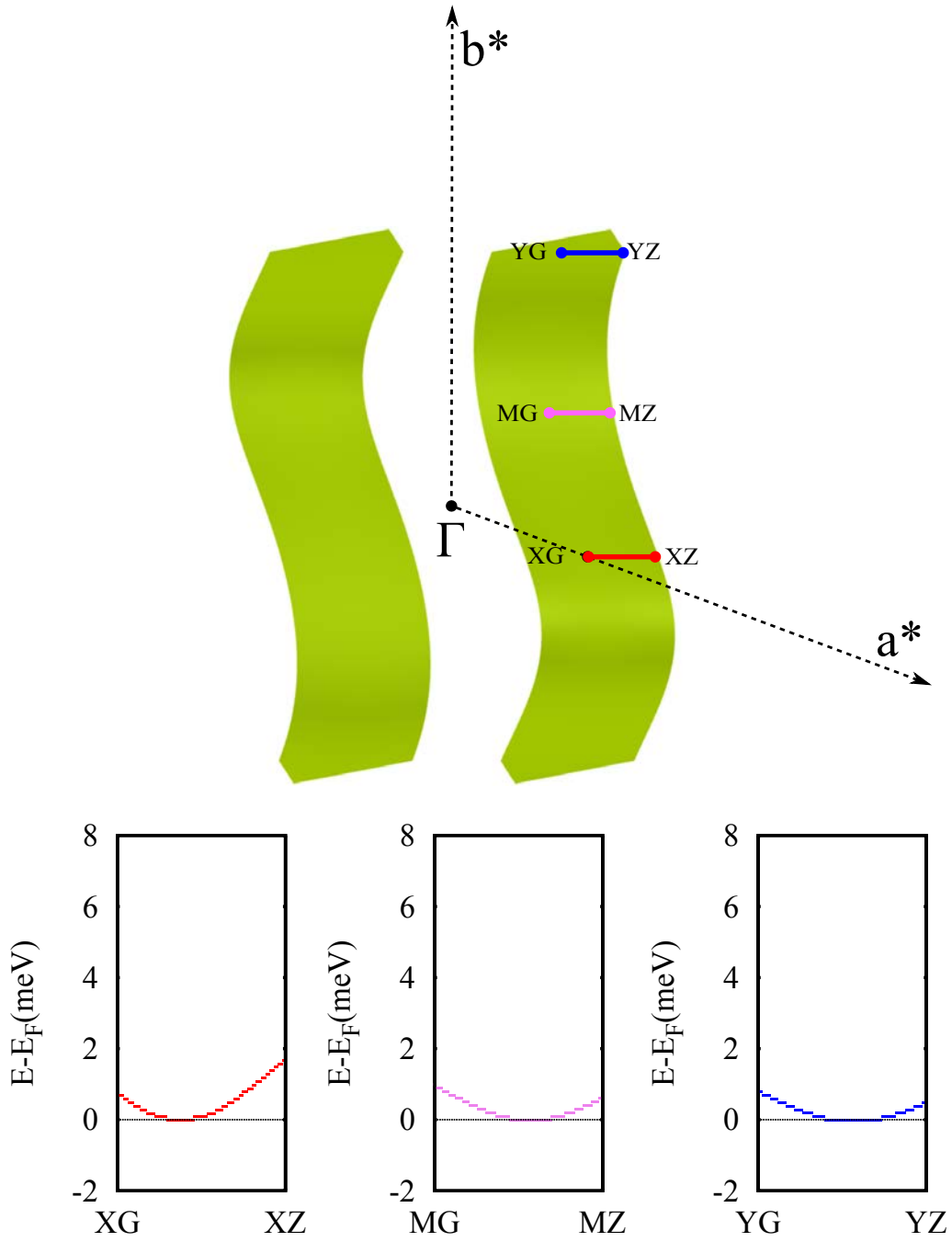

Figure C.1: Fermi surface warping of $(TMTSF)_2PF_6$ along the c^* direction. One can note that $(TMTSF)_2PF_6$ has basically no warping along this direction within the precision of the method.

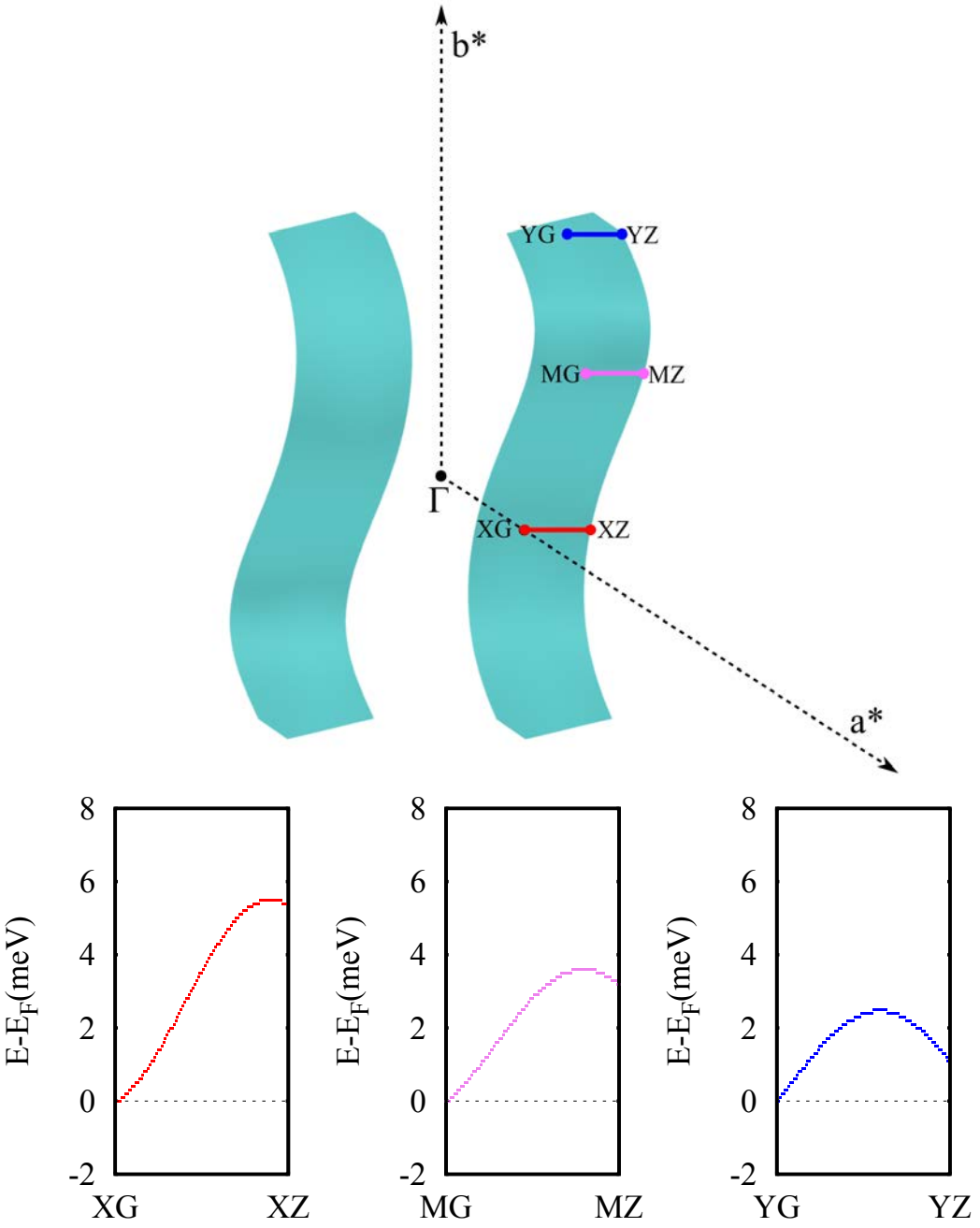

Figure C.2: Fermi surface warping of $(TMTSF)_2ClO_4$ along the c^* direction. One can note that $(TMTSF)_2ClO_4$ has non-negligible warping along this direction within the precision of the method.

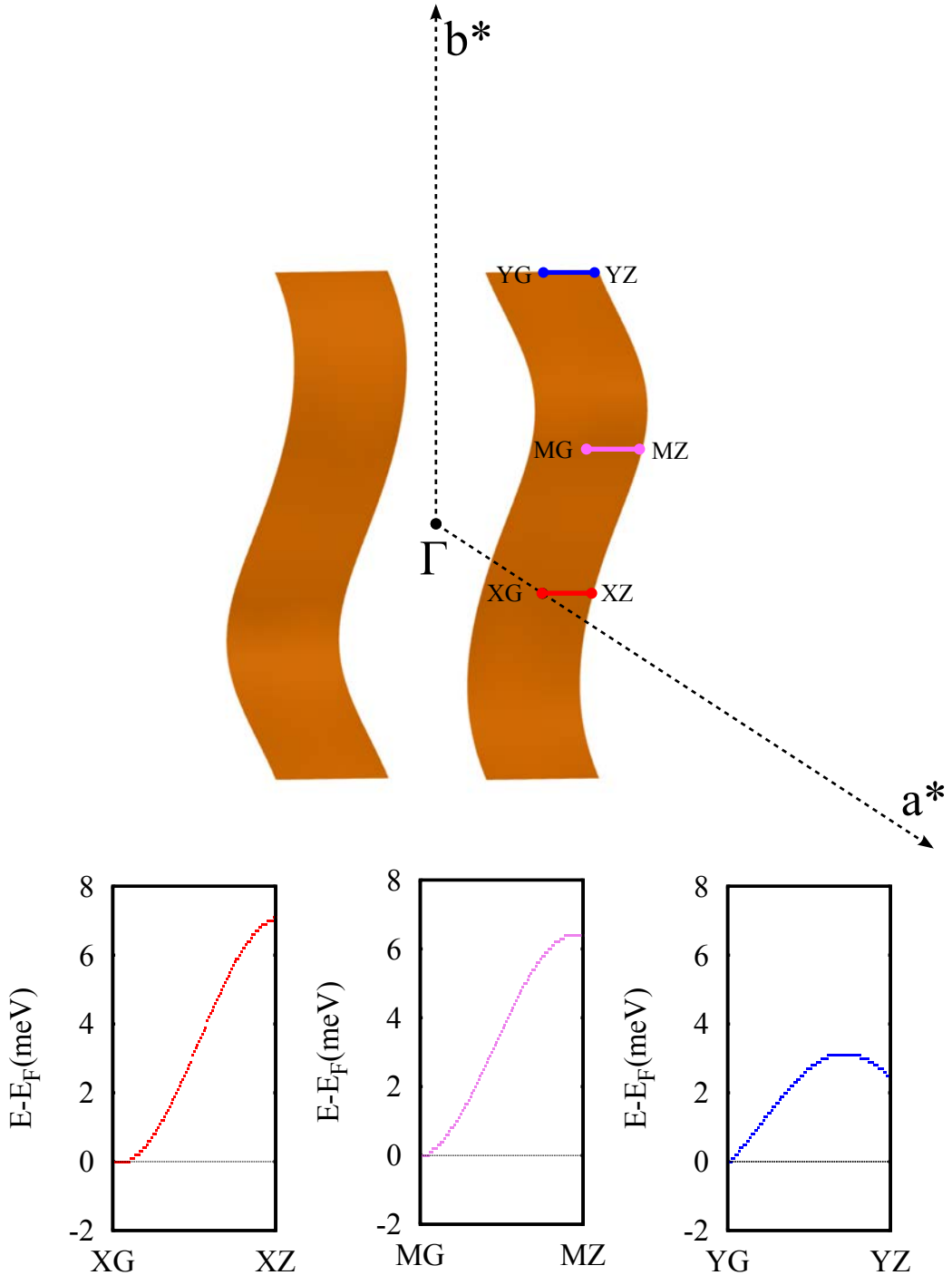

Figure C.3: Fermi surface warping of $(TMTSF)_2NO_3$ along the c^* direction. One can note that $(TMTSF)_2NO_3$ has non-negligible warping along this direction within the precision of the method.

BIBLIOGRAPHY

[1] R. Peierls. Zur Theorie der elektrischen und thermischen Leitfähigkeit von Metallen. *Annalen der Physik*, 396(2):121–148, 1930.

[2] H. Fröhlich. On the Theory of Superconductivity: The One-Dimensional Case. *Proc. R. Soc. A*, 223, 1954.

[3] R.E. Peierls. *Quantum Theory of Solids*. International Series of Monographs on Physics. Clarendon Press, 1996.

[4] R. Comès, M. Lambert, H. Launois, and H. R. Zeller. Evidence for a Peierls Distortion or a Kohn Anomaly in One-Dimensional Conductors of the Type $K_2Pt(CN)_4Br_{0.30}{\cdot}xH_20$. *Phys. Rev. B*, 8:571–575, 1973.

[5] J.A. Wilson, F.J. Di Salvo, and S. Mahajan. Charge-density waves and superlattices in the metallic layered transition metal dichalcogenides. *Adv. Phys.*, 24(2):117–201, March 1975.

[6] P. M. Williams, G. S. Parry, and C. B. Scrub. Diffraction evidence for the Kohn anomaly in 1T-TaS_2. *Philos. Mag.*, 29:695–699, 1974.

[7] J. L. Hodeau, M. Marezio, C. Roucau, R. Ayroles, A. Meerschaut, J. Rouxel, and P. Monceau. Charge-density waves in $NbSe_3$ at 145 K: crystal structures, x-ray and electron diffraction studies. *J. Phys. C.: Solid State Phys.*, 11:4117–4134, 1978.

[8] P. Monceau, N. P. Ong, A. M. Portis, A. Meerschaut, and J. Rouxel. Electric Field Breakdown of Charge-Density-Wave-Induced Anomalies in $NbSe_3$. *Phys. Rev. Lett.*, 37:602–606, 1976.

[9] J. Dumas and C. Schlenker and J. Marcus and R. Buder. Nonlinear Conductivity and Noise in the Quasi One-Dimensional Blue Bronze $K_{0.30}MoO_3$. *Phys. Rev. Lett.*, 50:757–760, 1983.

[10] L. B. Coleman, M. J. Cohen, D. J. Sandman, F. G. Yamagishi, A. F. Garito, and A. J. Heeger. Superconducting fluctuations and the Peierls instability in an organic solid. *Solid State Commun.*, 12:1125–1132, 1973.

[11] J. P. Ferraris, D. O. Cowan, V. V. Walatka, and J. H. Perlstein. Electron transfer in a new highly conducting donor-acceptor complex. *J. Am. Chem. Soc.*, 95:948, 1973.

[12] D. Jérome, A. Mazaud, M. Ribault, and K. Bechgaard. Superconductivity in a synthetic organic conductor $(TMTSF)_2PF_6$. *J. Phys. Lett.*, 41:L95–L98, 1980.

[13] P. Monceau. Electronic crystals: an experimental overview. *Advances in Physics*, 61(4):325–581, 2012.

[14] Y. Cao, A. Mishchenko, G. L. Yu, E. Khestanova, A. P. Rooney, E. Prestat, A. V. Kretinin, P. Blake, M. B. Shalom, C. Woods, J. Chapman, G. Balakrishnan, I. V. Grigorieva, K. S. Novoselov, B. A. Piot, M. Potemski, K. Watanabe, T. Taniguchi, S. J. Haigh, A. K. Geim, and R. V. Gorbachev. Quality Heterostructures from Two-Dimensional Crystals Unstable in Air by Their Assembly in Inert Atmosphere. *Nano Letters*, 15(8):4914–4921, 2015.

[15] G. R. Bhimanapati, Z. Lin, V. Meunier, Y. Jung, J. Cha, S. Das, D. Xiao, Y. Son, M. S. Strano, V. R. Cooper, L. Liang, S. G. Louie, E. Ringe, W. Zhou, S. S. Kim, R. R. Naik, B. G. Sumpter, H. Terrones, F. Xia, Y. Wang, J. Zhu, D. Akinwande, N. Alem, J. A. Schuller, R. E. Schaak, M. Terrones, and J. A. Robinson. Recent Advances in Two-Dimensional Materials beyond Graphene. *ACS Nano*, 9:11509–11539, 2015.

[16] M. Born and R. Oppenheimer. Zur Quantentheorie der Molekeln. *Annalen der Physik*, 389(20):457–484, 1927.

[17] D. R. Hartree. The Wave Mechanics of an Atom with a Non-Coulomb Central Field. Part I. Theory and Methods. *Mathematical Proceedings of the Cambridge Philosophical Society*, 24(1):89–110, 1928.

[18] V. Fock. Näherungsmethode zur Lösung des quantenmechanischen Mehrkörperproblems. *Zeitschrift für Physik*, 61(1):126–148, Jan 1930.

[19] J. C. Slater. The Self Consistent Field and the Structure of Atoms. *Phys. Rev.*, 32:339–348, 1928.

[20] J. C. Slater. Note on Hartree's Method. *Phys. Rev.*, 35:210–211, Jan 1930.

[21] J. C. Slater. A Simplification of the Hartree-Fock Method. *Phys. Rev.*, 81:385–390, 1951.

[22] L. H. Thomas. The calculation of atomic fields. *Mathematical Proceedings of the Cambridge Philosophical Society*, 23(5):542–548, 1927.

[23] E. Fermi. Un Metodo Statistico per la determinazione di Alcune priorieta dell' atome. *Rend. Accad. Naz. Lincei*, 6:602, 1927.

[24] Richard M. Martin. *Electronic Structure: Basic Theory and Practical Methods*. Cambridge University Press, 2004.

[25] P. Hohenberg and W. Kohn. Inhomogeneous Electron Gas. *Phys. Rev.*, 136:B864–B871, Nov 1964.

[26] W. Kohn and L. J. Sham. Self-Consistent Equations Including Exchange and Correlation Effects. *Phys. Rev.*, 140:A1133–A1138, Nov 1965.

[27] J. M. Soler, E. Artacho, J. D Gale, A. García, J. Junquera, P. Ordejón, and D. Sánchez-Portal. The SIESTA method for ab initio order-N materials simulation. *J. Physics: Condens. Matter*, 14:2745–2779, 2002.

[28] E. Artacho, E. Anglada, O. Diéguez, J. D. Gale, A. García, J. Junquera, R. M. Martin, P. Ordejón, J. M. Pruneda, D. Sánchez-Portal, and J. M. Soler. The SIESTA method; developments and applicability. *J. Physics: Condens. Matter*, 20:064208, 2008.

[29] J. Junquera, Ó. Paz, D. Sánchez-Portal, and E. Artacho. Numerical atomic orbitals for linear-scaling calculations. *Phys. Rev. B*, 64:235111, 2001.

[30] W. Kohn. Image of the Fermi Surface in the Vibration Spectrum of a Metal. *Phys. Rev. Lett.*, 2:393–394, May 1959.

[31] J. Lindhard and K. Dan. On the properties of a gas of charged particles. *Vidensk. Selk. Mat. Fys. Medd.*, 28:8, 1954.

[32] B. Mihaila. Lindhard function of a d-dimensional Fermi gas. *https://arxiv.org/pdf/1111.5337.pdf*, 2011.

[33] X. Zhu, J. Guo, J. Zhang, and E. W. Plummer. Misconceptions associated with the origin of charge density waves. *Advances in Physics: X*, 2(3):622–640, 2017.

[34] G. Grüner. *Density Waves in Solids*. Frontiers in physics. Addison-Wesley Publishing Company, Advanced Book Program, 1994.

[35] M. H. Whangbo, E. Canadell, P. Foury, and J. P. Pouget. Hidden Fermi Surface Nesting and Charge Density Wave Instability in Low-Dimensional Metals. *Science*, 252(5002):96–98, 1991.

[36] S K Chan and V Heine. Spin density wave and soft phonon mode from nesting Fermi surfaces. *Journal of Physics F: Metal Physics*, 3(4):795–809, apr 1973.

[37] J. P. Pouget, B. Hennion, C. Escribe-Filipini, and M. Sato. Neutron-scattering investigations of the Kohn anomaly and on the phase and amplitude charge-density-wave excitations of the blue bronze $K_{0.3}MoO_3$. *Phys. Rev. B*, 43:8421–8430, 1991.

[38] H. Requardt, J. E. Lorenzo, P. Monceau, R. Currat, and M. Krisch. Dynamics in the charge-density-wave system $NbSe_3$ using inelastic X-ray scattering with meV energy resolution. *Phys. Rev. B*, 66:214303, Dec 2002.

[39] N. Wakabayashi, H.G. Smith, and R. Shanks. Two dimensional Kohn anomally in $NbSe_2$. *Physics Letters A*, 50(5):367–368, 1974.

[40] B. Guster, E. Canadell, M. Pruneda, and P. Ordejón. First principles analysis of the CDW instability of single-layer 1 T -$TiSe_2$ and its evolution with charge carrier density. *2D Materials*, 5(2):025024, 2018.

[41] B. Guster, M. Pruneda, P. Ordejón and E. Canadell, 2019. work in progress.

[42] B. Guster, M. Pruneda, P. Ordejón, E. Canadell, and J.-P. Pouget. Evidence for the weak coupling scenario of the Peierls transition in the blue bronze. *Phys. Rev. Materials*, 3:055001, May 2019.

[43] B. Guster, M. Pruneda, P. Ordejón, E. Canadell, and J.-P. Pouget, 2019. Work in progress.

[44] M. D. Johannes, I. I. Mazin, and C. A. Howells. Fermi-surface nesting and the origin of the charge-density wave in $Nbse_2$. *Phys. Rev. B*, 73:205102, May 2006.

[45] N. J. Doran. A calculation of the electronic response function in $2H$-$NbSe_2$ including electron-phonon matrix element effects. *Journal of Physics C: Solid State Physics*, 11(24):L959–L962, dec 1978.

[46] G. Travaglini, I. Morke, and P. Wachter. CDW evidence in one-dimensional $K_{0.3}MoO_3$ by means of Raman scattering. *Solid State Commun.*, 45:289–292, 1983.

[47] J. Chaussy, P. Haen, J.C. Lasjaunias, P. Monceau, G. Waysand, A. Waintal, A. Meerschaut, P. Molinié, and J. Rouxel. Phase transitions in $NbSe_3$. *Solid State Communications*, 20(8):759–763, 1976.

[48] J. Á. Silva-Guillén, P. Ordejón, F. Guinea, and E. Canadell. Electronic structure of $2H$-$NbSe_2$ single-layers in the CDW state. *2D Materials*, 3(3):035028, sep 2016.

[49] J. P. Pouget, C. Noguera, A. H. Moudden, and R. Moret. Structural study of the charge-density-wave phase transition of the blue bronze: $K_{0.3}MoO_3$. *J. de Physique*, 46:1731–1742, 1985.

[50] K. Rossnagel. On the origin of charge-density waves in select layered transition-metal chalcogenides. *J. Phys.:Condens. Matter*, 23:213001, 2011.

[51] Kitomi Tsutsumi, T. Tamegai, S. Kagoshima, H. Tomozawa, and M. Sato. Transport Properties of the Charge-Density-Wave State in $K_{0.30}MoO_3$. *Journal of the Physical Society of Japan*, 53(11):3946–3951, 1984.

[52] S. F. Meyer, R. E. Howard, G. R. Stewart, J. V. Acrivos, and T. H. Geballe. Properties of intercalated $2H$-$NbSe_2$, $4Hb$-TaS_2, and $1T$-TaS_2. *The Journal of Chemical Physics*, 62(11):4411–4419, 1975.

[53] F. J. Di Salvo, D. E. Moncton, and J. V. Waszczak. Electronic properties and superlattice formation in the semimetal $TiSe_2$. *Phys. Rev. B*, 14:4321–4328, Nov 1976.

[54] G. Li, W. Z. Hu, D. Qian, D. Hsieh, M. Z. Hasan, E. Morosan, R. J. Cava, and N. L. Wang. Semimetal-to-Semimetal Charge Density Wave Transition in $1T$-$TiSe_2$. *Phys. Rev. Lett.*, 99:027404, 2007.

[55] P. Chen, W. W. Pai, Y.-H. Chan, A. Takayama, C.-Z. Xu, A. Karn, S. Hasegawa, M. Y. Chou, S.-K. Mo, A.-V. Fedorov, and T.-C. Chiang. Emergence of charge density waves and a pseudogap in single-layer $TiTe_2$. *Nature Communications*, 8(1):516, 2017.

[56] K. Dolui and S. Sanvito. Dimensionality-driven phonon softening and incipient charge density wave instability in TiS_2. *EPL*, 115:47001, 2016.

[57] C. Riekel. Structure Refinement of $TiSe_2$ by Neutron Diffraction. *J. Solid. State Chem.*, 17:389–392, 1976.

[58] O. Anderson, G. Karschnick, R. Manzke, and M. Skibowski. The phase transition in the electronic structure of $1T$-$TiSe_2$. *Solid State Commun.*, 53:339–342, 1985.

[59] K. Rossnagel, L. Kipp, and M. Skibowski. Charge-density-wave transition in $1T$-$TiSe_2$: Excitonic insulator versus band-type Jahn-Teller mechanism. *Phys. Rev. B*, 65:235101, 2002.

[60] T. Pillo, J. Hayoz, H. Berger, F. Levy, Schlapbach L., and P. Aebi. Photoemission of bands above the Fermi level: The excitonic insulator phase transition in $1T$-$TiSe_2$. *Phys. Rev. B*, 61:16213–16222, 2000.

[61] H. Cercellier, C. Monney, F. Clerc, C. Battaglia, L. Despont, M. G. Garnier, H Beck, P. Aebi, L. Patthey, H. Berger, and L. Forro. Evidence for an Excitonic Insulator Phase in $1T$-$TiSe_2$. *Phys. Rev. Lett.*, 99:146403, 2007.

[62] T. Rohwer, S. Hellman, M. Wiesenmayer, A. Sohrt, A. Stangre, B. Slomski, A Carr, Y. Liu, L. M. Avila, M. Kallane, S. Mathias, L. Kipp, K. Rossnagel, and M. Bauer. Collapse of long-range charge order tracked by time-resolved photoemission at high momenta. *Nature (London)*, 471:490, 2011.

[63] M. M. May, C. Brabetz, C. Janowitz, and R. Manzke. Charge-Density-Wave Phase of $1T$-$TiSe_2$: The Influence of Conduction Band Population. *Phys. Rev. Lett.*, 107:176405, 2011.

[64] F. Weber, S. Rosenkranz, J.-P. Castellan, R. Osborn, G. Karapetrov, R. Hott, R. Heid, K.-P. Bohnen, and A. Alatas. Electron-Phonon Coupling and the Soft Phonon Mode in $1T$-$TiSe_2$. *Phys. Rev. Lett.*, 107:266401, 2011.

[65] M. Cazzaniga, H. Cercelier, M. Holzmann, C. Monney, P. Aebi, G. Onida, and V. Olevano. *Ab initio* many-body effects in $TiSe_2$: A possible excitonic insulator scenario from GW band-shape renormalization. *Phys. Rev. B*, 85:195111, 2012.

[66] A. Kogar, M. S. Rak, S. Vig, A. A. Hussain, F. Flicker, Y. I. Joe, L. Venema, G. J. MacDougall, T. C. Chiang, E. Fradkin, J. van Wezel, and P. Abbamonte. Signatures of exciton condensation in a transition metal dichalcogenide. *Science*, 358:1314–1317, 2017.

[67] T. Kaneko, Y. Ohta, and S. Yunoki. Exciton-phonon cooperative mechanism of the triple-q charge-density-wave and antiferroelectric electron polarization in $TiSe_2$. *Phys. Rev. B*, 97:155131, Apr 2018.

[68] E. Morosan, H. W. Zandbergen, B. S. Dennis, J. W. G. Bos, Y. Onose, T. Klimczuk, A. M. Ramirez, N. P. Ong, and R. J. Cava. Superconductivity in Cu_xTiSe_2. *Nature Physics*, 2:544, 2006.

[69] A. F. Kusmartseva, B. Sipos, H. Berger, L. Forró, and E. Tutis. Pressure induced Superconductivity in Pristine 1T-$TiSe_2$. *Phys. Rev. Lett.*, 103:236401, 2009.

[70] M. Rösner, S Haas, and T. O. Wehling. Phase diagram of electron-doped dichalcogenides. *Phys. Rev. B*, 90:245105, 2014.

[71] J.-P. Peng, J.-Q. Guan, H.-M. Zhang, C.-L. Song, L. Wang, K. He, Q.-K. Xue, and X.-C. Ma. Molecular beam epitaxi growth and scanning tunneling microscopy study of $TiSe_2$ ultrathin films. *Phys. Rev. B*, 91:121113(R), 2015.

[72] K. Sugawara, Y. Nakata, R. Shimizu, P. Han, T. Hitosugi, T. Sato, and T. Takahashi. Unconventional Charge-Density-Wave Transition in Monolayer 1T-$TiSe_2$. *ACS Nano*, 10:1341–1345, 2016.

[73] P. Chen, Y.-H. Chan, X.-Y. Fang, Y. Zhang, M.Y. Chou, S.-K. Mo, Z Hussain, A.-V. Fedorov, and Chiang T.-C. Charge density wave transition in single-layer titanium diselenide. *Nature Communications*, 6:8943, 2015.

[74] D. L. Duong, G. Ryu, A. Hoyer, C. Lin, M. Burghard, and K. Kern. Raman Characterization of the Charge Density Wave Phase of 1T-$TiSe_2$: From Bulk to Atomically Thin Layers. *ACS Nano*, 11:1034–1040, 2017.

[75] P. Goli, J. Khan, D. Wickramaratne, R. K. Lake, and A. A. Balandin. Charge Density Waves in Exfoliated Films of van der Waals Materials: Evolution of Raman Spectrum in 1T-$TiSe_2$. *Nano Lett.*, 12:5941–5945, 2012.

[76] Y. Noat, J. A. Silva-Guillén, T. Cren, V. Cherkez, C. Brun, S. Pons, F. Debontridder, D. Roditchev, W. Sacks, L. Cario, P. Ordejón, A. García, and E. Canadell. Quasiparticle spectra of 2H-$NbSe_2$: Two-band superconductivity and the role of tunneling selectivity. *Phys. Rev. B*, 92:134510, Oct 2015.

[77] L. J. Li, E. C. T. O. O'Farrell, K. P. Loh, G. Eda, B. Özyilmaz, and A. H. Castro-Neto. Controlling many-body states by the electric-field effect in a two-dimensional material. *Nature*, 529:185, 2016.

[78] A. Zunger and A. J. Freeman. Band structure and lattice instability of $TiSe_2$. *Phys. Rev. B*, 17:1839–1842, 1978.

[79] N. Suzuki, A. Yamamoto, and K. Motizuki. Microscopic Theory of the CDW State in 1T-$TiSe_2$. *J. Phys. Soc. Jpn.*, 54:4668–4679, 1985.

[80] K. Motizuki. *Structural Phase Transitions in Layered Transition Metal Compounds*. Reidel: Dordrecht, The Netherlands, 1986.

[81] M. H. Whangbo and E. Canadell. Analogies between the concepts of molecular chemistry and solid-state physics concerning structural instabilities. Electronic origin of the structural modulations in layered transition metal dichalcogenides. *J. Am. Chem. Soc.*, 114(24):9587–9600, 1992.

[82] C. M. Fang, R. A. de Groot, and C. Haas. Bulk and surface electronic structure of 1T-TiS_2 and 1T-$TiSe_2$. *Phys. Rev. B*, 56:4455–4463, 1997.

[83] R. A. Jishi and H. M. Alyahyaei. Electronic structure of superconducting copper intercalated transition metal dichalcogenides: First-principles calculations. *Phys. Rev. B*, 78:144516, 2008.

[84] Zh. Zhu, Y. Cheng, and U. Schwingenschlögl. Origin of the charge density wave in 1T- $TiSe_2$. *Phys. Rev. B*, 85:245133, 2012.

[85] M. Calandra and F. Mauri. Charge-density wave and superconducting dome in $TiSe_2$ from electron-phonon interaction. *Phys. Rev. Lett.*, 106:196406, May 2011.

[86] Zh. Zhu, Y. Cheng, and U. Schwingenschlögl. Pressure controlled transition into a self-induced topological superconducting surface state. *Sci. Rep.*, 4:4025, 2014.

[87] M. Hellgren, J. Baima, R. Bianco, F. Calandra, M. Mauri, and L. Wirtz. Critical Role of the Exchange Interaction for the Electronic Structure and Charge.Density-Wave Formation in $TiSe_2$. *Phys. Rev. Lett.*, 119:176401, 2017.

[88] R. Bianco, M. Calandra, and F. Mauri. Electronic and vibrational properties of $TiSe_2$ in the charge-density-wave phase from first principles. *Phys. Rev. B*, 92:094107, 2015.

[89] D. L. Duong, M. Burghard, and J. C. Schön. Ab-initio computation of the transition temperature of the charge density wave transition in $TiSe_2$. *Phys. Rev. B*, 92:245131, 2015.

[90] Z.-G. Fu, Z.-Y. Hu, Y. Yang, Y. Lu, F.-W. Zheng, and P. Zhang. Modulation of doping and biaxial strain on the transition temperature of the charge density wave transition in 1T-$TiSe_2$. *RSC Advances*, 6:76972–76979, 2016.

[91] Z.-G. Fu, J.-H. Wang, Y. Yang, W. Yang, L.-L. Liu, Z.-Y. Hu, and P. Zhang. Doping stability and charge-density-wave transition of strained 1T-$TiSe_2$. *EPL*, 120:17006, 2017.

[92] B. Singh, C.-H. Hsu, W.-F. Tsai, V. M. Pereira, and H. Lin. Stable charge density wave phase in a 1T–$TiSe_2$ monolayer. *Phys. Rev. B*, 95:245136, 2017.

[93] P. Chen, Y.-H. Chan, M.-H. Wong, X.-Y. Fang, M. Y. Chou, S.-K. Mo, Z. Hussain, A.-V. Fedorov, and T.-C. Chiang. Dimensional Effects on the Charge Density Waves in Ultrathin Films of $TiSe_2$. *Nano Lett.*, 16:6331–6336, 2016.

[94] J. Heyd, G. E. Scuseria, and M. Ernzerhof. Hybrid functionals based on a screened Coulomb potential. *J. Chem. Phys.*, 118:8207–8215, 2003.

[95] .-F. Fang, H. Hong, P. Chen, and T.-C. Chiang. X-ray study of the charge-density-wave transition in single-layer $TiSe_2$. *Phys. Rev. B*, 95:201409(R), 2017.

[96] P. Hohenberg and W. Kohn. Inhomogeneous Electron Gas. *Physical Review*, 136(3B):B864–B871, nov 1964.

[97] W. Kohn and L. J. Sham. Self-Consistent Equations Including Exchange and Correlation Effects. *Physical Review*, 140(4A):A1133–A1138, nov 1965.

[98] J. P. Perdew, K. Burke, and M. Ernzerhof. Generalized Gradient Approximation Made Simple. *Phys. Rev. Lett.*, 77(18):3865–3868, 1996.

[99] N. Troullier and J. L. Martins. Efficient pseudopotentials for plane-wave calculations. *Phys. Rev. B*, 43:1993–2006, 1991.

[100] L. Kleinman and D. M. Bylander. Efficacious Form for Model Pseudopotentials. *Phys. Rev. Lett.*, 48:1425–1428, 1982.

[101] E. Artacho, D. Sànchez-Portal, P. Ordejón, A. García, and J. M. Soler. Linear-Scaling ab-initio Calculations for Large and Complex Systems. *Phys. Stat. Solidi (b)*, 215:809–817, 1999.

[102] S. G. Louie, S. Froyen, and M. L. Cohen. Nonlinear ionic pseudopotentials in spin-density-functional calculations. *Phys. Rev. B*, 26:1738–1742, 1982.

[103] H. J. Monkhorst and J. D. Pack. Special points for Brillouin-zone integrations. *Phys. Rev. B*, 13:5188–5192, 1976.

[104] J.A. Wilson, F.J. Di Salvo, and S. Mahajan. Charge-density waves and superlattices in the metallic layered transition metal dichalcogenides. *Adv. Phys.*, 24(2):117–201, March 1975.

[105] A. H. Castro Neto. Charge Density Wave, Superconductivity, and Anomalous Metallic Behavior in 2D Transition Metal Dichalcogenides. *Physical Review Letters*, 86:4382, 2001.

[106] M. M. Ugeda, A. J. Bradley, Y. Zhang, S. Onishi, Y. Chen, W. Ruan, C. Ojeda-Aristizabal, H. Ryu, M. T. Edmonds, H.-Z. Tsai, A. Riss, S.-K. Mo, D. Lee, A. Zettl, Z. Hussain, Z.-X. Shen, and M. F. Crommie. Characterization of collective ground states in single-layer $2H$-$NbSe_2$. *Nature Physics*, 12(12):92, 2016.

[107] X. Xi, L. Zhao, Z. Wang, H. Berger, L. Forró, J. Shan, and K. F. Mak. Strongly enhanced charge-density-wave order in monolayer $NbSe_2$. *Nature Nanotechnology*, 10(9):765–769, Sep 2015.

[108] D. K. G. de Boer, C. F. van Bruggeb, G. W. Bus, R. Coehoorn, C. Haas, and G. A. Sawatzky. Titanium ditelluride: Band structure, photoemission, and electrical and magnetic properties. *Phys. Rev. B*, 29:6797, 1984.

[109] Y. Koike, O. Okamura, T. Nakanomyo, and T. Fukase. Log T Dependence of Resistivity and Negative Magnetoresistancebin the Layered Compound $TiTe_2$. *J. Phys. Soc. Jpn.*, 52:597, 1983.

[110] P. B. Allen and N. Chetty. $TiTe_2$: Inconsistency between transport properties and photoemission results. *Phys. Rev. B*, 50:14855, 1994.

[111] S. Fragkos, R. Sant, C. Alvarez, A. Bosak, P. Tsipas, D. Tsoutsou, H. Okuno, G. Renaud, and A. Dimoulas. Room Temperature Commensurate Charge Density Wave in Epitaxial Strained $TiTe_2$ Multilayer Films. *Advanced Materials Interfaces*, 0(0):1801850, 2019.

[112] A. V. Krukau, O. A. Vydrov, A. F. Izmaylov, and G. E. Scuseria. Influence of the exchange screening parameter on the performance of screened hybrid functionals. *The Journal of Chemical Physics*, page 224106, 2006.

[113] B. Guster, R. Robles, M. Pruneda, E. Canadell, and P. Ordejón. 2×2 charge density wave in single-layer $TiTe_2$. *2D Materials*, 6(1):015027, dec 2018.

[114] Y. Arnaud and M. Chevreton. Etude comparative des composés TiX_2 (X = S, Se, Te). Structures de $TiTe_2$ et TiSeTe. *J. Sol. State Chem.*, 39:2230, 1981.

[115] S.-M. Choi, S.-H. Jhi, and Y.-W. Son. Controlling Energy Gap of Bilayer Graphene by Strain. *Nano Lett.*, 10:3486–3489, 2010.

[116] P. Johary and U. B. Shenoy. Tuning the electronic properties of semiconducting transition metal dichalcogenides by applying mechanical strains. *ACS Nano*, 6:5449–5456, 2012.

[117] R. Biele, E. Flores, J. R. Ares, C. Sánchez, I. J. Ferrer, G. Rubio-Bollinger, A. Castellanos-Gomez, and R. D'Agosta. Strain-induced band gap engineering in layered TiS_3. *Nano Research*, 11:225–232, 2018.

[118] R. Roldán, L. Chirolli, E. Prada, J. A. Silva-Guillén, P. San-Jose, and F. Guinea. Theory of 2D crystals: graphene and beyond. *Chem. Soc. Rev.*, 46(15):4387–4399, 2017.

[119] C. Xu, P. A. Brown, and K. L. Shuford. Strain-induced semimetal-to-semiconductor transition and indirect-to-direct band gap transition in monolayer 1T-TiS_2. *RSC Adv.*, 5:83876, 2015.

[120] A. Samanta, T. Pandey, and A. K. Singh. Strain-induced electronic phase transition and strong enhancement of thermopower of TiS_2. *Phys. Rev. B.*, 90:174301, 2014.

[121] G. Kresse and J. Furthmüller. Efficient iterative schemes for ab initio total-energy calculations using a plane-wave basis set. *Physical Review B*, 54:11169–11186, 1996.

[122] P. E. Blöchl. Projector augmented-wave method. *Physical Review B*, 50:17953, 1994.

[123] G. Kresse and D. Joubert. From ultrasoft pseudopotentials to the projector augmented-wave method. *Physical Review B*, 59:1758, 1999.

[124] X. Zhu, Y. Cao, J. Zhang, E. W. Plummer, and J. Guo. Classification of charge density waves based on their nature. *Proceedings of the National Academy of Sciences*, 112(8):2367–2371, 2015.

[125] D. E. Moncton, J. D. Axe, and F. J. DiSalvo. Neutron scattering study of the charge-density wave transitions in 2H-$TaSe_2$ and 2H-$NbSe_2$. *Physical Review B*, 16(2):801, 1977.

[126] E. Revolinsky, E. P. Lautenschlager, and C. H. Armitage. Layer structure superconductor. *Solid State Communications*, 1(3):59–61, August 1963.

[127] A. Meerschaut and C. Deudon. Crystal structure studies of the 3R-$Nb_{1.09}S_2$ and the 2H-$NbSe_2$ compounds: correlation between nonstoichiometry and stacking type (= polytypism). *Materials Research Bulletin*, 36(9):1721–1727, July 2001.

[128] C. D. Malliakas and M. G. Kanatzidis. Nb-Nb Interactions Define the Charge Density Wave Structure of 2H-$NbSe_2$. *Journal of the American Chemical Society*, 135(5):1719–1722, February 2013.

[129] F. Zheng, Z. Zhou, X. Liu, and J. Feng. First-principles study of charge and magnetic ordering in monolayer $NbSe_2$. *Phys. Rev. B*, 97:081101, Feb 2018.

[130] C.-S. Lian, C. Si, and W. Duan. Unveiling Charge-Density Wave, Superconductivity, and Their Competitive Nature in Two-Dimensional $NbSe_2$. *Nano Letters*, 18(5):2924–2929, 2018.

[131] C. E. Sanders, M. Dendzik, A. S. Ngankeu, A. Eich, A. Bruix, M. Bianchi, J. A. Miwa, B. Hammer, A/ A. Khajetoorians, and P. Hofmann. Crystalline and electronic structure of single-layer TaS_2. *Phys. Rev. B*, 94:081404, Aug 2016.

[132] O. R. Albertini, A. Y. Liu, and M. Calandra. Effect of electron doping on lattice instabilities in single-layer $1H - TaS_2$. *Phys. Rev. B*, 95:235121, Jun 2017.

[133] S. Kim and Y.-W. Son. Quasiparticle energy bands and Fermi surfaces of monolayer $NbSe_2$. *Phys. Rev. B*, 96:155439, Oct 2017.

[134] S. Lebègue and O. Eriksson. Electronic structure of two-dimensional crystals from *ab initio* theory. *Phys. Rev. B*, 79:115409, Mar 2009.

[135] M. Calandra, I. I. Mazin, and F. Mauri. Effect of dimensionality on the charge-density wave in few-layer 2H-$NbSe_2$. *Phys. Rev. B*, 80:241108, Dec 2009.

[136] M. D. Johannes, I. I. Mazin, and C. A. Howells. Fermi-surface nesting and the origin of the charge-density wave in $NbSe_2$. *Phys. Rev. B*, 73:205102, May 2006.

[137] J. Tersoff and D. R. Hamann. Theory of the scanning tunneling microscope. *Phys. Rev. B*, 31:805–813, Jan 1985.

[138] B. Guster, C. Rubio-Verdú, R. Robles, J. Zaldívar, P. Dreher, M. Pruneda, J. A. Silva-Guillén, D.-J. Choi, J. I. Pascual, M. M. Ugeda, P. Ordejón, and E. Canadell. Coexistence of Elastic Modulations in the Charge Density Wave State of 2H-NbSe2. *Nano Letters*, 19(5):3027–3032, 2019.

[139] C. Schlenker, J. Dumas, M. Greenblatt, and S. van Smaalen, editors. *Physics and Chemistry of Low-Dimensional Inorganic Conductors*. NATO ASI Series B, Physics Vol. 354. Plenum, New York, USA, 1996.

[140] J. Rouxel, editor. *Crystal Chemistry and Properties of Materials with Quasi-One-Dimensional Structures*. Reidel, Dordrecht, The Netherlands, 1986.

[141] C. Schlenker, editor. *Low Dimensional Electronic Properties of Molybdenum Bronzes and Oxides*. Series: Physics and Chemistry of Materials with Low-Dimensional Structures. Springer Netherlands, 1989.

[142] J. P. Pouget. Structural and Dynamical Aspects of the Charge Density Wave instability. In C. Schlenker, J. Dumas, M. Greenblatt, and S. van Smaalen, editors, *Physics and Chemistry of Low-Dimensional Inorganic Conductors*, chapter 11, pages 185–217. NATO ASI Series B, Physics Vol. 354, Plenum, New York, USA, 1996.

[143] S. Barisic. Rigid-Atom Electron-Phonon Coupling in the Tight-Binding Approximation. I. *Phys. Rev. B*, 5:932–941, 1972.

[144] S. Barisic. Self-Consistent Electron-Phonon Coupling in the Tight-Binding Approximation. II. *Phys. Rev. B*, 5:941–951, 1972.

[145] J. Friedel. Phase change and electron-phonon coupling in perfect crystals. In T. Riste, editor, *Electron-Phonon Interactions and Phase Transitions*, pages 1–49. NATO ASI B vol. 29, Plenum Press: New York, USA, 1977.

[146] M. J. Rice and S. Strässler. Theory of quasi-one-dimensional band-conductor. *Sol. State Comm.*, 13:125–128, 1973.

[147] W. L. McMillan. Microscopic model of charge-density waves in $2H$-$TaSe_2$. *Phys. Rev. B*, 16:643–650, 1977.

[148] J. P. Pouget. The Peierls instability and charge density wave in one-dimensional electronic conductors. *C. R. Physique*, 17:332–356, 2016.

[149] P. Y. Le Daeron and S. Aubry. Metal-Insulator Transition in Incommensurate Peierls Chains By Extintion of the Frolich Conductivity. *J. Phys. Coll.*, 44:C3.1573, 1983.

[150] W. M. Lomer. Electronic Structure of Chromium Group Metals. *Proc. Phys. Soc.*, 80:489–496, 1962.

[151] M.-H. Whangbo and L. F. Schneemeyer. Band electronic structure of the molybdenum blue bronze $A_{0.30}MoO_3$ (A = K, Rb). *Inorg. Chem.*, 25:2424–2429, 1986.

[152] A. J. Berlinsky. Organic Metals. *Contemp. Phys.*, 17:331–354, 1976.

[153] M. D. Johannes and I. I. Mazin. Fermi surface nesting and charge density waves in metals. *Phys. Rev. B*, 77:165135, 2008.

[154] J. Graham and A. D. Wadsley. The crystal structure of the blue potassium molybdenum bronze, $K_{0.28}MoO_3$. *Acta Cryst.*, 20:93–100, 1966.

[155] J. L. Mozos, P. Ordejón, and E. Canadell. First-principles study of the blue bronze $K_{0.30}MoO_3$. *Phys. Rev. B*, 65:233105, 2002.

[156] G.-H. Gweon, J. W. Allen, R. Claessen, J. A. Clack, D. M. Poirier, P. J. Benning, C. G. Olson, W. P. Ellis, Y.-X. Zhang, L. F. Schneemeyer, J. Marcus,

and C. Schlenker. Fermi surfaces and single-particle spectral functions of low-dimensional inorganic non-cuprate compounds: the molybdenum bronzes. *J. Phys.: Condens. Matter*, 8:9923–9938, 1996.

[157] J. P. Pouget, S. Kagoshima, C. Schlenker, and J. Marcus. Evidence for a Peierls transition in the blue bronzes $K_{0.3}MoO_3$ and $Rb_{0.3}MoO_3$. *J. Phys. (Paris) Lett.*, 44:L113–L120, 1983.

[158] G. Travaglini, P. Wachter, J. Marcus, and C. Schlenker. The blue bronze $K_{0.3}MoO_3$: A new one-dimensional conductor. *Solid State Comm.*, 37:599–603, 1981.

[159] J. P. Pouget, C. Escribe-Filipini, B. Hennion, R. Currat, A. H-Moudden, R. Moret, J. Marcus, and C. Schlenker. Neutron and X Ray studies of the quasi one dimensional conductor $K_{0.3}MoO_3$. *Mol. Cryst. Liq. Cryst.*, 121:111–115, 1985.

[160] M. Ghedira, J. Chenavas, M. Marezio, and J. Marcus. Crystal structure, dimensionality, and 4d electron distribution in $K_{0.3}MoO_3$ and $Rb_{0.3}MoO_3$. *J. Sol. State Chem.*, 57:300–313, 1985.

[161] E. Canadell and M.-H. Whangbo. Conceptual aspects of structure-property correlations and electronic instabilities, with applications to low-dimensional transition-metal oxides. *Chem. Rev.*, 91:965–1034, 1991.

[162] U. V. Waghmare, H. Kim, I. J. Park, N. Modine, P. Maragakis, and E. Kaxiras. HARES: an efficient method for first-principles electronic structure calculations of complex systems. *Comput. Phys. Commun.*, 137:341–360, 2001.

[163] A. V. Fedorov, S. A. Brazovskii, V. N. Muthukumar, P. D. Johnson, J. Xue, L.-C. Duda, K. E. Smith, W. H. McCarroll, M. Greenblatt, and S. L. Hulbert. Direct observation of temperature-dependent Fermi surface nesting vectors in a quasi-one-dimensional conductor. *J. Phys.: Condens. Matter*, 12:L191–L198, 2000.

[164] K. E. Smith, J. Xue, L. Duda, A. Fedorov, P. D. Johnson, S. L. Hulbert, W. McCarroll, and Greenblatt M. Recent high resolution photoemission studies of electronic structure in quasi-one-dimensional conductors. *J. Electron Spectrosc. Relat. Phenom.*, 117-118:517–526, 2001.

[165] G.-H. Gweon, J. D. Denlinger, J. W. Allen, R. Claessen, C. G. Olson, H. Höchst, J. Marcus, C. Schlenker, and L. F. Schneemeyer. ARPES line shapes in FL and non-FL quasi-low-dimensional inorganic metals. *J. Electron Spectrosc. Relat. Phenom.*, 117-118:481–502, 2001.

[166] L. Perfetti, S. Mitrovic, G. Margartondo, M. Grioni, L. Forró, L. Degiorgi, and H. Höchst. Mobile small polarons and the Peierls transition in the quasi-one-dimensional conductor $K_{0.3}MoO_3$. *Phys. Rev. B*, 66:075107, 2002.

[167] H. Ando, T. Yokoya, K. Ishizaka, S. Tsuda, T. Kiss, S. Shin, T. Eguchi, M. Nohara, and H. Takagi. Angle-resolved photoemission study of $K_{0.3}MoO_3$: direct observation of temperature-depedent Fermi surface across the Peierls transition. *J. Physics: Condens. Matter*, 17:4935–4940, 2005.

[168] M. Grioni, S. Pons, and E. Frantzeskakis. Recent ARPES experiments on quasi-1D bulk materials and artificial structures. *J. Phys.: Condens. Matter*, 21:023201, 2009.

[169] H. Y. Liu, I. Gierz, J. C. Petersen, S. Kaiser, A. Simoncig, A. L. Cavalieri, C. Cacho, I. C. E. Turcu, E. Springate, F. Frassetto, L. Poletto, S. S. Dhesi, Z.-A. Xu, T. Cuk, R. Merlin, and A. Cavalleri. Possible observation of parametrically amplified coherent phasons in $K_{0.3}MoO_3$ using time-resolved extreme-ultraviolet angle-resolved photoemission spectroscopy. *Phys. Rev. B*, 188:045104, 2013.

[170] D. Mou, R. M. Konik, A. M. Tsvelik, I. Zaliznyak, and X. Zhou. Charge-density wave and one-dimensional electronic spectra in blue bronze: Incoherent solitons and spin-charge separation. *Phys. Rev. B*, 89:201116, 2014.

[171] W. J. Schutte and J. L. De Boer. The incommensurately modulated structures of the blue bronzes $K_{0.3}MoO_3$ and $Rb_{0.3}MoO_3$. *Acta Crystallogr. B*, 49:579–591, 1988.

[172] E. Machado-Charry, P. Ordejón, E. Canadell, C. Brun, and Z. Z. Wang. Analysis of scanning tunneling microscopy images of the charge-density-wave phase in quasi-one-dimensional $Rb_{0.3}MoO_3$. *Phys. Rev. B*, 74:155123, 2006.

[173] C. Noguera and J.-P. Pouget. Temperature dependence of the Peierls wavevector in quasi one dimensional conductors. *J. Phys. I*, 1:1035–1054, 1991.

[174] D. Allender, J. W. Bray, and J. Bardeen. Theory of fluctuation superconductivity from electron-phonon interactions in pseudo-one.dimensional systems. *Phys. Rev. B*, 9:119–129, 1974.

[175] G. A. Toombs. Quasi-one-dimensional conductors. *Physics Reports.*, 40:181–240, 1978.

[176] S. Girault, A. H. Moudden, and J. P. Pouget. Critical X-ray scattering at the Peierls transition of the blue bronze. *Phys. Rev. B*, 39:4430–4434, 1989.

[177] J.-P. Pouget, P. Alemany, and E. Canadell. Donor-anion interactions in quarter-filled low-dimensional organic conductors. *Materials Horizons*, 5:590–640, 2018.

[178] P. A. Lee, T. M. Rice, and P. W. Anderson. Fluctuation effects at a Peierls transition. *Phys. Rev. Lett.*, 31:462–465, 1973.

[179] H. J. Schultz. The crossover from one to three dimensions: Peierls and spin-Peierls transitions. In D. Jérome and L. G. Caron, editors, *Low-Dimensional Conductors and Superconductors*, page 95. NATO ASI B155, Plenum Press: New York, USA, 1987.

[180] R. Comès and G. Shirane. Neutron-Scattering Analysis of the Linear-Displacement Correlations in $KTaO_3$. *Phys. Rev. B*, 5:1886–1891, 1972.

[181] R. Currat, R. Comès, B. Dorner, and E. Wiesendanger. Inelastic neutron scattering in orthorhombic $KNbO_3$. *J. Phys. C: Solid State Phys.*, 7:2521–2539, 1974.

[182] R. Currat, H. Buhay, C. H. Perry, and A. M. Quittet. Inelastic neutron scattering study of anharmonic interactions in orthorhombic $KNbO_3$. *Phys. Rev. B*, 40:10741–10746, 1989.

[183] J.-P. Pouget, S. M. Shapiro, and K. Nassau. Neutron scattering study of the ferroelectric phase transition in SbSI. *J. Phys. Chem. Solids*, 40:267–277, 1979.

[184] A. Ottolenghi and J.-P. Pouget. Evidence of High Critical Temperature Charge Density Wave Transitions in the $(PO_2)_4(WO_3)_{2m}$ Family of LowDimensional Conductors for m$\geq$8. *J. Phys. I*, 6:1059–1083, 1996.

[185] P. Foury-Leylekian and J.-P. Pouget. Peierls transition in two-dimensional metallic monophospate tungsten bronzes. *Solid State Sci.*, 4:387–396, 2002.

[186] C. Escribe-Filipini, J.-P. Pouget, R. Currat, B. Hennion, and J. Marcus. Neutron Studies of the Blue Bronzes $K_{0.3}MoO_3$ and $Rb_{0.3}MoO_3$. In Gy. Hutiray and Sólyom, editors, *Charge Density Waves in Solids*, pages 71–75. Lecture Notes in Physics vol. 217, Springer-Verlag, Berlin, Germany, 1985.

[187] J. W. Brill. Elastic Properties of Low-Dimensional Materials. In M. Levy, H. Bass, and R. Stern, editors, *Handbook of Elastic Properties of Solids, Liquids and Gases*, volume II: Elastic Properties of Solids; Theory, Elements and Compounds, Novel Materials, Alloys and Building Materials, chapter 10, pages 143–162. Academic Press, 2000.

[188] B. Hennion, J. P. Pouget, and M. Sato. Charge-density-wave Phase Elasticity of the Blue Bronze. *Phys. Rev. Lett.*, 68:2374–2377, 1992.

[189] S. Ravy, H. Requardt, D. Le Bolloc'h, P. Foury-Leylekian, J.-P. Pouget, R. Currat, P. Monceau, and M. Krisch. Inelastic x-ray scattering study of

charge-density-wave dynamics in the $Rb_{0.3}MoO_3$ blue bronze. *Phys. Rev. B*, 69:115113, 2004.

[190] H. Requardt, J. E. Lorenzo, R. Currat, P. Monceau, and M. Krisch. Dynamics in the charge-density-wave system $NbSe_3$ using inelastic x-ray scattering with meV energy resolution. *Phys. Rev. B*, 66:214303, 2002.

[191] S. van Smaalen, J. L. de Boer, A. Meetsma, H. Graafsma, H.-S. Sheu, A. Daroskikh, P. Coppens, and F. Levy. Determination of the structural distortions corresponding to the q^1- and q^2-type modulations in niobium triselenide $NbSe_3$. *Phys. Rev. B*, 45:3103–3106, 1992.

[192] J. P. Pouget, R. Moret, A. Meerschaut, L. Guemas, and J. Rouxel. X-ray observation of 1-d precursor effects in $NbSe_3$ and new diffuse scattering features in $FeNb_3Se_{10}$. *J. Phys. Colloques*, 44:C3–1729, 1983.

[193] M. Maschek, S. Rosenkranz, R. Heid, A. H. Said, P. Giraldo-Gallo, I. R. Fischer, and M. Weber. Wave-vector-dependent electron-phonon coupling and the charge-density-wave transition in $TbTe_3$. *Phys. Rev. B*, 91:235146, 2015.

[194] E. Canadell and M.-H. Whangbo. Charge-density-wave instabilities expected in monophosphate tungsten bronzes. *Phys. Rev. B*, 43:1894–1902, 1991.

[195] E. Sandre, P. Foury-Leylekian, S. Ravy, and J. P. Pouget. *AbInitio* Fermi Surface Calculation for Charge-Density Wave Instability in Transition Metal Oxide Bronzes. *Phys. Rev. Lett.*, 86:5100–5103, 2001.

[196] B. Guster, D. Boskovic, M. Pruneda, P. Ordejón, E. Canadell, and J.-P. Pouget, 2019. work in progress.

[197] P. Foury and J. P. Pouget. Charge-density-wave transitions in two-dimensional transition metal oxides and bronzes. *Int. J. Mod. Phys. B*, 7:3973–4003, 1993.

[198] E. H. Lieb and D. C. Mattis. *Mathematical Physics in One Dimension*. Academic Press, New York, 1965.

[199] M. Steiner, J. Villain, and C. G. Windsor. Theoretical and experimental studies on one-dimensional magnetic systems. *Adv. Phys.*, 25:87–209, 1976.

[200] D. Jérome and H. J. Schulz. Organic conductors and superconductors. *Adv. Phys.*, 31:299–490, 1982.

[201] C. Bourbonnais and D. Jérome. Interacting Electrons in Quasi-One-Dimensional Organic Superconductors. In Andrei Lebed, editor, *The Physics of Organic Superconductors and Conductors*, chapter 12, pages 357–412. Springer, Berlin, Heidelberg, 2008.

[202] A. Pashkin, M. Dressel, M. Hanfland, and C. A. Kuntscher. Deconfinement transition and dimensional crossover in the Bechgaard-Fabre salts: Pressure- and temperature-dependent optical investigations. *Phys. Rev. B*, 81:125109, 2010.

[203] M. Weger. The metallic state in organic materials at Helium temperatures. *J. Phys. Colloques*, 39:C6–1456, 1978.

[204] V. J. Emery. Some basic questions in organic superconductivity. *J. Phys. Colloques*, 44:C3–977, 1983.

[205] C. Bourbonnais. The Dimensionality Crossover in Quasi-1D Conductors. *Mol. Cryst. Liq. Cryst.*, 119:11–18, 1985.

[206] L. G. Caron and C. Bourbonnais. Renormalization of transverse hopping integral in quasi-1D conductors. *Synth. Met.*, 27:A67–A74, 1988.

[207] S. Biermann, A. Georges, and A. Lichtenstein. Deconfinement Transition and Luttinger to Fermi Liquid Crossover in Quasi-One-Dimensional Systems. *Phys. Rev. Lett.*, 87:276405, 2001.

[208] T. Giamarchi. Theoretical framework for quasi-one dimensional systems. *Chem. Rev.*, 104:5037–5056, 2004.

[209] S. Ishibasi and M. Kohyama. Ab initio pseudopotential calculation for TTF-TCNQ and TSeF-TCNQ. *Phys. Rev. B*, 62:7839–7844, 2000.

[210] N. Thorup, G. Rindorf, H. Soling, and K. Bechgaard. The structure of di(2,3,6,7-tetramethyl-1,4,5,8-tetraselenafulvalenium) hexafluorophosphate, $(TMTSF)_2PF_6$, the first superconducting organic solid. *Acta Crystallogr. B*, 37:1236–1240, 1981.

[211] J. Moser, M. Gabay, P. Auban-Senzier, D. Jérome, K. Bechgaard, and J. M. Fabre. Transverse transport in organic conductors: possible evidence for a Luttinger liquid. *Eur. Phys. J. B*, 16:39–46, 1998.

[212] C. Coulon, P. Delhaes, S. Flandrois, R. Lagnier, E. Bonjour, and J. M. Fabre. A new survey of the physical properties of the $(TMTTF)_2$ X series. Role of the counterion ordering. *J. Phys. France*, 43:1059–1067, 1982.

[213] J. M. Delrieu, M. Roger, Z. Toffano, A. Moradpour, and K. Bechgaard. N.M.R. proton lineshape in $(TMTSF)_2X$: incommensurability of nesting vector and order parameter. *J. Phys. France*, 47:839–861, 1986.

[214] T. Takahashi, Y. Maniwa, H. Kawamura, and G. Saito. Determination of SDW Characteristics in $(TMTSF)_2PF_6$ by ^{1}H-NMR Analysis. *J. Phys. Soc. Jpn.*, 55:1364–1373, 1986.

[215] L. Ducasse, M. Abderraba, and B. Gallois. Temperature dependence of the Fermi surface topography in the $(TOTSF)_2X$ and $(TMTTF)_2X$ families. *J. Phys. C: Solid State Phys.*, 18:L947–L951, 1985.

[216] P. Alemany, J.-P. Pouget, and E. Canadell. Electronic structure and anion ordering in $(TMTSF)_2ClO_4$ and $(TMTSF)_2NO_3$: A first-principles study. *Phys. Rev. B*, 89:155124, 2014.

[217] P. M. Grant. Electronic structure of 2:1 charge transfer salts of TMTCF. *J. Phys.(Paris)*, 44:C3–847, 1983.

[218] P. Auban-Senzier, D. Jérome, N. Doiron-Leyraud, S. René de Cotret, A. Sedeki, C. Bourbonnais, L. Taillefer, P. Alemany, E. Canadell, and K. Bechgaard. The metallic transport of $(TMTSF)_2X$ organic conductors

close to the superconducting phase. *J. Phys.: Condens. Matter*, 23:345702, 2011.

[219] K. Nakamura, Y. Nohara, Y. Yosimoto, and Y. Nomura. Ab initio GW plus cumulant calculation for isolated band systems: Application to organic conductor $(TMTSF)_2PF_6$ and transition-metal oxide $SrVO_3$. *Phys. Rev. B*, 93:085214, 2016.

[220] K. Yamaji. Semimetallic SDW state in Quasi One-Dimensional Conductors. *J. Phys. Soc. Jpn.*, 51:2787, 1983.

[221] K. Yamaji, T. Ishiguro, and G. Saito. *Organic Superconductors*. 2nd edition, Springer-Verlag, Berlin, 1998.

[222] G. Montambaux. Metal-spin-density-wave transition in a quasi-one-dimensional conductor: Pressure and magnetic field effects. *Phys. Rev. Lett.*, 38:4788–4795, 1988.

[223] L. Degiorgi, M. Dressel, A. Schwartz, B. Alavi, and C. Grüner. Direct Observation of the Spin-Density-Wave Gap in $(TMTSF)_2PF_6$. *Phys. Rev. Lett.*, 76:3838–3841, 1996.

[224] J.-P. Pouget. Structural Aspects of the Bechgaard and Fabre Salts: An Update. *Crystals*, 2:466–520, 2012.

[225] J. P. Pouget, R. Moret, R. Comès, and K. Bechgaard. X-Ray Diffuse Scattering Study of Superstructure Formation in $(TMTSF)_2ReO_4$ and $(TMTSF)_2NO_3$. *J. Physique Lett.*, 42:L543–L546, 1981.

[226] J. P. Pouget, G. Shirane, K. Bechgaard, and J. M. Fabre. X-ray evidence of a structural phase transition in di-tetramethyltetraselenafulvalenium perchlorate $[(TMTSF)_2C10_4]$, pristine and slightly doped. *Phys. Rev. B*, 27:5203–5206, 1983.

[227] G. Montambaux. Low Dimensional Conductors and Superconductors. In D. Jeróme and L. G. Caron, editors, *Low Dimensional Conductors and Superconductors*, pages 233–242. NATO ASI B 155, Plenun Press, 1987.

[228] Y. Hasegawa and K. Kishigi. Nesting of the Fermi surface and the wave-vector-dependent susceptibility in quasi-one-dimensional electron systems. *Phys. Rev. B*, 81:235118, 2010.

[229] Y. Hasegawa and K. Kishigi. Generalized susceptibility of a quasi-one-dimensional system with periodic potential: A model for the organic superconductor $(TMTSF)_2ClO_4$. *Phys. Rev. B*, 78:045117, 2008.

[230] T. Vuletic, P. Auban-Senzier, C. Pasquier, S. Tomic, D. Jérome, M. Héritier, and K. Bechgaard. Coexistence of superconductivity and spin density wave orderings in the organic superconductor $(TMTSF)_2PF_6$. *Eur. Phys. J. B*, 25:319–331, 2002.

[231] P. Foury-Leylekian, S. Petit, I. Mirebeau, G. André, M. de Souza, M. Lang, E. Ressouche, A. Moradpour, and J.-P. Pouget. Low-temperature structural effects in the $(TMTSF)_2PF_6$ and AsF_6 Bechgaard salts. *Phys. Rev. B*, 88:024105, 2013.

[232] Y. Barrens, J. Gaultier, S. Bracchetti, P. Guionneau, D. Chasseau, and J. M. Fabre. Low temperature structural properties of the $(TMTSF)_2NO_3$ salt. *Synth. Met.*, 103:2042–2043, 1999.

[233] J. P. Pouget, R. Moret, R. Comès, K. Bechgaard, J. M. Fabre, and L. Giral. X-Ray Diffuse Scattering Study of Some $(TMTSF)_2X$ and $(TMTTF)_2X$ Salts. *Mol. Cryst. Liq. Cryst.*, 79:485–499, 1982.

[234] W. Kang and O. H. Chung. Quasi-one-dimensional Fermi surface of $(TMTSF)_2NO_3$. *Phys. Rev. B*, 79:045115, 2009.

[235] R. Moret, S. Ravy, J. P. Pouget, R. Comès, and K. Bechgaard. Anion-Ordering Phase Diagram of Di(tetramethyltetraselenafulvalenium) Perrhenate, $(TMTSF)_2Re0_4$. *Phys. Rev. Lett.*, 57:1915–1918, 1986.

[236] P. Wzietek, F. Creuzet, C. Bourbonnais, D. Jérome, K. Bechgaard, and P. Batail. Nuclear relaxation and electronic correlations in quasi-one-dimensional organic conductors. II. Experiments. *J. Phys. I France*, 3:171–201, 1993.

[237] M. Ribault, J. P. Pouget, D. Jérome, and K. Bechgaard. Superconductivity and absence of a Kohn anomaly in the quasi-one-dimensional organic conductor $(TMTSF)_2AsF_6$. *J. Physique Lett.*, 41:L607–L610, 1980.

[238] According to the data in refs. [233, 224] the BOW response of $(TMTSF)_2ClO_4$ diverges in a Curie-Weiss manner $\chi_{BOW} \sim 1/(T+\theta)$, with $\theta = 10\pm5$ K.

[239] N. Cao, T. Timusk, and K. Bechgaard. Unconventional Electrodynamic Response of the Quasi-One-Dimensional Organic Conductor $(TMTSF)_2ClO_4$. *J. Phys. I France*, 6:1719–1726, 1996.

[240] J. M. Delrieu, M. Roger, C. Coulon, R. Laversanne, and E. Dupart. Determination of SDW vector and amplitude by NMR and anisotropy by EPR in $(TMTTF)_2SbF_6$ and $(TMTSF)_2ClO_4$. *Synth. Met.*, 27:35–40, 1998.

[241] M. Roger, J. M. Delrieu, and E. W. Mbougue. Theoretical explanation of the antiferromagnetic anisotropy in organic superconductors: A probe for the spin-density-wave amplitude and nesting vector. *Phys. Rev. B*, 34:4952–4955, 1996.

[242] K. Hiraki, T. Nemoto, T. Takahasi, H. Kang, Y. Jo, W. Kang, and O.-H. Cung. NMR studies of the exotic members of the Bechgaard salts NO_3 and FSO_3 salts. *Synth. Met.*, 135-136:691–692, 2003.

[243] H. Satsukawa, K. Hiraki, T. Takahashi, H. Kang, Y. J. Jo, and W. Kang. ^{1}H-NMR analysis of the SDW properties of $(TMTSF)_2NO_3$. *J. Phys. IV France*, 114:133–134, 2004.

[244] G. Grüner. The dynamics of spin-density waves. *Rev. Mod. Phys.*, 60:1–24, 1994.

[245] S. Nagata, M. Misawa, Y. Ihara, and A. Kawamoto. Commensurability of the Spin-Density-Wave State of $(TMTSF)_2PF_6$ Observed by ^{13}C-NMR. *Phys. Rev. Lett.*, 110:167001, 2013.

[246] W. G. Clark, M. E. Hanson, W. H. Wong, and B. Alavi. Evidence that the SDW phase transition in $(TMTSF)_2PF_6$ is first order. *Physica B*, 194-196:285–286, 1994.

[247] P. Bak. Theory of Elastic Phase Transitions and Soft Acoustic Modes. In A. Pekalski and J. A. Przystawa, editors, *Modern Trends in the Theory of Condensed Matter*, pages 414–431. Lecture Notes in Physics vol. 115, Springer-Verlag, Berlin Heidelberg, 1980.

[248] More explicitly, if for simplicity one only considers fluctuations associated to the equal maxima q_1 and q_2 of the Lindhard function at T_{SDW} for $(TMTSF)_2PF_6$, the free energy Landau development associated to the complex order parameters η_1 and η_2, corresponding to the q_1 and q_2 modulations, respectively, can be schematically written as $F = a_1 \mid \eta_1 \mid^2 + a_2 \mid \eta_2 \mid^2 + u_1 \mid \eta_1 \mid^4 + u_2 \mid \eta_2 \mid^4 + w \mid \eta_1 \mid^2 \mid \eta_2 \mid^2$. The treatment of F using renormalization group methods should lead to a regime where the fourth order terms are no longer positive definite, which conducts to a first order transition.

[249] J. P. Pouget and S. Ravy. X-ray evidence of charge density wave modulations in the magnetic phases of $(TMTSF)_2PF_6$ and $(TMTTF)_2Br$. *Synth. Met.*, 85:1523–1528, 1997.

[250] A. Ardavan, S. Brown, S. Kagoshima, K. Kanoda, M. Kuroki, H. Mori, M. Ogata, S. Uji, and J. Wosnitza. Recent Topics of Organic Superconductors. *J. Phys. Soc. Jpn.*, 81:011004, 2012.

[251] D. Jérome and S. Yonezawa. Novel superconducting phenomena in quasi-one-dimensional Bechgaard salts. *C. R. Physique*, 17:357–375, 2016.

[252] A. Sedeki, D. Bergeron, and C. Bourbonnais. Extended quantum criticality of low-dimensional superconductors near a spin-density-wave instability. *Phys. Rev. B*, 85:165129, 2012.

[253] D. Zanchi and G. Montambaux. Sign Reversals of the Quantum Hall Effect in Quasi-1D Conductors. *Phys. Rev. Lett.*, 77:366–369, 1996.

[254] P. Foury-Leylekian, J.-P. Pouget, Y.-J. Lee, R. Nieminen, P. Ordejón, and E. Canadell. Density-wave instability in $\alpha-(\text{BEDT-TTF})_2\text{KHg(SCN)}_4$ studied by X-ray diffuse scattering and by first-principles calculations. *Phys. Rev. B*, 82:134116, 10 2010.

[255] A. Meerschaut and J. Rouxel. Pseudo-one-dimensional MX_3 and MX_4 transition metal chalcogenides. In J. Rouxel, editor, *Crystal Chemistry and Properties of Materials with Quasi-One-Dimensional Structures*, pages 205–279. D. Reidel Publishing Company, Dordrecht, Holland, 1986.

[256] E. Canadell, S. Jobic, R. Brec, J. Rouxel, and M.-H. Whangbo. Importance of short interlayer Te...Te contacts for the structural distortions and physical properties of CdI_2-type layered transition-metal ditellurides. *Journal of Solid State Chemistry*, 99:189–199, 1992.

[257] G. A. Papoian and R. Hoffmann. Hypervalent Bonding in One, Two, and Three Dimensions: Extending the Zintl-Klemm Concept to Nonclassical Electron-Rich Networks. *Angew. Chem. Int. Ed. Engl.*, 39:2409–2448, 2000.

[258] R. Patschke and M. G. Kanatzidis. Polytelluride compounds containing distorted nets. *Phys. Chem. Chem. Phys.*, 4:3266–3281, 2002.

[259] E. Canadell, S. Jobic, R. Brec, and J. Rouxel. Electronic structure and properties of anionic mixed valence and layered $CrTe_3$: The question of extended tellurium bonding in transition metal ditellurides. *Journal of Solid State Chemistry*, 98:59–70, 1992.

[260] K. Selte, A. Kjekshus. On the Crystal Structure of $NbTe_4$. *Acta Chemica Scandinavica*, 18(3):690–696, 1964.

[261] E. Bjerkelund, A. Kjekshus. On the Crystal Structure of $TaTe_4$. *Journal of the Less Common Metals*, 7(3):231–234, 1964.

[262] Y. Gao, L. Xu, Y. Qiu, Z. Tian, S. Yuan, and J. Wang. Anisotropic large magnetoresistance in $TaTe_4$ single crystals. *Journal of Applied Physics*, 122:135101, 2017.

[263] X. Luo,F. C. Chen,Q. L. Pei,J. J. Gao, J. Yan,W. J. Lu,P. Tong,Y. Y. Han,W. H. Song,Y. P. Sun. Resistivity plateau and large magnetoresistance in the charge density wave system $TaTe_4$. *Applied Physics Letters*, 110:092401, 2017.

[264] X. Yang, Y. Zhou, M. Wang, H. Bai, X. Chen, Ch. An, Y. Zhou, Q. Chen, Y. Li, Z. Wang, J. Chen, Ch. Cao, Y. Li, Y. Zhou, Z. Yang, and Z.-A. Xu. Pressure induced superconductivity bordering a charge-density-wave state in $NbTe_4$ with strong spin-orbit coupling. *Scientific Reports*, 8:6298, 2018.

[265] B. S. de Lima, N. Chaia, T. W. Grant, L. R. de Faria, J. C. Canova, F. S. de Oliveira, F. Abud, and A. J. S. Machado. Large enhancement of the CDW resistivity anomaly and traces of superconductivity in imperfect samples of $NbTe_4$. *Materials Chemistry and Physics*, 326:95–99, 2019.

[266] K. D. Bronsema, S. van Smaalen, J. De Boer, G. A. Wiegers, F. Jellinek, J. Mahy. The determination of the commensurately modulated structure of Tantalum tetratelluride. *Acta Crystallographica Section B*, 43(4):305–313, 1987.

[267] J. Kusz, H. Böhm. The Low Temperature Structure of $NbTe_4$. *Acta Crystallographica Section B*, 50(6):649–655, 1994.

[268] S. van Smaalen, K. D. Bronsema, J. Mahy. The determination of the incommensurately modulated structure of Niobium tetrateluride. *Acta Crystallographica Section B*, 42(1):43–50, 1986.

[269] F. W. Boswell, A. Prodan, and J. K. Brandon. Charge-density waves in the quasi-one-dimensional compounds $NbTe_4$ and $TaTe_4$. *J. Phys. C: Solid State Physics*, 16:1067–1076, 1983.

[270] M.-H. Whangbo, P. Gressier. Band Structure of $NbTe_4$. *Inorganic Chemistry*, 23(9):1228–1232, 1984.

[271] S. Tadaki, N. Hino, T. Sambongi, K. Nomura, and F. Lévy. Electrical properties of $NbTe_4$ and $TaTe_4$. *Synthetic Metals*, 38:227–234, 1990.

[272] D. W. Bullet. p-d Band overlap and the Electronic Structure of $NbTe_4$. *Physics C: Solid State Physics*, 17(2):253–257, 1984.

[273] F. Zwick, H. Berger, M. Grioni, G. Margaritondo, L. Forró, J. LaVeigne, D. B. Tanner, M. Onellion. Coexisting one-dimensional and three-dimensional spectral in $TaTe_4$. *Physical Review B*, 59(11):7762–7766, 1999.

[274] F. W. Boswell J. C. Bennett A. Prodan J. M. Corbett, L. G. Hiltz. Determination of the symmetry of Charge-Density-Wave modulations in $TaTe_4$ by HREM. *Ultramicroscopy*, 26(1-2):43–50, 1988.